Excitonic States and Optoelectronic Properties of Organic Semiconductors - A Quantum-Chemical Study Focusing on Merocyanines and Perylene-Based Dyes Including the Influence of the Environment

Dissertation zur Erlangung des naturwissenschaftlichen Doktorgrades
der
Julius-Maximilians-Universität Würzburg

vorgelegt von

Christof Walter

aus
Bamberg

Würzburg, 2015

Eingereicht bei der Fakultät für Chemie und Pharmazie am

_____

Gutachter der schriftlichen Arbeit

1. Gutachter: _____

1. Gutachter: _____

Prüfer des öffentlichen Promotionskolloqiums

1. Prüfer: _____

2. Prüfer: _____

3. Prüfer: _____

Datum des öffentlichen Promotionskolloqiums

_____

Doktorukunde ausgehändigt am

_____

I don't pretend we have all the answers. But the questions are certainly worth thinking about...

(Arthur C. Clarke)

Contents

1 Introduction

Over the last decades the relevance of computational chemistry has significantly increased for the academic[1] as well as for the industrial research.[2] It is an invaluable tool for the rationalization of experimental findings and helps to provide insight and understanding. Applications range from the elucidation of reaction mechanisms and the exploration of the electronic structure of novel compounds to the interpretation of spectra. However, apart from rationalizing, corroborating and extending the experimentally obtained data, computational chemistry can also make predictions and thus guide the experiments in new and promising directions. For instance, the most suitable candidates of a class of compounds for a certain application can be selected. Such a prescreening based on *in silico* predictions makes it possible to prepare only the most promising molecules, which is much more efficient than synthesizing all, e.g. via high-throughput screening. Similarly, it is possible to optimize molecules by choosing suitable substituents and finding the best substitution patterns. These procedures are most efficient in close collaboration with the experiment creating an iterative circle.

The scope of computational chemistry and especially of the quantum chemical methods is broadened by the increasing computer power and more importantly by the introduction of new methods and the development of more efficient codes. However, it is equally important to establish the applicability of the developed methods for the different fields of chemistry, thus providing the basis for an assessment of the possibilities and the quality of the predictions.

In this thesis the applicability of the toolkit of computational chemistry is investigated for different fields. The main focus is on the description of systems with an unusual electronic structure, such as the excitonic states in organic semiconductors, but a boron-containing bipolaron (Bis(borolyl)thiophene dianion) with low-lying triplet states and the excited states of pyracene are also examined. The investigation of the latter two systems, however, also involves questions important for organic semiconductors. Concerning the semiconductors the focus is laid on organic solar cells based on small organic molecules. Organic solar cells are of great interest, since their production is cheap and highly flexi-

ble and even transparent systems can be created.[3,4] With efficiencies of 10-15% being in principle possible and the current world record cell achieving 12%,[5] these devices seem very promising. However, despite the very encouraging reports on the efficiencies, one should keep in mind that the test cells are small and the data obtained cannot directly be transferred to the operating conditions of an actual cell in an application. Furthermore, the durability of the modules is still an issue. In order to create improved cells and to find new materials or optimize the currently used molecules, a fundamental insight into the elementary processes is needed. Computational chemistry can provide insight by separating effects that are experimentally inseparable, creating models and providing data for a molecule under idealized conditions, thus showing the in principle obtainable performance of a certain material. Small organic molecules are especially suitable for a theoretical modeling, since they exhibit definite structure-property relationships. Thus computational chemistry should be able to help to find the guidelines for a rational design and to give practical advice via prescreenings. However, in order to be able to do this, the applicability of the different tools needs to be investigated.

Obviously, this goal is pursued by many groups around the world.[i] This thesis focuses on the description of excitonic states, since one of the most important elementary processes in organic solar cells is the exciton diffusion (see below). However, the description of an excitonic state in such molecules is far from simple, because possibility of charge-transfer states makes the application of standard methods like TDDFT troublesome. Additionally, the size of the molecules and the fact that the exciton is not necessarily localized on one monomer makes the application of accurate methods, like CC2 or CASPT2, often computationally impossible. Furthermore, the environment can play an important role and hence needs to be included, which makes the problem even more demanding. In this work the applicability and the performance of the toolkit of computational chemistry is investigated with regard to questions related to optoelectronic devices. Whenever possible ways to improve the performance are suggested.

While the focus is laid on the modeling of excitonic states with the inclusion of the environment, other points important for the performance in the cell are also addressed. The aim is to provide guidelines which computational methods are applicable and to add another piece in the quest for a fundamental understanding of organic optoelectronic devices, which hopefully will prove useful for the design of future cells.

In this field the study mainly covers two classes of compounds, the merocyanines and the

[i] See for instance[6–15] and references therein.

perylene-based dyes, which both are applied in devices.
The other two systems investigated in this thesis also provide challenges for computational chemistry. The electronic structure of the Bis(borolyl)thiophene dianion is highly interesting due to possible biradical resonance contributors and demands for multi-reference methods. Bipolarons are currently investigated due to their appearance in conducting polymers. Because of the strain on the naphthalene core of pyracene due to the bridges the interplay between ring strain and electronic effects is of special interest. Since the first two exited states can (depending on the geometry) become energetically quite close, a theoretical description is challenging.
This thesis is organized as follows: After a very short overview of organic solar cells, the most important computational methods for the calculation of excited states are reviewed. Then, different ways to include the environment in the calculations are discussed.
A selection of these methods is then applied to the merocyanines and the perylene-based dyes. In the chapter on the merocyanines, at first the polarizable continuum methods for excited states are used to describe a photochemical isomerization observed experimentally. Apart from being photochemically very interesting, this isomerization is also of the utmost importance for the exciton transport, since it involves a twisted minimum energy structure in the excited state that offers a possible deactivation channel. In the second part, the possibility of an assessment of the most suitable molecules for the application in organic optoelectronic devices with quantum-chemical methods is discussed. It is also addressed whether a correlation between calculated HOMO energies and measured open-circuit voltages can be found. Furthermore, it is investigated how the environment influences the molecular properties and the question is addressed whether an effective ϵ can be used to model the crystal environment via PCM methods. A potential application of VB/MM-type methods is also briefly covered.
The subsequent chapter investigates the applicability of TDDFT and semi-empirical methods for the modeling of excitonic states in perylene-based dyes, especially for the description of a potential exciton trapping mechanism based on intermolecular degrees of freedom in a dimer.[16–18] As a test system for the benchmark, the longitudinal shift of two π-stacked monomers against each other is used. The applicability or the failure of the different functionals and methods for this system is rationalized using a simple approximate character analysis. It is furthermore shown that the semi-empirical methods already fail to provide an accurate description of the ground state. Having identified two suitable TDDFT approaches, two corresponding applications are presented briefly.
In the last part of this chapter, the inclusion of the environment via a QM/MM approach

is discussed. It is shown that the standard force fields fail to reproduce the ground-state potential energy curve of the longitudinal shift. The failure is attributed to the isotropic modeling of the closed-shell repulsion between two atomic centers. Hence an improved force field (OPLS-AA$_O$) that relies on an anisotropic overlap-based description of the closed-shell repulsion is presented and tested for its performance and generality. A brief demonstration of the use of the anisotropic repulsion as a correction term for the semi-empirical methods for the ground state is also given.

Using the novel force field and the results from the benchmark on the TDDFT approach, a QM/MM calculation of the excited states in a π-stacked tetramer using the inner dimer as QM-part and an electrostatic embedding scheme is discussed.

The last chapter covers the studies on the theoretical description of Bis(borolyl)thiophene and pyracene, which are also related to organic semiconductors. For the elucidation of the electronic structure of the bipolaron the amount of biradical character and the singlet-triplet gap are of special importance. The calculation of singlet-triplet gaps demands for high-level methods like CASPT2, especially for biradical systems, but the size of the compound makes only UDFT methods applicable. Thus, the accuracy of UDFT for the prediction of the singlet-triplet gap is evaluated against CASPT2 calculations on a simplified model system.

The second study is concerned with the electronic structure of pyracene, especially in its excited states and focuses on the interplay between steric and electronic effects. A special focus is laid on the prediction of the vibrational frequencies in the excited state using CC2 and ADC(2). These two studies are aimed at completing the information gained by experimentally working groups.

2 Organic Photovoltaics

The growing population of the world combined with the economic growth and the rising wealth in the newly industrialized countries leads to a significant increase in the energy demands. It is estimated that by 2050, the energy need might be the quadruple of today.[19] While the deposits of fossil fuels are limited and their use is one of the main reasons for pollution, nuclear energy is controversial and there is still neither a satisfactory solution for the ultimate storage of the nuclear waste nor an estimation of associated costs for future generations.[20] Thus alternatives making use of wind and solar energy are in the focus of the research and the energy policy of many countries. Several of these technologies are however still economically uncompetitive, which often leads to a conflict between market forces and the goals of an environmentally sustainable policy. Furthermore, many promising technologies look less attractive if one considers the whole eco-balance.

The direct use of solar energy is one of the most appealing ideas, since it is the principle that nature applies in the photosynthesis and that drives the atmospheric processes. The constant energy flow from the sun is not only ultimately responsible for the production of food and fossil fuels, but also for many other energy resources, like flowing water and wind.[20]

Although silicon-based solar cells give a good performance and are well established, their high production costs and the huge amount of energy that is needed in the process lessen their economical and ecological efficiency. Hence, their application is often only sensible in regions with a high amount of solar irradiation, which are not necessarily the regions with a high energy consumption.

Due to the cheap production costs organic solar cells[21] should be economically more efficient and thus be profitable even under non-optimal conditions. The interest in the whole field of organic electronics has steadily increased during the last half century.[22] The market for cheap and flexible devices is huge and many applications apart from organic photovoltaic cells have been devised, like organic light-emitting diodes (OLEDs)[23] or organic field-effect transistors (OFETs).[24] While several applications relying on OLEDs (e.g. TV sets) are already on the market,[25] only few devices using organic photovoltaic cells are

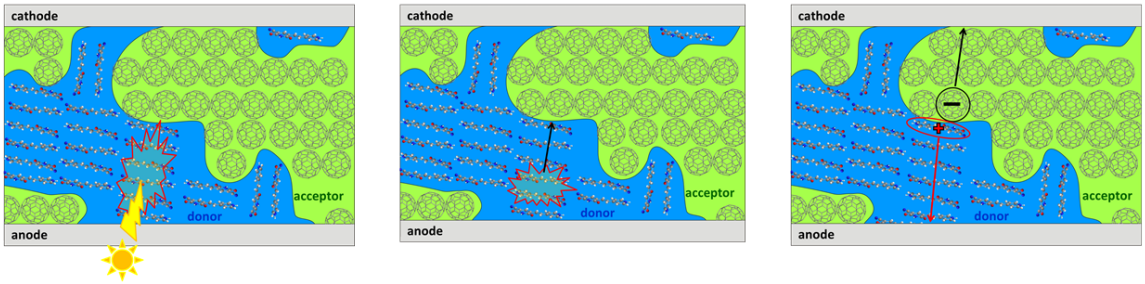

Figure 2.1: Elementary processes of organic photovoltaics in a typical bulk heterojunction solar cell. Left: Excitation, Middle: Formation of a localized exciton and exciton diffusion, Right: Exciton dissociation at the interface and charge transport

commercially produced. Due to world's energy needs organic solar cells are nevertheless of special interest. Contrary to solar cells based on inorganic materials, where the deposition is energy intensive, organic solar cells can in principle be solution-processed, which is reason for the decreased production costs.[20] Furthermore the production of standard organic materials needs less energy than for instance silicon, which has to be manufactured at high temperatures using electric-arc furnaces starting from quartz.[20] Using the established structure-property relationships and the immense synthetic toolbox of organic chemistry makes it in principle possible to rationally design tailored materials. As already metioned flexible and transparent devices are possible, which would ideally fit to the modern urban architecture. Not long after the preparation of the first bilayer solar cell was reported by Tang,[26] there has hence been a growing research activity[i] in this field since the early 1990s.[20]

Organic solar cells typically consist of two materials, an electron donor and an electron acceptor, which form the analog of the p-n junctions in silicon-based cells.[20] The elementary processes in an organic solar cell are schematically depicted in Fig. 2.1. While in the latter the light absorption leads directly to free charge carriers, which move in bands, in an organic solar cell at first a so-called Frenkel exciton, a localized excitation is created. This exciton can be localized on one or several monomers. The exciton binding energy is quite high in organic solar cells and therefore the exciton does not dissociate into charge carriers by itself. At first it needs to diffuse to the donor-acceptor interface, where charges

[i] Of course the organic solar cells are also challenged by other developments like dye-sensitized solar cells (the so-called Grätzel cells),[27] thin film techniques based on a-Si, cadmium telluride (CdTe) or copper indium gallium selenide (CIGS)[20] and most recently the preovskite-based cells.[28–30]

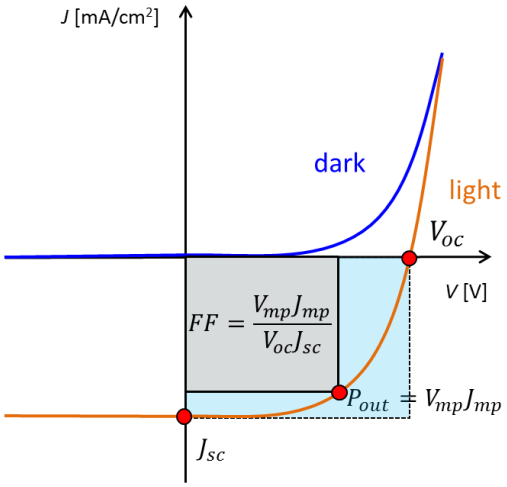

Figure 2.2: Schematic plot of a current-voltage curve in the dark and under illumination.[3] For the explanation of the essential parameters, see text.

can be created due to the driving force created by the correct level alignment of donor and acceptor (see below).[3,11,20] The exact mechanism of the exciton dissociation is still actively discussed, especially the role of "hot" states (see[31–33] and references therein). Since the exciton needs to reach the interface before it decays, the distance to the interface at each point should be as small as possible, which can be achieved by using a bulk heterojunction arrangement, where donor and acceptor materials do not simply form two planar films, but an interpenetrating network.[20] Thus the diffusion to the interface is facilitated, but the morphology needs of course to be carefully controlled, since the created charges must be able to travel to the electrodes in order to create a current.

All these processes, i.e. exciton formation, diffusion and dissociation as well as charge transport have to be optimized to arrive at a working cell with a high efficiency.[11] For inorganic solar-cells a theoretical maximum efficiency has been derived, the so-called Shockley-Queisser limit, which depends on properties like the band gap.[34] This limit was adapted to materials with a non-negligible exciton binding energy and is for current state-of-the art materials around 22%.[35ii]

The efficiency is typically measured via current-voltage (J-V) curves.[3] One such curve is shown schematically in Figure 2.2. The short circuit current J_{sc} is the maximal photocurrent that can be obtained with the solar cell (when no external resistance is there)

[ii] One currently actively discussed topic is to exploit singlet-fission to go beyond the Shockley-Queisser limit, see[36–38] and references therein.

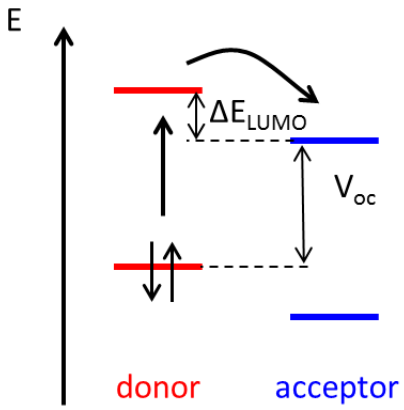

Figure 2.3: Energy level diagram of a solar cell.

and is influenced by the number of absorbed photons (up to a certain level, where saturation occurs), device thickness and charge transport properties.[3] V_{oc} is the maximum voltage obtainable with the solar cell (when the current is zero) and is typically believed to be dependent on the energetic levels of the frontier orbitals (see Figure 2.3).[3] Hence the higher the gap between the HOMO of the donor and the LUMO of the acceptor, the higher V_{oc}. However optimizing a solar cell is inherently a multiparameter problem, since the HOMO-LUMO gap of the donor should of course fit to the solar spectrum and the offset between the LUMOs of donor and acceptor ΔE_{LUMO} should not be too small, since it is the driving force for the charge transfer at the interface.[39] The overall efficiency of the solar cell is given by the ratio of the output power an the input power (i.e. the power of the incident radiation).[3] The maximum output power is located in Fig. 2.2 at the point of the curve, where the product of V and J is maximal, i.e. V_{mp} and J_{mp}. The power conversion efficiency, η can also be expressed in terms of V_{oc} and J_{sc}, which are more easily interpreted (and measured) by introducing the fill-factor FF,[3]

$$\eta = \frac{P_{out}}{P_{in}} = \frac{V_{mp}J_{mp}}{P_{in}} = \frac{V_{oc}J_{sc}FF}{P_{in}}. \tag{2.1}$$

The fill factor is given by

$$FF = \frac{V_{mp}J_{mp}}{V_{oc}J_{sc}}, \tag{2.2}$$

which corresponds to the ratio of the two rectangular surfaces in Fig. 2.2. The fill-factor is influenced by the balance between the charge carrier recombination and the transport processes.

The transport of the excitons and the charges is usually assumed to work via a hopping process.[40,41] One of the drawbacks of organic solar cells is that the charge mobility is typically quite low compared to inorganic solar cells. However, contrary to band transport, which becomes less efficient with increasing temperature,[iii] due to scattering processes at the phonons, the thermally activated hopping becomes more efficient. While the standard test conditions demand a constant temperature of 25 °C, this is far from typical operating conditions, where much higher temperatures are observed. Thus it is believed that the test conditions are biased towards inorganic solar cells, since they will perform better than under operating conditions, while organic solar cells are expected to perform worse.[43]

Most organic solar cells use a p-conducting material and C_{60}-PCBM as electron conductor,[20] but a significant amount of research is going into the design of stable n-conducting materials, whose sensitivity towards gases and humidity is more problematic than for p-conductors.[44] Stability and thus also durability is another significant problem for organic solar cells, since the organic compounds are more prone to degradation than their inorganic counterparts.[20]

The exciton diffusion length in typical organic solar cells is also quite short (5-10 nm) and hence only excitons created in a volume element with this distance to the interface can contribute to the current.[3] Apart from the low mobility, the band gap of organic semiconductors is typically too large compared to the solar spectrum and hence the synthesis of low-band gap materials is heavily investigated.[45,46] Some of the disadvantages of organic solar cells are offset by the strong absorption coefficients, which makes it possible to produce ultrathin devices, which nevertheless show a considerable light absorption. The use of thin films together with the bulk-heterojunction arrangement also decrease the problem of the low exciton diffusion lengths.

The plethora of possible organic compounds and the possibility to fine tune them provides a huge parameter space for the optimization of organic solar cells, which leads to a higher flexibility than in inorganic cells. Due to these immense possibilities there is still a high potential for significantly improving the solar cells. Up to now, a lot of the research

[iii] In regions with intense solar radiation the solar panels can obviously become quite hot, which makes the reduced efficiency with increasing temperature of silicon-based solar cells problematic. It furthermore leads to the paradox situation that, for instance, the photovoltaic systems installed in Germany reach their peak performance in spring instead of July, where the intensity of the solar radiation is actually higher.[42] In order to circumvent this problem, cooling systems can be used.[42]

for new materials is based on trial and error, which is not very efficient. In order to devise rules for a rational and efficient design the electronic structure of the materials and the elementary processes need to be fundamentally understood and structure-property relationships have to be established and improved.

3 Computational Methods for the Calculation of Excited States

Although TDDFT is currently the workhorse for large- and medium-sized molecules, computational chemistry provides a plethora of methods for the description of excited states.[47] At first, the theoretical foundations, i.e. Hartree-Fock (HF) theory and ground-state density functional theory (DFT) are summarized, since they provide the starting point for most methods. Some basic concepts for the description and classification of excited states are also introduced. Afterwards, an overview of the most important methods and their scope and limitations is given. At first the approaches, which rely directly on variational theory, are covered and then linear response and propagator methods are described. The last section gives a very short outline of other methods, which are recent developments or less common and/or have not been used in the context of this thesis.

3.1 Theoretical Foundations

3.1.1 Hartree-Fock and Density Functional Theory

If the time evolution of the system in question is not of interest (and relativistic effects like spin-orbit coupling can be neglected) the wave function can be obtained by solving the time-independent Schrödinger equation

$$\hat{H} \left|\Psi\right\rangle = E \left|\Psi\right\rangle , \tag{3.1}$$

with the molecular Hamiltonian[48]

$$\begin{aligned}\hat{H} &= \hat{T}_e + \hat{T}_n + \hat{V}_{en} + \hat{V}_{ee} + \hat{V}_{NN} \\ &= -\sum_{i=1}^{N}\frac{1}{2}\nabla_i^2 - \sum_{A=1}^{N_{nuc}}\frac{1}{2M_A}\nabla_A^2 - \sum_{i=1}^{N}\sum_{A=1}^{N_{nuc}}\frac{Z_A}{\mathbf{r}_{iA}} + \sum_{i=1}^{N}\sum_{j>i}^{N}\frac{1}{\mathbf{r}_{ij}} + \sum_{A=1}^{N_{nuc}}\sum_{B>A}^{N_{nuc}}\frac{Z_A Z_B}{\mathbf{R}_{AB}},\end{aligned} \tag{3.2}$$

with N being the number of electrons, N_{nuc} the number of nuclei and ∇ the nabla-operator. The shorthand $\mathbf{r}_{ij} = |\mathbf{r}_i - \mathbf{r}_j|$ has been used. In electronic structure theory the **Born-Oppenheimer approximation**[48] is usually applied, which leads to the electronic Hamiltonian

$$\begin{aligned}\hat{H} &= \hat{T}_e + \hat{V}_{en} + \hat{V}_{ee} \\ &= -\sum_{i=1}^{N}\frac{1}{2}\nabla_i^2 - \sum_{i=1}^{N}\sum_{A=1}^{N_{nuc}}\frac{Z_A}{\mathbf{r}_{iA}} + \sum_{i=1}^{N}\sum_{j>i}^{N}\frac{1}{\mathbf{r}_{ij}} \\ &= \sum_{i=1}^{N}\hat{h}_i + \sum_{i<j}^{N}\hat{g}_{ij}.\end{aligned} \tag{3.3}$$

The nuclear repulsion energy V_{NN} is just a classical term and is usually added to the electronic energy after the electronic structure calculation is finished.
The lowest eigenvalue E_0 corresponds to the ground-state energy, while the higher eigenvalues E_i with $i \neq 0$ are the energies of the different excited states. A specific excitation energy is thus given as the difference $\omega_i = E_i - E_0$.
Since the high-dimensionality of the molecular wave function combined with the antisymmetry condition imposed by the Pauli principle[48] make an analytical or direct numerical solution impossible (except for very simple cases) even within the Born-Oppenheimer approximation, further approximation have to be introduced.
As a first step we assume that the ground-state wave function Ψ can be modeled by a single **Slater determinant** Φ_0,

$$\Phi_0 = \frac{1}{\sqrt{N!}}\begin{vmatrix}\chi_1(1) & \chi_2(1) & \dots & \chi_N(1) \\ \chi_1(2) & \chi_2(2) & \dots & \chi_N(2) \\ \vdots & \vdots & \ddots & \vdots \\ \chi_1(N) & \chi_2(N) & \dots & \chi_N(N)\end{vmatrix} = |\chi_1\chi_2\cdots\chi_N|, \tag{3.4}$$

with the spin orbitals $\{\chi_i\}$ (one-electron wave functions), that can be written as a product of a spatial and a spin part $\chi_i(\mathbf{x}) = \phi_i(\mathbf{r})\sigma(\omega)$. In order to find the optimal orbitals

the **variational principle** is applied.[48] This ansatz defines the **Hartree-Fock (HF) method**[48–51]

$$E_{HF} = \min E[\Phi_0] = \min \frac{\langle \Phi_0 | \hat{H} | \Phi_0 \rangle}{\langle \Phi_0 | \Phi_0 \rangle}, \quad \text{with} \quad \langle \chi_i | \chi_j \rangle = \delta_{ij}. \tag{3.5}$$

In Hartree-Fock theory the orbitals are optimized in order to find the minimum of the energy expectation value, with the restriction that they have to be orthonormal. The orthonormality of the orbitals ensures that the Slater determinant can also normalized by a simple constant. The optimization with constraints can be performed by minimizing the corresponding Lagrangian L with respect to the orbitals by introducing the Lagrange multipliers λ_{ij}

$$\delta L = \delta E[\Phi_0] + \sum_{ij}^{N} \lambda_{ij} \left(\langle \delta\chi_i | \chi_j \rangle - \langle \chi_i | \delta\chi_j \rangle \right) = 0. \tag{3.6}$$

The energy expectation value of a Slater determinant $E[\Phi_0]$ is given as

$$E[\Phi_0] = \sum_{i}^{N} h_{ii} + \sum_{i}^{N} \sum_{j>i}^{N} \left(J_{ij} - K_{ij} \right), \tag{3.7}$$

with

$$h_{ii} = \langle \chi_i | \hat{h}(1) | \chi_i \rangle \tag{3.8}$$

$$\hat{h}(1) = -\frac{1}{2} \nabla(1)^2 - \sum_{A}^{N_{nuc}} \frac{Z_A}{|\mathbf{R}_A - \mathbf{r}_1|} \tag{3.9}$$

$$J_{ij} = \langle \chi_i | \hat{J}_j(1) | \chi_i \rangle = \langle \chi_i \chi_j | \chi_i \chi_j \rangle = \int\int \chi_i^*(1) \chi_i(1) \frac{1}{\mathbf{r}_{12}} \chi_j(2) \chi_j^*(2) dx_1 dx_2 \tag{3.10}$$

$$K_{ij} = \langle \chi_i | \hat{K}_j(1) | \chi_i \rangle = \langle \chi_i \chi_j | \chi_j \chi_i \rangle = \int\int \chi_i^*(1) \chi_j^*(1) \frac{1}{\mathbf{r}_{12}} \chi_i(2) \chi_j(2) dx_1 dx_2 \tag{3.11}$$

Here the Coulomb ($\hat{J}$) and exchange ($\hat{K}$) operators have been introduced.[49] This ansatz leads after a transformation to canonical orbitals, which yield a diagonal Lagrange multipliers matrix, to the well known Fock equation[48,49]

$$\hat{f}(1) \chi_i(1) = \epsilon_i \chi_i(1) \tag{3.12}$$

$$\hat{f}(1) = \hat{h}(1) + \sum_{j}^{N} \left(\hat{J}_j(1) + \hat{K}_j(1) \right) = \hat{h}(1) + V_{HF}(1), \tag{3.13}$$

with the Fock operator $\hat{f}$. Since the Fock equations are obtained as result of the minimization condition, the Fock operator is not directly connected to the total energy, but rather to the stationarity condition. The Fock equations are effective one particle equations, but since all orbitals have to be known (because they are included in the Coulomb and exchange operators) the equations have to be solved iteratively, until a **self-consistent field (SCF)** is obtained. Solving the Fock equations is equivalent to finding the optimal orbitals for a determinantal wave function. Usually, the molecular orbitals (MOs) are expanded in an atomic orbital basis (typically atom-centered Gaussian functions[48]),

$$\phi_i(\mathbf{r}) = \sum_{\mu=1}^{N_{bas}} c_{i\mu}\varphi_\mu(\mathbf{r}), \tag{3.14}$$

which leads to analytically solvable matrix elements and discretizes the Fock operator. This is often called the LCAO-approach (**l**inear **c**ombination of **a**tomic **o**rbitals). In this approach, so-called virtual orbitals (i.e., orbitals which are not occupied in the ground-state configuration) are also obtained. The optimization can also be understood as a rotation in the orbital space between occupied and virtual orbitals.
Writing the Fock equation in the atomic orbital basis leads to the so-called Roothaan-Hall equation[48]

$$\mathbf{FC} = \mathbf{SCE}. \tag{3.15}$$

with $\mathbf{F}$, $\mathbf{C}$, $\mathbf{E}$ being the Fock matrix, the matrix of the coefficients, and the overlap matrix. $\mathbf{E}$ is a matrix containing the orbital energies as diagonal elements. In order to solve this pseudo-eigenvalue equation the basis is orthogonalized by a Löwdin orthogonalization,[52]

$$^{\lambda}\mathbf{F} = \mathbf{S}^{-1/2}\mathbf{F}\mathbf{S}^{-1/2} \tag{3.16}$$

$$^{\lambda}\mathbf{C} = \mathbf{S}^{1/2}\mathbf{C} \tag{3.17}$$

$$^{\lambda}\mathbf{S} = \mathbf{1} \tag{3.18}$$

with λ specifying the respective quantity in the orthogonalized basis. The remaining eigenvalue equation,

$$^{\lambda}\mathbf{F}\,^{\lambda}\mathbf{C} =^{\lambda} \mathbf{CE}, \tag{3.19}$$

can be solved by standard methods.
Due to the determinantal ansatz, the **Pauli principle** is fulfilled in Hartree-Fock theory and the pair density of two electrons with the same spin is zero if both electrons are

located at the same point in space. The pair density for two electrons with opposite spin, however, is constant, i.e., these electrons do not interact, although they are charged particles. Thus this **Coulomb correlation** of the electrons is missing completely. This is due to the fact that each electron only interacts with the mean field generated by the other electrons (via the Coulomb and exchange operator) and the nuclei. In reality, however, each electron "feels" the individual presence of all other electrons. The true wave function is more complex than an antisymmetrized product of one-electron wave functions. Thus the Hartree-Fock method is said to describe the electrons as non-interacting fermions moving in some mean field. Due to the SCF procedure, this mean field is optimized to represent the electron-electron interaction as good as possible, but the one-determinantal ansatz has its limits. Although the Hartree-Fock method can be considered as a rather good approximation, since it recovers around 99% of the exact energy, its acccuracy is insufficient, because the energy of chemical bonds is in the same order of magnitude as the missing 1%.[48] The difference between the exact and the Hartree-Fock energy is called correlation energy. Some molecules like F_2 are even predicted to be unbound by Hartree-Fock theory.[53]

The **independent-particle picture** invoked by a single determinant is thus not sufficient for an accurate ground-state description and even less for the excited states. However, it is a useful starting point and provides the conceptual framework for the qualitative description and characterization of excited states.[51] A determinant with a so-called non-Aufbau occupation can be constructed by shifting electrons from occupied to virtual orbitals. Such a determinant is called an excited determinant (or configuration) and can be used as a qualitative approximation and pictorial representation of an excited state.

The Lagrange multipliers ϵ_i are called orbital energies. According to **Koopmans' theorem**[48,49] the orbital energy of an occupied orbital is an approximation for the energy necessary to remove an electron from this orbital,

$$\epsilon_i = \langle \chi_i | \, \hat{h}_i \, | \chi_i \rangle + \sum_{j}^{N_{occ}} \langle \chi_i \chi_j || \chi_i \chi_j \rangle. \tag{3.20}$$

In fact, it can indeed be shown that the energy difference between a determinant with M and one with $M-1$ electrons is equal to the energy of the orbital k from which the electron has been removed,[48]

$$E[\Phi_M] - E[\Phi_{M-1}] = \epsilon_k. \tag{3.21}$$

Of course, this ansatz neglects the fact that the orbitals rearrange after ionization (this is sometimes called frozen-density approximation), but this leads to a favorable error cancellation with the also neglected differential correlation between the ion and the neutral molecule. The correlation energy is generally higher for the neutral molecule, since it has one electron more. The energy of a virtual orbital is given by[48]

$$\epsilon_a = \langle \chi_a | \hat{h} | \chi_a \rangle + \sum_j^{N_{occ}} \langle \chi_a \chi_j || \chi_a \chi_j \rangle. \tag{3.22}$$

Since the sum runs over all occupied orbitals, the "virtual" electron "feels" N other electrons. Thus, the energy of a virtual orbital is connected to the $N+1$ electron system and therefore approximates the electron affinity. Hence, the orbital energy difference cannot be expected to be a good approximation for the excitation energy, which will become important for the calculation of excited states (see below).

Apart from providing a qualitative picture of excited states, the excited configurations can also be used to include correlation into the ground-state wave function. The various so-called **post-HF methods**[48–50] go beyond the HF approximation by adding excited determinants to the wave function. The different classes of methods use different techniques to select the excited determinants. **Configuration interaction** uses a (truncated) linear expansion of the configurations, **coupled-cluster theory** uses a truncated non-linear expansion based on an exponential excitation operator and the **Møller-Plesset** approach uses **perturbation theory** to select the configurations.[48–50,54]

Another ansatz, which includes correlation, is **density functional theory (DFT)**. The electronic wave function of an N- electron system is $3N$-dimensional, while the electron density is always 3-dimensional, regardless of the system size. Thus, using the electron density instead of the wave function is very attractive. This is the basic idea of density functional theory. In the last decades, the importance of density functional theory in chemistry has significantly increased.[53,55] It is now the most commonly applied method for ground-state calculations and has in part outstripped the post-HF methods, due to its computational efficiency and robust performance. Although the Hartree-Fock-Slater (HFS) method[56] devised by Slater in 1951 can be regarded as a first local density approximation and is an ancestor of Kohn-Sham DFT (KSDFT) and although Thomas, Fermi, and Dirac developed early density functionals using the uniform electron gas,[53] the birth year of DFT is considered to be 1964,[53] when the Kohn-Hohenberg theorems[57,58] were introduced, which provides the theoretical basis and justification of DFT.[53] The first the-

orem states that the full many-particle ground state is a unique functional of the electron density, since there is a one-to-one mapping between the electron density of a system and its external potential, which also determines the molecular Hamiltonian. Thus all properties are uniquely defined by the density.[59] The second theorem states that the energy functional yields the minimal energy (i.e. the exact ground state energy) if and only if the exact ground state density is used. The second theorem is an equivalent to the variational theorem in wave mechanics. Although the Kohn-Hohenberg theorems guarantee the existence of such a functional, they do not give its actual form.
From wave function theory, it seems evident that the energy functional can be split into different contributions,[48] namely the kinetic energy, the electron-nucleus interaction and the electron-electron interaction,

$$\mathbf{E}[\rho] = \mathbf{T}[\rho] + \mathbf{E}_{ne}[\rho] + \mathbf{E}_{ee}[\rho]. \tag{3.23}$$

While the form of the functional for the external potential $\mathbf{E}_{ne}[\rho]$ (i.e. the electron-nucleus interaction) and the Coulomb part ($\mathbf{J}[\rho]$) of the electron-electron interaction ($\mathbf{E}_{ee}[\rho]$) can be readily derived from the corresponding classical expressions,[48] this is not the case for the kinetic energy $\mathbf{T}[\rho]$ and the non-classical (i.e. exchange) part of the electron-electron interaction.[48] Therefore approximations have to be introduced. The first functionals that relied solely on the density like the Thomas-Fermi model showed poor performance for molecules, since the approximation in the kinetic energy functional were too severe.[48] In fact, the Thomas-Fermi model cannot bind molecules.[53] By reintroducing orbitals, the **Kohn-Sham approach** is circumventing this problem, since the exact form of the kinetic energy functional ($\mathbf{T}_{SD}$) is known for a Slater determinant,[48]

$$\mathbf{T}_{SD} = \sum_{i=1}^{N} \langle \phi_i | -\frac{1}{2}\nabla^2 | \phi_i \rangle . \tag{3.24}$$

The density can easily be generated from the Kohn-Sham orbitals $\phi(\mathbf{r})$

$$\rho(\mathbf{r}) = \sum_{i=1}^{N} |\phi_i(\mathbf{r})|^2, \tag{3.25}$$

and thus the $\mathbf{E}_{ne}[\rho]$ and $\mathbf{J}[\rho]$ can also be calculated. There are, however, two problems: Firstly, the calculation is performed for a system that is described by a Slater determinant, i.e. a non-interacting system and not for the real system.

Since the energy is a unique functional of the density and thus depends solely on the density, the exact energy can in principle be obtained from any reference system, as long as its density is identical to the one of the real system. Thus, the use of a non-interacting Kohn-Sham system is valid, as long as its density is equal to the real density. Of course the question arises if the density of any real system can be represented by a single Slater determinant, but this is beyond the scope of this chapter (see[59] and references therein for details).

Assuming that the exact density can be reproduced by the Kohn-Sham system, the second problem still arises: the exact functional is needed. The difference between the true kinetic energy and the energy calculated with the determinant together with the difference between the exact electron-electron interaction and the classical Coulomb interaction ($\mathbf{J}[\rho]$) forms the so-called **exchange-correlation (xc) functional** $\mathbf{E}_{xc}[\rho]$[59]

$$\begin{aligned} \mathbf{E}_{KS}[\rho] &= \mathbf{T}_{SD}[\rho] + \mathbf{E}_{ne}[\rho] + \mathbf{J}[\rho] + \mathbf{E}_{xc}[\rho] && (3.26) \\ \mathbf{E}_{xc} &= (\mathbf{T}[\rho] - \mathbf{T}_{SD}[\rho]) + (\mathbf{E}_{ee}[\rho] - \mathbf{J}[\rho]). && (3.27) \end{aligned}$$

If the exact exchange-correlation functional was known, the approach could thus in principle yield the exact energy.[48] Since the exact form of $\mathbf{E}_{xc}$ is not known and has to be approximated, the Kohn-Sham approach just seems to defer the problem at first sight. However, that is not quite true. In the original orbital-free approaches, the kinetic energy functional had to approximated, which yields severe errors. In the Kohn-Sham approach, however, the kinetic energy is calculated accurately for the non-interacting system and only the correction to the kinetic energy and the exchange have to be approximated, which is less severe and yields much better results.[59]

The Kohn-Sham orbitals (and thus the density) are constructed similarly to Hartree-Fock theory, since the second Kohn-Hohenberg theorem ensures the existence of a variational principle. In fact the final Kohn-Sham equations take a very similar form to the Fock equations,[59]

$$\mathbf{F}^{KS}\phi_i = \left(-\frac{1}{2}\nabla^2 + V_{KS}\right)\phi_i = \epsilon_i^{KS}\phi_i \tag{3.28}$$

with

$$V_{KS} = V_{ext} + V_c + \frac{\delta \mathbf{E}_{xc}}{\delta \rho}, \tag{3.29}$$

with V_{ext} being the external potential (i.e. the electron nuclei interaction) and V_c being the Coulomb interaction with the electron density. Contrary to Hartree-Fock theory,

DFT includes correlation via the exchange correlation functional. Thus while the use of a single determinant is a severe approximation in Hartree-Fock theory, it is different in Kohn-Sham DFT, because the determinant is only used for building up the density of a non-interacting reference system that is afterwards corrected.[59] The big advantage of DFT, that the three-dimensional electron density instead of the high-dimensional wave function is used, is of course partly lifted by the Kohn-Sham approach, since the density is simply constructed from the occupied orbitals.[48] Nevertheless DFT is much less demanding than most post-HF methods.

The biggest challenge for the density functional community is to find expressions for the exchange-correlation functional. Since it is possible to derive functionals for a uniform electron gas, the simplest approach is to treat the electron density locally as a uniform electron gas at each point, which yields to the **local density approximation (LDA)** and **local spin density approximation (LSDA)**, respectively.[48] This can be refined, by also involving the gradient of the electron density, which forms the class of the **generalized gradient approximations (GGA)**.[48] A typical example is the BLYP functional.[60,61] A third level, formed by the so-called **meta-GGA** functionals, is obtained if the Laplacian of the electron density or the spin kinetic energy densities are included in the functional.[48,62] The Minnesota functionals developed by Truhlar and coworkers are one popular example.[62] The so-called **hybrid or hyper-GGA** functionals mix a certain amount of exact Hartree-Fock exchange into $\mathbf{E}_{xc}$, which often yields an improved description.[48] In principle one might assume that the partitioning

$$\mathbf{E}_{xc} = \mathbf{E}_x^{HF} + \mathbf{E}_c^{KS} \tag{3.30}$$

might be ideal, since the exchange is taken from Hartree-Fock (which is exact) and the correlation must be taken from DFT. However, this is not the case.[59] It can be explained using the **exchange-correlation hole**.[59] The hole function h_{xc} is defined as

$$h_{xc}(x_1, x_2) = \frac{\rho_2(x_1, x_2)}{\rho(x_1)} - \rho(x_2), \tag{3.31}$$

with $\rho_2(x_1, x_2)$ being the pair density. $\rho_2(x_1, x_2)dx_1dx_2$ is the probability of finding electron one between x_1 and $x_1 + dx_1$ and electron two between x_2 and $x_2 + dx_2$. If there is no correlation, the pair density is equivalent to the product of the one-particle densities, i.e. $\rho_2(x_1, x_2) = \rho(x_1)\rho(x_2)$ and $h_{xc}(x_1, x_2) = 0$. In reality the electrons repel each other. Hence, $h_{xc}(x_1, x_2)$ should only be close to zero for $|x_1 - x_2| >> 0$ and should become

negative for $x_1 \approx x_2$. Thus, it is rather localized. The contribution to this hole function can be split into a correlation and an exchange hole. The exact hole functions have been calculated for the H_2 molecule.[59] The exact exchange and correlation hole are delocalized and by themselves bad approximations for the total hole.[59] Combined however, they yield the correct localized result. The separation of $\mathbf{E}_{xc}$ in exchange and correlation is artificial, anyway, since it just stems form the choice of reference system (i.e. the Slater determinant).[59] In contrast to the exact exchange and correlation holes, the holes from LDA and GGA are local in nature, because they are based solely on the local density or the local density and its gradient at a particular point, respectively.[59] A partitioning in the spirit of equation 3.30 combines the exact delocalized exchange hole with the approximated localized correlation hole and thus no cancellation between the holes can occur and the total exchange-correlation hole has the wrong characteristics.[59] Hence, calculating both contributions based on the local electron gas model is more sensible and provides a better description. In fact it is discussed that the local exchange holes of the standard functionals reproduce the effect of exact exchange plus static correlation, while the correlation functional covers the effect of dynamical correlation.[59]

In order to make use of the exact exchange in hybrid functionals a more sophisticated approach using the adiabatic connection formula[48,53] is used (see[59] for details). The adiabatic connection formula provides the prescription for designing $\mathbf{E}_{xc}$, by connecting it with the exchange-correlation hole.[53] The hybrid functionals derived in this approach do not abandon the DFT exchange completely, but just mix in the exact exchange. For instance the very popular B3LYP functional[48,60,61,63,64] uses the following partitioning

$$\mathbf{E}_{xc}^{B3LYP} = (1-a)\mathbf{E}_X^{LSDA} + a\mathbf{E}_x^{HF} + b\mathbf{E}_x^{B88} + (1-c)\mathbf{E}_c^{LSDA} + c\mathbf{E}_c^{LYP}. \tag{3.32}$$

b and c control the contribution of the gradient corrections, while a controls the amount of Hartree-Fock exchange.[59] The parameters have been determined by fitting procedures to be approximately $a \approx 0.2$,$b \approx 0.7$ and $c \approx 0.8$.[48] There is theoretical justification that an amount around 20% of exact exchange is reasonable, however it is clear, that this parameter cannot be universal.[59,65]

Using hybrid functionals often reduces the so-called **self-interaction error**, since Hartree-Fock itself is self-interaction free.[48] As the name implies, the self-interaction involves an electron interacting with itself.[59] In a one-electron system the exchange and the correlation energy exactly cancel each other in Hartree-Fock theory ($J - K = 0$), as it should be the case. This is however not true for DFT. The classical term $\mathbf{J}[\rho]$ is not zero for a one-

electron system, since it contains the interaction of the density with itself.[59] This should be canceled by $\mathbf{E}_{xc}[\rho]$, but since the exchange-correlation functional is only approximated, this is not completely fulfilled. This self-interaction error can sometimes have severe consequences for calculations of bond dissociation energies and transition states.[59]
Another problem of the current functionals is that the **long-range behavior of the exchange-correlation potential** V_{xc}, which is given by

$$V_{xc} = \frac{\delta \mathbf{E}_{xc}}{\delta \rho}, \tag{3.33}$$

is not correctly reproduced. The Coulomb potential

$$V_C(\mathbf{r}_1) = \int \frac{\rho(\mathbf{r}_2)}{\mathbf{r}_{12}} d\mathbf{r}_2 \tag{3.34}$$

shows the behavior $\frac{N}{\mathbf{r}}$ for $r \to \infty$. Thus, in order to cancel the self-interaction V_{xc} should behave like $a - 1/\mathbf{r}$ in the limit.[59] However, the exchange potential of most functionals decays exponentially, i.e. too fast and hence the functionals are less attractive than the correct one. This is also connected to the fact, that the ionization energy I is not equal to the absolute value of the highest occupied Kohn-Sham orbital energy ϵ_{max}, as it should be using the exact functional,[59,66]

$$I = -\epsilon_{\max}. \tag{3.35}$$

The incorrect long-range behavior also leads to problems with charge-transfer (CT) states in TDDFT (see below).
Although only the HOMO energy has a rigorous physical meaning in KSDFT, the other occupied orbital energies can be used as approximations to the corresponding ionization energy.[67] In fact it works even better than for HF.[68]
The virtual orbitals "see" $N - 1$ electrons (instead of N in Hartree-Fock) and thus their energy is not an approximation to the electron affinity. However, contrary to HF an orbital energy difference is a (rough) approximation to the excitation energy.[68,69]
KSDFT has also problems with **dispersion interactions**.[i] The asymptotic induced dipole-dipole interaction energy should have the London form, i.e. $-C_6/R^6$, but also the interaction energy of most functionals falls of exponentially.[53] Since dispersion interactions are highly important for applications in biology as well as in material sciences, several approaches to correct this deficiency have been devised, among them the use of

[i] Strictly speaking, this is only true for non-overlapping densities, i.e. long-range dispersion interactions.

double-hybrids, which include second-order perturbation theory,[53] density-based corrections like the one of Corminboeuf et al.,[70] which uses the exchange-hole dipole of Becke and Johnson,[71] or empirical dispersions corrections like the popular DFT-D3 method of Grimme et al.[53,72]

The problems with processes like charge transfer and dispersive interactions or long-range effects are due to the fact that these are inherently non-local effects, which cannot be treated by the local functionals that depend only on $\rho(\mathbf{r})$ or $\nabla\rho(\mathbf{r})$.[53] They "*only "see" their direct neighborhood and are completely "unaware" of what is going on farther away.*"[59] Hybrids perform a bit better due to the inclusion of non-local exchange, but still have problems.[53]

The different levels (LDA, GGA, meta-GGA, hyper-GGA) are often arranged in a hierarchy known as Jacob's ladder.[73] The functionals on the fifth rung (above the hybrids) also use virtual orbitals, for instance by including a Møller-Plesset-type term in the functional as in the double hybrids.[73,74] However, the use of virtual orbitals in KSDFT also sparked criticism.[53]

Thus the development of novel functionals is still an active area of research. It should be noted that most of the common functionals include parameters that have been fitted to empirical data and are thus strictly speaking no *ab initio* methods. From that point of view DFT could even be considered as a semi-empirical method.[75] Nevertheless, since there are also parameter-free functionals[65] and since the exact functional (if it was known) would yield the exact energy without the need for any empirical parameters, it is also justified to classify DFT as *ab initio* method.[53]

Nowadays a massive variety of different functionals is available, which can be distinguished by the form of the xc-functional. This great variety offers great opportunities, but since one cannot judge the quality of a given functional *a priori* one needs to be careful to use the functional that gives the correct description of the system and not the functional that gives the desired result. Another problem is that contrary to the wave function (*ab initio*) methods, DFT offers no way to systematically improve the results.[48] Therefore one has to rely on benchmark calculations in the literature or perform one's own benchmark computations using high-level methods or experimental results as reference points for the system of interest.

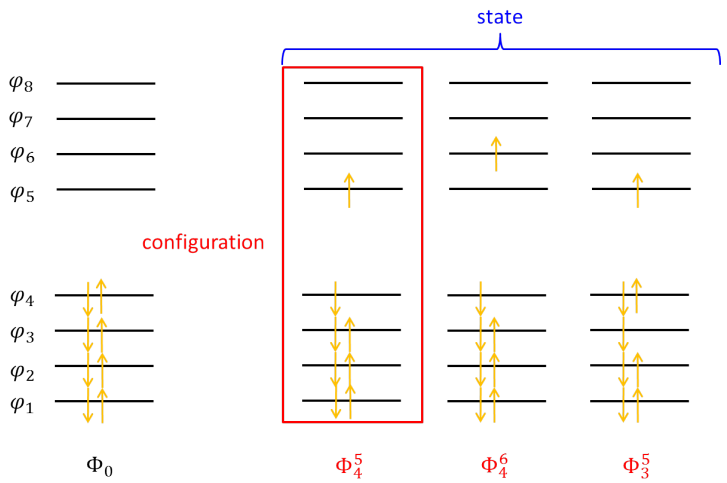

Figure 3.1: On the left-hand side a typical ground-state configuration is given, while several excited configurations are depicted on the right-hand side. They are usually named according to the excitation which generates them from the ground-state determinant with Aufbau occupation.

3.1.2 Classification of Excited States

As already mentioned above, excited states are usually classified in the framework of the independent-particle picture.[51] Thus qualitatively an excited **state** is often approximated by a single **configuration**, i.e. an excited determinant. This picture is also directly applied in the Δ-SCF method (see below). Although this can be a fairly good qualitative approximation for some of the lowest excited states (especially the HOMO→LUMO transition), usually several configurations are needed for the correct description of an excited state. If high numerical accuracy is required (i.e. dynamic correlation has to be included), the number of necessary configurations can be immense.[48] However, usually only a few configurations have a significant contribution and these are generally used to classify the state. An example is given in Figure 3.1. If for instance the configuration Φ_4^5 is dominant and the contribution of the others is negligible, the state is classified as consisting mainly of the HOMO→LUMO transition. The concept of several configurations is directly incorporated in the framework of configuration interaction, where a state is written as a linear combination of several determinants (see below).

Aside from its composition an excited state is often called **bright** or **dark**. These terms are connected to the oscillator strength and thus to the question of whether the corresponding transition can be observed experimentally. There is however no clear definition how low (or high) the oscillator strength should be in order to give rise to a dark (or

bright) state.
If the dominant configuration can be generated by the excitation of one electron from an occupied to a virtual orbital the corresponding state is called a **singly excited state**, if it is generated by the excitation of two electrons it is designated as a **doubly excited state**.
Furthermore one can distinguish between **valence** and **core** excited states, as well as **Rydberg** states. In a valence excited state the dominant configurations are generated by a transition of valence electrons into the virtual levels, while electrons of the inner shells get excited in a core excited state. A Rydberg state is formed if the electrons are excited into very diffuse orbitals, which are spatially very far away form the nuclei.[76] Therefore the interaction between the electron and the rest of the molecule resembles approximately the interaction between an electron and a single positive charge (i.e. the hydrogen atom, hence the name).
Considering the limitations of TDDFT an important distinction is between **neutral** and **charge-transfer states**.[77] A charge-transfer state is formed if the excitation leads to a significant shift of charge, while there is only a negligible shift of charge for a neutral state. If the state can be sufficiently described by a single configuration, this is also visible in the contributing orbitals, otherwise the character is less apparent. Visual inspection of transition and difference densities[77] or natural transition orbitals (NTOs)[78] is also often useful. The actual amount of charge-transfer character can also be derived by analyzing the one-electron transition density matrix.[79] Several characteristic indices have also been devised, which are based on the inner product of the moduli of the contributing orbitals,[80] the electron-hole distance[81] or the detachment and attachment densities overlap.[82]

3.2 Variational Methods

Δ-SCF as well as configuration interaction theory rely directly on the variational theorem. That means a set of parameters (i.e. the expansion coefficients of the orbitals and/or configurations) is optimized until a stationary point of the energy is found. These methods calculate the absolute energy of the excited state, which means that the excitation energy is given as the difference to the ground-state energy.
The multi-configurational complete active space self-consistent field method (CASSCF) as well as multi-reference configuration interaction (MRCI) are also variational methods. The multi-reference method CASPT2 is (due to its use of perturbation theory) not variational,

but is nevertheless covered in this chapter because of its close relation to CASSCF and MRCI.

3.2.1 Δ-SCF

The conceptually most straightforward way to calculate an excited state is to do basically the same as in ground-state calculations, but using an excited determinant (i.e. a determinant with **non-Aufbau occupation**). Usually an unrestricted formalism has to be applied, i.e. orbitals with α- and β-spin are allowed to have a different spatial form.[48] The energy of the excited state is then obtained by variationally optimizing the orbitals - either using Hartree-Fock theory or KSDFT. This scheme is called Δ-SCF.[83–85] Conceptually, this means that the optimization should not lead to the minimum (i.e. the ground state) of the variational space, but to a saddle point. If the excited state has a different multiplicity or belongs to a different irreducible representation than the ground state, this is quite straightforward. If this is however not the case, the SCF procedure can collapse to the ground state (i.e. the minimum).
In a normal SCF procedure the orbitals with the lowest energy eigenvalues are occupied after each iteration. Even if one imposes the restriction that for instance the lowest $N-1$ orbitals and the $(N+1)$th orbital are occupied, the density can collapse to the ground state density.[85] Since the orbitals are optimized the occupied, "virtual" orbital can be rotated out of the occupied space and the ground-state occupation is reestablished.[85] In order to prevent this collapse occupation conditions relying on an overlap criterion can be imposed. In the **maximum overlap approach**,[86,87] those of the new orbitals are occupied that overlap most with the old occupied orbitals, thus making sure that the Aufbau scheme does not deviate from the ones of the guess.[86] Therefore using the orbitals from a converged ground state calculation as a guess is reasonable.[85] It is important to note that the maximum overlap approach does not impose a restriction to the variational space, which is exactly the same as in a standard Hartree-Fock/KSDFT calculation. Its only function is to force the optimization to converge on a saddle point of the desired order instead of the minimum.
Although the Δ-SCF concept has been introduced early[83,84] it is not widely used. One problem is that the Kohn-Hohenberg theorem is only valid for the ground state,[88] therefore there is no uniquely defined functional for the excited states.[85] The easiest approach is thus to evaluate the state energy with the ground state functional and the occupied

Δ-SCF orbitals[85]

$$E^{ex} = E\left[\phi_i^{\Delta\text{-SCF}}\right]. \tag{3.36}$$

Although this may seem questionable, there is some theoretical justification for this approach (see section 3.4).[85,89,90]

One problem of Δ-SCF lies in the fact that a single determinant is generally no eigenfunction of the S^2-operator. This can be corrected by using the spin purification formula.[84,85] The main problem of the method is, however, that it is questionable, whether the representation of a state by a single configuration is reasonable. Moreover it is uncertain, if a unique variational theory for excited states exists in DFT.[90] The computed states will furthermore be non-orthogonal, which could lead to problems in the calculation of properties like transition dipole moments.[87,90] Arriving at a converged result for the excited state can also be quite difficult.[89]

Nevertheless Δ-SCF gives excitation energies of a similar accuracy as TDDFT for the HOMO→LUMO transition,[85] but it is doubtful whether this is also the case for states higher in energy,[89] because they can be inherently multi-configurational in nature.

Although TDDFT does not suffer from most of the limitations of Δ-SCF, charge-transfer transition are generally better described by Δ-SCF.[90]

3.2.2 Configuration Interaction

As the name implies, in configuration interaction (CI), different configurations interact with each other. The wave function of each state is written as a linear combination of excited determinants[48–50,91]

$$|\Psi_{CI}\rangle = \sum_n c_n \Phi_n = |\Phi_0\rangle + \sum_{id} c_i^d \,|\Phi_i^d\rangle + \sum_{i<j,d<e} c_{ij}^{de} \,|\Phi_{ij}^{de}\rangle + ... \tag{3.37}$$

Using creation ($\hat{a}_i^\dagger$) and annihilation ($\hat{a}_i$) operators[50,91] the same equation can be written as

$$|\Psi_{CI}\rangle = |0\rangle + \sum_{id} c_i^d \,\hat{a}_d^\dagger \hat{a}_i \,|0\rangle + \sum_{i<j,d<e} c_{ij}^{de} \,\hat{a}_e^\dagger \hat{a}_d^\dagger \hat{a}_j \hat{a}_i \,|0\rangle + ... \tag{3.38}$$

For N electrons and $2n$ spin orbitals, there are $\binom{2n}{N}$ possible Slater determinants. In a so-called **Full-CI** all of them or at least all in the subspace with the correct irreducible representation and multiplicity are included. Usually the determinants are combined to configuration state functions (CSFs), which are eigenfunctions of the S^2-operator and only

those CSFs with the desired symmetry and multiplicity are included in the CI treatment. The Full-CI gives the exact result in the limit of the used basis set.[49] The CI equations can be derived by applying the variational principle with respect to the coefficients. However, the same result can be obtained by plugging the Full-CI wave function into the Schrödinger equation and projecting onto an arbitrary state $\langle\Phi_m|$,

$$\sum_n c_n \langle\Phi_m| \hat{H} |\Phi_n\rangle = E \sum_n c_n S_{mn}. \tag{3.39}$$

By applying the orthonormality condition $S_{mn} = \delta_{mn}$ the final matrix equation reads

$$(\mathbf{H} - E\mathbf{I})\,\vec{c} = 0. \tag{3.40}$$

According to the **Slater-Condon rules**[49] only Hamiltonian matrix elements between configurations which differ in the excitation degree by less than three can be different from zero. The **Brillouin theorem**[49] further states that using canonical orbitals (from a converged Hartree-Fock calculation) the matrix elements between the reference (i.e. Hartree-Fock) configuration and the single excited determinants are zero,

$$\langle\Phi_0| \hat{H} |\Phi_i^d\rangle = 0. \tag{3.41}$$

This is due to the fact that these elements are identical to off-diagonal Fock matrix elements, which are zero in a converged calculation.[48] Thus equation 3.41 can also be taken as a condition for the optimal SCF ground-state solution. Due to the high computational cost the level of the excitation is usually truncated after singles or doubles, which is called CIS or CISD, respectively. The doubles add a significant part of the correlation and improve the description of the ground state significantly.
Another possibility to define the truncation is to use the seniority number, i.e. the number of singly occupied orbitals in a determinant,[92] but this is less common.
Although **CIS** does not give an improved description of the ground state due to the Brillouin theorem, it is nevertheless a useful first approximation for the description of excited states. Following the notation of Dreuw and Head-Gordon[77] the CIS matrix equation can be written as

$$\mathbf{AX} = \omega\mathbf{X} \tag{3.42}$$

$$\mathbf{A}_{ia,jb} = (\epsilon_a - \epsilon_i)\,\delta_{ij}\delta_{ab} + (ia||jb) \tag{3.43}$$

with i and j signifying occupied and a and b virtual orbitals, respectively. $\mathbf{X}$ contains the eigenvectors (i.e. the coefficients of the linear combination) and ω is a matrix with the excitation energies as the diagonal elements.[77] CIS is rather cost-efficient and can thus be applied to larger systems. For an atomic orbital basis set of fixed size and a sufficiently large molecule it scales quadratically with the system size, while an increase of the basis on a defined molecule leads to an $\mathcal{O}(n^4)$ scaling behavior.[77] It gives reasonable results for states that are dominated by a single configuration, although it tends to overestimate the excitation energies severely (0.5-2 eV).[47,77] This is on the one hand due to the missing correlation, which is bigger in excited states, on the other hand due to the leading term in the energy expression.[77] The excitation energy of the CIS is given by[77]

$$\omega_{CIS} = \sum_{ia}(c_i^a)(\epsilon_a - \epsilon_i) + \sum_{ia,jb} c_i^a c_j^b (ia||jb). \tag{3.44}$$

The specific state is defined by the coefficients, which are obtained from the eigenvalue equation. Assuming one configuration is dominant, the leading term is given by the corresponding orbital difference (as in the independent-particle picture) plus two-electron integrals, which (partly) take the electron interaction into account. The overestimation is due to the fact that the leading term contains Hartree-Fock orbitals, which are a poor approximation for the excitation energy, since their difference is approximately the difference of the ionization energy (I) and the electron affinity (A) (see above).[68] Thus the Hartree-Fock orbitals are not an especially good basis for the description of excitation processes and in order to arrive at accurate results a wave function with a higher flexibility to overcome the deficiency is necessary (e.g., CISD).[77]

For a **charge-transfer state**, however, the orbitals are well-suited. Assuming orbital a is located on molecule A and i on molecules B and the distance is high enough so that the overlap is approximately zero. The orbital difference approximates the correct limit $A_a - I_i$ and the remaining two-electron integrals of coulomb type give the correct distance behavior of $1/R$,[68]

$$\omega_{CT} \approx A_a - I_i - \frac{1}{R}. \tag{3.45}$$

Thus CIS has no intrinsic problems with charge transfer states[47] and gives often qualitatively correct results for the potential energy surface of the lowest excited states. Furthermore pure singlet and triplet states can be calculated.

The **Thomas-Reiche-Kuhn dipole sum rule**, according to which the total number of electrons is equal to the sum of the transition dipole moments is however not obeyed by

CIS.[77]

CIS is also the only truncated CI method, which is size-consistent.[77] Using a semi-empirical parametrization of CIS, like in the INDO/S method[93] can yield improved numerical results,[47,94] but does not solve the main limitations.

Using a higher excitation level, like CISD is often too expensive for excited states and is thus rarely used. An interesting alternative is the difference-dedicated CI (**DDCI**) proposed by Malrieu and coworkers.[95] This approach aims at including only those determinants in the CI treatment that are needed to describe the energy difference between two states (i.e. the transition energy).

3.2.3 Multi-Configurational and Multi-Reference Methods

Hartree-Fock theory provides the optimal orbitals for a single determinant and thus gives a qualitatively correct description for systems for which a single determinant is a reasonable approximation. There are however systems which need more than one configuration for a qualitatively correct description. The hydrogen molecule at the dissociation limit is a typical case, where (in a minimal basis) the HF and the doubly excited determinant contribute equally to the ground state. Using only the HF determinant gives a 50:50 ratio of the weights of the ionic and covalent resonance contributors and thus a wrong dissociation behavior, since the weight of the ionic structure should drop to zero for $r \rightarrow \infty$.[48,96] Including the second determinant introduces the freedom to variationally optimize the ratio of the two structures.[96] This is easily shown by expanding the corresponding VB determinants ($\Phi_{HF} = |\sigma\overline{\sigma}|$) and $\Phi_D = |\sigma^*\overline{\sigma^*}|$ in a minimal basis: $\sigma = s_1 + s_2$ and $\sigma^* = s_1 - s_2$ and recollecting the terms in Valence Bond determinants (the normalization constants have been omitted for the sake of clarity):[91,96]

$$\Phi_{HF} = |\sigma\overline{\sigma}| = (|s_1\overline{s_2}| - |\overline{s_1}s_2|) + (|s_1\overline{s_1}| + |s_2\overline{s_2}|) \tag{3.46}$$

$$\Phi_{CI} = c_1\Phi_{HF} + c_2\Phi_D = (c_1 + c_2)(|s_1\overline{s_2}| - |\overline{s_1}s_2|) + (c_1 - c_2)(|s_1\overline{s_1}| + |s_2\overline{s_2}|) \tag{3.47}$$

Another well-known example is the rigid rotation of the CH_2-groups in ethene against each other,[97] that disrupts the π-system, thus generating a biradical. While CISD provides an accurate description for the H_2 dissociation, which is not surprising, since in this case it is a Full-CI, the results for the ethene rotation are less satisfying. These are typical cases with degenerate states that demand a multi-configurational treatment.

The so-called **multi-configurational self-consistent field methods (MCSCF)**[50] pro-

vide optimal orbitals for multi-configurational systems and offer a qualitatively correct description for them.

The most commonly used MCSCF approach is the **complete active space self-consistent field method (CASSCF)**[48,98] developed by Roos and coworkers. In this approach, the orbital space is divided into three subspaces, formed by the inactive, active and secondary (virtual) orbitals. The inactive orbitals are always doubly occupied, while the secondary orbitals are always empty. In the active orbital space (usually the highest occupied and lowest unoccupied orbitals), however, a Full-CI is performed. No excitations involving MOs outside of the active space are included. In order to provide the optimal orbitals, the orbital expansion coefficients are optimized as well as the configuration interaction expansion coefficients.[48] This is generally performed in the **super-CI** framework,[99,100] which is based on the generalized Brillouin or **Brillouin-Levy-Berthier theorem** (BLB)[101]

$$\langle 0|\, \hat{H}(\hat{E}_{pq} - \hat{E}_{qp})\, |0\rangle = 0, \tag{3.48}$$

with $|0\rangle$ being the variationally optimized MCSCF wave function, i.e. the wave function with optimal orbitals. The operators $\hat{E}_{pq}$ and $\hat{E}_{qp}$ are spin-averaged excitation operators (the generators of the unitary group)[100]

$$\hat{E}_{pq} = \sum_{\sigma} \hat{a}^{\dagger}_{p\sigma} \hat{a}_{q\sigma}, \tag{3.49}$$

with the spin σ,[100] which generate the single excitations. The indices p and q refer to any orbital that is part of the complete orbital space.[98] Thus similar to the Brillouin theorem the BLB theorem provides a condition for the orbital rotation for the state described by $|0\rangle$. This condition is applied using the super-CI wave function $|SCI\rangle$, which is a sum of $|0\rangle$ and all single excitations relative to $|0\rangle$[100]

$$|SCI\rangle = |0\rangle + \sum_{p<q} x_{pq}(\hat{E}_{pq} - \hat{E}_{qp})\, |0\rangle = |0\rangle + \sum_{p<q} x_{pq}\, |p \to q\rangle\,. \tag{3.50}$$

The typical steps of an MCSCF procedure involve:[99]

1. The normal CI secular equations for the MCSCF wave function are solved with guess orbitals (e.g., from a Hartree-Fock calculation) in order to obtain the CI expansion coefficients.

2. The Super-CI wave function is constructed and the corresponding secular equation

is solved in order to obtain x_{pq}.

3. The new orbitals are generated according to

$$\phi_p^{(1)} = \phi_p^{(0)} + \sum_{p \neq q} x_{pq} \phi_q^{(0)}. \tag{3.51}$$

These steps are repeated until convergence is achieved, which means that no correction to the orbitals is necessary anymore, i.e. $x_{pq} = 0$. Thus the inclusion of the singles does not yield an improved description (i.e. a lower ground-state energy) anymore, from which it follows that the Hamiltonian matrix elements between $|0\rangle$ and $|p \to q\rangle$ must be zero. Hence the BLB theorem is fulfilled.[99] In most implementations the orbital update is performed using the natural orbitals[48] of $|SCI\rangle$ (see[102] for details). With n_i inactive and n_a active orbitals the n_i natural orbitals with the highest occupation numbers are used for the inactive orbitals and the next n_a are used as active orbitals.[98] This is directly possible, because the CASSCF wave function is invariant to a rotation in the active orbitals.[100] The super-CI approach demands the calculation of Hamiltonian matrix elements between $\langle 0|$ and the singlet excited states $(\hat{E}_{pq} - \hat{E}_{qp})\,|0\rangle$, which is quite expensive. A remedy is to use approximate expressions, which still yield converged orbitals.[98,100]

The MOs can be optimized for each state in question, but usually a **state-averaged** calculation is performed, that means that several roots that belong to a certain irreducible representation are calculated and a single set of orbitals is obtained that are averaged for all states in question. This facilitates the convergences and provides orthogonal states, which are not contaminated by each other as in a single-state approach.[47]

The CASSCF method provides a qualitatively correct description for ground-state systems with multi-configurational character as well as for excited-state surfaces and the corresponding excitation energies and transition moments. Rydberg states often pose a problem, since the Rydberg orbitals are easily rotated out of the active space, because their inclusion does not provide a significant contribution to the correlation energy. It is sometimes difficult to find the correct active space, especially if a reaction path is calculated, since the space has to be equally suited for all points along the potential energy surface.[47,103] The static correlation, which is for example necessary for the correct dissociation behavior of H_2 is obviously covered by the CASSCF wave function, but using a standard-sized active space, almost no dynamic correlation[i] is included.[105] Therefore

[i] There is no strict general definition of static and dynamic correlation. Static correlation is connected to the correct dissociation behavior and the shape of the potential energy surfaces and can usually be

excitation energies calculated by CASSCF are far from spectroscopic accuracy.[47] Since the CASSCF wave function is usually qualitatively correct, the orbitals, coefficients and population numbers can be used to analyze and understand molecules with a complex electronic structure (like transition metal compounds) and thus to provide insight.[91]
In order to include dynamic correlation similar schemes as in the post-HF methods can be applied. In configuration interaction excited configurations are defined relative to the Hartree-Fock configuration. In systems where several determinants are necessary for a qualitatively correct description of the state, the excited determinants have to be defined relative to all important configurations, the so-called reference space. For instance if two determinants play an important role (e.g., in the case of the dissociation of H_2) excited configurations relative to both determinants have to be added to provide a balanced description. Otherwise, correlation would be added only to one part of the wave function. Systems for which this multi-reference treatment provides a significantly improved description as compared to a standard single-reference approach are called **multi-reference systems**. They usually involve close-lying states and (near) degeneracies. Typical cases are biradicals, homopolar dissociations and many excited states. There is however no clear definition.[106] Excited states are very likely to show multi-reference character, because they are often rather close in energy. Thus multi-reference treatments are often needed to provide results of high accuracy.
In **multi-reference CI (MRCI)**[47,48,107] excitations are generated relative to the reference space, which is formed by the most important configurations for the state in question using the framework of configuration interaction. Usually the excitations involve singles and doubles, which is then called MRDCI or MRCISD. Obviously, MRDCI is equivalent to CISDT if all single excitations relative to the HF determinant are included in the reference space. However, only a few single excitations are generally needed and often some double excitations are also important. Thus MRDCI provides a more efficient and balanced description than a configuration interaction treatment with higher excitation degree. It is however difficult to find the correct reference space, therefore an accurate MRCI treatment needs experience. Typically at first, a CASSCF calculation is performed and the orbitals are used for the MRCI calculation. The most important configurations in the CASSCF are also a good starting point for selecting the appropriate reference space.

taken care of by including only a few determinants with a significant contribution. These determinants typically involve excitations from the highest occupied to the lowest unoccupied orbitals. In order to include dynamic correlation, which is necessary for numerical accuracy, usually a huge amount of determinants with a small contribution is necessary. However, the transition form one to the other is gradual.[104]

MRCI is one of the most accurate methods for the calculation of excited-state surfaces and excitation energies, however, it is only applicable to very small molecules and suffers also from the lack of size-consistency.[47] The last problem can partly be solved by applying the Davidson correction.[108] Algorithms that exploit the sparcity of the CI matrix can speed up the calculations and make computations of larger molecules applicable,[109] but the scope of MRCI is nevertheless limited.

Excited determinants can also be added by the use of perturbation theory, similar to Møller-Plesset in ground-state calculations. This might be surprising at first sight, since due to near-degeneracies standard perturbation theory should not be applicable to excited states. In **multi-reference perturbation theory MRPT**, the reference wave function must therefore include all relevant configurations in order to prevent problems with near degeneracies.

The basis is as in ground-state calculations the Rayleigh-Schrödinger perturbation theory.[48,91] The Hamiltonian is divided into the zeroth-order Hamiltonian $\hat{H}_0$ with the eigenfunctions $\{\Phi_i\}$ and energies $\{E_i\}$ and the perturbation $\hat{H}'$ which can be scaled by a parameter λ

$$\hat{H} = \hat{H}_0 + \lambda \hat{H}'. \tag{3.52}$$

The eigenfunction Ψ and energy W of $\hat{H}$ are expanded as a Taylor series in powers of λ,

$$W = \lambda^0 W_0 + \lambda^1 W_1 + \lambda^2 W_2 + ... \tag{3.53}$$

$$\Psi = \lambda^0 \Psi_0 + \lambda^1 \Psi_1 + \lambda^2 \Psi_2 + ..., \tag{3.54}$$

where $\Psi_0 = \Phi_0$ and $W_0 = E_0$ are the zeroth-order wave function and energy (and the eigenfunction and -energy of $\hat{H}_0$) and Ψ_1 and W_1 the first-order corrections. One of the most common forms of multi-reference perturbation theory is the **CASPT2** method developed by Roos and coworkers.[110,111] The zeroth-order wave function $|\Psi_0\rangle = |0\rangle$ is a multi-configurational CASSCF wave function for the state in question and spans the space V_0. The first-order wave function is written as a linear combination of the state functions in the space V_{SD}

$$\Psi_1 = \sum_j C_j \left|j\right\rangle, \tag{3.55}$$

with $|j\rangle \in V_{SD}$. V_{SD} contains all configurations that are generated by single and double excitations of $|0\rangle$ and which are not already included in the complete active space. V_0 is not identical to the CAS, since not all configurations within the the active space are a

part of $|0\rangle$. The CAS is spanned by V_0 combined with its orthogonal complement (within the active space)[ii] V_k.[50,110] In order to arrive at an expression for the coefficients C_j of the first-order wave function and the second-order energy correction, the Taylor expansions of Ψ and W are plugged into the Schrödinger equation, which gives[48]

$$(\hat{H}_0+\lambda\hat{H}')(\lambda^0\Psi_0+\lambda^1\Psi_1+\lambda^2\Psi_2+...) = (\lambda^0 W_0+\lambda^1 W_1+\lambda^2 W_2+...)(\lambda^0\Psi_0+\lambda^1\Psi_1+\lambda^2\Psi_2+...). \tag{3.56}$$

The equation must hold for any value of λ, which is only fulfilled if it holds for each power of λ separately, leading to the perturbation equations.

$$\lambda^0 : \hat{H}_0\Psi_0 = W_0\Psi_0 \tag{3.57}$$

$$\lambda^1 : \hat{H}_0\Psi_1 + \hat{H}'\Psi_0 = W_0\Psi_1 + W_1\Psi_0 \tag{3.58}$$

$$\cdots$$

$$\lambda^n : \hat{H}_0\Psi_n + \hat{H}'\Psi_{n-1} = \sum_{i=0}^{n} W_i\Psi_{n-i} \tag{3.59}$$

By multiplying equation 3.59 from the left with Φ_0 and integration one obtains an expression for the nth order energy correction,

$$W_n = \langle 0|\, \hat{H}' \,|\Psi_{n-1}\rangle\,. \tag{3.60}$$

Thus the second-order energy correction can be obtained from the first-order correction to the wave function. By multiplying $|i\rangle$ with $i \in V_{SD}$ from the left to equation 3.58 and integration one obtains

$$\langle i|\, \hat{H}_0 \,|\Psi_1\rangle + \langle i|\, \hat{H}' \,|0\rangle = W_0\langle i|\Psi_1\rangle + W_1\langle i|0\rangle. \tag{3.61}$$

Plugging the result in the expansion of Ψ_1 and rearranging yields

$$\sum_j C_j \,\langle i|\, \hat{H}_0 - E_0 \,|j\rangle = -\,\langle i|\, \hat{H} \,|0\rangle\,. \tag{3.62}$$

The orthogonality $\langle i|0\rangle = 0$ and the identity $\langle i|\, \hat{H}' \,|0\rangle = \langle i|\, \hat{H} - \hat{H}_0 \,|0\rangle = \langle i|\, \hat{H} \,|0\rangle$ have been used. The linear set of equations (3.62) are used to obtain the coefficients of the first-order energy correction.[110]

[ii] V_k thus contains all configurations that are included in the CAS and are orthogonal to $|0\rangle$.

The zeroth-order Hamiltonian is chosen in a way in order to achieve an efficient implementation, a rapidly converging perturbation expansion and and an equivalency to the Møller-Plesset [iii] zeroth-order Hamiltonian in the limiting case of a single closed-shell determinant as reference. This is fulfilled using the following definition[111]

$$\hat{H}_0 = \hat{P}_0\hat{F}\hat{P}_0 + \hat{P}_k\hat{F}\hat{P}_k + \hat{P}_{SD}\hat{F}\hat{P}_{SD} + \hat{P}_{TQ..}\hat{F}\hat{P}_{TQ...} \tag{3.63}$$

The projection operators project onto V_0, V_k, V_{SD} and the space spanned by the higher excitations that have not been included in the other subspaces.[111] The form of the one-particle operator $\hat{F}$ is also determined by the fact[iv] that it has to be identical to the Møller-Plesset definition ($F = \sum_i f_i$) in the limiting case of a single determinant[111]

$$\hat{F} = \sum_{pq} f_{pq}\hat{E}_{pq}, \tag{3.64}$$

with f_{pq} being the spin-averaged expectation value of the operator $F_{pq\sigma}$ and

$$f_{pq} = \frac{1}{2}\sum_{\sigma} \langle 0| F_{pq\sigma} |0\rangle \tag{3.65}$$

$$F_{pq\sigma} = \hat{a}_{p,\sigma}[\hat{H}, \hat{a}^\dagger_{q\sigma}] - \hat{a}^\dagger_{p\sigma}[\hat{H}\hat{a}_{q\sigma}]. \tag{3.66}$$

Since there are three orbital subspaces, the Fock matrix consists of three times three blocks. One can also give an explicit expression for the fock matrix using the one-particle density matrix $\mathbf{D}$,[110]

$$f_{pq} = h_{qp} + \sum_{rs} D_{rs}\left[(pq|rs) - \frac{1}{2}(pr|qs)\right]. \tag{3.67}$$

The CASPT2 procedure starts with a converged CASSCF calculation. Each of the three blocks of the Fock matrix are then diagonalized and the system of linear equations is solved and the second order energy correction is calculated (for details see[110,111]).
Since CASPT2 relies on perturbation theory it is vital that the CASSCF reference includes all configuration state functions with significant contributions. Otherwise, these

[iii] In Møller-Plesset perturbation theory the zeroth-order Hamiltonian is defined as a sum of Fock operators,[48]

$$\hat{H}_0 = \sum_i \hat{F}_i.$$

[iv] In multi-reference cases the definition of the Fock operator is not unique.[104]

are added in the perturbation treatment, which is not in line with a small perturbation. These intruder states are often Rydberg states, which lead to small energy denominators in the perturbation treatment, which consequently "blows up."[104] Therefore the weight of the reference wave function and configurations with small denominators have to be inspected carefully.[47]

If different states of the same symmetry are calculated with standard CASPT2 (single state CASPT2, SS-CASPT2), they are not orthogonal to each other and therefore slightly mixed, which is usually of no importance, but can lead to problems at avoided crossings or states with valence-Rydberg mixing.[47] A solution is the use of **multistate CASPT2 (MS-CASPT2)**.[112] In MS-CASPT2 the reference space consists of states computed from a state-averaged CASSCF. An effective Hamiltonian matrix is diagonalized in the reference space to generate the different MS-CASPT2 states. The diagonal elements correspond to the single-state CASPT2 state energies and the off-diagonal elements introduce a coupling between the states.

For systems where all potentially participating orbitals can be included in the active space of the CASSCF, CASPT2 provides very accurate results and is fairly straightforward to use. Especially for π-systems with their well-defined active spaces CASPT2 provides a robust performance. There is no bias towards either charge-transfer or neutral excited states. Therefore it is the standard method for the calculation of the valence excited states of small- and medium-sized molecules and often provides the theoretical best estimates,[113] but it is nevertheless by no means a black-box method and demands an experienced user.[104]

If the systems become larger and one has to carefully choose which orbitals to include, it is less straightforward to arrive at accurate results and intruder states can become a massive problem. In systems, where the active space is not clearly defined (e.g., σ-π-mixing), CASPT2 calculations can become exceedingly tricky. Furthermore, including more orbitals in the reference space is computationally very demanding. Including more orbitals than needed to cover the static correlation is undesirbale and leads to a poor convergence of the CASSCF calculation due to multiple minima.[104]

CASPT2 is usually slightly less accurate than MRCI, but easier to use and can be applied to somewhat larger systems.

There are also quite promising approaches and developments in the field of **multi-reference coupled cluster (MRCC)** methods,[114] but those are still no standard tools of quantum chemistry.

3.2.4 Semi-Empirical Methods for Excited States

Contrary to the post-HF methods, which go beyond Hartree-Fock theory and are more expensive, semi-empirical methods[48,115] introduce further approximations in order to speed up the calculations by reducing the scaling behavior. Formally Hartree-Fock scales with the fourth power of the basis functions.[48] This is due to the number of two-electron integrals that are needed to build the Fock matrix. Semi-empirical methods neglect some of these integrals and try to compensate the error by introducing parameters for the remaining integrals, which have been fitted to experimental or theoretical reference data.[115] The empirical parameters include correlation effects implicitly. Thus ideally the semi-empirical methods should be faster and more accurate than Hartree-Fock theory.
In the following the atomic basis functions are denoted with $\mu, \nu, \lambda, \sigma$, their number with M, and the centers with $A, B, \ldots$. In the basis of atomic orbitals the Fock operator is thus defined as[48]

$$F_{\mu\nu} = h_{\mu\nu} + \sum_{\lambda\sigma}^{M} D_{\lambda\sigma}(\langle\mu\nu|\lambda\sigma\rangle - \langle\mu\lambda|\nu\sigma\rangle), \tag{3.68}$$

with $D_{\lambda\sigma} = \sum_{j}^{occ.MO} c_{\lambda j} c_{\sigma j}$ being the density matrix that contains the MO coefficients. Typically a minimal basis set with Slater-type functions is used and only valence electrons are treated explicitly. Therefore the modeling of core-core repulsion is quite important (see below). The semi-empirical model is defined by the used approximations (i.e. which integrals are neglected) and how the remaining integrals are evaluated/parameterized. The three standard levels of approximations are complete neglect of differential overlap (CNDO), intermediate neglect of differential overlap (INDO) and the neglect of differential diatomic overlap (NDDO).[115] In the **NDDO** approximation, the differential overlap of basis functions is set to zero if they are on different centers,

$$\mu_A(1)\nu_B(1) = 0 \quad \text{for} \quad A \neq B. \tag{3.69}$$

Thus it follows[48]

$$S_{\mu\nu} = \delta_{\mu\nu}\delta_{AB}. \tag{3.70}$$

Furthermore all three-center interactions in the one-electron integrals (one from the operator and two from the basis functions) and all three- and four-center interactions of the two-electron integrals are neglected,[48]

$$\langle\mu_A\nu_B|\lambda_C\sigma_D\rangle = \delta_{AC}\delta_{BD}\langle\mu_A\nu_B|\lambda_A\sigma_B\rangle. \tag{3.71}$$

In the INDO approach further approximations are introduced. It neglects for instance also all two-center two-electron integrals that are not of the Coulomb type.[48] The CNDO makes use of even sterner approximations. CNDO and INDO only retain monopoles of the charge distribution in the two-center interactions, while NDDO also includes higher multipoles.[115]

Most of the standard semi-empirical methods rely on the **modified neglect of differential overlap (MNDO)** model,[116] which is based on the NDDO integral approximation. The one-center one-electron terms are defined as[48]

$$h_{\mu\nu} = \delta_{\mu\nu} U_\mu + \sum_B V_{\mu\nu,B} \tag{3.72}$$

$$U_\mu = \langle \mu_A | -\frac{1}{2}\nabla^2 - V_A | \mu_A \rangle . \tag{3.73}$$

The first term corresponds to the kinetic and potential energy of a single electron moving in the potential of the nucleus A, while the second represents the potential of the other nuclei, which are partly shielded by the core electrons.[116] The two-center-one-electron terms are written as a product of the overlap and two atomic parameters. These resonance integrals are most important for covalent bonding,[115] as can be inferred from qualitative MO theory.[117]

$$\langle \mu_A | \hat{h} | \nu_B \rangle = \frac{1}{2} S_{\mu\nu} (\beta_\mu + \beta_\nu) \tag{3.74}$$

Since the overlap integral $S_{\mu\nu}$ is calculated explicitly, the model is called *modified* neglect of differential overlap. Due to the approximations only five types of one-center-two-electron terms and 22 types of two-center-two-electron terms remain.[48] The first are parameterized using atomic spectroscopy data, while the latter are modeled as interactions between multipoles.[48,115] The semi-empirical *methods* MNDO, Austin Model 1 (AM1),[118] Recife Model 1 (RM1)[119] and the Parametric Method 3 (PM3)[120] all rely on the MNDO *model*.[48] They differ in the way the parameters are assigned and in the modeling of the core-core interaction. Since only valence electrons are treated explicitly the core-core repulsion is no longer just a simple classical term, because it has to incorporate the effect of the inner shells. In MNDO and AM1 it takes the form[48]

$$V_{nn}^{MNDO}(A,B) = Z'_A Z'_B \langle s_A s_A | s_B s_B \rangle \left(1 + e^{-\alpha_A R_{AB}} + e^{-\alpha_B R_{AB}}\right) \tag{3.75}$$

$$V_{nn}^{AM1}(A,B) = V_{nn}^{MNDO}(A,B) + \frac{Z'_A Z'_B}{R_{AB}} \sum_k \left(a_{kA} e^{-b_{kA}(R_{AB}-c_{kA})^2} + a_{kB} e^{-b_{kB}(R_{AB}-c_{kB})^2} \right) \tag{3.76}$$

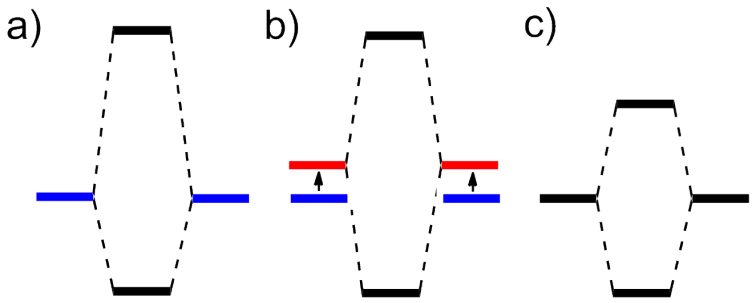

Figure 3.2: Qualitative energy splitting in the LCAO approach with a) non-orthogonal atomic orbitals, b) orthogonalized atomic orbitals and c) in the NDDO approximation.

RM1 is a reparameterization of AM1 and also PM3 uses essentially the same expressions. While MNDO and AM1 were parameterized more or less "by hand", automatic optimization techniques were used for PM3 and hence larger training sets could be used.[48] This training set has been even further enlarged in the PM6 method.[121]

The **OMx methods** by Thiel and cowokers[115,122–124] go beyond the MNDO model by introducing orthogonalization corrections. In Hartree-Fock theory the Roothan-Hall equations are transformed using a Löwdin orthogonalization,[52] which yields

$$ {}^{\lambda}\mathbf{F}\,{}^{\lambda}\mathbf{C} = {}^{\lambda}\mathbf{C}\mathbf{E} \tag{3.77} $$

in the NDDO approximation the overlap matrix is directly a unit matrix, thus implying

$$ {}^{NDDO}\mathbf{F} \approx {}^{\lambda}\mathbf{F} \tag{3.78} $$

Therefore no explicit orthogonalization is performed, which however introduces errors. If two atomic orbitals are combined to construct two molecular orbitals, the energetic splitting is unsymmetric due to the overlap[117] (see Figure 3.2a). The orthogonalization removes the overlap, thus leading to a symmetric splitting, but also changes the atomic orbital basis. The basis functions become delocalized (via orthogonalization tails), more contracted and higher in energy.[123] Therefore the same splitting with respect to the original atomic orbitals is obtained, see Figure 3.2b.

In the NDDO approximation, the overlap is neglected and no orthogonalization is performed, thus leading to a symmetric splitting (see Figure 3.2c). Therefore the gap between bonding and antibonding orbitals is underestimated, which leads to wrong excitation energies. Also in order to fully recover the Pauli exchange repulsion, the orbitals need to

be properly orthogonal.[123] Hence the closed-shell repulsion (e.g., in the helium dimer), as well as barriers are insufficiently described in the standard NDDO approaches.[115] The orthogonalization corrections are designed to overcome these deficiencies. They account for the Pauli exchange repulsion and lead to an improved HOMO-LUMO gap.
The orthogonalization can be performed for the one- (**H**) and two-electron part (**G**) separately:

$$^{\lambda}\mathbf{F} = {}^{\lambda}\mathbf{H} + {}^{\lambda}\mathbf{G} \tag{3.79}$$

$$^{\lambda}\mathbf{H} = \mathbf{S}^{-1/2}\mathbf{H}\mathbf{S}^{-1/2} \tag{3.80}$$

$$^{\lambda}\mathbf{G} = \mathbf{S}^{-1/2}\mathbf{G}\mathbf{S}^{-1/2} \tag{3.81}$$

The orthogonalization corrections for the two-electron part are rather small and thus neglected in the OMX methods.[123] For the one-electron terms the corrections are introduced via the expansion of the transformation matrix $\mathbf{S}^{-1/2}$ [115,122,123]

$$\mathbf{S}^{-1/2} = (\mathbf{1} + \mathbf{S}')^{-1/2} = \mathbf{1} - \frac{1}{2}\mathbf{S}' + \frac{3}{8}\mathbf{S}'^2 - ... \tag{3.82}$$

With $\mathbf{S}'$ containing the off-diagonal elements of the overlap matrix and zero diagonal matrix elements. This expansion is plugged into equation 3.80 and only terms up to the second power in $\mathbf{S}'$ are included, which leads to expressions for the orthogonalization corrections.[123] In the OM1 method the corrections are applied to the one-center terms of the core Hamiltonian.[122] Thus this method involves only one- and two-center interactions, since the corrections only involve a second atom.[115] The OM2 approach also contains three-center interactions, since the corrections are also applied to the two-center part of the core Hamiltonian (i.e. the resonance integrals), which introduces interactions with a third atom. The full expression is given by[115]

$$^{\lambda}H_{\mu\nu} = \beta_{\mu\nu} - \frac{1}{2}\sum_{\rho}^{C}\left(S_{\mu\rho}\beta_{\rho\lambda} + \beta_{\mu\rho}S_{\rho\lambda}\right) + \frac{1}{8}\sum_{\rho}^{C} S_{\mu\rho}S_{\rho\lambda}\left(H_{\mu\mu} + H_{\lambda\lambda} - 2H_{\rho\rho}\right). \tag{3.83}$$

$\beta_{\mu\nu}$ is the empirical resonance integral, which can be parameterized according to equation 3.74, but this is not in line with an orthogonal atomic orbital basis and other expressions such as

$$\beta_{\mu\nu} = \frac{1}{2}\left(\beta_{\mu}^{A} + \beta_{\lambda}^{B}\right)\sqrt{R_{AB}}e^{-\left(\alpha_{\mu}^{A}+\alpha_{\lambda}^{B}\right)R_{AB}^{2}} \tag{3.84}$$

have been derived.[123] The resonance integral may already contain local orthogonalization corrections (depending on the parametrization). The other terms in equation 3.83 represent the three-center corrections. The corrections increase the computational effort, but since the three-center terms are heavily distance-dependent, cutoffs can be applied, which leads to the same scaling behavior as standard semi-empirical methods. OM3 neglects some of the smaller correction terms, which should speed up the calculation without significant loss of accuracy.[125]

The semi-empirical computations are much faster than post-HF or even DFT methods and can thus be applied to much larger systems. However, they are also less reliable and show less systematic errors,[115] since their accuracy depends on how similar the investigated system is compared to the molecules included in the training set. Thus in order to arrive at an estimation of the accuracy semi-empirical methods should only be applied after previous benchmark calculations.

The methods introduced so far are all ground-state methods, since the underlying framework is Hartree-Fock theory. In order to use semi-empirical methods for excited states a configuration interaction formalism can be applied. INDO/S[93] is a parametrization of the INDO approximation for CIS. CIS has however many disadvantages (see above), most prominently the lack of correlation in the excited states (although in the case of INDO/S it can partly be included via the parametrization). In *ab initio* theory the inclusion of higher excitations is quite expensive, but due to the integral approximations it is much cheaper for semi-empirical methods. The GUGA-CI[126] of Thiel and co-workers, which is implemented in the MNDO99 program package,[127] allows for an MRCI treatment in an active orbital space with different semi-empirical methods. These methods are used in their standard ground-state parametrization. In an *ab initio* MRCI calculation, the orbitals are usually first optimized in an MCSCF treatment. Due to the very limited flexibility of the minimal basis, this is however not necessary when using semi-empirical methods.[126]

The leading term in the CI excitation energy is the orbital energy difference (see above). Thus one should assume that the OMx methods, with their improved orbital energies should give better results for excited states than MNDO or AM1. This was indeed found to be true in an extensive benchmark.[94] The mean absolute deviation (MAD) of the vertical singlet excitation energies of MNDO and AM1 for 104 tested molecules is 1.35 and 1.19 eV, respectively, while OM1, OM2 and OM3 yield MADs of 0.45, 0.50 and 0.45 eV, respectively. INDO/S shows a similar accuracy (MAD 0.51 eV), but its results scatter more strongly than the values of the OMx methods. All semi-empirical methods included

in the benchmark tend to underestimate the excitation energies.[94] Similar to the ground-state calculations, the applicability of any semi-empirical method for the excited state of the system of interest should be tested in a previous benchmark.

3.3 Methods Based on Linear Response and Propagators

3.3.1 Linear Response Theory and Propagators

TDHF, TDDF as well as CC2 for excited states belong to the so-called linear response methods, while ADC(2), SOPPA and many others rely on propagators. Both approaches are closely related to the so-called Green's functions. This section aims at briefly reviewing the theoretical background of propagators, Green's functions and linear response.
Linear response is well-known from information theory and statistical mechanics.[128] If a system is subjected to a force, linear response theory calculates the output, i.e. the response, assuming it is linear in the force.[51] The response function is closely related to the concept of Green's functions.[51]
The solution of an inhomogeneous differential equation of a linear system, $x_{linear}(t)$, can be found by calculating the convolution of the corresponding **Green's function** $G(t-t')$ and the inhomogeneity $F(t)$.[129,130]

$$x_{linear}(t) = \int_0^t G(t-t')F(t')dt' \tag{3.85}$$

The Green's function is the solution of the differential equation if the inhomogeneity is the Dirac delta function.[49] Thus the convolution can be viewed as summing up the effect of several infinitesimal forces to yield the solution of the equation.[129] It can also be considered as the first term of a Volterra series[130] (of which the Green's functions are the coefficients),[131] which is used for nonlinear systems with memory.[i] For linear systems the Green's function approach provides the exact solution. In the case of non-linear systems using just the first term (the linear response) is an approximation, since higher-order terms of the Volterra series may become important. Thus in linear response theory, one assumes

$$x(t) \approx \int_0^t G(t-t')F(t')dt'. \tag{3.86}$$

[i] Contrary to a Taylor series, where the response at the time t can be calculated at this point in time, it depends on the whole evolution in time in a Volterra series.[130]

As an example for the Green's function approach (taken from [49]) let $\hat{H}_0$ be some Hermitian differential operator, fulfilling the equation

$$(E - \hat{H}_0)a(x) = b(x), \tag{3.87}$$

with the inhomogeneity $b(x)$. Expanding $a(x)$ and $b(x)$ into the eigenfunctions $\psi_\alpha(x)$ of $\hat{H}_0$

$$a(x) = \sum_\alpha a_\alpha \psi_\alpha(x) \tag{3.88}$$

$$b(x) = \sum_\alpha b_\alpha \psi_\alpha(x) \tag{3.89}$$

and keeping in mind that $b_\alpha = \int dx' \psi_\alpha^*(x') b(x')$ equation 3.87 can be written as

$$\sum_\alpha a_\alpha (E - \hat{H}_0)\psi_\alpha(x) = \sum_\alpha a_\alpha (E - E_\alpha^{(0)})\psi_\alpha(x) = \sum_\alpha b_\alpha \psi_\alpha(x). \tag{3.90}$$

Multiplying with ψ_α^* from the left and integrating yields

$$a_\alpha (E - E_\alpha^{(0)}) = b_\alpha. \tag{3.91}$$

Substituting this into the expansion for $a(x)$ gives

$$a(x) = \sum_\alpha \frac{b_\alpha}{E - E_\alpha^{(0)}} \psi_\alpha(x). \tag{3.92}$$

Inserting the expression for b_α one arrives at

$$a(x) = \int dx' \left[\sum_\alpha \frac{\psi_\alpha(x)\psi_\alpha^*(x')}{E - E_\alpha^{(0)}} \right] b(x). \tag{3.93}$$

The term in brackets defines the Green's function $G_0(x, x', E)$,

$$G_0(x, x', E) = \sum_\alpha \frac{\psi_\alpha(x)\psi_\alpha^*(x')}{E - E_\alpha^{(0)}}. \tag{3.94}$$

It can easily be shown that this is the solution of the equation for $b(x) = \delta(x - x')$.[49] This example shows that a Green's function can also be constructed for the one-particle Schrödinger equation. However, since the eigenfunctions have to be known, there seems

to be no benefit. This changes if a perturbation $V(x)$ is added,

$$\hat{H} = \hat{H}_0 + V(x). \tag{3.95}$$

In order to find the Green's function, we can write

$$(E - \hat{H}_0 - V(x))G(x, x', E) = \delta(x - x'). \tag{3.96}$$

This can be rewritten as

$$(E - \hat{H}_0)G(x, x', E) = \delta(x - x') + V(x)G(x, x', E). \tag{3.97}$$

This is however similar to equation 3.87 with $a(x) = G(x, x', E)$ and $b(x) = \delta(x - x') + V(x)G(x, x', E)$. Thus we can write the solution via the known Green's function $G_0(x, x', E)$[49]

$$G(x, x', E) = \int dx'' G_0(x, x'', E)[\delta(x'' - x') + V(x'')G(x'', x', E)]. \tag{3.98}$$

After integrating the term with the delta function one obtains the integral equation[49]

$$G(x, x', E) = G_0(x, x', E) + \int dx'' G_0(x, x', E)V(x'')G(x'', x', E). \tag{3.99}$$

Using a matrix representation, it can be written as

$$\mathbf{G}(E) = \mathbf{G}_0(E) + \mathbf{G}_0(E)\mathbf{V}\mathbf{G}(E). \tag{3.100}$$

This type of equation is often found in Green's function theory and provides a recipe for finding solutions to the perturbed problem.
This example used the single-particle Schrödinger equation. For many-body systems similar functions can be derived, which are often also called Green's function due to their similarity to the classical Green's functions, although they do not always fulfill the definition in a strict mathematical sense.[132]
In the case of Hartree-Fock theory a one-particle many-body Green's function can be derived,

$$G_0(\mathbf{x}, \mathbf{x}', E) = \sum_i \frac{\chi_i(\mathbf{x})\chi_i^*(\mathbf{x})}{E - \epsilon_i}, \tag{3.101}$$

with the spin orbitals $\chi_i(\mathbf{x})$. This Green's function has poles at the HF orbital energies. In order to go beyond Hartree-Fock theory and to obtain accurate single-particle energies (e.g., electron affinities and ionization energies), Dyson introduced an effective energy-dependent potential, which leads to an equation similar to 3.100, which is called the **Dyson equation**

$$\mathbf{G}(E) = \mathbf{G}_0(E) + \mathbf{G}_0(E)\mathbf{\Sigma}(E)\mathbf{G}(E), \tag{3.102}$$

with the so-called self-energy in matrix representation $\mathbf{\Sigma}(E)$.[49] $\mathbf{G}(E)$ is the exact **many-body Green's function (MBGF)**. Of course in order to solve the Dyson equation one has to introduce approximations. For instance, a perturbation expansion of $\mathbf{\Sigma}(E)$ can be used.[49]

Green's function theory can also be used for time-dependent perturbations. In fact, a very analogous expression to equation 3.85 arises naturally if the linear response of a quantum mechanical operator B to a time-dependent perturbation

$$H'(t) = AF(t) \tag{3.103}$$

is calculated with first-order perturbation theory. The derivation follows McWeeny.[51] A is a Hermitian operator determining the shape of the perturbation. The perturbed ground state Ψ_0' is expanded in the complete set of the time-independent wave functions $\{\Psi_n\}$ (i.e. eigenfunctions of the unperturbed Hamiltonian). Using the interaction picture one obtains

$$\Psi_0' = \Psi_0 + \sum_{n\neq 0} c_n(t) e^{-i\omega_{0n}t}\Psi_n, \tag{3.104}$$

with $\omega_{0n} = (E_n E_0)/\hbar$. First-order perturbation theory yields[51]

$$c_n(t) = \frac{1}{i\hbar}\int_{-\infty}^{t} \langle\Psi_n|\, A\,|\Psi_0\rangle\, F(t')e^{i\omega_{0n}t'}dt'. \tag{3.105}$$

Thus the first-order wave function is completely determined and hence the expectation value of B can be calculated. The response of B (defined by the fluctuation $\delta\langle B\rangle = \langle B\rangle - \langle B\rangle_0$) is then found to be[51]

$$\delta\langle B\rangle = \int_{-\infty}^{t} K(BA|t-t')F(t')dt'. \tag{3.106}$$

Thus the linear response of an operator can also be calculated, if the corresponding response/Green's function is known. The response function $K(BA|t-t')$ is also completely determined by the first-order time-dependent perturbation treatment[51]

$$\begin{aligned} K(BA|t-t') = \frac{1}{i\hbar} \sum_{n(\neq 0)} \Big[&\langle \Psi_0 | B | \Psi_n \rangle \langle \Psi_n | A | \Psi_0 \rangle e^{-i\omega_{0n}(t-t')} \\ &- \langle \Psi_0 | A | \Psi_n \rangle \langle \Psi_n | B | \Psi_0 \rangle e^{i\omega_{0n}(t-t')} \Big]. \end{aligned} \tag{3.107}$$

$K(BA|t-t')$ can also be regarded as a "**time-correlation function**", since it connects the time dependency of the fluctuation $\delta\langle B\rangle$ at time t with the strength of the perturbation A at an earlier time t'.[51]

As mentioned above, the perturbation can also be seen as a series of infinitesimal short perturbative impulses $F(t')$, which are propagated in time by $K(BA|t-t')$ and summed up to produce the effect on $\langle B\rangle$. Thus $K(BA|t-t')$ can also be considered as a **propagator**.[51] The concepts of Green's functions and propagators are related and sometimes used interchangeably.

For a single oscillatory perturbation one can easily transform $H'(t)$ to the frequency domain,

$$H'(\omega) = \frac{1}{2}\left(A_\omega e^{-i\omega t} + A_{-\omega} e^{i\omega t}\right). \tag{3.108}$$

The two terms are necessary to ensure hermiticity. Using this expression the whole propagator $K(BA|t-t')$ can be transformed,[51]

$$\Pi(BA_\omega|\omega) = \int_{-\infty}^{\infty} \theta(\tau) K(BA_\omega|\tau) e^{i\omega\tau} d\tau. \tag{3.109}$$

$\theta(\tau)$ is the Heaviside step function,

$$\theta(\tau) = \begin{cases} 0 & (\tau < 0), \\ 1 & (\tau > 0). \end{cases} \tag{3.110}$$

The propagator in the frequency domain is sometimes called **frequency-dependent polarizability** (FDP)[51] and can be shown to be[51]

$$\Pi(BA_\omega|\omega) = \lim_{\epsilon\to 0} \frac{1}{\hbar} \sum_{n\neq 0} \left\{ \frac{\langle \Psi_0 | B | \Psi_n \rangle \langle \Psi_n | A_\omega | \Psi_0 \rangle}{\omega + i\epsilon - \omega_{0n}} - \frac{\langle \Psi_0 | A_\omega | \Psi_n \rangle \langle \Psi_n | B | \Psi_0 \rangle}{\omega + i\epsilon + \omega_{0n}} \right\} \tag{3.111}$$

The FDP has poles if the frequency of the perturbation is in resonance with the system, i.e. if it is equal to the energy difference between two eigenstates ($\omega = \omega_{0n}$). Thus the concept of a propagator arises naturally from a first-order perturbation treatment.
In the **general treatment of propagators**, the Heisenberg picture[ii] is used and the propagator is defined as

$$\langle\langle B(t); A(t')\rangle\rangle = \frac{1}{i\hbar} \langle\Psi| \hat{T}[B(t)A(t')] |\Psi_0\rangle , \tag{3.112}$$

with $\hat{T}$ being the time-ordering operator bringing the operators in chronological order. Assuming that A and B are number-conserving operators one obtains, after taking the Fourier transform,

$$\langle\langle B; A\rangle\rangle_\omega = \lim_{\epsilon\to 0} \frac{1}{\hbar} \sum_{n\neq 0} \left\{ \frac{\langle\Psi_0| B |\Psi_n\rangle \langle\Psi_n| A |\Psi_0\rangle}{\omega + i\epsilon - \omega_{0n}} - \frac{\langle\Psi_0| A |\Psi_n\rangle \langle\Psi_n| B |\Psi_0\rangle}{\omega - i\epsilon + \omega_{0n}} \right\}, \tag{3.113}$$

which is almost the same expression[iii] as equation 3.111.[51] $\langle\langle B; A\rangle\rangle_\omega$ is called the polarization propagator.[51,133] The excitation energies are again found at the poles of the propagator in its "spectral form". This means that the excitation energies can be obtained without explicit calculation of the excited state, just by considering the response of the ground state to an oscillating perturbation. For instance, in a CASSCF treatment the states are calculated explicitly and the transition energies are obtained as the differences of the state energies. Using linear response theory the calculation of the actual excited state is bypassed.[51]

[ii] While the wave function in the typically used Schrödinger representation is time-dependent, it is independent of the time in the Heisenberg picture. Since the expectation value of an operator A must be invariant to this change of representation, it follows that the corresponding operator in the Heisenberg picture is defined as

$$A^H(t) = exp\left(\frac{i\hat{H}t}{\hbar}\right) A^S exp\left(-\frac{i\hat{H}t}{\hbar}\right).$$

Thus the operators, rather than the wave functions are now time-dependent.

[iii] The propagator in equation 3.113 is called the "causal" propagator, while 3.111 is called the "retarded propagator". But these fine distinctions are beyond the scope of this chapter, see[51] for details.

Starting from equation 3.112 and explicitly plugging in A and B in second quantization[51]

$$A = \sum_{r,r} A_{rs} a_r^\dagger a_s \tag{3.114}$$

$$B = \sum_{r,s} B_{rs} a_r^\dagger a_s, \tag{3.115}$$

one obtains the expression for the **general polarization propagator**. A typical matrix element ($A_{rs} = B_{rs} = 1$) in the spectral representation is given by[51,132]

$$\begin{aligned}\Pi_{rs,r's'}(\omega) &= \sum_{n\neq 0} \frac{\langle\Psi_0| a_r^\dagger a_s |\Psi_n\rangle \langle\Psi_n| a_{s'}^\dagger a_{r'} |\Psi_0\rangle}{\omega + i\epsilon - \omega_{0n}} - \sum_{n\neq 0} \frac{\langle\Psi_0| a_s^\dagger a_r |\Psi_n\rangle \langle\Psi_n| a_{r'}^\dagger a_{s'} |\Psi_0\rangle}{\omega - i\epsilon + \omega_{0n}}. \\ &= \Pi^+_{rs,r's'}(\omega) + \Pi^-_{rs,r's'}(\omega)\end{aligned} \tag{3.116}$$

From this equation it is obvious that the transition properties can also be obtained, since the transition moment of any (single-particle) operator $\hat{D}$ can be written as

$$T_n = \langle\Psi_n| \hat{D} |\Psi_0\rangle = \sum_{pq} D_{pq} \langle\Psi_n| a_p^\dagger a_q |\Psi_0\rangle . \tag{3.117}$$

Thus they are obtained by analyzing the residues[iv] of the propagator.
Apart from determining excitation properties, the Green's function approach can also be used to calculate expectation values. For the exact propagator the complete set of stationary state eigenfunctions has to be known. However, in general approximate expressions for the propagator are used. In the standard derivation of time-dependent Hartree-Fock theroy (TDHF, random-phase approximation) the propagator is typically calculated using time-dependent variation theory, i.e. by finding an approximate solution to the time-dependent Schrödinger equation with a single oscillating perturbation.[51,77] This means that basically the equation of motion for the wave function is solved. Since the propagator is a well-defined mathematical quantity, it can be assumed that its time evolution also follows some sort of equation of motion. Indeed, such an equation can be

[iv] In complex analysis the so-called Laurent series, which is a generalization of the Taylor series to include negative powers, is defined as

$$f(z) = \sum_{n=-\infty}^{+\infty} a_n (z - z_0)^n$$

The coefficient of the term $(z - z_0)^{-1}$ is called the residue of $f(z)$ at the pole z_0. For details see[134].

derived and its solution provides a very efficient way to calculate the actual (approximate) form of a defined propagator. In fact, the TDHF equations can also be derived from this approach.[51]

3.3.2 TDDFT and TDHF

As already mentioned the time-dependent Hartree-Fock equations (TDHF) can be derived in different frameworks. This chapter focuses on the derivation of the time-dependent DFT (TDDFT) equations, since the TDHF equations are then easily obtained from the corresponding expression for a hybrid functional. The theoretical foundation of time-dependent DFT is the **Runge-Gross theorem**, which states that the one-body time-dependent density is sufficient to calculate all observable properties of a many-electron system that evolves from a fixed initial state.[135] This is due to a one-to-one mapping of the time-dependent external potential $v_{ext}(\mathbf{r}, t)$, which includes the field from the nuclei and the time-dependent part (e.g., a laser field) and the one-body density $\rho(r, t)$ of such a system.[135] As in ground-state DFT a non-interacting reference system, that is supposed to reproduce the exact density, i.e. the Kohn-Sham approach, is generally used. Of course, as in ground-state theory, the question of the non-interacting v-representability arises, that means the question if the (time-dependent) density of any system can be reproduced by a Kohn-Sham auxiliary system. This has been proved under certain conditions[v].[136]
Similar to TDHF, there are also several ways to arrive at the TDDFT equations. One possible approach is to directly find an expression for the **response function** within time-dependent KSDFT and its spectral representation (equation 3.111), respectively. This ansatz will only shortly be outlined here (for details see[135]) to introduce the connection between TDDFT and linear response/Green's functions theory and the actual derivation will be based on a density matrix formalism, which also uses the time-dependent Kohn-Sham equations.[77] The latter approach is more common in the computational chemistry community.
The external potential can be split into a stationary part and a time-dependent perturbation,

$$v_{ext}(\mathbf{r}, t) = v_{ext,0}(\mathbf{r}) + \delta v_{ext}(\mathbf{r}, t). \tag{3.118}$$

[v]For details on the KS-existence see[135] and references therein.

It is assumed that the density $\rho(\mathbf{r})$ can be expressed as a Taylor series with respect to $\delta v_{ext}(\mathbf{r}, t)$,

$$\rho(\mathbf{r}, t) = \rho_0(\mathbf{r}) + \rho_1(\mathbf{r}, t) + \rho_2(\mathbf{r}, t) + ... \tag{3.119}$$

Since linear response only deals with the first-order term, terms of higher-order than ρ_1 can be neglected. In order to calculate the linear response of the density to the time-dependent perturbation, we need the corresponding response function, which basically means defining the operators A and B from the previous chapter explicitly in the DFT framework. Since we are interested in the response of the density, we need the so-called density-density response function $\chi(\mathbf{r}t, \mathbf{r}'t')$, that connects the linear response of the density $\rho_1(\mathbf{r}, t)$ with the perturbation $\delta v_{ext}(\mathbf{r}, t)$.

$$\rho_1(\mathbf{r}, t) = \int_0^\infty dt' \int d^3r' \chi(\mathbf{r}t, \mathbf{r}'t') \delta v_{ext}(\mathbf{r}', t') \tag{3.120}$$

Similar to the derivation of equation 3.111 the spectral representation of the density-density response function can be obtained using first-order time-dependent perturbation theory[135]

$$\chi(\mathbf{r}t, \mathbf{r}'t') = \sum_I \left\{ \frac{\langle\Psi_0|\,\hat{\rho}(\mathbf{r})\,|\Psi_I\rangle\,\langle\Psi_I|\,\hat{\rho}(\mathbf{r}')\,|\Psi_0\rangle}{\omega - \Omega_I + i0^+} - \frac{\langle\Psi_0|\,\hat{\rho}(\mathbf{r}')\,|\Psi_I\rangle\,\langle\Psi_I|\,\hat{\rho}(\mathbf{r})\,|\Psi_0\rangle}{\omega + \Omega_I + i0^+} \right\}. \tag{3.121}$$

with $\hat{\rho}$ being the density operator, which can be defined as[vi] $\hat{\rho}(\mathbf{r}) = \sum_{i=1}^N \delta(\mathbf{r} - \mathbf{r}_i)$. The summation is over all interacting excited states Ψ_I, with $\Omega_I = E_I - E_0$.[135] 0^+ represents a small positive number and is thus a shorthand for the limit $\epsilon \to 0$ used above.
Because the time-dependent Kohn-Sham equations (see below) can in principle generate the time-dependent density in an exact way, the response of the KS system can be used to calculate the response of the density

$$\rho_1(\mathbf{r}, t) = \int_0^\infty dt' \int d^3r' \chi_{KS}(\mathbf{r}t, \mathbf{r}'t') \delta v_{KS}(\mathbf{r}', t'). \tag{3.122}$$

[vi] $\delta(\mathbf{r} - \mathbf{r}_i)$ is the Dirac delta function and the summation is over all electron indices. The expectation value of the density operator with a general determinant wave function $\Phi = |\phi_1\phi_2 \dots \phi_N|$ is given by

$$\langle\Phi|\,\hat{\rho}(\mathbf{r})\,|\Phi\rangle = \sum_{i=1}^N \phi_i(\mathbf{r})^2 = \rho(\mathbf{r}).$$

That means the exact linear density response can be calculated using the linear response of a non-interacting reference system that is subjected to a perturbation δv_{KS}.[135] In the spectral representation the KS density-response function is given by (see[135] for details),

$$\chi_{KS}(\mathbf{r},\mathbf{r}',\omega) = \lim_{\eta\to 0^+}\sum_{k,j}(f_k - f_i)\delta_{\sigma_k\sigma_j}\frac{\varphi_k(\mathbf{r})\varphi_j(\mathbf{r})\varphi_j(\mathbf{r}')\varphi_k(\mathbf{r}')}{\omega - (\epsilon_j - \epsilon_k) + i\eta}. \tag{3.123}$$

$\delta v_{KS}(\mathbf{r},t)$ can be written as (see[135] for details),

$$\delta v_{KS}(\mathbf{r},t) = \delta v_{ext}(\mathbf{r},t) + \int d^3\mathbf{r}'\frac{\rho_1(\mathbf{r}',t)}{|\mathbf{r}-\mathbf{r}'|} + \int dt' \int d^3\mathbf{r}' f_{xc}[\rho_o](\mathbf{r}t,\mathbf{r}'t')\rho_1(\mathbf{r}',t'), \tag{3.124}$$

with the time dependent xc kernel f_{xc} which is defined as the functional derivative of the xc potential,[135]

$$f_{xc}[\rho_0](\mathbf{r}t,\mathbf{r}'t') = \left.\frac{\delta v_{xc}[\rho](\mathbf{r},t)}{\delta\rho(\mathbf{r}',t')}\right|_{\rho=\rho_0} \tag{3.125}$$

at the initial ground state density ρ_0. The poles of the KS response function (3.123) are however not the poles of the true response function, $\chi(\mathbf{r}t,\mathbf{r}'t')$. The latter can be derived by setting equation 3.120 equal to equation 3.122 and plugging in the expression for $\delta v_{KS}(\mathbf{r},t)$ (3.124) one obtains a Dyson-like[137] equation.[135]

$$\begin{aligned}\chi[\rho_0](\mathbf{r}t,\mathbf{r}'t') = \chi_{KS}[\rho_0](\mathbf{r}t,\mathbf{r}'t')+ \\ \int dt_1\int d^3r_1\int dt_2\int d^3r_2\chi_{KS}[\rho_0](\mathbf{r}t,\mathbf{r}'t') \\ \left[\frac{\delta(t-t')}{|\mathbf{r}_1-\mathbf{r}_2|} + f_{xc}[\rho_0](\mathbf{r}_1t_1,\mathbf{r}_2t_2)\right]\chi[\rho_0](\mathbf{r}_2t_2\mathbf{r}'t')\end{aligned} \tag{3.126}$$

Equation 3.126 "*plays the central role in TDDFT linear response calculations.*"[135] By taking the Fourier transform and integrating against δv_{ext} a condition for the true excitation energy can be found that leads to an eigenvalue problem which determines the excitation spectrum (see[135] for details).

Today most electronic structure codes work with the so-called **Casida equations**, which are similar to the TDHF equations.[51,135] They are equivalent to the eigenvalue equation, which can be derived from 3.126. Casida obtained them by analyzing the poles and residues of the frequency-dependent polarizability.[135,138] However, as stated above, in this chapter a different approach based on the density matrix is followed, which is less formal.[51,77] The derivation follows closely the review by Dreuw and Head-Gordon.[77] In the

case of TDHF the starting equation is the time-dependent Hartree-Fock equation, which can be derived by time-dependent variation theory under the assumption that the system can be described by a single Slater determinant at all times[51]

$$F(r,t)\varphi_i(r,t) = i\frac{\partial}{\partial t}\varphi_i(r,t). \tag{3.127}$$

In the case of TDDFT the **time-dependent Kohn-Sham equations** are used, which can be derived using the Runge-Gross theorem and the action integral,[77]

$$F^{KS}(r,t)\phi_i(r,t) = i\frac{\partial}{\partial t}\phi_i(r,t). \tag{3.128}$$

The time dependent Kohn-Sham operator contains a time-dependent non-local xc-kernel. However usually the so-called **adiabatic local density approximation (ALDA)** is applied, which uses a time-independent local xc-kernel (i.e. it is assumed that the density varies only slowly with time). In order to arrive at a matrix representation, single-particle wave functions (i.e. orbitals) $\{\chi_i(r)\}$ can be used used as basis

$$\phi_p(r,t) = \sum_j^{N_{bas}} c_{pj}(t)\chi_j(r), \tag{3.129}$$

leading to

$$i\frac{\partial}{\partial t}\mathbf{C} = \mathbf{F}^{KS}\mathbf{C}. \tag{3.130}$$

It is important to note that the basis $\{\chi_i(r)\}$ consists of molecular orbitals and not atomic basis functions. The time-dependent coefficients $c_{pj}(t)$ are nothing else than the occupation numbers and are either zero or one in the time-independent SCF ground state. From this equation an analogon to the von Neumann equation[139] can be derived, using the density matrix $\mathbf{P}$. The density matrix is connected to the expansion coefficients and the density $\rho(r,t)$ via[77]

$$\rho(r,t) = \sum_{p,q}^{N_{bas}} c_p(t)c_q^*(t)\chi_p(r)\chi_q^*(r) = \sum_{p,q}^{N_{bas}} P_{pq}\chi_p(r)\chi_q^*(r). \tag{3.131}$$

Taking the time derivative of the density matrix and multiplying with the imaginary unit i yields[140]

$$i\frac{\partial}{\partial t}\mathbf{P} = i\frac{\partial}{\partial t}\mathbf{C}\mathbf{C}^\dagger = i\mathbf{C}\left(\frac{\partial}{\partial t}\mathbf{C}^\dagger\right) + i\left(\frac{\partial}{\partial t}\mathbf{C}\right)\mathbf{C}^\dagger \tag{3.132}$$

Using equation 3.130 and its hermitian conjugate one obtains

$$i\frac{\partial}{\partial t}\mathbf{P} = -\mathbf{C}\mathbf{C}^{\dagger}\mathbf{F}^{KS} + \mathbf{F}^{KS}\mathbf{C}\mathbf{C}^{\dagger} = \mathbf{F}^{KS}\mathbf{P} - \mathbf{P}\mathbf{F}^{KS}. \tag{3.133}$$

This von Neumann-type equation is the basis for the further derivation. Looking at a single matrix element the final equation reads[77]

$$\boxed{\sum_{q}\{F_{pq}P_{qr} - P_{pr}F_{qr}\} = i\frac{\partial}{\partial t}P_{qr}} \tag{3.134}$$

Let us assume the energy variation of the system is described by the Kohn-Sham (or Fock operator) $F^{(0)}$. Introducing the time-dependent perturbation $A\widetilde{F}(t)$ we obtain

$$F = F^{(0)} + A\widetilde{F}(t). \tag{3.135}$$

Due to the perturbation the density matrix P will change, which can be described by adding a term ΔP. Since the Kohn-Sham operator contains all orbitals and hence depends on the density matrix, it will respond to the change in the density matrix, giving rise to the term ΔF

$$P = P^{(0)} + \Delta P = P^{(0)} + P^{(1)} \tag{3.136}$$

$$F = F^{(0)} + A\widetilde{F}(t) + \Delta F = F^{(0)} + F^{(1)} \tag{3.137}$$

with

$$\Delta F_{pq} = \sum_{st}\frac{\partial F^{0}_{pq}}{\partial P_{st}}\Delta P_{st}. \tag{3.138}$$

If we take only a single oscillatory perturbation into account, the time-dependent perturbation can be written as

$$AF(t) = \frac{1}{2}\left(A_{\omega}e^{-i\omega t} + A_{-\omega}e^{i\omega t}\right). \tag{3.139}$$

As before two terms are necessary in order to define a Hermitian operator. By analogy the perturbation of the density matrix can be written as[77,140]

$$P^{(1)}_{pq} = \frac{1}{2}\left(d_{pq}e^{-i\omega t} + d^{*}_{qp}e^{i\omega t}\right). \tag{3.140}$$

Plugging the expressions for F and P into equation 3.134 and collecting all terms of first order yields

$$\sum_{q}^{N_{bas}} \left[F_{pq}^{(0)} P_{qr}^{(1)} - P_{pq}^{(1)} F_{qr}^{(0)} + F_{pq}^{(1)} P_{qr}^{(0)} - P_{pq}^{(0)} F_{qr}^{(1)}\right] = i\frac{\partial}{\partial t} P_{pr}^{(1)}. \tag{3.141}$$

Inserting the definitions yields on the right-hand side

$$i\frac{\partial}{\partial t} P_{pr}^{(1)} = i\frac{1}{2}\frac{\partial}{\partial t}\left(d_{pr} e^{-i\omega t} + d_{rp}^{*} e^{i\omega t}\right) = \frac{1}{2}\omega d_{pr} e^{-i\omega t} - cc.$$

and

$$\frac{1}{2}\sum_{q}^{N_{bas}} \Bigg[F_{pq}^{(0)} d_{qr} - d_{pq} F_{qr}^{(0)} + \left(A_{pq} + \sum_{st} \frac{\partial F_{pq}^{(0)}}{\partial P_{st}} d_{st}\right) P_{qr}^{(0)} - P_{pq}^{(0)} \left(A_{qr} + \sum_{st} \frac{\partial F_{qr}^{(0)}}{\partial P_{st}} d_{st}\right)\Bigg] e^{-i\omega t} + cc.$$

on the left-hand side. Just looking at the terms with $e^{-i\omega t}$ gives

$$\sum_{q}^{N_{bas}} \Bigg[F_{pq}^{(0)} d_{qr} - d_{pq} F_{qr}^{(0)} + \left(A_{pq} + \sum_{st} \frac{\partial F_{pq}^{(0)}}{\partial P_{st}} d_{st}\right) P_{qr}^{(0)} - P_{pq}^{(0)} \left(A_{qr} + \sum_{st} \frac{\partial F_{qr}^{(0)}}{\partial P_{st}} d_{st}\right)\Bigg] = \omega d_{pr}.$$

Using the idempotency of P[51,77] one obtains

$$PP = P^{(0)}P^{(0)} + P^{(0)}P^{(1)} + P^{(1)}P^{(0)} + P^{(1)}P^{(1)} = P^{(0)} + P^{(0)}P^{(1)} + P^{(1)}P^{(0)} = P. \tag{3.142}$$

It follows for the first-order change that

$$P^{(0)}P^{(1)} + P^{(1)}P^{(0)} = P^{(1)}. \tag{3.143}$$

For a single matrix element the equation can be written as

$$\sum_{q}^{N_{bas}} \left\{P_{pq}^{(0)} P_{qr}^{(1)} + P_{pq}^{(1)} P_{qr}^{(0)}\right\} = P_{pr}^{(1)}. \tag{3.144}$$

With this equation we can derive which elements of P_{pq} and thus d_{pq} (see eq. 3.140) are non-zero. Since $P^{(0)}$ refers to the time-independent unperturbed SCF ground state, the following relations hold:

$$P_{ij}^{(0)} = \delta_{ij} \tag{3.145}$$

$$P_{ia}^{(0)} = P_{ai}^{(0)} = P_{ab}^{(0)} = 0, \tag{3.146}$$

with i, j being occupied and a, b being virtual orbitals. Thus for a matrix element of two occupied orbitals $P_{ij}^{(0)}$ it follows

$$\sum_{q}^{N_{bas}} \left\{ P_{iq}^{(0)} P_{qj}^{(1)} + P_{iq}^{(1)} P_{qj}^{(0)} \right\} = P_{ij}^{(1)} \tag{3.147}$$

$$\sum_{q}^{N_{occ}} \left\{ \delta_{iq} P_{qj}^{(1)} + \delta_{qj} P_{iq}^{(1)} \right\} = P_{ij}^{(1)} \tag{3.148}$$

$$P_{ij}^{(1)} + P_{ij}^{(1)} = P_{ij}^{(1)} \tag{3.149}$$

This is only fulfilled if $P_{ij}^{(0)} = 0$. Similar for a matrix element between two virtual orbitals P_{ab} it follows

$$\sum_{q}^{N_{bas}} \left\{ P_{aq}^{(0)} P_{qb}^{(1)} + P_{aq}^{(1)} P_{qb}^{(0)} \right\} = P_{ab}^{(1)} \tag{3.150}$$

$$\sum_{q}^{N_{occ}} \left\{ \delta_{aq} P_{qb}^{(1)} + \delta_{qb} P_{aq}^{(1)} \right\} = P_{ab}^{(1)} \tag{3.151}$$

$$P_{ab}^{(1)} + P_{ab}^{(1)} = P_{ab}^{(1)} \tag{3.152}$$

Thus only matrix elements between the occupied and virtual blocks (d_{ia}, d_{ai}) can be non-zero. Furthermore $P^{(0)}$ and $F^{(0)}$ are diagonal. Using the so-called zero-frequency limit ($A = 0$), which is equivalent to assuming an infinitesimal perturbation and setting $\mathbf{d} = \mathbf{x} + \mathbf{y}$ one obtains two coupled equations[77]

$$F_{aa}^{(0)} x_{ai} - x_{ai} F_{ii}^{(0)} + \sum_{bj} \left\{ \frac{\partial F_{ai}^{(0)}}{\partial P_{bj}} x_{bj} + \frac{\partial F_{ai}^{(0)}}{\partial P_{jb}} y_{bj} \right\} P_{ii}^{(0)} = \omega x_{ai} \tag{3.153}$$

$$F_{ii}^{(0)} y_{ai} - y_{ai} F_{aa}^{(0)} + P_{ii}^{(0)} \sum_{bj} \left\{ \frac{\partial F_{ia}^{(0)}}{\partial P_{bj}} x_{bj} + \frac{\partial F_{ia}^{(0)}}{\partial P_{jb}} y_{bj} \right\} = \omega y_{ai}. \tag{3.154}$$

At this stage a definition for F has to be given, which can be plugged into equations 3.153 and 3.154. Looking at the most general case of a hybrid functional, with the Kohn-Sham operator

$$F_{ai}^{(0)} = \int d^3r \phi_a(r) \left\{ -\frac{1}{2}\nabla^2 + \sum_{K=1}^{M} \frac{-Z_K}{|r-R_K|} + \int d^3r' \frac{\rho(r')}{|r-r'|} \right. \\ \left. -c_{HF} \int d^3r' \frac{\rho(r,r')}{|r-r'|} + (1-c_{HF}) \frac{\delta E_{xc}}{\delta \rho(r)} \right\} \phi_i(r), \quad (3.155)$$

the derivative of F is given by

$$\frac{\partial F_{ai}}{\partial P_{bj}} = \frac{\partial}{\partial P_{bj}} \int d^3r \int d^3r' \frac{\phi_a(r) \sum_{p,q} P_{p,q} \phi_p(r') \phi_q(r') \phi_i(r)}{|r-r'|} \\ - c_{HF} \frac{\phi_a(r) \sum_{p,q} P_{p,q} \phi_p(r) \phi_q(r') \phi_i(r')}{|r-r'|} \\ - (1-c_{HF}) \phi_a(r) \frac{\delta E_{xc}}{\delta \rho(r)} \phi_i(r). \quad (3.156)$$

Thus the response of the Kohn-Sham operator can be written as[77]

$$\frac{\partial F_{ai}}{\partial P_{bj}} = (ia|jb) - c_{HF}(ij|ab) + (1-c_{HF})(ia|f_{xc}|jb). \quad (3.157)$$

Equation 3.153 and 3.154 are the so-called Casida equations, which are generally formulated as a matrix equation

$$\boxed{\begin{bmatrix} \mathbf{A} & \mathbf{B} \\ \mathbf{B}^* & \mathbf{A}^* \end{bmatrix} \begin{bmatrix} X \\ Y \end{bmatrix} = \omega \begin{bmatrix} 1 & 0 \\ 0 & -1 \end{bmatrix} \begin{bmatrix} X \\ Y \end{bmatrix}} \quad (3.158)$$

Keeping in mind that $F_{ii}^{(0)} = \epsilon_i$ the matrix elements can be written as (again for a hybrid functional)[77]

$$A_{ia,jb} = \delta_{ij}\delta_{ab}(\epsilon_a - \epsilon_i) + (ia|jb) - c_{HF}(ij|ab) + (1-c_{HF})(ia|f_{xc}|jb) \quad (3.159)$$

$$B_{ia,bj} = (ia|bj) - c_{HF}(ib|aj) + (1-c_{HF})(ia|f_{xc}|bj). \quad (3.160)$$

The Casida equations have the same form for TDHF and TDDF, although the matrix elements are of course different. Setting c_{HF} to zero yields the elements for pure TDDFT, while $c_{HF} = 1$ gives TDHF. Setting the elements of the matrix $\mathbf{B}$ to zero yields **CIS** in

the case of TDHF and the so-called **Tamm-Dankoff approximation (TDA)**[141] in the case of TDDFT.

Since the matrix **B** include de-excitations, **TDHF** is an extension to CSI. The Y amplitudes which are included via the matrix **B**, are a measure of the ground-state correlation that is introduced. The use of a Hartree-Fock wave function is thus only justified if these elements are small, because otherwise the HF reference is a bad approximation.[77] This fact shows the main problem of TDHF: it can only give a significant improvement over CIS if Y and **B** have a relevant size, but in this case its applicability is doubtful. Since the cost of TDHF is about twice that of CIS it is rarely used in practical calculations.[77] The excitation energies are generally slightly less severely overestimated than with CIS and TDHF obeys the Thomas-Reiche-Kuhn sum rule, but it is questionable if these benefits are worthwhile the additional costs. Triplet states are usually poorly described due to the HF reference, which can even lead to triplet instabilities.[77] TDHF has no inherent bias towards neutral or charge-transfer states (see below) and can thus be used if qualitatively correct results, e.g. the shape of potential energy surfaces, are required. Its scope for the prediction of spectra is however limited due to the high quantitative error in the excitation energies.

TDDFT is nowadays the most popular method for the calculation of excitation energies and electronic spectra, since it is cost efficient, shows a robust performance, has broad applicability and leads to excitation energies with a typical error range of 0.1 - 0.5 eV for valence excited states.[77] Thus it is much more accurate than TDHF. Hybrid TDDFT is slightly more expensive, since the response of the xc-potential has to be computed (typically numerically).[77] Similar to ground-state DFT, the fact that the true exchange-correlation functional is not known poses significant problems. Again the quality of a functional is not known a priori and benchmarks have to be performed, due to the "zoo of functionals". This has been done extensively in the literature and justifies the existence of a review article on TDDFT benchmarks.[142]

The locality and (derived from that) the incorrect long-range behavior of the exchange-correlation functionals is responsible for the main problem of TDDFT, the **charge-transfer excitations**. This can be shown using a four-orbital-four-electron model system. Let the orbitals i, j be located at molecule A and a, b at molecule B. Let furthermore the intermolecular distance be high enough, so that the overlap of orbitals on different molecules can be neglected. The matrix elements in equations 3.159 and 3.160 then

simplify to[77]

$$A_{ia,jb} = \delta_{ij}\delta_{ab}(\epsilon_a - \epsilon_i) - c_{HF}(ij|ab) \quad (3.161)$$

$$B_{ia,bj} = 0 \quad (3.162)$$

The **B** matrix reduces to a zero matrix and in the **A** matrix only the orbital difference and the Coulomb term $(ij|ab)$ (which originates form the response of the non-local Hartree-Fock exchange integral) remain. The response of the Coulomb integral (i.e. an exchange integral), as well as the response of the local xc-functional, vanish if the overlap is zero. In TDHF (similar to CIS, see above) the orbital difference is a good approximation for the difference of ionization energy and electron affinity and the Coulomb term reproduces the correct $\frac{1}{R}$ distance behavior.

In the case of a pure density functional ($c_{HF} = 0$) the Coulomb term also vanishes and contrary to Hartree-Fock theory the orbital energy of the virtual orbital is not connected to the electron affinity and thus the the charge-transfer energy is badly underestimated. Furthermore the term is just a constant and thus the correct distance behavior cannot be reproduced.[68,69] Hybrid functionals generally perform somewhat better, but for an accurate description a very high amount of HF exchange is needed, which decreases the performance for valence excited states. Since pure TDDFT underestimates the energy of charge-transfer excitations and pure TDHF tends to overestimate all excitation energies, a whole range of values can be obtained, depending on the actual amount of HF exchange. This is not very satisfying, but can be used to calibrate a functional for a certain system.[143]

Since charge-transfer excitations play an important role (e.g., for push-pull systems, excitations in oligomers, charge transfer at interfaces in organic optoelectronic devices, etc) there has been a massive effort to correct this deficiency of TDDFT. One possibility might be to go beyond linear response, by including higher-order terms. With these terms even LDA was shown to give a qualitatively correct description[vii] of CT states.[144] Most approaches are however based on **long-range corrections**. The first steps in this direction were taken by Savin et al.[146,147] as well as Gill and coworkers.[148,149] Since HF exchange shows the correct long-range behavior, the idea is to use the DFT exchange functional for the short-range and the exchange integral for the long-range interaction. This connection

[vii] Ziegler et al. also showed that these higher order terms necessary for DFT are zero in TDHF, thus explaining, why this problem does not arise here.[144] Thus they are also called spurious "self-interaction terms".[145] For range separated hybrids, these terms do not vanish, but are rather small, which is inline with their improved performance.

is achieved via a separation of the two-electron operator using an Ewald split[150]

$$\frac{1}{r_{12}} = \frac{1 - erf(\mu r_{12})}{r_{12}} + \frac{erf(\mu r_{12})}{r_{12}}. \tag{3.163}$$

The parameter μ controls the ratio of short- (first term) and long-range interaction (second term). This ansatz was successfully applied to GGA functionals by Hirao et al.[150,151] In this approach the percentage of HF exchange is zero for $r_{12} = 0$ and 100 for $r_{12} \to \infty$. For comparison, in B3LYP it is constant at about 20 %. The splitting was generalized to hybrid functionals by Handy and coworkers in the CAM-B3LYP (CAM = Coulomb attenuating method) functional.[152] In order to work for a hybrid functional, two additonal parameters were included in the splitting

$$\frac{1}{r_{12}} = \frac{1 - [\alpha + \beta \cdot erf(\mu r_{12})]}{r_{12}} + \frac{\alpha + \beta \cdot erf(\mu r_{12})}{r_{12}}. \tag{3.164}$$

In CAM-B3LYP the values of the parameters are $\alpha = 0.19$ and $\alpha + \beta = 0.65$, which leads to about 19% of HF exchange at $r_{12} = 0$ and 65 % at the long-range limit. Other examples of long-range corrected hybrids are LC-ωPBE[153] and ωB97XD.[154] These functionals sufficiently improve the description of charge-transfer and Rydberg states[viii].[77,142]

It has been argued that the range separation with a fixed parameter is unphysical, since μ should depend on the density.[155] One pragmatic way to go beyond a fixed parameter is to find the optimal parameter for each system. Since using the exact functional the ionization energy should be identical to the HOMO energy, the optimal parameter can be found by minimizing the difference

$$\delta_{IP} = \left| \epsilon_{HOMO} - (E_{gs}(\mu, N) - E_{gs}(\mu, N-1)) \right|. \tag{3.165}$$

This "IP-tuning"[156] gives an improved description and allows for the definition of the optimal value of μ in a consistent way,[155] but is also quite demanding, because the minimization has to be performed prior to the actual calculation. Another problem of the approach is the loss of size-consistency.[157]

Double excitations are not included in the linear response of the Kohn-Sham system, since it requires the interaction with two photons. Thus doubly excited states cannot be

[viii] Rydberg states are also a problem of TDDFT, which is connected to the local nature of the xc-functional. Thus it is often seen as being identical to the CT problem. However this is not quite true, as Rydberg states can be described accurately, if the one-electron energies are reproduced correctly, since the contributions from the xc-kernel are usually small (see[69] for details).

calculated with standard LR-TDDFT.[158]
Nevertheless, despite its deficiencies and problems TDDFT is one of the most widely applicable methods, when calculations of larger systems are needed.

3.3.3 Second-Order Approximate Coupled-Cluster Singles and Doubles (CC2)

Contrary to CI, where the wave function is a linear expansion of determinants, a non-linear expansion based on an exponential operator is used in coupled-cluster (CC) theory,[48,50,159]

$$\Psi_{CC} = e^{\hat{T}}\Phi_0, \tag{3.166}$$

with

$$\hat{T} = \hat{T}_1 + \hat{T}_2 + ...\hat{T}_N, \tag{3.167}$$

and

$$\hat{T}_1\Phi_0 = \sum_{i,a} t_i^a \Phi_i^a \tag{3.168}$$

$$\hat{T}_2\Phi_0 = \sum_{i<j}\sum_{a<b} t_{ij}^{ab}\Phi_{ij}^{ab}. \tag{3.169}$$

The operators $\hat{T}_i$ with $i > 2$ generate the higher excitations accordingly. The coefficients t are called amplitudes. In order to see the effect of the exponential operator the Taylor expansion can be used,[48]

$$e^{\hat{T}} = 1 + \hat{T}_1 + \left(\hat{T}_2 + \frac{1}{2}\hat{T}_1^2\right) + \left(\hat{T}_3 + \hat{T}_2\hat{T}_1 + \frac{1}{6}\hat{T}_1^3\right) + \left(\hat{T}_4 + \hat{T}_3\hat{T}_1 + \frac{1}{2}\hat{T}_2^2 + \frac{1}{2}\hat{T}_2\hat{T}_1^2 + \frac{1}{24}\hat{T}_1^4\right) + ... \tag{3.170}$$

Writing the CI wave function in the same formalism yields

$$\Psi_{CI} = \left(1 + \hat{T}\right)\Phi_0 = \left(1 + \hat{T}_1 + \hat{T}_2 + \hat{T}_3 + ...\right)\Phi_0. \tag{3.171}$$

Truncating both wave functions after doubles (CISD, CCSD), i.e. taking only $\hat{T}_1$ and $\hat{T}_2$ into account, leaves only $\hat{T}_1$ and $\hat{T}_2$ in the CI expansion, while also terms like $\hat{T}_1^2$ (disconnected double), $\hat{T}_2^2$ (disconnected quadruple) and $\hat{T}_2\hat{T}_1$ (disconnected triple) remain

in the coupled-cluster wave function, due to the non-linear expansion. Thus higher-order terms are included, despite the truncation. These terms are responsible for the size-consistency of truncated coupled-cluster methods. While Møller-Plesset perturbation theory adds excitation types up to a certain order, coupled cluster theory includes defined types of excitations to infinite order.[48]

The energy of the coupled-cluster wave function is usually obtained by projecting the coupled-cluster wave function onto the reference wave function Φ_0, since a variational approach is too demanding.[48,50] Due to the Slater-Condon rules and the Brillouin theorem ony the double excitations can contribute to the CC correlation energy expression.

$$E_{CC} = \langle\Phi_0|\,\hat{H}e^{\hat{T}}\,|\Phi_0\rangle = E_0 + \langle\Phi_0|\,\hat{T}_2 + \frac{1}{2}\hat{T}_1^2\,|\Phi_0\rangle = E_0 + \sum_{i<j}\sum_{a<b}\left(t_{ij}^{ab} + t_i^a t_j^b - t_i^b t_j^a\right)\langle\Phi_0|\,\hat{H}\,|\Phi_{ij}^{ab}\rangle\,. \tag{3.172}$$

It is noteworthy that the coefficients of the singles are also included via the disconnected doubles. All higher excitations do not enter the energy expression, but are involved in the equation for the amplitudes. It should be noted that $\hat{T}_1^2$ as well as $\hat{T}_2$ generate all doubly excited states. Thus going from CCS to CCSD does not increase the number of generated determinants, but leads to an improved description of the amplitudes.[ix] The equations for the amplitudes can be obtained by projecting onto excited configurations. It is often convenient to use the similarity transformed Hamiltonian, which is obtained by multiplying the Schrödinger equation from the left with the de-excitation operator $e^{-\hat{T}}$[50]

$$e^{-\hat{T}}\hat{H}e^{\hat{T}}\Phi_0 = E_{CC}e^{-\hat{T}}e^{\hat{T}}\Phi_0 = E_{CC}\Phi_0. \tag{3.173}$$

The equations can then be written as

$$\langle\Phi_0|\,e^{-\hat{T}}\hat{H}e^{-\hat{T}}\,|\Phi_0\rangle = E_{CC} \tag{3.174}$$

$$\langle\mu_i|\,e^{-\hat{T}}\hat{H}e^{-\hat{T}}\,|\Phi_0\rangle = 0,\ \text{for } i = 1, 2, \ldots \tag{3.175}$$

with $\langle\mu_1|$ representing the singly excited manifold, $\langle\mu_2|$ the doubly excited manifold and so on,

$$|\mu_i\rangle = \hat{\tau}_{\mu_i}\,|\Phi_0\rangle\,. \tag{3.176}$$

[ix] In fact the singles amplitudes are zero for CCS and thus it does not yield an improved description of the ground state, if canonical orbitals are used (similar to CIS).[48]

The amplitude equations 3.175 form a non-linear system, which has to be solved iteratively.[50]

By itself coupled-cluster is a ground-state method, but it can be used for excited states via an equation-of-motion (EOM) or linear-response formalism. In this chapter the linear response of the **CC2**[160] wave function is discussed. CC2 is an approximation to the CCSD wave function. When dealing with the CCSD often the $\hat{T}_1$-transformed Hamiltonian $\widetilde{H}$ is used,

$$\widetilde{H} = e^{-\hat{T}_1} \hat{H} e^{\hat{T}_1}. \tag{3.177}$$

Thus the amplitude equations reads [x]

$$\langle \mu_i | \, e^{-\hat{T}_2} \widetilde{H} e^{\hat{T}_2} \, | \Phi_0 \rangle = 0. \tag{3.178}$$

Using the BCH (Baker-Campbell-Hausdorff) expansion,[50]

$$e^{-\hat{T}_2} \widetilde{H} e^{\hat{T}_2} = \widetilde{H} + [\widetilde{H}, \hat{T}_2] + \frac{1}{2}[[\widetilde{H}, \hat{T}_2]\hat{T}_2] + \frac{1}{6}[[[\widetilde{H}, \hat{T}_2]\hat{T}_2], \hat{T}_2] + ... \tag{3.179}$$

and plugging the result into 3.178 yields[50,160]

$$\langle \mu_1 | \, \widetilde{H} + [\widetilde{H}, \hat{T}_2] \, | \Phi_0 \rangle = 0 \tag{3.180}$$

$$\langle \mu_2 | \, \widetilde{H} + [\widetilde{H}, \hat{T}_2] + \frac{1}{2}[[\widetilde{H}, \hat{T}_2]\hat{T}_2] \, | \Phi_0 \rangle = 0. \tag{3.181}$$

The higher-order terms vanish, since the $\hat{T}_1$-transformed Hamiltonian is a one- and two-electron operator. The Hamiltonian can be written in the spirit of Møller-Plesset theory as a sum of the Fock operator and the fluctuation potential $\hat{U}$,

$$\hat{H} = \hat{F} + \hat{U}. \tag{3.182}$$

Analyzing the CCSD wave function in terms of perturbation theory[50] reveals that its energy is accurate up to third order in the fluctuation potential (while the wave function is accurate up to first order). The singles amplitudes as well as the doubles amplitudes are accurate to second order.[50] Taking the singles equation from CCSD (second order)

[x] Since the excitation operators commute there is no problem with the order of the operators, i.e.

$$e^{\hat{T}_1 + \hat{T}_2} = e^{\hat{T}_1} e^{\hat{T}_2}.$$

and including the doubles in the doubles equation just to first order as in MP2 leads to the CC2 equations.[160]

$$\Omega_{\mu_1} \equiv \langle \mu_1 | \widetilde{H} + [\widetilde{H}, \hat{T}_2] | \Phi_0 \rangle = 0 \tag{3.183}$$

$$\Omega_{\mu_2} \equiv \langle \mu_2 | [\hat{F}, \hat{T}_2] + \widetilde{H}] | \Phi_0 \rangle = 0 \tag{3.184}$$

This is equivalent to approximating the connected doubles amplitudes by the corresponding MP2 expression, but with $\hat{T}_1$-transformed integrals,[161]

$$t_{aibj} = \frac{1}{1 + \delta_{ij}\delta_{ab}} \frac{\widetilde{(ai|bj)}}{\epsilon_i - \epsilon_a + \epsilon_j - \epsilon_b}. \tag{3.185}$$

The CC2 energy is accurate to second order in the fluctuation potential, while the wave function is still accurate to first order.[50] Thus the 2 in CC2 denotes the perturbation order as in Møller Plesset theory. While CCSD scales as $\mathcal{O}(n^6)$, CC2 scales as $\mathcal{O}(n^5)$.[160] In the original derivation of CC2 Jørgensen et al. did not aim at developing a new ground-state method, since they expected CC2 to be of similar quality as MP2. They intended to develop an approximate coupled-cluster method for which a response function could be derived, with a structure comparable to the true response function, for the calculation of excitation energies and transition properties.[160] Applying a time-dependent perturbation $\hat{H} = \hat{H}^{(0)} + V(t)$ the time-dependent CC2 equations can be derived

$$\langle \mu_1 | \widetilde{H} + [\widetilde{H}, \hat{T}_2] | \Phi_0 \rangle = i \frac{\partial t_{\mu_1}}{\partial t} \tag{3.186}$$

$$\langle \mu_2 | [\hat{F} + \widetilde{V}, \hat{T}_2] + \widetilde{H}] | \Phi_0 \rangle = i \frac{\partial t_{\mu_2}}{\partial t}. \tag{3.187}$$

Deriving the response function leads to the Jacobian[xi] $\mathbf{A}_{\mu_i\nu_j} = \frac{\partial \Omega_{\mu_i}}{\partial t_{\nu_j}}$, from which the excitation energies can be derived as eigenvalues[162]

$$\mathbf{A}_{\mu_i\nu_j} = \begin{pmatrix} \langle \mu_1 | [\widetilde{H}, \tau_{\nu_1}] + [[\widetilde{H}, \tau_{\nu_1}], \hat{T}_2] | \Phi_0 \rangle & \langle \mu_1 | [\widetilde{H}, \tau_{\nu_2}] | \Phi_0 \rangle \\ \langle \mu_2 | [\widetilde{H}, \tau_{\nu_1}] | \Phi_0 \rangle & \delta_{\mu_2\nu_2}\epsilon_{\mu_2} \end{pmatrix}. \tag{3.188}$$

The doubles-doubles bock simply consists of the orbital energy difference $\epsilon_{aibj} = \epsilon_a - \epsilon_i + \epsilon_b - \epsilon_j$. In modern implementations the diagonality of the doubles-doubles block $\mathbf{A}_{\mu_2\nu_2}$ is used to construct an effective Jacobian for the singles block. This leads to a reduction of the dimensionality and reduces memory requirements, but makes the eigenvalue problem

[xi] For the derivation see[160] and references therein.

non-linear.[161]

Since the matrix is non-symmetric, the left and right eigenvectors are not identical. Thus for gradients[163] and excitation properties[162] both eigenvectors have to be calculated. Thus a left and a right transition moment exist and the oscillator strength has to be calculated from the average.[162] The non-symmetry of the Jacobian also leads to problems at conical intersections.[164]

Similar to MP2 the performance of CC2 can be improved by introducing spin-component scaling.[165–167] In this method the same and opposite spin contributions are scaled by empirical parameters, which is then called SCS-CC2.

A benchmark for the vertical excitation energies yielded a mean absolute error of 0.32 eV for CC2[113] and a study of 0-0-transitions showed a mean absolute error of 0.07 eV for CC2 and 0.05 for SCS-CC2.[168] The largest molecule in the latter study had 78 atoms. (SCS-)CC2 can treat charge-transfer and neutral excited states on an equal level, but fails if the contribution from the doubles excitations is significant, since the doubles-doubles block is just given by the orbital energy difference, which is a heavy approximation. It can also loose accuracy if the excited state is clearly multiconfigurational.[47] In cases, where the ground state is multiconfigurational, the errors become even larger.[47]

It is also possible to derive response functions for higher-order methods, like CCSD and CC3,[160] but they become increasingly expensive and multi-reference methods can become competitive.

SCS-CC2 can be applied to medium-sized and also larger molecules for which it often features the best ratio between accuracy and cost. For small systems high-level methods can (and probably should) be used and for large systems, especially if geometry optimizations, properties or solvent effects (see below) are of interest, TDDFT has to be applied.

3.3.4 Algebraic Diagrammatic Construction to Second Order (ADC(2))

Although being derived in a very different framework the algebraic diagrammatic construction to second order, ADC(2),[169,170] is similar to CC2. Instead of using the linear response of a coupled cluster wave function, the idea behind ADC(2) is the perturbative expansion of the transition function, which is related to the polarization propagator $\Pi_{pq,rs}(\omega)$ (equation 3.116). The derivation presented in this chapter follows references[169] and[132] closely.

Since the terms $\mathbf{\Pi}^{+}(\omega)$ and $\mathbf{\Pi}^{-}(\omega)$ of the polarization propagator contain the same in-

formation usually only the first term is considered. The corresponding matrix equation is given as[169]

$$\mathbf{\Pi}^{+}(\omega) = \mathbf{x}^{\dagger}(\omega\mathbf{1} - \mathbf{\Omega})^{-1}\mathbf{x}, \tag{3.189}$$

with $\Omega_{nn} = E_n - E_0$ being a diagonal matrix containing the excitation energies and $x_{n,rs} = \langle\Psi_n| a_r^{\dagger}a_s |\Psi_0\rangle$. ϵ in the general expression for the polarization propagator (equation 3.116) is usually set to zero, whenever unessential.[170] As already mentioned the excitation energies can be obtained as poles of the propagator and the transition moments from the residues at the corresponding poles. The transition function $T(\omega)$ is given as[132]

$$T(\omega) = \mathbf{D}^{\dagger}\mathbf{\Pi}^{+}(\omega)\mathbf{D}, \tag{3.190}$$

with $\mathbf{D}$ containing the matrix elements D_{rs} of a transition operator (usually the dipole operator). Using equation 3.189 the transition function can also be written as

$$T(\omega) = \mathbf{T}^{\dagger}(\omega\mathbf{1} - \mathbf{\Omega})^{-1}\mathbf{T}, \tag{3.191}$$

with $\mathbf{T}_n = \langle\Psi_n| \hat{D} |\Psi_0\rangle = \sum_{rs} D_{rs} \langle\Psi_n| a_r^{\dagger}a_s |\Psi_0\rangle$. The transition function has the same poles as the polarization propagator and the transition moments can be obtained directly from its residues.

Taking the same partitioning of the Hamiltonian as in Møller-Plesset perturbation theory (see equation 3.182) the perturbation series can be written as

$$T(\omega) = \sum_{n=0}^{\infty} T^{(n)}(\omega) = \sum_{n=0}^{\infty} \mathbf{D}^{\dagger}\mathbf{\Pi}^{+(n)}(\omega)\mathbf{D} \tag{3.192}$$

The expansion can be expressed using a diagrammatic approach, i.e. by constructing the corresponding Feynman or Goldstone diagrams,[xii] respectively and translating them to the corresponding algebraic expressions. The complete derivation is beyond the scope of this chapter (see[170] for details), but the most important steps are outlined.

In order to arrive at the working equations, the following assumptions are made:[170]

1. The polarization propagator can be written as

$$T(\omega) = \mathbf{F}^{\dagger}\mathbf{\Gamma}(\omega)\mathbf{F} \quad \text{with} \quad \mathbf{\Gamma}(\omega) = [\omega\mathbf{1} - (\mathbf{K} + \mathbf{C})]^{-1}. \tag{3.193}$$

[xii] The idea to use a diagrammatic representation of the perturbation expansion was developed by Feynman for quantum electrodynamics. It was later adapted to quantum chemistry, which led to Hugenholtz and Goldstone diagrams. These diagrams can be constructed from simple graphical rules and then be translated to the corresponding algebraic expression.[49]

$\mathbf{F}$ is the vector of the so-called modified transition moments and $\mathbf{K}$+$\mathbf{C}$ is a Hermitian matrix independent of ω.

2. $\mathbf{F}$, $\mathbf{\Gamma}(\omega)$, $\mathbf{K}$ and $\mathbf{C}$ are defined in terms of singly, doubly, ... excited configurations with respect to the unperturbed HF ground state. Especially $\mathbf{K}$ is the diagonal matrix of the zeroth-order excitation energies (i.e. orbital energy differences),

$$K_{jk,jk} = \epsilon_j - \epsilon_k \tag{3.194}$$

$$K_{ijkl,ijkl} = \epsilon_j + \epsilon_j - \epsilon_k - \epsilon_l. \tag{3.195}$$

3. $\mathbf{C}$ and $\mathbf{F}$ can also be expanded in a perturbation series,

$$\mathbf{F} = \sum_{n=0}^{\infty} \mathbf{F}^{(n)} \tag{3.196}$$

$$\mathbf{C} = \sum_{n=1}^{\infty} \mathbf{C}^{(n)}. \tag{3.197}$$

4. The expressions for $\mathbf{F}^{(n)}$ and $\mathbf{C}^{(n)}$ can be determined by demanding that $T_n(\omega)$, which is obtained by plugging the expansions for $\mathbf{F}$ and $\mathbf{C}$ into equation 3.193, is identical up to nth order with the perturbation expansion of $T(\omega)$ (equation 3.192). This order n is the order of the ADC treatment (i.e. ADC(n)).

For the justification of these assumptions, see.[170] Equation 3.193 can be obtained from equation 3.191 by replacing $\mathbf{T}$ and $\mathbf{\Omega}$ with the transformed properties $\mathbf{F} = \mathbf{YT}$ and $\mathbf{K} + \mathbf{C} = \mathbf{Y\Omega Y}^\dagger$.
It is obvious that the poles of $\mathbf{\Gamma}(\omega)$ are identical to the poles of $T(\omega)$. They can be obtained by solving the eigenvalue equation of the ADC matrix[132,169]

$$(\mathbf{K} + \mathbf{C})\mathbf{Y} = \mathbf{Y\Omega}. \tag{3.198}$$

The eigenvalues Ω_{nn} thus contain the excitation energies. The eigenvectors are used to derive the transition properties, via $\mathbf{T} = \mathbf{Y}^\dagger\mathbf{F}$.
The elements of the ADC matrix $\mathbf{K} + \mathbf{C}$ are constructed as outlined in point four.[170] The configurational space of ADC(2) consists of particle-hole (p-h) excitations (i.e. singles) and 2p-2h excitations (i.e. doubles). The singles block of the ADC(2) matrix is given by

terms up to second order,

$$(\mathbf{K}+\mathbf{C})_{jk,j'k'} = (\epsilon_j - \epsilon_k)\delta_{jj'}\delta_{kk'} - \langle jk'|\,|j'k\rangle + C^{(2)}_{jk,j'k'}. \tag{3.199}$$

The term $C^{(2)}_{jk,j'k'}$ consists of three distinct contributions (see[170]). The p-h/2p-2h coupling block is given by a first-order contribution of $\mathbf{C}$,

$$C_{jk,i'j'k'l'} = \delta_{ji'}\,\langle k'l'|\,|kj'\rangle - \delta_{jj'}\,\langle k'l'|\,|ki'\rangle - \delta_{kk'}\,\langle jl'|\,|ij'\rangle + \delta_{kl'}\,\langle jk'|\,|i'j'\rangle\,. \tag{3.200}$$

and the 2p-2h block is simply given by the diagonal matrix of the zeroth-order excitation energies, i.e. the orbital energy difference.
The modified transition moments of zeroth and first order are given by

$$F^{(0)}_{jk} = D_{jk} \tag{3.201}$$

$$F^{(1)}_{jk} = \sum_{rs}\frac{\langle js|\,|rk\rangle}{\epsilon_a - \epsilon_j + \epsilon_b + \epsilon_i}D_{rs}, \tag{3.202}$$

while $F^{(2)}$ contains 13 contributions (see[170]).
Since the ADC(2) approach is based on the expansion of the polarization propagator and not on the response of a ground state, there is no unique definition of total energies. Furthermore (as in linear-response methods) the excited state is not calculated explicitly. Therefore properties and gradients cannot be computed directly. This problem was solved using the **intermediate-state representation**,[171] an alternative derivation of the ADC(2) equation starting from a defined correlated ground-state wave function $|\Psi_0\rangle$. A set of orthogonal basis functions is constructed, by acting with excitation operators on $|\Psi_0\rangle$ and subsequent orthogonalization. With these "intermediate states" a CI matrix using the shifted Hamiltonian $\hat{H} - E_0$ can be constructed. Taking n-th order MP theory for $|\Psi_0\rangle$ and E_0 yields the ADC(n) equations.[132]
The ADC(2) matrix is very similar to the CC2 Jacobian. The structure (i.e. the type of blocks) is the same and from first inspection one can also see that the doubles-doubles block is completely identical. In fact ADC(2) can be seen as an approximation to CC2, where the cluster amplitudes of the ground state singles have been neglected.[168] Furthermore the ADC(2) has the advantage of relying on a Hermitian matrix. This leads to a better description of conical intersections and to an improved performance for properties and gradients, since contrary to CC2 left and right moments are identical and hence only one has to be computed.[164] A benchmark[168] of 0-0 excitation energies showed that

ADC(2) gives slightly larger errors than CC2, but its performance and its scope are otherwise comparable.
The ADC(2) scheme presented above is sometimes called ADC(2)-s, since it is of strict second order. It is possible to include the first order 2p-2h term, $C^{(1)}_{ijkl,i'j'k'l'}$, into the doubles-doubles block, which comes from the expansion of the transition function up to third order (ADC(3)). This defines the extended ADC(2) method, ADC(2)-x, which gives an improved description for excited states with significant contributions from double excitations.[172] However, since the inclusion of a single term from third order does not give a balanced description, the overall accuracy is reduced in ADC(2)-x. Using a Davidson algorithm,[48] the scaling of ADC(2)-s is $\mathcal{O}(M^5)$, like CC2, and ADC(2)-x scales like $\mathcal{O}(M^6)$. Of course also other orders of the perturbation expansion are possible. ADC(1) yields CIS excitation energies and first-order moments. ADC(3) has been implemented recently and is like ADC(2)-x an $\mathcal{O}(M^6)$ method, while showing a very promising performance.[173]

3.4 Other Methods and recent Developments

In this section several other methods and newer developments are covered briefly.

The **SAC-CI method**[174] (**s**ymmetry **a**dapted **c**luster) is based on a cluster expansion of the wave function Ψ_g^{SAC}, which is different from the coupled-cluster expansion, since it is symmetrized. Similar to coupled-cluster theory some terms are neglected in actual calculations. Excited state functions are defined in a CI form,by acting with an excitation operator on Ψ_g^{SAC} and projecting out the ground state. The state is then expressed in CI form.[174]

Another method based on the cluster expansion is **equation-of-motion coupled-cluster (EOM-CC)**.[175,176] The EOM approach does not directly involve neither propagators, nor linear response theory. Instead, generalized excitation operators are defined and attempted to be determined.[51]
The operator $\hat{R}(f)$ generates an excited state $|f\rangle$ from the ground state $|0\rangle$. $|f\rangle$ and $|0\rangle$ are eigenfunctions of a general (not necessarily Hermitian) operator $\hat{H}$,[176]

$$\hat{R}(f)\,|0\rangle = |f\rangle\,. \tag{3.203}$$

It should be noted that $\hat{R}$ is not a simple Fock space excitation operator since it creates the exact eigenfunction $|f\rangle$ from the ground state. The operator can be defined by a projection

$$\hat{R}(f) \equiv |f\rangle \langle 0| . \tag{3.204}$$

Let the commutator $[\hat{H}, \hat{R}(f)]$ act on an arbitrary reference state $|\widetilde{0}\rangle$. If the reference has a non-zero overlap with the exact ground state it follows[176]

$$[\hat{H}, \hat{R}(f)] |\widetilde{0}\rangle = \omega_{0f} \hat{R}(f) |\widetilde{0}\rangle . \tag{3.205}$$

Thus the exact excitation energy can in principle be obtained without explicitly calculating the exact initial and final states if the corresponding operator is known.[176] By defining a general de-excitation operator $\hat{L}(f)$ and multiplying with $\hat{L}(f) |\widetilde{0}\rangle$ from the left one obtains

$$\omega_{0f} = \frac{\langle \widetilde{0}| \hat{L}(f)[\hat{H}, \hat{R}(f)] |\widetilde{0}\rangle}{\langle \widetilde{0}| \hat{L}(f)\hat{R}(f) |\widetilde{0}\rangle}. \tag{3.206}$$

This EOM functional is quite general and the starting point for the derivation of different methods.[i] Of course for any practical method the general excitation operators have to be replaced by less general operators ($\widetilde{R}(f)$,$\widetilde{L}(f)$) that are defined with respect to an approximate reference state, rather than the exact eigenstate,

$$\widetilde{R}(f) \equiv |f\rangle \langle \widetilde{0}| . \tag{3.207}$$

Furthermore they are expanded into a set of operators:

$$\widetilde{R}(f) = \sum_k r_k^f \rho_k. \tag{3.208}$$

Using the first variation of the functional (equation 3.206) with respect to $\widetilde{R}$ and $\widetilde{L}$, the following equations can be derived[176]

$$(\hat{\mathbf{H}} - E_0)\mathbf{R} = \mathbf{R}\boldsymbol{\Omega}, \tag{3.209}$$

$$\mathbf{L}(\hat{\mathbf{H}} - E_0) = \boldsymbol{\Omega}\mathbf{L}, \tag{3.210}$$

with $E_0 = \langle \widetilde{0}| \hat{H} |\widetilde{0}\rangle$. $\mathbf{R}$ and $\mathbf{L}$ contain the expansion coefficients of the excitation opera-

[i] For instance the correct choice of the excitation manifold (singles) and reference state (single determinant) yields the TDHF equations.

tors and $\mathbf{\Omega}$ contains the transition energies.
In order to solve this secular problem the Hamiltonian, the operators and the reference have to be defined. In EOM-CC $\hat{H}$ is the similarity transformed Hamiltonian $\hat{H} = e^{-T}He^{T}$ and the reference $|\widetilde{0}\rangle$ is a single Slater determinant. Consequently, $\widetilde{R}(f)$ and $\widetilde{L}(f)$ are also defined with respect to the reference and hence their basis are the standard Fock space excitation and de-excitation operators. Typically the cluster operator T is truncated at the same level as $\widetilde{R}$ and $\widetilde{L}$.[176]
Excitation energies are usually computed at the EOM-CCSD level (EOM-EE-CCSD), which scales similar to CISD as $\mathcal{O}(n^6)$. The accuracy is typically between 0.1 and 0.3 eV.[176] EOM-EE-CCSD can deal with excited states with near-degeneracies, but fails when the ground state acquires multi-reference[ii] character.[47,176] The operators $\widetilde{R}$ and $\widetilde{L}$ need not be electron-conserving, which is interesting for applications to ionized or electron attached states (EOM-IP/EA).[176]

The **second-order polarization propagator approach (SOPPA)**[177] is also based on a consistent second-order perturbation expansion of the polarization propagator, similar to ADC(2). Due to the different approach (superoperator)[iii] the working equations are quite different. Nevertheless, the results seem to be similar to ADC(2).[169]

The so-called **GW-method**[178] relies on many-body Green's function theory. It is based on the Dyson equation (3.102), typically using KSDFT. The self-energy is approximated as depending on the product of a Green's function (G) and a screened Coulomb interaction (W).[178,179] The GW method corrects the deficiencies of the single-particle energies (and thus the band gaps) for the artifacts of typical xc-functionals.[178]The Bethe-Salpeter equation can be used to include effects that are not covered by the effective interaction $\mathbf{W}$.[178] GW is well-known in solid-state physics and has recently been applied to the calculation of single molecules. Using GW+BSE in conjunction with TDDFT has also resulted in significantly improved excitation energies.[178]

In recent years the **density matrix renormalization group (DMRG)** algorithm,

[ii]The EOM spin-flip method, which uses a high spin reference, is an interesting alternative for biradicals and other multi-reference systems.[176]
[iii]The Hamiltonian superoperator generates the commutator if it acts on an arbitrary operator[51]

$$\hat{H}B = [H, B].$$

which was originally introduced in solid-state physics, has become increasingly important in quantum chemistry.[180–182] The main problem of CI-type approaches is the factorial scaling. The full-CI (FCI) wave function for the state A with N electrons is given by

$$\Psi_A^{(N)} = \Phi_{A,FCI}^{(N)} = \sum_I^{\infty} C_I^{(A)} \Phi_I^{(A)}(\phi_{I_1}, \phi_{I_2}, \cdots, \phi_{I_N}) \tag{3.211}$$

The number of configuration state functions $\Phi_I^{(A)}$ and thus the size of the Hilbert space scales factorially with the size of the orbital space.[181] Since the vector of the CI coefficients is sparse, only a subspace is important for an accurate description. Of course one cannot know in advance which determinants are important and which can be neglected. This is only known after the CI matrix has been diagonalized. Therefore, all possible configurations have to be included somehow, but, if one wants to avoid the factorial scaling, without explicitly representing them. The idea behind the DMRG algorithm is to select the important configurations iteratively and include them implicitly, instead of simply truncating the sum after a certain excitation level, as in a CIS or CISD (see above).
The DMRG state can be written as a linear combination of N-electron basis functions $\Omega_K^{(N)}$, which are themselves wave functions of CI-type (for instance describing some subspaces),[182]

$$\Psi_A^{(N)} = \Phi_{A,DMRG}^{(N)} = \sum_K^{M'} B_K^{(A)} \Omega_K^{(N)}(\{\Phi_I^{(N)}\}), \tag{3.212}$$

with

$$\Omega_K^{(N)} = \sum_L D_L^{(K)} \Phi_L^{(N)}. \tag{3.213}$$

If the basis functions $\Omega_K^{(N)}$ were known, the coefficients $B_K^{(A)}$ and thus the DMRG state could be obtained by diagonalizing the Hamiltonian. However, calculating the CI-type basis functions the normal way (i.e. construction in terms of Slater determinants and subsequent diagonalization to obtain the coefficients $D_L^{(K)}$) gives a CI method and the scaling would still be factorial. In fact, if one uses a full-CI for $\Omega_K^{(N)}$, then $M' = 1$ and the DMRG wave function is of course identical to FCI. Thus the expansion coefficients $D_L^{(K)}$ have to be constructed without knowing the configurations explicitly.[182] The DMRG algorithm achieves this by using an adaptive many-body basis.[183]
In this iterative approach the spin orbital space is at first partitioned into blocks. At the beginning there is an active system block (AS), two additional spin orbitals forming the blocks B_L and B_R and a complementary block (CS), sometimes called the environment

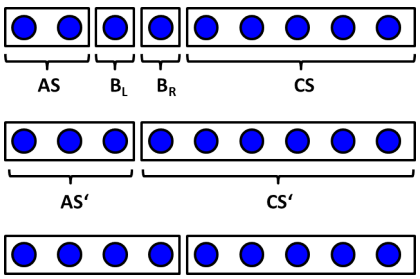

Figure 3.3: DMRG scheme: At first, the spin-orbital space (often called sites[183]) is divided into four subspaces (the "blocks"), AS, B_L, B_R and CS, for which the Slater states are constructed explicitly. Then, the combined blocks are formed and the decimation is used to reduce the dimensionality. In the next blocking steps the active system is enlarged stepwise and the complementary system is diminished accordingly

(see Figure 3.3).[180,183]

It can be shown that the operators describing the combined block $AS' = ASB_L$ can be constructed from the matrix representation of the operators of the subblocks and the quantum number of the states and hence no knowledge of their actual composition (i.e. the expansion in Slater determinants) is necessary.[183] This is exploited in the DMRG algorithm.

At first the active system is chosen to be small and hence its composition (all contributing Slater determinants) and the corresponding operators can be calculated explicitly. The same is true for the blocks B_L and B_R. The composition of CS has to be guessed in some way.[181] This means that in the first step, all spaces are constructed as Slater states, i.e. the expansion is given explicitly, as in a CI. Thus it is possible to calculate the matrix representations of all operators of interest for all subspaces.

Then the "blocking" takes place, which means the spaces are enlarged: $AS' = ASB_L$ and $CS' = CSB_R$ (see Figure 3.3). As stated above, using the matrix representations of the operators of the subblocks one can construct the Hamiltonian of the new blocks. The whole wave function is given as a tensor product of the wave functions for the active and the complementary system [iv]

$$\Psi_A^{(N)} = \Phi_{A,DMRG}^{(N)} = \sum_{IJ} W_{IJ}^{(A)} [\Omega_{AS',I}^{(N')} \otimes \Omega_{CS',J}^{(N'')}]. \tag{3.214}$$

[iv] It should be noted that the information which spin orbitals are occupied and which are unoccupied was not used in the definition of the blocks. Hence all states with different particle numbers have to be taken into account. If the active system contains i spin orbitals 2^i states are thus needed, since each orbital can be empty or occupied. The boundary condition is $N' + N'' = N$.[182]

The Hamiltonian is then diagonalized and the coefficients W_{IJ} can be calculated. These are used to construct the reduced density matrix of the system block by tracing out the environment basis states,[180]

$$\rho_{IK}^{(AS)} = \sum_J W_{IJ} W_{KJ}. \tag{3.215}$$

The crucial step is the so-called "decimation". The m eigenstates of the reduced density matrix with the highest eigenvalues[v] can be used as the new basis.[182] The Hamiltonian and the second quantization operators (or their matrix representation, respectively) are transformed to this basis. The Hamiltonian and all other operators are hence "renormalized" in this step. This terminates the first iteration step. The block AS' is now no longer represented by its Slater states, but the corresponding operators are known in the renormalized basis.

In the next step, the active system is enlarged by another orbital and the size of the environment is reduced accordingly. Since the matrix representation of the operators of the previous active system AS' is known from the renormalization and the operators of the single orbital can be constructed explicitly, the Hamiltonian of the new active system can be computed. The dimension of the active system has thus been enlarged from m to $2m$. However in the following decimation step, again only m eigenvectors are used and thus the size of dimension is retained.[182]

This iterative process consisting of blocking and decimation is repeated until the active space contains all orbitals and none remain in the complementary system. This terminates the first sweep.[181,182] Since the guess for the complementary system introduces an error, the algorithm is then run again with reversed orbital ordering, i.e. the orbital added in the last step is now the starting point. Thus the previously constructed active space is now used as complementary system. Repeating these macroiterations gives the final DMRG result.[182]

As all observables can be constructed from the renormalized matrix representation of the creation and annihilation operators, explicit knowledge of the structure in terms of Slater determinants is not needed. The iterative construction of an adaptive many-body basis without explicit calculation of the expansion in Slater determinants leads to a polynomial scaling.[183]

A very recent development is the **constricted variational DFT (CV-DFT)** method[90,145]

[v] For details on why the eigenstates with the highest eigenvalues of the reduced density matrix provide a good basis, see[182,184] and references therein.

by Ziegler and coworkers. The appealing feature of this theory is that two seemingly different methods, TDDFT and Δ-SCF, can be derived from it. While Δ-SCF optimizes the MOs of a determinant with non-Aufbau occupation, TDDFT uses the response of the ground-state density due to a time-dependent perturbation. Yet both can be seen as special cases of SCF-CV(N)-DFT.[145]

At first the second-order method, CV(2)-DFT is described briefly. The starting point is a Slater determinant. Each occupied orbital is then allowed to vary by mixing in a fraction of each virtual orbital. This can be written as[145]

$$\phi_i' = \phi_i + \sum_a^{vir} U_{ai}\phi_a - \frac{1}{2}\sum_j^{occ}\sum_a^{vir} U_{ai}U_{aj}\phi_j. \tag{3.216}$$

The new orbitals are orthonormal to second order in U. The density matrix of the determinant is given by

$$\rho'(1,1') = \rho^{(0)}(1,1') + \Delta\rho'(1,1'), \tag{3.217}$$

where $\Delta\rho'(1,1')$ contains all terms up to second order in U.[145] Using this density, the Kohn-Sham energy functional gives

$$E_{KS}[\rho'] = E_{KS}[\rho^{(0)}] + \dot{U}^\dagger(A^{KS} + B^{KS})\dot{U}, \tag{3.218}$$

with $\dot{U}$ being a column vector containing the elements U_{ai} and $(A^{KS}+B^{KS})$ is the ground state Hessian with the elements[145]

$$A^{KS}_{ai,bj} = \delta_{ab}\delta_{ij}(\epsilon_a^0 - \epsilon_i^0) + K^{KS}_{ai,bj}; \quad B^{KS}_{ai,bj} = K^{KS}_{ai,jb}. \tag{3.219}$$

The excitation energy can simply be calculated as the difference

$$E_{KS}[\Delta\rho'] = E_{KS}[\rho'] - E_{KS}[\rho^0]. \tag{3.220}$$

However an optimization without constraints would lead to $E_{KS}[\Delta\rho'] = 0$.[145] Thus it is demanded that the excitation involves an excitation of an electron from the occupied space $\Delta\rho_{occ} = -\sum_{ija} U_{ai}U^*_{aj}\phi_i(1')\phi^*_j(1)$ to the virtual space $\Delta\rho_{vir} = -\sum_{iab} U_{ai}U^*_{bi}\phi_a(1')\phi^*_b(1)$, which is done using the Lagrangian[145]

$$L = E_{KS}[\rho'] + \lambda\left(1 - \sum_{ai} U_{ai}U^*_{ai}\right). \tag{3.221}$$

Demanding that L is stationary to any real variation in U leads to the eigenvalue equation[145]

$$(A^{KS} + B^{KS})\dot{U}^{(I)} = \lambda_{(I)}\dot{U}^{(I)}. \tag{3.222}$$

Using the Tamm-Dancoff approximation this expression is identical to the adiabatic TDDFT-TDA expression.[145]

As mentioned above Ziegler et al. showed that the linear response approach is responsible for the incorrect description of charge-transfer states in TDDFT, rather than the quality of the functional itself.[144] The higher-order terms, which go beyond linear response, can be incorporated, by taking CV-DFT beyond second order (CV(n)-DFT). In order to arrive at an expression accurate to all orders, a general unitary transformation matrix Y is used, which can be written as[145]

$$Y = e^U = I + U + \frac{U^2}{2} + \cdots \tag{3.223}$$

A set of occupied orbitals orthonormal to any order of U is given by[145]

$$\phi_i' = \sum_j^{occ} Y_{ji}\phi_j + \sum_a^{vir} Y_{ai}\phi_a. \tag{3.224}$$

Similar to the second-order density an all-order density can be derived and using the same restriction as before, a corresponding expression for the excitation energy is obtained.[145] This energy can be calculated to all orders in U_{ai}, with $\dot{U}$ being optimized according to equation 3.222 (i.e. second order). Alternatively $\dot{U}$ can be optimized self-consistently for all orders, which is called SCF-CV(n)-DFT.[145]

Δ-SCF can be derived as a special case from the latter. Contrary to TDDFT Δ-SCF incorporates the higher-order self-interaction terms.[145] The practical applicability and scope of CV-DFT are not yet well established.[145] As a theoretical framework, however, it seems to be quite powerful. The variational approach to excited states is well accepted in HF theory, but not in DFT.[145] The link between the variational approach and the (via the Runge-Gross theorem) theoretically well-founded TDDFT is thus very interesting.

The spectroscopically oriented CI (**SORCI**)[185] proposed by Neese relies on concepts from MRCI and MRPT, as well as the difference-dedicated CI (DDCI). At first a CASSCF or RASSCF is performed, which is used to select the dominant configurations for the reference space S. This reference space is rediagonalized to give the zeroth-order wave function.

Then an MRPT2 calculation is performed using this wave function. The second-order energy is computed from the CSFs in the so-called first-order interacting space (FOIS) R. The SORCI uses concepts from DDCI to select the relevant configurations. The MRPT2 energy expression is then used to partition R into a strongly (R') and a weakly interacting subspace (R''), according to the contributions of the CSFs to the energy.[186]
The strongly interacting configurations together with the reference space are used as the ineracting space for an MRCI. That means that in the next step the Hamiltonian matrix is diagonalized in the space $R' + S$. The contribution from the weakly interacting configurations is obtained with a second MRPT2 step. In the last step the approximate average natural orbitals (AANO) are calculated from the averaged reduced density matrices of the computed states. With these AANOs the complete procedure is repeated (second iteration) to obtain the final energies
For reasons of efficiency the first iteration, which generates the AANOs, uses the DDCI2 space (R=DDCI2), which grows only quadratically with molecular size. In the second computation the larger space DDCI3 is used (R=DDCI3). The SORCI furthermore uses the Davidson correction and the RI approximation.[185]

4 Environmental Effects on Ground and Excited States

The investigation of intermolecular interactions has become increasingly important in the last decades, or as Mark Ratner put it, "chemistry of the 20th century was about intramolecular interactions; chemistry of the 21st century will be about intermolecular interactions."[53] They are responsible for the folding of proteins and consequently determine the shape of binding pockets, they keep the strains of the DNA together and are also important for polymers, the interface- and bulk structure of organic semiconductors and other applications in biology and material sciences. The interaction with a solvent can stabilize or destabilize ground and excited states and is responsible for solvatochromism. Furthermore some reactions (typically involving ions) are only exergonic in solution. Hence the modeling of intermolecular interactions with computational methods has become of increasing importance.[187]

In many cases the problem can be reduced to the inclusion of environmental effects on some system of interest (so-called "focused models"[188]). If for instance an optical spectrum for a solvated chromophore is of interest, it is not efficient (and unnecessary) to calculate the excited states of the whole system (i.e. chromophore + solvent molecules). Instead the computation of the chromophore with incorporation of environmental effects is desirable. The same is true for crystal defects[188] (see Figure 4.1) or the calculation of monomers and small oligomers in a crystal environment, e.g. for the computation of transport properties. A focused model can even be formulated for the active center of an enzyme.

The Hamiltonian of a focused model consists of the focused part $\hat{H}^F$, the remainder (the environment) $\hat{H}^R$ and the interaction between the two parts,[188]

$$\hat{H}^{FR}(r_F, r_R) = \hat{H}^F(r_F) + \hat{H}^R(r_R) + \hat{H}^{int}(r_F, r_R), \tag{4.1}$$

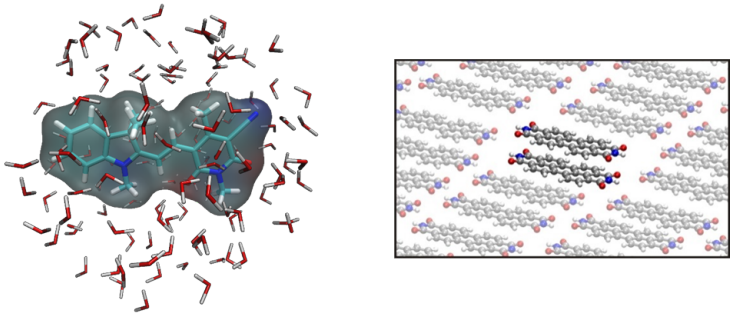

Figure 4.1: Sketch of a solvated single molecule (plotted with VMD[189]) and a shifted dimer in an organic crystal as examples of a focused model.

with r_F and r_R representing the degrees of freedom of the respective parts. Apart from the obvious electrostatic and van der Waals interactions, also dative bonds (coordination), H-bonds, or even covalent bonds can contribute to the interaction between the two parts. While covalent bonds are for instance typically encountered in the modeling of proteins, so-called explicit solvation effects (like coordination) can be essential for the stabilization of solvated molecules.

Regarding crystal and protein environments it is often important to give an atomistic description of the surrounding molecules, atoms and residues. For instance the exact positions of the atomic charges are well defined and thus may be important for a realistic modeling. This atomistic picture is recovered by the so-called **quantum mechanical/ molecular mechanical hybrid methods (QM/MM)**.

For solvation effects an atomistic modeling is often less important. On the one hand, depending on the investigated process, the effect of solvation is a dynamical quantity and thus the positions of the surrounding molecules are not fixed and an average is needed. Experimentally measured effects like solvatochromic shifts result on the other hand from a macroscopic amount of molecules, which all experience a different environment at each point in time. Thus in both cases an atomistic modeling would demand a sampling of different solvent configurations. A very elegant approach to include the (electrostatic) effect of the solvent on the solute without an atomistic resolution is provided by **continuum solvation methods**.

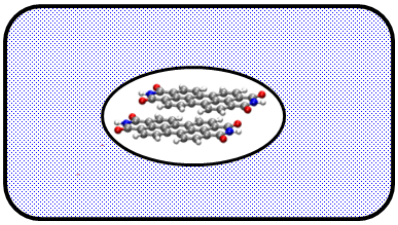

Figure 4.2: Schematic depiction of a continuum solvation model

4.1 Continuum Solvation Models

Since most experimental work is performed in solution it is important to find a way to include solvation effects into the quantum chemical calculations. Continuum solvation models are rather straightforward to use and are hence nowadays often applied in the calculation of molecules in solution as a black box method. The introduction provided in this chapter follows the reviews[188,190] by Tomasi and Persicio and by Tomasi, Mennucci and Cammi closely.

4.1.1 Ground State

In continuum solvation models[48,188,190] the solute is placed into a defined void cavity, surrounded by a continuous polarizable medium that mimics the solvent (see Figure 4.2). The solution is assumed to be dilute (i.e. each solute molecule is only surrounded by solvent molecules) and the solvent is usually taken to be isotropic. The Hamiltonian is formulated as an effective Hamiltonian, since the explicit description of the solvent is not important, only the interaction,

$$\hat{H}^{FR}_{eff} = \hat{H}^{F} + \hat{V}^{int}(\Psi). \tag{4.2}$$

In the standard models the interaction is restricted to the electrostatics. The charge distribution of the solute polarizes the medium and the generated charges interact with the solute. Since $\hat{V}^{int}$ thus depends on the (charge) density and hence on the wave function, the Hamiltonian is non-linear. As in classical electrostatics the polarization[i] of

[i]The polarization or poarization vector is defined as the average dipole moment per unit volume.

the medium can be written as (neglecting non-linear effects and using Gaussian units)[188]

$$\vec{P} = \chi^{(1)}\vec{E} = \frac{\epsilon - 1}{4\pi}\vec{E} \tag{4.3}$$

The only parameter distinguishing different solvents is the permittivity (dielectric constant) ϵ. The polarization of the environment in turn affects the solute, which interacts with the generated charges. Thus an iterative approach seems obvious, which is applied in the so-called **self-consistent reaction field models (SCRF)**.
The cavity is defined differently, depending on the actual model. It should exclude the solvent, but still contain most of the solute charge distribution and reproduce the molecular form.[188] Probably the most accurate description is obtained with isodensity surfaces.[188] However, usually a set of interlocked atomic spheres is used to define the cavity.[ii] Different ways to define the radii of the spheres, which are typically in the range of the van der Waals values, have been devised (e.g. UFF or Bondi).[188]
In order to compute the polarization $\vec{P}$ the electric field is needed, which can be computed from the gradient of the total electrostatic potential $V(\vec{r})$.[188]

$$\vec{P}(\vec{r}) = -\frac{\epsilon - 1}{4\pi}\nabla\vec{V}(\vec{r}) \tag{4.4}$$

The total potential consists of the potential V_M generated by the molecular charge distribution ρ_m and the reaction potential V_R generated by the polarization of the medium (environment),[188]

$$V(\vec{r}) = V_M(\vec{r}) + V_R(\vec{r}). \tag{4.5}$$

Using V_M alone is not sufficient, since the charges induced in the medium also polarize each other. Since one needs the polarization to determine V_R an iterative procedure is used. In the first iteration one can set $V_R(\vec{r}) = 0$ in equation 4.5 and only use V_M (which can be extracted from a quantum mechanical calculation) to compute $\vec{P}(\vec{r})$. The polarization can then be used to calculate a first guess for $V_R(\vec{r})$. Solving this classical electrostatic problem involves the Poisson equation, which links the reaction potential with the (induced) charge distribution in the medium. The different continuum solvation models can be distinguished by the approximations used in this process (see below).
After the solution of the classical problem, the final environmental charges have to be

[ii] A spherical solvent molecule (probe) can be used to define the solvent excluded surface (SES) and the solvent accessible surface (SAS). The center of such a spherical molecule rolling on the cavity surface generates the SAS and the point of contact with the cavity generates the SES.[188]

included in the quantum mechanical Hamiltonian.[188] Since an accurate computation of V_M is only possible with the correct environment charges, again an iterative solution is necessary, which is the SCRF approach mentioned above.

For the solution of the electrostatic problem, several methods have been devised, like the multipole expansion (MPE) methods based on the works of Kirkwood and Onsager, the generalized Born (GB) approaches and the **apparent surface charge (ASC) methods**. In this chapter only the latter will be presented, see[188] and references therein for the others. In the ASC methods the reaction potential is calculated from a charge distribution $\sigma(s)$ on the cavity surface Γ. This means the charges induced in the medium by the molecular charge distribution (which are the source of the reaction potential) are projected onto the cavity surface[188]

$$V_R = V_\sigma(\vec{r}) = \int_\Gamma \frac{\sigma(\vec{s})}{|\vec{r} - \vec{s}|} d^2 s \tag{4.6}$$

This ansatz is in principle exact. The integral is usually discretized by approximating Γ in terms of finite elements (so-called tesserae). This ansatz can be combined with the boundary element method (BEM). The charge distribution is then reduced to an environment point charge q_k at each tessera,

$$V_\sigma(\vec{r}) \approx \sum_k \frac{q_k}{|\vec{r} - \vec{s}_k|}. \tag{4.7}$$

As stated above the environment charges affect each other and hence the value of each q_k depends on all other surface charges.[188]

The oldest ASC method is the **polarizable continuum model (PCM)**,[191] which is now also often called **dielectric PCM (D-PCM)**, since other PCM methods have been devised like C-PCM and IEFPCM. All members of the PCM family allow in principle for an unlimited number of solutes and cavities that interact through the dielectric. It is also possible to describe processes like dissociation, where the system starts with one cavity and ends up with two. The different cavities divide the system into different regions. For one cavities there are just two regions: inside and outside the cavity. The polarization of the region i can be calculated from the gradient of the total potential,

$$\vec{P}_i(\vec{r}) = -\frac{\epsilon_i - 1}{4\pi} \nabla \vec{V}(\vec{r}) = -\frac{\epsilon_i - 1}{4\pi} \nabla (\vec{V}_M(\vec{r}) + \vec{V}_\sigma(\vec{r})) \tag{4.8}$$

with ϵ_i being the dielectric constant at the region i. The ASC distribution σ_{12} at the boundary of two regions can be calculated from the polarization via

$$\sigma_{12} = -(\vec{P}_1 - \vec{P}_2) \cdot \vec{n}_{12}, \tag{4.9}$$

with $\vec{n}_{12}$ being the unit vector at the boundary pointing from region 1 to region 2, i.e. from inside the cavity ($\epsilon_1 = 1,\ \vec{P}_1 = 0$) to the outside ($\epsilon_2 = \epsilon,\ \vec{P}_2 = \vec{P}$). Using equations 4.8 and 4.9 and the boundary conditions, the basic PCM equation can be derived,[188]

$$\sigma(s) = \frac{\epsilon - 1}{4\pi\epsilon} \frac{\partial}{\partial \vec{n}} (V_M + V_\sigma)_{in}. \tag{4.10}$$

$\vec{n}$ denotes the unit vector normal to the cavity surface and the suffix in reflects that the gradient on the internal part of the surface is used.
Equation 4.10 can be used to compute $\sigma(s)$ and equations 4.6 or 4.7, respectively can be used to calculate the reaction potential corresponding to $\sigma(s)$, which can again plugged into equation 4.10. Thus using these equations an iterative solution of the problem is possible.
In the **conductor-like screening model (COSMO)**[192] devised by Klamt and Schüürmann the dielectric constant is set to infinity, $\epsilon = \infty$, which corresponds to a conductor. One consequence is that the total potential $V(\vec{r})$ cancels out on the cavity surface, and $\sigma(s)$ is now determined by the local value of the electrostatic potential instead of its gradient as above.[188] The so obtained unscreened charge density σ^* is then scaled to the finite value of ϵ,

$$\sigma(s) = f(\epsilon)\sigma^*(s), \tag{4.11}$$

with

$$f(\epsilon) = \frac{\epsilon - 1}{\epsilon + k}. \tag{4.12}$$

In the original publication[192] the value of k was set to 0.5, which is used in the TURBOMOLE program package.[193] The C-PCM method[194] is the implementation of the conductor-like screening model in the PCM framework as used in the Gaussian program package.[195] Using a statistical mechanics treatment COSMO can be extended to COSMO-RS, which is of special importance for quantum chemical calculations in the chemical industry.[2]
The **integral equation formalism PCM (IEFPCM)**[196] by Cancés and Mennucci is the default PCM formalism of the Gaussian program package. The potentials in 4.5 are

reformulated in terms of Green's functions of the corresponding operators and the integral equations are solved. Similar to COSMO this approach also avoids the dependency on the gradient of the potential.[188] It can be shown that COSMO, as well as D-PCM can be derived from the IEFPCM equations.[188]

Apart form the electrostatic problem, the **quantum mechanical problem** needs to be solved, i.e. the Schrödinger equation for the effective Hamiltonian

$$\hat{H}_{eff} \left|\Psi\right\rangle = E \left|\Psi\right\rangle \tag{4.13}$$

with

$$\hat{H}_{eff} = \hat{H}_M^0 + \hat{V}^{int}(\Psi). \tag{4.14}$$

The Fock-operator in the atomic orbital basis can be written as

$$F_{\mu\nu} = h_{\mu\nu} + G_{\mu\nu} + \left\langle\mu\right| \hat{V}^{int} \left|\nu\right\rangle \tag{4.15}$$

The exact form of $\hat{V}^{int}$ of course depends on the method applied to the electrostatic problem, in the case of the ASC approach the interaction is formulated in terms of the point charges on the cavity.[190] The interaction with a point charge is given by a simple one-electron integral. Thus the description of solvent effects is reduced to a set of one-electron operators.[197]

The PCM calculation is solved in an iterative process. The most straightforward algorithm is organized as follows:[188] At first one starts with an approximate molecular charge distribution ρ_m^0, which can be taken from a quantum chemical calculation of the solute in vacuum. With this fixed distribution the electrostatic problem is solved iteratively. In the first iteration the charge distribution is used to compute a first set of apparent point charges $\{q_k^{0,0}\}$ using equation 4.10 or the corresponding C-PCM/IEFPCM expression by setting V_σ equal zero. The mutual polarization of the surface charges is hence not yet included in this set. This is corrected in the next iterations. The reaction potential V_R can be calculated using equation 4.6 (or 4.7 respectively) and $\{q_k^{0,0}\}$. With this potential a new set of charges $\{q_k^{0,1}\}$ can be calculated and so on, until convergence is achieved.

The final self-polarized surface charges $\{q_k^{0,f}\}$ are then used for another QM calculation, which yields a new QM charge density ρ_m^1. With this density a new set of mutual polarized surface charges $\{q_k^{1,f}\}$ can be calculated.

The whole process is continued until self-consistency. Different and more involved algorithms are typically used in modern implementations, but the principle is the same.[188,190]

The method can be similarly formulated for DFT and post-HF methods like MP2. Gradients are also available.[188]

The PCM ansatz replaces the linear Schrödinger equation by two non-linear effective equations (one for the solute[iii] and one for the solvent) and both have to be solved self-consistently.[198] Continuum solvation models are well-suited for the description of reactions in solution and provide good results for the solvation effect on reaction barriers and thermodynamics, as long as explicit solvation effects can be neglected. Of course in actual calculations many intricacies regarding the size of the cavity or the outlying charges can cause problems. Nevertheless the methods usually give a robust performance for ground-state calculations.

4.1.2 Excited States

The investigation of photochemical reactions has become an important field in physical chemistry. This is partly due to the vast advance in laser technology and spectroscopy. The ultra fast spectroscopy makes it possible to study the dynamics of excited states (typically via pump-probe techniques), which evolve on pico-second timescales. Furthermore there has been some progress in quantum control of chemical reactions. Also in organic and inorganic chemistry, there has been an increased interest in preparative photochemical reactions. In the growing field of organic optoelectronics, the characterization of novel compounds via standard UV/vis absorption and fluorescence experiments is of vital importance, too. Most of these investigations are carried out in solution rather than in the gas phase. A computational model that neglects the effect of the solvent is bound to lack the accuracy to rationalize and reproduce the experimental results, let alone predict them. But contrary to ground-state calculations, where the solvent is usually adapted perfectly to the molecule (via its surface charges), things are more complex, when a transition between states is involved.

In an absorption process the light interacts with the solute and excites it to a higher-lying eigen state. It is usually assumed that this proceeds on a significantly faster timescale than the reorientation of the solvent molecules, which thus stay in an orientation optimal for the ground state. The electronic polarization of the solvent molecules, however, can change instantaneously and thus has to be adapted in the model. After the excitation the molecular geometry relaxes to the minimum energy structure of the excited state. In

[iii] Of course the effective equation is not really solved for the environment, but only for its effect on the system using a classical expression for its polarization.

the case of fluorescence it is generally assumed that the solvent had enough time to relax and is thus completely adapted to the excited state.
Therefore is is important to distinguish between equilibrium and non-equilibrium conditions.[188,199] In the first case the solvent is completely adapted to the excited-state density, which is usually the choice for modeling fluorescence. In the latter case only the fast (i.e. electronic polarization), but not the slow degrees of freedom (i.e. reorientation of the solvent molecules) are adapted to the excited state.
The time-dependent polarization can be written as[188]

$$\vec{P}(t) = \int_{-\infty}^{t} dt' G(t-t')\vec{E}(t'). \tag{4.16}$$

After Fourier transformation, the frequency dependent form is obtained,

$$\vec{P}(\omega) = \frac{\epsilon(\omega)-1}{4\pi}\vec{E}(\omega), \tag{4.17}$$

with the frequency-dependent complex dielectric constant

$$\epsilon(\omega) = \epsilon'(\omega) + i\epsilon''(\omega). \tag{4.18}$$

The actual frequency dependence is usually not of interest, but only if the orientational polarization (i.e. the polarization due to the reorientation of the molecule) should be adapted or not, thus a partitioning of the polarization into two components,

$$\vec{P} \approx \vec{P}_{slow} + \vec{P}_{fast}, \tag{4.19}$$

seems reasonable. There are different ways of implementing this splitting, but the details are beyond the scope of this chapter (see[188]). Typically it involves the characterization of each solvent by two permittivities, the static one ϵ and the permittivity at optical frequencies ϵ_∞. The latter corresponds to the dielectric constant at a frequency, where the orientational polarization can no longer adapt to the changes in the field.[188]
To include solvation effects to excited states based on a PCM, several theoretical frameworks exist. The conceptionally most straightforward approach is the **state-specific solvation (SS-PCM)**,[200] where the solvent reaction-field is iterated until it is self-consistent with the excited-state density. This was typically used in conjunction with CI or MCSCF wave functions.[188]
For non-equilibrium conditions a splitting in the spirit of equation 4.19 is performed, with

iterative adaption of $\vec{P}_{fast}$. The drawback is that each state has to be calculated separately, i.e. a calculation of several excited states in a single run is not possible.
In TDDFT, where the wave function of the excited state is not computed explicitly, the state-specific method is difficult to apply. However, it is possible to arrive at a state-specific model using a series of iterative TDDFT calculations,[200] in which the solvent is adapted to the excited-state density. During these iterations, however, the solvent is also changed for the ground state, since TDDFT relies on its response. After having reached convergence, the effect of the ground-state solvation is subtracted via correction terms. The distinction between equilibrium and non-equilibrium is included in the definition of the PCM operator in the time-dependent Kohn-Sham equations (via the choice of the permittivity) and thus in the iterative treatment, but the correction terms also take a different form.[200] Apart from the high cost due to the iterative scheme, the SS-scheme for TDDFT has the disadvantage that it is sometimes unstable.
The iterative scheme can be circumvented by using **linear-response solvation (LR-PCM)**.[197,201] Additionally to the solvent interaction, a time-dependent interaction term is included in the Hamiltonian,

$$\hat{H}_{eff}(t) = \hat{H}_M^0 + \hat{V}_{int} + \hat{W}(t). \tag{4.20}$$

Following a similar approach as in the derivation of TDHF and TDDFT leads to the working equations (see[197] for details). One advantage of LR-PCM is that several roots can be computed in a single run.
The formal and practical differences between the LR- and the SS-approach have been studied thoroughly.[198,202] As one might imagine, the self-consistent adaption of the fast degrees of freedom to the excited state is explicitly taken into account by state-specific solvation, while this is not the case in the LR-approach, where the two contributions are taken into account in a single response. The latter includes, however, a dynamical correction to the excited-state energy missing in the standard SS-approach.[198] The solvent contribution to the excitation energy in an SS calculation depends primarily on the difference in dipole moment between ground and excited state, while it depends on the transition dipole moment in the LR approach. Thus for dark states the solvent effect on the excitation energy will be negligible using an LR-PCM, which is not necessarily correct, since ground- and excited-state dipole moments may nevertheless differ significantly.
It is also possible to go beyond the LR-PCM approach using the **corrected linear response approach (cLR)** by Mennucci et al.,[199] which recovers a state-specific picture

from a response function using TDDFT. It takes the relaxation of the excited-state response into account using a perturbative approach. In a standard LR approach the excitation energy ω_K^0, which is computed with a solvent shell that is frozen to the ground-state conditions, is obtained. In order to arrive at a state-specific picture from an LR approach, the relaxation part of the density matrix ΔP is needed, which takes the orbital relaxation effects into account. With ΔP a corresponding set of surface charges Δq can be calculated. The interaction between the solvent and these "new" surface charges can be evaluated in order to correct ω_K^0 to first order. The matrix ΔP can be computed via the analytic energy gradient. The cLR approach gives results similar to the SS-ansatz, but the computational effort is significantly diminished (in fact it is not much higher than a standard LR-approach), it is also more stable and several states can be computed in a single run.[199]

4.2 Hybrid QM/MM methods

If the atomistic nature of the surrounding is of importance, hybrid quantum mechanical/ molecular mechanical methods (QM/MM) can be used to include environmental effects. Their popularity has increased steadily since the 1990s. They are well established for applications on biomolecules, but more recently they have also been used for questions regarding material sciences and other fields. The nobel price in chemistry 2013 has been awarded to Martin Karplus, Michael Levitt, and Arieh Warshel, "for the development of multiscale models for complex chemical systems."[203] The seminal publication[204] of Warhsel and Levitt in 1976 introduced the QM/MM method, but the widespread acceptance only arose after the work of Field, Bash and Karplus starting with their publication[205] from 1990.[206] Nowadays, there exist several excellent reviews on the QM/MM methodology (see for instance[206–210] and references therein).

The QM/MM method is a multiscale method. The main idea is to couple a classical description for the environment (**O**) using molecular mechanics (MM) with a quantum mechanical description for the system of interest (**I**).[i] The partitioning is shown in Figure 4.3. The ingenuity lies in the fact that the advantages of both approaches are combined. QM methods are able to describe chemical reactions and excited states, which is not possible with molecular mechanics, but they cannot be applied to larger systems. Those in turn can be treated using the cheap MM methods. However, many applications (for in-

[i] Hence QM/MM is also a focused model.

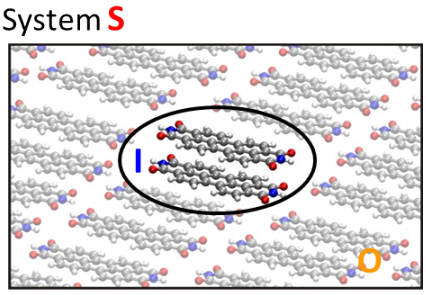

Figure 4.3: QM/MM partitioning using a crystal defect (shifted dimer) as an example. The whole system is designated (**S**), the MM part (**O**) and the QM part (**I**).

stance enzyme reactions or the description of excitonic states in organic crystals) demand both - the modeling of large systems and a QM treatment. This problem is solved by the QM/MM partitioning. There are different ways to write the energy expression for the total system (**S**). In the so-called **subtractive scheme**[206] the energy is written as[ii]

$$E^{sub}_{QM/MM}(\mathbf{S}) = E_{MM}(\mathbf{S}) + E_{QM}(\mathbf{I}) - E_{MM}(\mathbf{I}). \tag{4.21}$$

The whole system is calculated on the MM level, while the QM region has to be calculated on the QM as well as the MM level. This simple scheme has the advantage that no special interface needs to be implemented. Any standalone QM and MM codes can be used. It is also the basis of the ONIOM methods.[211] The disadvantage is that on this simple level the QM region is not influenced by the environment.[206] Although the subtractive scheme can be improved by introducing the electrostatic interaction,[206] most current QM/MM codes rely on an additive scheme.
In the **additive scheme** the energy is written as,[206]

$$E^{add}_{QM/MM} = E_{MM}(\mathbf{O}) + E_{QM}(\mathbf{I}) + E_{QM/MM}(\mathbf{I}, \mathbf{O}). \tag{4.22}$$

Thus an explicit coupling term is introduced, which describes the interaction between the QM and the MM region. This interaction term takes different forms depending on the so-called embedding scheme. Before the embedding schemes and details to the QM/MM-boundaries are described, a brief introduction to molecular mechanics is given.

[ii]For the moment it is assumed that the QM/MM-boundary does not cut through any covalent bonds (see below).

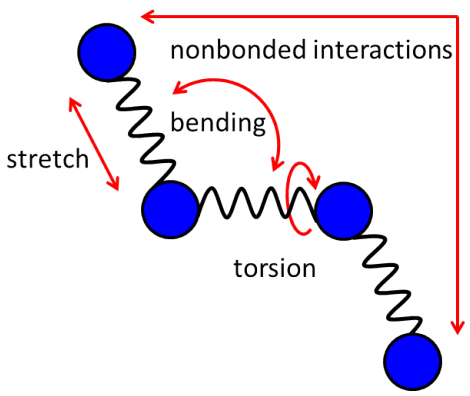

Figure 4.4: Molecular mechanical modeling of a molecule.

4.2.1 Molecular Mechanics

The fact that one distinguishes between different configurations and even conformations in chemistry shows that the atomic nuclei do not feature very significant quantum aspects.[48] This is exploited in molecular mechanics,[48,212] where a molecule is described using a classical ball and spring model. The parameters are derived from quantum chemical calculations or fitted to reproduce a set of reference data as accurately as possible.[48] The different types of interactions are depicted in Figure 4.4. The energy expression[iii] can be split into different contributions,[48]

$$E_{MM} = E_{stretch} + E_{bend} + E_{tors} + E_{el} + E_{vdw} + E_{cross} + \cdots \tag{4.23}$$

with $E_{stretch}$ referring to the bond stretching, E_{bend} to the angle bending, E_{tors} to the torsions, E_{el} the electrostatic interactions, E_{vdw} to the van der Waals interactions and E_{cross} to the cross terms that couple the different contributions.[48] Which terms are used and their mathematical form defines the particular force field.

The bond stretching potential can for instance be modeled using a harmonic approximation by also including higher terms or via a Morse potential. The van der Waals interactions are often described using the Lennard-Jones formula, but several other potentials exist.[48]

As an example the energy expression of the OPLS (optimized potentials for liquid simu-

[iii] For sp^2-hybridized atoms an additional out-of-plane bending energy term E_{oop} can be added. Often an "improper" torsion angle is used to account for the energy necessary to remove the planarity.

lations) all-atoms force field (OPLS-AA)[213,214] is given as

$$E_{stretch} = \sum_{bond} K_r(\mathbf{r} - r_{eq})^2 \tag{4.24}$$

$$E_{bend} = \sum_{angles} K_\phi(\phi - \phi_{eq})^2 \tag{4.25}$$

$$E_{torsion} = \sum_i \left\{ \frac{V_1^i}{2}\left[1 + \cos(\phi_i + f_i 1)\right] + \frac{V_2^i}{2}\left[1 - \cos(2\phi_i + f_i 2)\right] + \frac{V_3^i}{2}\left[1 + \cos(3\phi_i + f_i 3)\right] \right\} \tag{4.26}$$

$$E_{ab} = \sum_i^{\text{on } a} \sum_j^{\text{on } b} \left[\frac{q_i q_j e^2}{\mathbf{r}_{ij}} + 4\epsilon_{ij}\left(\frac{\sigma_{ij}^{12}}{\mathbf{r}_{ij}^{12}} - \frac{\sigma_{ij}^{6}}{\mathbf{r}_{ij}^{6}} \right) \right] f_{ij} \tag{4.27}$$

with $f1$, $f2$, $f3$ being phase angles, and E_{ab} containing all non-bonded interactions (i.e. Coulomb + Lennard-Jones). The non-bonded interactions are active between different molecules and the same expression applied to intramolecular non-bonded interactions when the atoms are separated by three or more bonds. $f_{ij} = 1$ except for intramolecular 1,4-interactions, where it is 0.5. The choice of the parameters (K_r, r_{eq}, K_ϕ, ϕ_{eq}, V_j^i, q_i, ϵ_{ij}, σ_{ij}) is of course crucial for the accuracy of the force field.

For the modeling of environmental effects the intermolecular terms are of special importance. Using perturbation theory (see below) the molecular interaction energy is often divided into four categories:[215,216] electrostatic, induction, dispersion and exchange-repulsion energy. The electrostatic interaction in OPLS-AA is based on atomic point charges. Other force fields rely on bond dipoles or include higher-order multipoles.[48] The inclusion of higher multipoles systematically improves the long-range electrostatic contribution.[215] The short-range electrostatic effects, i.e. charge penetration, can also be included using correction terms.[217]

Usually the atomic charges are fixed and not influenced by the environment, but it is possible to add polarization terms and thus to include induction. AMOEBA[218] is a typical example for a polarizable force field.

It is difficult to include the exchange-repulsion properly, since it is a short-range effect[219] that is purely quantum mechanical and arises due the overlap between the wave functions of the monomers (see below).[215]

Molecular mechanics computations are very cheap and hence applicable to very large systems. However, it can sometimes be tedious to find the correct parameters and the

accuracy is never known in advance. Similar to semi-empirical methods, a force field can be astonishingly accurate, if the molecule in question is close to the set for which the force field was parameterized, but it is likely that it will fail completely if the system of interest has a very different electronic structure. Typically, the parameters are assigned to functional groups and are hence transferable. This is in line with the chemists understanding that the properties of functional groups are the same in different molecules. This has the benefit that the force field is rather general. However, it is often necessary to refine the parameters for a special molecule. There is also the completely different philosophy of generating a unique force field for each type of molecule. One example is the quantum mechanically derived force field (QMDFF)[220] by Grimme.
Chemical reactions cannot be described within the standard force-field model and also molecules with a complex electronic structure will usually be treated poorly. Molecular mechanics is, however, well-suited for the investigations of the conformational space of "standard" organic molecules and their potential surfaces.
Typically, a force field is designed to describe a certain class of compounds. For instance for proteins and nucleic acids and carbohydrates very good force fields have been devised, since most force-field development has been performed for biological systems.[2] It is more difficult to find reasonable parameters and accurate force fields for systems from material sciences. There are also universal force-fields, which can be applied to molecules containing any atom of the periodic table, but of course they usually provide less accurate results. An additional benefit is that any barrier height, reaction enthalpy or interaction energy can be decomposed into the different contributions, which gives some insight not so easily obtained with *ab initio* methods.[212]

4.2.2 Atomic Charges in Molecular Mechanics

Several force fields like OPLS-AA or AMBER rely on atom-centered point charges.[48] Atomic charges are no observables and hence the question arises how they can be obtained. One way to determine the value for the charges is to simply use the general fitting procedure for the force field, which means treating them as parameters, just as K_r or K_ϕ. In this approach several effects are folded into the charges implicitly, for instance the effect of higher order multipoles or the compensation of the deficiency of the other terms. How physical these charges are depends on the focus of the fitting procedure. If intramolecular reference data like bond lengths and angles are used, it is likely that they are unphysical in the sense that they do not reproduce the electrostatic field of the molecule[208] and provide

a poor approximation for the intermolecular electrostatic interaction. In OLPS, however, the charges are fitted to reproduce the properties of organic liquids[214] (i.e. inherently intermolecular properties are used), and hence the OPLS charges should be much better suited to describe the intermolecular electrostatic interaction.
Other force fields like AMBER fit the charges to reproduce the molecular electrostatic potential, which is calculated using DFT or *ab initio* methods.[48] The **electrostatic potential (ESP)** ϕ_{esp} of the molecule at the point $\mathbf{r}$, which is given by

$$\phi_{esp}(\mathbf{r}) = \sum_{a}^{N_{nuc}} \frac{Z_a}{|\mathbf{R}_a - \mathbf{r}|} - \int \frac{\Psi^2(\mathbf{r}')}{|\mathbf{r}' - \mathbf{r}|} d\mathbf{r}'. \tag{4.28}$$

This means the charges are chosen in a way that they reproduce the ESP at a certain distance of the molecule by minimizing an error function,[48]

$$ErrF(Q) \sum_{r}^{N_{points}} = \left(\phi_{esp}(\mathbf{r}) - \sum_{a}^{N_{atoms}} \frac{Q_a(\mathbf{R}_a)}{|\mathbf{R}_a - \mathbf{r}|} \right)^2. \tag{4.29}$$

In order to arrive at the correct charges, the electrostatic potential is sampled for several points $\mathbf{r}$. One way to perform the sampling is the Merz-Kollman scheme.[221,222] In this approach, the points lie on the solvent-excluded surface (Connolly surface).[222] In the original publication Singh and Kollman used four SES surfaces for the sampling with the radii being equal 1.4, 1.6, 1.8, and 2.0 times the van der Waals radius.[222]
Charges obtained from the ESP fit have the advantage that they reproduce an (in principle) observable physical quantity, i.e. the electrostatic potential. Since it depends on the electron density, which is typically decently reproduced even by low-level methods, it is rather insensitive to the level of the calculation.[48] Charges obtained form an ESP fit are, however, dependent on the number of sampling points and the conformation of the molecule, which is a drawback. Nevertheless other well-known methods for the extraction of atomic charges from quantum chemical calculations (e.g. Mulliken, AIM, Hirshfeld, NBO) are rarely used for the generation for force-field charges.
Mulliken charges are obtained from the **Mulliken population analysis**, which is based on a partitioning of the electron density in terms of the basis functions. The number of electrons can be obtained by integrating and summing over all MOs ϕ_i, with the occupation number n_i,

$$N_{elec} = \sum_{i}^{N_{occ}} n_i \int \phi_i^2 d\mathbf{r}. \tag{4.30}$$

Expanding the MOs in basis functions yields[48]

$$N_{elec} = \sum_{\alpha\beta}^{M_{basis}} \left(\sum_{i}^{N_{occ}} n_i c_{\alpha i} c_{\beta i} \right) \int \chi_\alpha \chi_\beta d\mathbf{r} = \sum_{\alpha\beta}^{M_{basis}} D_{\alpha\beta} S_{\alpha\beta}. \tag{4.31}$$

With this equation the number of electrons can be partitioned onto the different atomic centers. The density in the atomic orbital α is calculated from the diagonal element $D_{\alpha\alpha}S_{\alpha\alpha}$ and one half of the off-diagonal elements $\frac{1}{2}D_{\alpha\beta}S_{\alpha\beta} + \frac{1}{2}D_{\beta\alpha}S_{\beta\alpha} = D_{\alpha\beta}S_{\alpha\beta}$, thus it follows for the density at atom A

$$\rho_A = \sum_{\alpha\in A}^{M_{basis}} \sum_{\beta}^{M_{basis}} D_{\alpha\beta} S_{\alpha\beta}. \tag{4.32}$$

With this atomic electron density atomic charges can be easily defined. Although conceptionally simple and computationally cheap, the Mulliken population analysis suffers from several problems. The most severe one is that a basis function centered on A with a small exponent describes electrons far from the atom A but is nevertheless counted to be belonging to A. This also leads to a high dependence on the basis set size. Typically the results obtained with a small rather contracted basis sets are more reliable.
Instead of partitioning the Hilbert space, the **atoms in molecules method (AIM)**, partitions the density by analyzing its topology and defining atomic basins. However the corresponding charges do not reproduce the molecular electrostatic potential sufficiently and are thus not useful for MM charges.[48]
Hirshfeld charges are obtained by defining a promolecular electron density ρ^{pro}, which is built up from atomic electron densities ρ_i^{at} [48,223]

$$\rho^{pro}(\mathbf{r}) = \sum_i \rho_i^{at}(\mathbf{r}). \tag{4.33}$$

$w_i(\mathbf{r})$ is a sharing function defined as the portion of the atomic density ρ_i^{at} in the promolecular density at the point $\mathbf{r}$,

$$w_i(\mathbf{r}) = \frac{\rho_i^{at}(\mathbf{r})}{\rho^{pro}(\mathbf{r})}. \tag{4.34}$$

The actual molecular density ρ^{mol} is partitioned according to the weighting factors w_i, i.e. the density at the bound atom i ($\rho_i^{b.a.}$) is given by

$$\rho_i^{b.a.}(\mathbf{r}) = w_i(\mathbf{r})\rho^{mol}(\mathbf{r}). \tag{4.35}$$

The atomic densities are typically defined as the spherically averaged ground-state densities of the neutral atoms. Using the deformation densities, $\delta\rho_i = \rho_i^{b.a.} - \rho_i^{at}$, atomic dipole moments can also be obtained.[223]

Charges can also be obtained from **natural atomic orbitals (NAOs)** using the natural population analysis (NPA).[224] The so-called natural orbitals are the eigenvectors of the first-order density matrix,[iv]

$$\rho_1(\mathbf{r}_1, \mathbf{r}_1') = N_{elec} \int \Psi^*(\mathbf{r}_1', \mathbf{r}_2, \ldots, \mathbf{r}_{N_elec})\Psi^*(\mathbf{r}_1, \mathbf{r}_2, .., \mathbf{r}_{N_{elec}})d\mathbf{r}_2 \ldots d\mathbf{r}_{N_{elec}}, \tag{4.36}$$

with the corresponding occupation numbers as eigenvalues.[48] If one arranges the density matrix into blocks, in a way that all orbitals centered on atom A form one block and all centered on atom B another block and so on, the natural atomic orbitals can be obtained by diagonalizing each block separately. However, these orbitals are non-orthogonal and a subsequent orthogonalization is performed. By summing all contributions from the NAOs at a certain center an atomic charge can be defined.

Force fields that rely on multipoles like AMOEBA often use the **distributed multipole analysis (DMA)** by Stone.[225] The electrostatic potential that arises due to the overlap of two atomic basis function can be reproduced by a multipole expansion around a point between the two nuclei.[48] The location of the point depends on the shape of the basis functions. In the DMA, the moments are calculated directly from the density matrix and the basis functions and no fitting procedure is necessary. One advantage of this method is that the multipole expansion is in principle finite, with the highest order of the multipoles being determined by the angular momenta of the basis functions. For practical calculations, not all M_{basis}^2 multipole points are used, which destroys the finiteness of the expansion (see[48] for details). Moreover the method is quite basis set dependent.[48]

[iv] As noted by McWeeny,[51] the name "matrix" is unfortunate, since $\rho_1(\mathbf{r}_1, \mathbf{r}_1')$ is better described as a density function. The name stems form the fact that $\rho_1(\mathbf{r}_1, \mathbf{r}_1')$ can be seen as derived from a matrix element ρ_{rs} by replacing the discrete indices with continuous variables.

4.2.3 Overlap-Based Description of the Repulsion

The repulsion between molecules is typically modeled via the $\frac{1}{\mathbf{r}_{ij}^{12}}$-term of the Lennard-Jones formula or the exponential Born-Mayer potential ($Ae^{-Br_{ij}}$).[48,219] Both approaches use isotropic atom-atom potentials and are hence based on the assumption that the molecules interact like a superposition of spherical charge distributions. Hence the model neglects the often non-spherical distribution of the valence electrons.[226] Although it has been shown that this is a often a valid approximation,[227] the anisotropy may become important of the exchange-repulsion term, since this is a short-range effect. Consequently there are cases, where the assumption of spherical distribution is no longer valid.[219] There are several possibilities to include the anisotropy.

In molecule-molecule potentials, where each molecule is treated as a unit, it was suggested by Corner to use a variant of the Lennard-Jones potential[228] with parameters dependent on the orientation.[219] Berne and Perchukas introduced a Gaussian overlap model, which models the angle dependence by considering the overlap of two ellipsoidal Gaussian charge distributions.[229]

Using atom-atom potentials, which are more suitable for larger molecules, a similar approach is in principle possible. The most straightforward way is again to choose the parameters of the potential to be dependent on the orientation Ω. For instance using the Born-Mayer potential: $A \rightarrow A(\Omega)$. This can be achieved by expanding $A(\Omega)$ in a series of spherical harmonic functions of the angular coordinates, but it leads to rather slowly converging series.[219] Price and Stone developed a more general approach,[230,231] where the repulsion between molecules A and B is written as

$$\begin{aligned} U_{rep}^{AB} &= \sum_{a\in A}\sum_{b\in B} U_{rep}^{AB} \\ &= K\sum_{a\in A}\sum_{b\in B} e^{[-\alpha_{ab}(\Omega_{ab})(R_{ab}-\rho_{ab}(\Omega_{ab}))]}, \end{aligned} \tag{4.37}$$

with α_{ab} being the hardness parameter for the interaction and ρ_{ab} determines the shape.[219] K is just a convenient energy unit. α_{ab} and ρ_{ab} are expanded in terms of the $\bar{S}$ functions,[219,230]

$$\rho_{ab}(\Omega) = \sum_{l_a l_b j k_a k_b} \rho_{l_a l_b j}^{k_a k_b} \bar{S}_{l_a l_b j}^{k_a k_b}, \tag{4.38}$$

$$\alpha_{ab}(\Omega) = \sum_{l_a l_b j k_a k_b} \alpha_{l_a l_b j}^{k_a k_b} \bar{S}_{l_a l_b j}^{k_a k_b}. \tag{4.39}$$

The $\bar{S}$ functions arise naturally if the Hamiltonian for the Coulomb interaction $\hat{H}'$ is expanded in terms of spherical harmonics.[219] Assuming molecules A and B are located at positions $\mathbf{A}$ and $\mathbf{B}$, with $\mathbf{R} = \mathbf{B} - \mathbf{A}$ and the atoms a and b are located at the points $\mathbf{A} + \mathbf{a}$ and $\mathbf{B} + \mathbf{b}$, the interaction can be written as[219]

$$\begin{aligned}\hat{H}' =& \frac{1}{4\pi\epsilon_0} \sum_{a\in A} \sum_{b\in B} \frac{e_a e_b}{|\mathbf{R} + \mathbf{b} - \mathbf{a}|} \\ =& \frac{1}{4\pi\epsilon_0} \sum_{l_1 l_2} \sum_{k_1 k_2} \binom{l_1 + l_2}{l_1} \hat{Q}^A_{l_1 k_1} \hat{Q}^B_{l_2 k_2} \bar{S}^{k_1 k_2}_{l_1 l_2 l_1 + l_2} R^{-l_1 - l_2 - 1}.\end{aligned} \tag{4.40}$$

$\hat{Q}$ are the multipole operators (formulated in terms of spherical harmonics), $R^{-l_1-l_2-1}$ describes the distance dependence and $\bar{S}^{k_1 k_2}_{l_1 l_2 l_1+l_2}$ the orientation dependence.[219] $\bar{S}$ consists of a linear combination of products of Wigner functions with a spherical harmonic.[219] These functions are well-suited as basis functions for the expansion of the intermolecular interaction energy.[230] Thus the expansion of α_{ab} and ρ_{ab} converges rapidly.

This ansatz has the disadvantage that the parameters α and ρ have to be defined, which can be done by fitting to data from *ab initio* calculations. These are, however, quite expensive since they have to be performed for different orientations. Hence methods that require less computational effort are desirable.[219] One of these is the overlap method.[215,219] The principle connection between the repulsion energy and the overlap has been investigated by several groups.[232–234] A simple approach is to use qualitative valence bond theory. The repulsion energy between two two-electron closed-shell systems[v] is given by[96]

$$\Delta E(A::B) = -\frac{4\beta S}{(1 - S^2)}, \tag{4.41}$$

with S being the overlap integral between the two fragment orbitals (i.e. the atomic orbitals of A and B). Since the reduced resonance integral is also approximately proportional to S for larger internuclear distances[235] the repulsion energy can be written as

$$E_{rep} \propto \frac{S^2}{(1 - S^2)} \tag{4.42}$$

Expanding the term in a power series and only keeping the first term (which also implies large internuclear distances) one obtains,[232]

$$E_{rep} \approx const \cdot S^2. \tag{4.43}$$

[v] Of course an analogous expression can also be derived by qualitative MO theory.[96,235]

Since we are dealing with intermolecular interactions, the assumption of large internuclear distances is justified. Of course, for bigger systems the problem is more involved, nevertheless it can be assumed that the proportionality to the squared overlap is still a sensible approximation.
Thus several groups used the **squared molecular orbital overlap**, defined as

$$S^2 = \sum_i^A \sum_j^B \langle \psi_i | \psi_j \rangle^2, \tag{4.44}$$

to model the exchange-repulsion,[215,236,237] with ψ_i and ψ_j being the molecular orbitals on the isolated monomers i and j. Sometimes the expression is weighted with the corresponding orbital energies[215]

$$S^2_{en} = \sum_i^A \sum_j^B -\frac{\epsilon_i \epsilon_j}{\epsilon_i + \epsilon_j} \langle \psi_i | \psi_j \rangle^2. \tag{4.45}$$

Thinking in terms of a perturbative treatment as it is for instance used in the Salem-Klopman equation,[117] where each MO on fragment A interacts with all the others on fragment B, this ansatz makes intuitively sense. The weighting factor takes care of the fact that orbitals which are equal in energy have a higher interaction. Sometimes a distance-dependent term is introduced, e.g.[236]

$$E_{rep} \approx K \frac{S^2}{R}. \tag{4.46}$$

The quite elaborate exchange-repulsion model[234] used in the EFP method (see below) also relies on the orbital overlap.[215]
Another ansatz is based on the **density overlap** introduced by Lee et al.[238]

$$E_{rep} \approx const S^n_\rho, \tag{4.47}$$

with

$$S_\rho = \int \rho_A(\mathbf{r}) \rho_B(\mathbf{r}) d^3\mathbf{r}. \tag{4.48}$$

They plotted empirical repulsive potentials against the density overlap for several rare gas dimers. It was found that the linear relationship is excellently reproduced and that the value of n should be close to 1.[219,238] The density overlap ansatz can also be motivated by empirical findings of Kita et al.[239] It was refined to be applicable to bigger systems by

several groups.[215,219,226] Wheatley and Price used an expansion in Gaussian functions to model the monomer densities (distributed overlap model) and devised a model potential for the overlap using the $\bar{S}$ functions,[226] while Gavezzotti developed a numerical integration technique to calculate the density overlap.[240] Ryde et al. expanded the monomer densities in Slater-type functions and approximated the resulting integrals via exponential functions.[215]

Since the charge-penetration term can also be approximated by the density overlap, it is possible to incorporate charge-penetration as well as exchange-repulsion into one term.[219] This can for instance be achieved by fitting the term to the difference of the *ab initio* energy and the other contributions.[241]

Obviously the orbital-based overlap ansatz is physically more grounded than the density-based overlap approach, however, this does not mean that it necessarily performs worse.[215]

4.2.4 QM/MM Interfaces

In order to define the QM/MM interface the boundary between the two regions as well as the embedding scheme has to be defined. If the boundary cuts through covalent bonds, one has to take care of the dangling bonds. One way is to introduce so-called link atoms to saturate the bonds. Other approaches rely on localized orbitals, for instance using the local self-consistent field algorithm or generalized hybrid orbitals.[208] In the case of organic crystals which are in the focus of this thesis, only intermolecular interactions are operate between the QM and the MM part and thus this problem does not occur. For more details on the boundary, see[208] and references therein.

There are three levels of embedding schemes that define the QM/MM coupling term: mechanical, electrostatic and polarizable.[208] The van der Waals interactions between the parts is usually always taken into account by summing over all atoms in the QM and MM region using the corresponding force-field expression. With the Lennard-Jones potential one obtains

$$E_{vdw,QM/MM} = \sum_{i}^{i\in I} \sum_{j}^{j\in O} 4\epsilon_{ij} \left(\frac{\sigma_{ij}^{12}}{\mathbf{r}_{ij}^{12}} - \frac{\sigma_{ij}^{6}}{\mathbf{r}_{ij}^{6}} \right) \tag{4.49}$$

This of course means that van der Waals parameters have to be defined for the QM region. The embedding schemes are distinguished by their treatment of the electrostatic interactions. At the simplest level, the **mechanical embedding**, these interactions are only

treated on the MM level,

$$V_{el,QM/MM}^{mech.emb.} = \sum_{i}^{N_{atoms}} \sum_{j}^{M_{atoms}} \frac{q_i q_j}{\mathbf{R}_{ij}} \text{ with } i \in I \text{ and } j \in O. \tag{4.50}$$

Th sum runs over all atomic charges in the QM and the MM part. In order to compute the electrostatic interaction, MM charges q_i have to be defined for the QM region.[208] This can sometimes lead to problems when a chemical reaction, during which the charges change, is investigated (e.g. a simple nucleophilic substitution). One has to keep in mind that if the QM system was easily describable by MM methods a QM/MM approach, would not have been necessary in the first place. Another disadvantage is that the QM part is completely uninfluenced by the environment and hence the electronic structure is the same as in the gas phase. This means that the QM system must be sufficiently large that its charge distribution is converged with respect to the boundary.[208] One way to circumvent this problem is to use more than two layers as in an ONIOM approach. The third buffer layer is typically a low-level QM method (e.g. semi-empirical MO theory).[208]
The **electrostatic embedding** includes the charges of the environment into the QM Hamiltonian,[206]

$$H_{el,QM/MM}^{el.emb.} = \sum_{i}^{N_{el}} \sum_{j}^{M_{atoms}} \frac{q_j}{|\mathbf{r}_i - \mathbf{R}_j|} + \sum_{a}^{N_{nuc}} \sum_{j}^{M_{atoms}} \frac{q_j Q_a}{|\mathbf{R}_a - \mathbf{R}_j|} \text{ with } i, a \in I \text{ and } j \in O. \tag{4.51}$$

The first term describes the interaction between the electrons in the QM region with the MM charges and translates to a simple one-electron matrix element in HF theory/DFT. The first sum thus runs over the electrons in I and the second over the atomic charges in O. The second term covers the interaction between the nuclei with the charge Q_a in I and the MM charges in O.
With this approach, the QM part "feels" the environment and thus the electronic structure (and hence excitation energies and other properties) can adapt to it. The use of MM charges for the QM Hamiltonian is, however, not always justified, since the charges do not necessarily reproduce the electrostatic potential of the environment (see above). At the boundary, especially when link atoms are used, overpolarization can occur, since MM charges may be very close to the boundary. There are several approaches to circumvent this problem. For instance one can delocalize the charges onto the surrounding MM atoms.[208]

The biggest disadvantage of the electrostatic embedding lies in the fact that the envi-

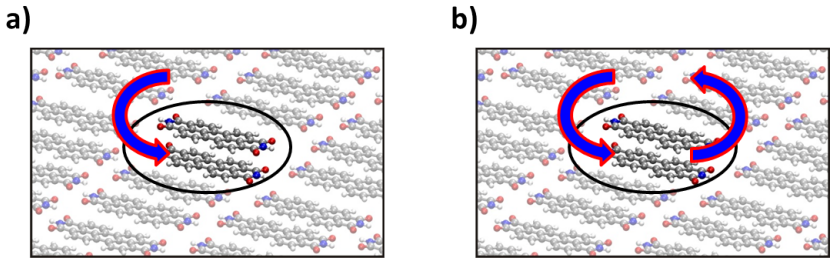

Figure 4.5: In an electrostatic embedding (a) the environment polarizes the QM part, but not vice versa. In a polarized embedding (b) a mutual polarization is possible.

ronment polarizes the QM part, but there is no polarization of MM part due to the QM charge distribution (see Figure 4.5a). If the charges in the QM part change (e.g. due to a reaction or excitations), this should polarize the environment. This is included using a **polarized embedding**, where QM and MM parts polarize each other mutually (see Figure 4.5 b). This demands an iterative approach and a polarizable force field.[208] Obviously polarizable embedding is rather expensive and necessitates accurate parameters for the polarization of the MM region. Astonishingly a polarized embedding was used in the very first publication by Warshel and Levitt.[204]

The quality of a QM/MM approach can not be judged directly, since it depends on a multitude of factors, like the size of the QM part, the applied force field, the used QM method, the embedding scheme and ultimately the system in question. There are several studies, which investigate these effects and calibrate the method for a certain system (see[242–245] and references therein). The quality for intermolecular interactions, which is especially important for organic crystals, has been benchmarked by Waller and coworkers.[246] They came to the conclusion, that the choice of force field has the biggest effect, with CHARMM and AMBER outperforming UFF and Dreiding.

QM/MM methods are difficult to perform and demand extensive calibrations,[208] which combined with the uncertain accuracy diminish the predictive power of the method. Furthermore, the development of improved DFT codes and the increase in computing performance makes the pure QM calculation possible for systems with increasing size.[2] Nevertheless QM/MM is one of the most powerful approaches for the description of large system that need a quantum mechanical treatment.

4.2.5 Valence Bond Theory in a QM/MM Framework: EVB and VB/MM

There are several methods that use valence bond (VB) theory[96] in a QM/MM framework, for example the MCMM method[247] by Truhlar et al. and the MM-VB method[248] by Robb and coworkers. This chapter focuses on the empirical valence bond (EVB) method[249,250] introduced in 1980 by Warshel and coworkers and the VB/MM theory[251] by Shurki et al. which couples *ab initio* VB calculations with the EVB methodology.

The **EVB method** exploits the fact that the VB resonance structures have a clear physical meaning, are easily interpreted and hence parameterized. Also the interaction with the environment is much easier defined. As mentioned above, the mechanical embedding of the QM part is sometimes difficult, since there is no uniquely defined way of generating the charges. In VB theory the wave function is written as a linear combination of neutral and ionic structures. Since these structures represent limiting cases, the interaction with the environment can be defined straightforward. An ionic structure has well defined charges and a neutral structure experiences approximately no electrostatic interactions. Since the EVB is an empirical method, i.e. no *ab initio* VB calculation is performed, the VB Hamiltonian matrix is parameterized using expressions from molecular mechanics. The EVB method can then be calibrated to reproduce experimental results, thus experimental data is directly incorporated into the Hamiltonian.[250]

An ionic cleavage reaction

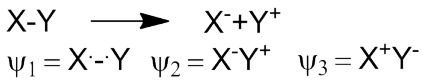

may serve as a simple example, taken from the original publication.[249] Three resonance structures (one neutral, two ionic) are needed for a complete description of this system. However, for such a reaction X is typically more electronegative than Y and hence ψ_3 can be neglected. In the gas phase the secular matrix can be written as[249]

$$\begin{vmatrix} H_{11}^g - E^g & H_{12}^g - E^g S_{12} \\ H_{21}^g - E^g S_{21} & H_{22}^g - E^g \end{vmatrix} = 0 \tag{4.52}$$

For the parametrization the overlap is neglected and the matrix element H_{11}^g is modeled as a Morse-type potential using experimental data for the parameters (see[249] for details).

The matrix element for the ionic resonance structure is written as

$$H_{22}^{g} = \Delta^{(2)} - \frac{e^2}{r} + V_{nb}^{(2)}, \tag{4.53}$$

with $\Delta^{(2)}$ being the gas-phase formation energy for the ionic resonance structure from the neutral atoms at infinite separation, which can be calculated from the ionization energy and the electron affinity of the neutral atoms ($\Delta^{(2)} = I_Y - EA_X$) and $V_{nb}^{(2)}$ represents the non-bonded interactions and is adjusted so that the minimum of $-\frac{e^2}{r} + V_{nb}^{(2)}$ is equal to the sum of the ionic radii. If the overlap is neglected, the off-diagonal elements can be calculated from the diagonal elements and the total energy. The latter is modeled as a Morse potential that reproduces the exact dissociation energy.[249]
Thus all matrix elements are expressed using molecular mechanics terms.
The solution Hamiltonian is assumed to be identical to the gas-phase Hamiltonian, except for the energy of the ionic structure, which is stabilized by the solvent interaction

$$H_{22}^{s} = H_{22}^{g} + G_{sol}^{(2)}. \tag{4.54}$$

The solvent stabilization can be either calculated, e.g. via an embedding, which is straightforward because the charges are clearly defined, or fitted so that the total energy reproduces experimental data, i.e. the dissociation energy. This calibration procedure ensures that the asymptotic limit of the potential energy surface is correctly described.[250] The potential energy surface can then be calculated by solving the secular equation for different intermolecular distances.

The **VB/MM method**[251] developed by Shurki and coworkers is based on a mechanical embedding of the individual VB structures, which are calculated using *ab initio* VB theory. Although the interaction with the environment is still calculated classically, it nevertheless influences the wave function, because the interaction is included in the VB Hamiltonian matrix. Similar to the EVB method it is exploited that the embedding of the interpretable ionic and covalent structures is straightforward.
At first a gas-phase VB calculation of the QM part is performed, which gives the Hamil-

tonian H^0 and the overlap matrix S,[vi]

$$H^0 = \begin{pmatrix} H^0_{11} & H^0_{12} \\ H^0_{21} & H^0_{22} \end{pmatrix} \tag{4.55}$$

$$S = \begin{pmatrix} S_{11} & S_{12} \\ S_{21} & S_{22} \end{pmatrix}. \tag{4.56}$$

Then the interaction between the two structures and the environment is calculated via molecular mechanics using individual parameters. The interaction terms H^{int}_{11} and H^{int}_{22} can easily be added to the diagonal terms of the gas-phase VB Hamiltonian elements. In the VB/MM framework it is assumed that the overlap matrix and the reduced resonance integral β,

$$\beta_{12} = H_{12} - \frac{1}{2}\left(H_{11} + H_{22}\right) S_{ij} \tag{4.57}$$

are invariant of the environment. At the crossing point of the energy surfaces of the diabatic states, the off-diagonal Hamiltonian matrix elements can thus be calculated as

$$H_{12} = H^0_{12} + \frac{1}{2}\left(H^{int}_{11} + H^{int}_{22}\right) S_{12}. \tag{4.58}$$

In the general case they are approximated as

$$H_{12} = H^0_{12} + \left(\omega_1 H^{int}_{11} + \omega_2 H^{int}_{22}\right) S_{12} \tag{4.59}$$

Thus the VB/MM Hamiltonian matrix can b written as:

$$H = \begin{pmatrix} H^0_{11} + H^{int}_{11} & H^0_{12} + \left(\omega_1 H^{int}_{11} + \omega_2 H^{int}_{22}\right) S_{12} \\ H^0_{21} + \left(\omega_1 H^{int}_{11} + \omega_2 H^{int}\right) S_{21} & H^0_{22} + H^{int}_{22} \end{pmatrix} \tag{4.60}$$

As in standard VB calculations, the Hamiltonian matrix can then be transformed according to

$$H^{trans} = S^{-\frac{1}{2}} H S^{-\frac{1}{2}}, \tag{4.61}$$

with subsequent calculation of the eigenvalues and eigenvectors of H^{trans}. From the eigenvectors the weights of the two structures can be calculated (after back transformation)

[vi] For simplicity two VB structures are assumed in the following, but the method can be extended to any number of VB structures.

using the Chirgwin-Coulson formula.

$$\omega_1 = c_1^2 + c_1 c_2 S_{12} \tag{4.62}$$

$$\omega_2 = c_2^2 + c_2 c_1 S_{21} \tag{4.63}$$

Since the weights are already needed to build up the VB/MM Hamiltonian matrix, an iterative approach has to be chosen. The final energy is calculated from the eigenvalue of the VB Hamiltonian plus the energy of the environment.

4.2.6 Other Developments

The **effective fragment potential method (EFP)**[252] by Gordon and coworkers was originally designed to describe solvation effects and was later generalized. In the EFP method, the total Hamiltonian is written as a sum of the Hamiltonian for the QM part and an interaction term V. This is not unsimilar to the continuum solvation methods, but contrary to those EFP is a discrete method. The interaction term includes the environment (e.g., solvent molecules) as effective fragments. The interaction includes Coulomb, induction and repulsion terms, which enter the Hamiltonian as one-electron terms. The interaction of an electron with the coordinate s of the QM part with the μth solvent molecule is given by

$$V_{el}(\mu, s) = \sum_{k=1}^{K} V_k^{Elec}(\mu, s) + \sum_{l=1}^{L} V_l^{Pol}(\mu, s) + \sum_{m=1}^{M} V_m^{Rep}(\mu, s) \tag{4.64}$$

Similar terms are used for the interaction with the nuclei and in between the fragments. The potentials for Coulomb and induction are obtained from *ab initio* computations of a single solvent molecule. The repulsion, which is inherently an intermolecular property, is more difficult to obtain and needs to be generated from first principles or fitted to *ab initio* data.[252] For water (EFP1) the Coulomb interaction is modeled using the DMA, a distributed multipolar polarizability expansion is used for the induction and the repulsion potential is modeled with atom-centered Gaussian functions. The exponents of the Gaussians are optimized in a fitting procedure. In the generalized approach (EFP2), the handling of the repulsion is more involved and relies on the orbital overlap. The exchange repulsion is obtained by subtracting the Coulomb energy as well as the monomer energies

from the Heitler-London energy expression,[252]

$$E_{exch} = \frac{\langle \psi_A \psi_B | \, \mathcal{A} \hat{H}_{AB} \, | \psi_A \psi_B \rangle}{\langle \psi_A \psi_B | \mathcal{A} \psi_A \psi_B \rangle} - \langle \psi_A \psi_A | \, V_{AB} \, | \psi_B \psi_B \rangle - E_A - E_B, \tag{4.65}$$

where ψ_A and ψ_B are the monomer wave functions and $\hat{H}_{AB} = \hat{H}_A + \hat{H}_B + V_{AB}$ is the supermolecular Hamiltonian. The antisymmetrizer $\mathcal{A}$ can be expanded in terms of permutation operators,

$$\mathcal{A} = 1 - P_1 + P_2 - \ldots, \tag{4.66}$$

which permute 1,2,.. electrons. Truncation after P_1 leads to an approximate expression for the exchange repulsion that is proportional to the square of the intermolecular overlap. The EFP method goes beyond QM/MM in the sense that the environment is included using quantum mechanical terms and not classical mechanics. Due to these benefits the interest in fragment methods has increased in the recent years.[253,254]

The **X-Pol** potential[255] by Gao and coworkers is also based on fragments. The wave function is written as a Hartree product of fragment wave functions, which are taken to be Slater determinants and are optimized in an SCF procedure. The van der Waals interaction between the molecules is modeled via a Lennard-Jones potential. The Hamiltonian of the system is written as

$$\hat{H} = \sum_{I}^{N} \hat{H}_I^0 + \frac{1}{2} \sum_{I}^{N} \sum_{J \neq I}^{N} \hat{H}_{IJ} \tag{4.67}$$

$\hat{H}_I^0$ is the Hamiltonian of the isolated molecule I and $\hat{H}_{IJ}$ denotes the interaction between two fragments. $\hat{H}_{IJ}$ contains the van der Waals term and the interaction of the electrons and nuclei of molecule I with the electrostatic potential of molecule J. In order to speed up the calculation, two further approximations are applied, a multipole expansion and NDDO.[255] After an initial guess the SCF procedure is performed for all fragments separately. Then the mutual polarization can be computed and with these interaction terms the fragment SCF procedure is performed anew. This double-SCF procedure is iterated until convergence. X-Pol is completely linear scaling and can either be used as an electronic structure theory for macromolecules or as a quantum force field for large-scale simulations.

4.3 Analyzing Intermolecular Interactions with Symmetry Adapted Perturbation Theory (SAPT)

Symmetry adapted perturbation theory (SAPT) can be used to calculate the intermolecular interaction energy very accurately and provides insight by decomposing the energy into different contributions.[256,257] The basic idea is to use **perturbation theory** to include the intermolecular interaction by writing the Hamiltonian of a molecular dimer AB as

$$\hat{H} = \hat{H}_A + \hat{H}_B + \zeta\hat{V} = \hat{H}_0 + \zeta\hat{V}, \tag{4.68}$$

with $\hat{H}_A$ and $\hat{H}_B$ being the monomer Hamiltonians and $\hat{V}$ the perturbation collecting the Coulomb interaction terms. ζ is a parameter determining the strength of the perturbation. Since it can be assumed that the intermolecular interaction is weak compared to the intramolecular interactions, i.e. it does not change the electronic structure of the monomers significantly, the perturbative ansatz is valid. The Schrödinger equation is given by

$$\hat{H}\Phi_{AB}(\zeta) = E_{AB}(\zeta)\Phi_{AB}(\zeta). \tag{4.69}$$

The wave function as well as the energy are expanded in a perturbative series. There are different approaches to solve this problem.[219,256] Jeziorski et al. used Rayleigh-Schrödinger theory and expanded the perturbation wave function into products of eigenfunctions of the monomer Hamiltonians.[258] When the perturbation is zero ($\zeta = 0$), the dimer energy is simply the sum of the eigenenergies of the monomer Hamiltonians, $E_{AB}(0) = E_A + E_B \equiv E_{AB}^{(0)}$. The corresponding wave function can be written as a product $\Phi_{AB}(0) = \Phi_A\Phi_B \equiv \Phi_{AB}^{(0)}$. $E_{AB}^{(0)}$ and $\Phi_{AB}^{(0)}$ are the zeroth-order energy and wave function. However, this ansatz does not fulfill the antisymmetry required. Using the correct ansatz $\mathcal{A}\Phi_0$ leads to problems with the perturbation theory, since the antisymmerized wave function is no eigenfunction of $\hat{H}_0$.[256] Thus Jeziorski et al. enforced the antisymmetry condition only in the final energy expression, which is called weak symmetry forcing approach.[258]

If a Hartree-Fock wave function is used for the monomers, the intramolecular correlation is missing. This can either be corrected by introducing a second perturbation, which includes correlation (the so-called double perturbtaion theory approach), or by using DFT.[258] Simply replacing the HF orbitals and orbital energies by their Kohn-Sham counterparts leads to the SAPT(KS) method,[259] which is not very accurate.[258] A more involved theory, that relies on the coupled-perturbed Kohn-Sham and time-dependent DFT equations led to the **DFT-SAPT** method.[258] The latter method is of similar accuracy as CCSD(T),[159]

but scales formally only as N^6 instead of N^7.[258] Using density fitting and other techniques, the scaling behavior could be reduced to N^5. The latter is implemented in the MOLPRO program package.[258,260]

The total interaction energy computed with SAPT can then be written as a sum of the different contributions that arise naturally from the perturbation treatment,

$$E_{int} = E_{el}^{(1)} + E_{exch}^{(1)} + E_{ind}^{(2)} + E_{exch-ind}^{(2)} + E_{disp}^{(2)} + E_{exch-disp}^{(2)} + \cdots \tag{4.70}$$

with $E_{el}^{(1)}$ being the electrostatic, $E_{el}^{(1)}$ the exchange, $E_{ind}^{(2)}$ the induction, $E_{exch-ind}^{(2)}$ the exchange-induction and $E_{exch-disp}^{(2)}$ the exchange-dispersion contribution.

SAPT can be used to provide high-level reference data for intermolecular interactions. Furthermore, due to the decomposition into different contributions, it provides insight into the nature of the interaction. It is also possible to parameterize the different terms of a force-field energy expression to reproduce the corresponding SAPT terms. Following this approach a physically-motivated intermolecular force field can be derived. If all terms produce the correct energy by themselves, the calculation gives "the right answer for the right reason," and the force field does not rely on an error compensation between the different terms.[217,261]

4.4 Excursion: π-π interactions

Non-covalent interactions involving π-systems, especially aromatic rings, have triggered a lot of interest in the recent years. On the one hand, this is due to the fact that π-π, as well as anion-π, cation-π and X-H-π interactions are important for many chemical and biochemical phenomena, as well as for material sciences.[262] The π-π interactions are especially important for optoelectronic devices using small organic molecules. On the other hand a lot of research is focused on these interactions, since their nature is still not completely understood.[262] In fact, it is not even completely resolved whether special π-π stacking interactions exist or not.[263,264] This excursion provides a short overview of the most important results and viewpoints in the literature.

The original model devised by Hunter and Sanders[265] in 1990 treats every atom as a local quadrupole that is formed by the positively charged nucleus and two negative charges above and below the molecular plane that arise due to the π-electrons. According to this model, the interaction of the quadrupoles on the different molecules determines the preferential geometry of the molecules and the effect of the substituent on it. The van

der Waals interactions have the biggest contribution to the overall binding energy but "*cannot be the force which controls the experimentally observed geometry of interaction. If they were,* [..] *a cofacial arrangement with no offset would be observed.*" [265]
The Polar/π model by Cozzi and Siegel[266] uses a similar ansatz based on the molecular quadrupole moment.
These models have proven to be quite useful for the rationalization and prediction of experimentally encountered stacking modes. However, they have several deficiencies and there are cases where they fail.[262] With high-level computational methods like CCSD(T) or SAPT becoming applicable to systems of a relevant size, several groups, especially Sherrill and coworkers,[267] started to investigate the binding situation in a theoretically profound way.[262] It was found that the prototypical sandwich and parallel displaced configurations of the benzene dimer are bound primarily by dispersion interactions and that the decrease in exchange-repulsion is responsible for the higher stability of the displaced isomer.
Several studies on the substituent effects contradicted some of the predictions of the Hunter-Sanders model (see[268] and references therein). Wheeler and Houk proposed[269] that the substituent effects do not act through a change in the π-electron density, but almost solely via direct interactions between the substiuent and the proximate vertex of the other molecule.[262,268] Thus the Hunter-Sanders model is currently challenged and probably needs revision or should be refined.[264]
In systems like the benzene dimer the term "aromatic interaction" is often used, although it was found that aromatic delocalization is actually hindering the π-π interaction and is hence a misnomer.[262] Martinez and Iverson made a strong case that the terms "π-π-stacking" and "π-π-interaction" are also misnomers.[264] They argue that they imply a preferred face-to-face arrangement, while T-shaped isomers are often encountered and furthermore insinuate a favorable interaction between the π-clouds that should favor a face-centered parallel stacking. According to them the Hunter-Sanders model provides a qualitatively correctly starting point, since it predicts the T-shaped of offset-stacked arrangements usually encountered correctly. Moreover, it also correctly predicts a face-centered configuration for dimers formed from electron-rich and electron-poor aromates. These complexes should be referred to as "donor-acceptor complexes."
The fact that π-stacked dimers are predominantly held together by dispersion forces raises indeed the question whether there is any difference to the interactions between saturated systems, i.e. if "*special non-covalent π-π stacking interactions really exist.*" [263] This question is the topic of a communication by Grimme.[263] He notes that cyclohexane and benzene

are both liquids at room temperature and hence similar forces should be active between the molecules. In fact, the parallel-displaced benzene dimer has a smaller binding energy than the pentane dimer (which has the same number of electrons). On the other hand the interactions between large polycyclic aromatic compounds seem to be different than between alkanes. Grimme studied several acenes and their hydrogenated analogues with *ab initio* and DFT methods. He comes to several conclusions: The interactions between the aromatic molecules are stronger than between the alkanes for systems with more than 10-15 carbon atoms. This π-stacking effect (PSE) is due to more favorable dispersion interactions, while the electrostatic interactions would favor saturated interactions. The π-system also has an indirect effect, since it allows a closer contact of the monomers, because the Pauli repulsion wall is softer. The parallel displacement found in the sandwich π-stacks is due to electrostatic effects, but also the Pauli-repulsion is decreased by the displacement. Hence he concludes that there are indeed special nonlocal electron correlations between the π electrons that are responsible for the PSE. However the term "π-π interactions" should be used with care, since there is little evidence of a special stabilization for systems with less than 10 carbon atoms. The term "π-π stacking" is best used as a geometrical descriptor of the interaction mode in unsaturated hydrocarbons.
This exemplary summary of the literature on the topic shows that the true nature of π-π interactions remains the topic of an open discussion. It seems to be clear that the importance of these special π-π interactions has been overestimated in the past and that they are more complex than the Hunter-Sanders model assumes. However, with regard to the work of Grimme it seems exaggerated to banish the term "π-π stacking interaction" completely.

5 Merocyanine dyes

Merocyanine (MC) dyes[i] consist of a donor and an acceptor moiety, linked by a methine or polymethine bridge and are therefore donor-bridge-acceptor-type compounds. Due to this push-pull pattern most of their properties can be understood in terms of two major resonance structures, namely a neutral and a zwitterionic one (see Figure 5.1a).
Merocyanines feature tunable optical properties and typically show intense absorption bands. Furthermore the synthetic possibilities lead to a high structural diversity.[273,274] These properties make the MCs highly interesting as organic semiconducting materials. The HOMO levels of the MCs are also relatively low, which should enable high open-circuit voltages in organic solar cells.[275] However, it is generally assumed that dipolar molecules are inapt for these applications, due to the large energetic disorder generated in the amorphous solid state which hinders charge transport.[276] Nevertheless, despite their high dipole moments merocyanines have been proven to be suitable candidates for the use as organic semiconducting materials in devices like photovoltaic cells by the groups of Würthner and Meerholz, with power conversion efficiencies reaching up to 6%.[277] This is attributed to the fact that merocyanine dyes self-assemble into strongly bound dimer aggegates, which leads to a cancellation of the dipole moment and thus to a small energetic disorder.[273,275] Furthermore the strong intermolecular forces between the monomers should be rather favorable for a significant electronic coupling and thus for an efficient exciton and charge transport. Due to their dipolarity MC crystals can be expected to have a high dielectric constant. This favors the dissociation of the exciton in free charges at the interface.[278] For further details on the advantages and disadvantages of zwitterions in organic-based materials, see[278] and references therein. In recent years, MCs have successfully been used in organic photovoltaic cells[3,273,275,277] and organic thin-film transistors[279,280] and are also well-known for their interesting non-linear optical properties.[281] The spectral properties of the MCs can be discussed in terms of a simple "**two-state**

[i] Parts of this chapter, especially of the section *Photoinduced Isomerization of 6-nitro BIPS* as well as the sections *A Valence Bond Approach to the Cyanine Limit: Does a Correlation between the Cyanine Limit and the Exciton Reorganization Energy Exist?* and *Charge and Exciton Reorganization Energy and Exciton diffusion length* have already been published in references[270,271] and[272].

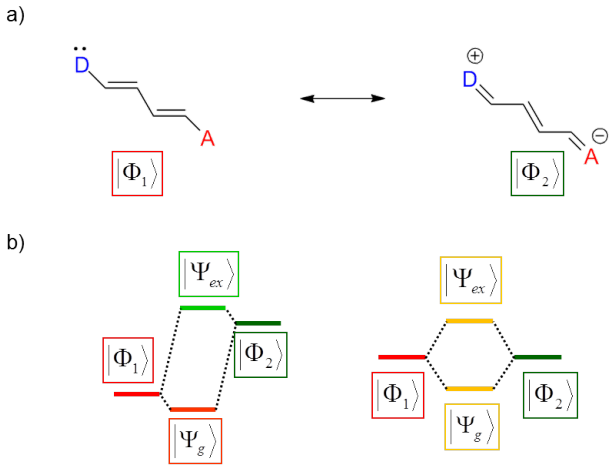

Figure 5.1: a) The two major resonance structures describing a merocyanine. Here, an MC with a C_4-bridge is depicted, the VB structures can, however, analogously be formulated for different bridge lengths. b) Composition of the ground and excited state in a two-state model with the contributing state functions having very different (left) and equal energies (right). *Reproduced with kind permission from AIP Publishing.*

model" using valence bond theory (see Figure 5.1b).[281–283] Neglecting the overlap between the two major resonance structures describing donor-bridge-acceptor molecules (see Figure 5.1 b)), the normalized wave functions of the ground and excited state can be written as

$$|\Psi_g\rangle = c\,|\Phi_1\rangle \pm \sqrt{1-c^2}\,|\Phi_2\rangle\,, \tag{5.1}$$

$$|\Psi_{ex}\rangle = d\,|\Phi_1\rangle \pm \sqrt{1-d^2}\,|\Phi_2\rangle\,. \tag{5.2}$$

Using the orthogonality condition and again neglecting the overlap one obtains

$$\langle\Psi_g|\Psi_{ex}\rangle = cd \pm \sqrt{1-c^2}\sqrt{1-d^2} = 0, \tag{5.3}$$

which gives

$$c^2d^2 = (1-c^2)(1-d^2) \Leftrightarrow d = \pm\sqrt{1-c^2}. \tag{5.4}$$

Thus one can reduce the degrees of freedom to one parameter c

$$|\Psi_g\rangle = c\,|\Phi_1\rangle + \sqrt{1-c^2}\,|\Phi_2\rangle\,, \tag{5.5}$$

$$|\Psi_{ex}\rangle = \sqrt{1-c^2}\,|\Phi_1\rangle - c\,|\Phi_2\rangle\,. \tag{5.6}$$

Within the model, the weight of structure one is then simply given by c^2, while the weight of structure two is given by $1 - c^2$. Of course, if the overlap was taken into account the equations would be less simple, but for a qualitative argumentation the approximations should be valid. From equations 5.5 and 5.6 one can see that if the ground state consists predominantly of one resonance structure, the excited state will consist mainly of the other. This can also be rationalized using a valence bond mixing diagram (i.e. perturbation theory)[96] as in Figure 5.1b. If one structure is significantly lower in energy than the other, the ground state will be dominated by the lower energy structure. Since the ionic structure is stabilized in polar environments, the weights will be highly dependent on the environment polarity. This makes the MCs ideal candidates for studying the effect of the environment on the optoelectronic properties of organic semiconductors.

In the case of merocyanines, the ground state is typically (but not always) dominated by the neutral structure and hence the zwitterionic resonance contributor is the major structure in the excited state. In this case the excitation can be expected to feature a significant amount of charge-transfer character. Since the bond length alternation pattern[ii] is different in the ground and excited state, a considerable amount of geometric reorganization will be induced by the excitation. Hence large vibrational progressions (i.e. broad bands) and high reorganization energies can be expected. A very polar environment should stabilize the predominantly ionic excited state much more than the ground state, leading hence to a large bathochromic solvatochromism.[iii]

If, however, both resonance structures are equal in energy, the ground and excited state will both consist of a 50:50 mixture of $|\Phi_1\rangle$ and $|\Phi_2\rangle$. This is called the "**cyanine limit**,"[283] since it is the case for symmetric cyanines. Consequently a molecule in the cyanine limit can be identified by having spectroscopic properties comparable to the cyanines. The character of the ground and excited state should be similar, and hence the excitation will be rather neutral in character, and its solvent dependence can be expected to be small. The geometric changes should also be small and hence the band rather sharp. Since the VB structures have the same energy, the excitation energy is dominated by the

[ii] The bond length alternation is typically defined as the difference between the average lengths of the carbon-carbon single and double bonds.[284] In this thesis the bond length alternation pattern refers to the pattern of alternating single and double bonds, which is opposite in the neutral and the ionic resonance structures.

[iii] When discussing solvatochromic shifts, one should keep in mind that the polar environment on the one hand stabilizes the ground and excited state for a fixed geometry to a different extent, but on the other hand also leads to a change of the geometry, especially the BLA. Thus both effects must be taken into account. Furthermore, the weights will be influenced indirectly by the change in geometry as well as directly due the effect of the polarity of the environment on the Hamiltonian.

resonance of the two structures and should hence typically be smaller than in the case of structures with strongly differing eigenenergies.
Going from the cyanine limit to the case, where the ionic resonance structure is dominating the ground state, the excitation energy and the band width should again increase. Furthermore a hypsochromic solvatochromism should be observed.
Würthner et al. investigated three merocyanines with different heteroatoms and substituents in solvents with different polarities.[285] They obtained c^2-values ranging from 0.3 to 0.58 (For details on how to estimate c^2-values from experimental data, see below). The first merocyanine had a predominantly neutral polyene-like structure ($c^2 \approx 0.3$). Increasing the solvent polarity led to a red-shift of the absorption and to sharper bands. This is in line with the two-state model, since the increasing polarity should shift the molecule in the direction of the cyanine limit. Of course the red shift by itself could in principle be explained solely by the stabilization of the excited state, due to the increasing reaction-field strength of the solvent, but the change in band shape is a strong indication for the change of character of the wave function.[281] The other two merocyanines used in the study were closer to the cyanine limit and showed with increasing solvent polarity a bathochromic shift that inverted to a hypsochromic shift for very polar solvents. The most bathochromically shifted spectra always showed cyanine-type band shapes. This indicates that the cyanine limit was reached and subsequently crossed.[285] Thus all findings were in accord with the model.
It is interesting to note that by changing the polarity of the environment, the qualitative character of the wave function changes. This high sensitivity is rather unusual and challenging for a computational modeling.

As stated above the c^2-values can be estimated from experimental data. This is also done with a two-state model (see[283] and references therein), which is, however, based on a molecular orbital picture. In this approach, the molecule is simply modeled by two atomic basis functions φ_1 and φ_2 separated by the distance l, see Figure 5.2. In order to derive a formula for c^2, at first the dependence of the transition dipole moment μ_{ag} and the difference between ground- and excited-state dipole moment $\Delta\mu$ on c^2 is calculated using the zero-differential overlap (ZDO) approximation and the two basis functions. Due to the ZDO approximation, the atomic orbital overlap is neglected and hence the two molecular

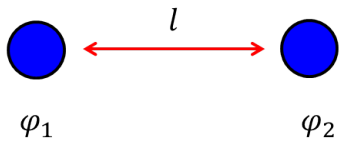

Figure 5.2: Two-state model for the calculation of the dependence of μ_{ag} and $\Delta\mu$ on c^2.

orbitals resulting from the two basis functions can be written as[283]

$$\phi_1 = \sqrt{1-\tilde{c}^2}\varphi_1 + \tilde{c}\varphi_2, \tag{5.7}$$

$$\phi_2 = \tilde{c}\varphi_1 - \sqrt{1-\tilde{c}^2}\varphi_2. \tag{5.8}$$

With these MOs the ground and singly excited state can be written in terms of configurations,

$$\Psi_1 = |\phi_1\bar{\phi}_1| \tag{5.9}$$

$$\Psi_2 = |\phi_1\bar{\phi}_2| + |\phi_2\bar{\phi}_1|. \tag{5.10}$$

It should be noted that despite the apparent similarity to the equations 5.5 and 5.6 the ansatz is quite different. $\tilde{c}$ is an LCAO-parameter describing the polarization of the bonding and antibonding MOs and is hence not identical to the coefficient of the VB structure c.

The expansion of the ground-state wave function Ψ_1 in VB determinants gives the following structures:[iv]

This is qualitatively the same as in ethene or donor-acceptor systems like aminoborane. It is obvious that they are not the same as the ones in Figure 5.1. This is due to the fact that just two basis functions are used, while at least four would be needed for a modeling of a donor-bridge-acceptor system with a C_2 bridge, that allows a transformation to the VB structures of the type in Figure 5.1. The MO model neglects the additional basis functions, which would describe the bridge. Hence the bridge is assumed to be of minor importance and is just modeled by the distance l. Thus structure I could be seen as an approximation

[iv] The formal charges have been omitted, since they depend on the actual system. In the case of ethene structure III features no charge separation, while it is structure I for donor-acceptor systems.

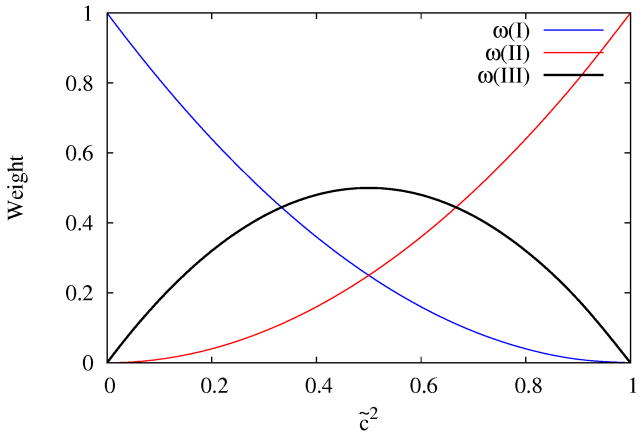

Figure 5.3: Dependence of the weights of the structures on the value of c^2,obtained by expanding $\Psi_1 = |\phi_1\bar{\phi}_1|$. For the calculation the overlap between the structures has been neglected.

for the neutral resonance contributor, while structure II is representing the ionic one. The charge separation in the ionic resonance structure is somewhat overestimated, because two electrons are moved from the donor to the acceptor. In the structure in Figure 5.1 the donor is only deficient of one electron, while the acceptor gains one, the remaining electrons are rearranged in the bridge. With increasing $\tilde{c}^2$ the weight of structure I decreases and the one of structure II increases quadratically (see Figure 5.3). The weight of structure III is zero at both limits and reaches a maximum at $\tilde{c}^2 = 0.5$.
Using the expressions for Ψ_1 and Ψ_2 and the model (Figure 5.2), expressions for μ_{ag} and $\Delta\mu$ can be derived, by calculating the corresponding matrix elements (see[283] for details),

$$\mu_{ag} = \sqrt{2}el\tilde{c}\sqrt{1-\tilde{c}^2}, \tag{5.11}$$

$$\Delta\mu = el(1-2\tilde{c}^2). \tag{5.12}$$

Thus the model predicts that the transition moment is at its maximum at $\tilde{c}^2 = 0.5$, i.e. the cyanine limit. This is not surprising, since with $\Delta\mu$ being zero not much electron rearrangement can take place[v] and hence the charge transfer character can be expected to be zero at the cyanine limit. At $\tilde{c}^2 = 0.5$ neither of the two MOs of the model are

[v]Strictly speaking a symmetric electron rearrangement would be possible as in the case of the PBI dimers (see below), however, due to the unsymmetric nature of the MCs this is not very likely here.

polarized. By rearranging the equations, one can obtain an expression for $\tilde{c}^2$,[285]

$$\tilde{c}^2 = \frac{1}{2}\left[1 - \Delta\mu(4\mu_{ag}^2 + \Delta\mu^2)^{-1/2}\right]. \tag{5.13}$$

Thus the value of $\tilde{c}^2$ can be calculated from quantities obtainable by UV/Vis and electrooptical measurements. In a similar fashion the behavior of the polarizability and the hyperpolarizability can be analyzed (see[283] for details). The model predicts that the polarizability is maximal at the cyanine limit while the first hyperpolarizability goes through zero at $\tilde{c}^2 = 0.5$. Marder et al.[284] plotted calculated hyperpolarizabilities against the bond length alternation, which should be connected to $\tilde{c}^2$ and indeed found the predicted behavior. For a recent study on the BLA and non-linear optical properties of π-conjugated systems, see.[286]

The MO-based two-center two-state model relies on heavy approximations, but nevertheless, it proved to be quite useful for the NLO community. The $\tilde{c}^2$-values measured by Würthner et al.[285] reported above also fit nicely to the spectroscopic properties of the corresponding MCs, which supports the validity of the model.

The valence bond picture on the other hand is qualitatively correct, since the major approximation is the modeling of the molecule with only two resonance structures, which has a solid theoretical justification if one uses block-localized determinants[287,288] for the individual structures. *Ab initio* valence bond theory thus provides a methodology of calculating the weights. As stated above the MO-based two-state model cannot be directly translated to the VB model of the MCs, since the three structures obtained for two centers and two electrons are different from the ones needed for a donor-bridge-acceptor system. Moreover the identification of structure I with the neutral and structure II with the ionic resonance contributor relies on heavy approximations. This, however, does not mean that no relation between c^2 and $\tilde{c}^2$ can be expected. Assuming the two-center model is a valid approximation of the frontier molecular orbitals, one can argue that the higher $\tilde{c}^2$ the more polarized is the the two-center model MO and thus the HOMO of the real system. Since the weight of the ionic structure should increase with increasing polarization, one should find a qualitative agreement between $\tilde{c}^2$ and c^2. A quantitative agreement between calculated and measured weights can, however, not be expected due to the involved approximations.

In the quest for optimal MCs for the use in organic semiconductors, guidelines for a rational design would be highly desirable due to the immense synthetic possibilities. It is

usually assumed that MCs close to the cyanine limit should exhibit excellent properties due to the low reorganization energy. However, this has never been evaluated critically. Furthermore, the cyanine limit needs to be reached in the crystal or thin-film environment, but the $\tilde{c}^2$-values are measured in solution. Since it is unclear how much the different environments shift the weights, it is not possible to extrapolate from solution data to the behavior in the crystal. Another parameter typically used is the HOMO energy, since it is assumed that the lower the HOMO energy the higher V_{oc}. HOMO energies can be measured using cyclovoltammetry[vi], but here also the question arises if a measurement in solution is suitable. Furthermore, since it can be assumed that the influence of the packing will be significant on the performance of the MCs in the device, the significance of purley molecular properties is uncertain.

The second section of this chapter deals with possible approaches to assess the suitability of a certain merocyanine for organic solar cells with quantum chemical methods. A special emphasis is laid on the influence of the packing and the environment. The usefulness of the HOMO energy, the BLA and their dependence on the environment is discussed, as well as possibilities to obtain information of the effect of the crystal environment. Furthermore the question of how to calculate c^2-values, its environment dependence and its importance are briefly addressed. While in the experiment typically macroscopic properties are measured, which are affected by many parameters, the individual effects can be studied separately with computational methods. Several people have been involved in this project. Hence only an overview of the results will be given in this thesis, while more details can be found in the Bachelor thesis of Andreas Heimbeck,[289] the Diploma thesis of Anca Boariu[290] and especially the Master thesis of Charlotte Brückner.[140]

Some MCs can interconvert into the spiropyran form. This is currently extensively studied due to its potential applications in optical switches, photonic crystals, and other fields of material sciences and biology (see for instance[291–294] and references therein). The first section of this chapter focuses on the less understood **photoinduced interconversion** of two isomers of the MC form of 6-nitro BIPS,[vii] which has been studied extensively with

[vi] Strictly speaking the HOMO energy cannot be measured, since is a theoretical construct. What can be measured is the ionization potential (e.g., via photoelectron spectroscopy) or the oxidation potential (via cyclovoltammetry). Using Koopmans' theorem these quantities are, however, related to the HOMO energy. It should be noted that the connection between the ionization/HOMO energy and V_{oc} is also based on heavy approximations.

[vii] 6-nitro-1',3',3'-trimethylspiro[2*H*-1-benzopyran-2,2'-indoline]

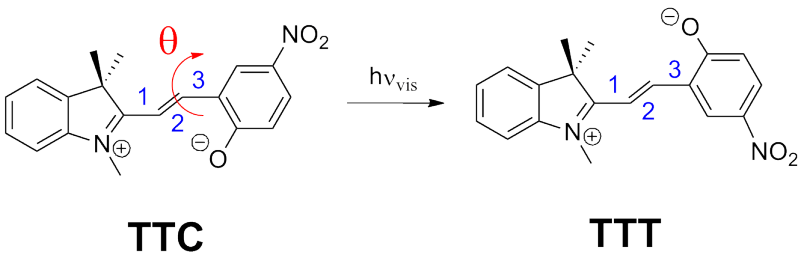

Figure 5.4: Photochemical interconversion between the TTC and TTT isomer. The depicted ionic structure only represents the multitude of possible zwitterionic structures. *Reproduced with kind permission from AIP Publishing.*

femtosecond transient absorption spectroscopy by Tobias Brixner and his group.[271,295] The results shown there have been obtained in close collaboration with Dr. Stefan Rützel as well as Prof. Patrick Nürnberger and Prof. Tobias Brixner. A fundamental understanding of the photochemistry of the MCs is of vital importance in order to assess their behavior in organic solar cells. Furthermore the computations were aimed at rationalizing and understanding the experimental results. In the course of this project a benchmark of theoretical methods has been carried out, which is also relevant for the computational characterization of the MCs.

5.1 Photoinduced Isomerization of 6-nitro BIPS

Irradiating the *trans-trans-cis* (TTC) isomer of 6-nitro BIPS leads to an interconversion to the *trans-trans-trans* (TTT) isomer. The photoinduced isomerization is depicted in Figure 5.4. The ground state of 6-nitro BIPS is best represented by the zwitterionic Lewis structure in polar environments (see below). According to the experimental results, the TTC isomer predominates in acetonitrile, while excitation in the visible range of the spectrum leads to an increase of the TTT isomer due to an ultrafast excited-state photoisomerization TTC $\rightarrow$ TTT within 200 fs.[295] The reverse reaction TTT $\rightarrow$ TTC is not observed. Signal oscillations in the transients at 170 and 360 cm^{-1} have been attributed to coherent vibrational wave-packet dynamics on the excited-state surface.[271,295] Although the spectroscopic studies provide an immense body of data, it is not sufficient for an interpretation and rationalization of the results. It was not clear why the reverse reaction (i.e. irradiation of TTT, with subsequent isomerization to TTC) does not occur nor which modes are responsible for the observed oscillations. Since the isomerization

involves a rotation around bond 3 in Fig. 5.4 one might assume that the minimum of the excited state is a twisted species and that fluorescence to the ground state occurs from this configuration. However, this is not in line with the experimentally observed small Stokes shift. Hence the shape of the potential energy surface on which the isomerization occurs could not be extracted from the experimental data.

Previous computations of the isomerization of the MC form were either focused on the ground state[296,297] or used simplified model systems.[298] Quantum-chemical calculations of the potential-energy surfaces (PES) and the vibrational modes of 6-nitro BIPS in ground and excited state are, however, needed to interpret the spectroscopic results. The theoretical description of the ground- and excited-state PES for the reaction coordinate is, however, challenging. The above mentioned susceptibility of the MCs to environmental effects as well as the possible occurrence of charge-transfer effects are quite demanding for the modeling. Acetonitrile is rather polar (ϵ=35.68)[195] and hence will have a significant influence. Furthermore, the dependence on the environment as well as the amount of charge-transfer character can be expected to vary strongly along the reaction coordinate, thus demanding on the one hand highly accurate methods, which describe neutral and charge-transfer states equally well, and on the other hand a sophisticated treatment of the solvent effects.

In the ground state, the neutral structure is likely to be important in the minimum geometry, but is becoming highly unstable if one ring is rotated, due to the fact that the π-system is disrupted. Therefore the weights will change significantly during the isomerization which hence influences the character of the excitation, the solvent dependence, and the other geometric degrees of freedom. This challenging entanglement of geometry and electronic character makes the MCs a very interesting model system for the investigation of environmental effects.

In this section the results from high-level *ab initio* and density functional calculations in the S_0 and S_1 state are presented. The PES was calculated along the reaction coordinate, which can be approximated by the rotation around bond 3 in Fig. 5.4, in order to elucidate the mechanism of the photoinduced isomerization. Additionally, frequency calculations in the S_1 state were used to identify the modes responsible for the oscillations in the experimental transients. Due to the complexity an extensive benchmark has been performed in order to find an accurate theoretical description of the excited states and the solvent effects.

At first a summary of the computational methods is given and the results of some preliminary computations are presented. Then the benchmark calculations concerning the

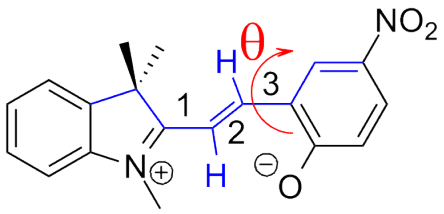

Figure 5.5: The dihedral angles restricted in the relaxed scan are marked in blue. *Reproduced with kind permission from AIP Publishing.*

excited state and the solvent effects are examined. In the third section the results are discussed and interpreted.

5.1.1 Computational Methods and Preliminary Calculations

In order to calculate the PES along the reaction coordinate, relaxed scans in the ground and excited state were performed by changing the angle θ of the rotation around bond 3 (see Fig. 5.4) step by step while all other degrees of freedom were optimized. For these calculations, the Gaussian09 program package[195] was used. The method for the treatment of the environmental effects will always be noted in the discussion below. If nothing is stated, the calculations were performed in the gas phase.
If only the angle θ (see Figure 5.5) is restricted in the relaxed scan, several atoms pyramidalize in the vicinity of the transition-state geometry. This has the consequence that the dihedral angle (which defines the reaction coordinate in the scan) and the angle between the two planes defined by the ring systems differ significantly, thus making the interpretation of the PES difficult. To ensure a direct interpretability of the rotational (dihedral) angle, the dihedral angles in the vicinity of the rotational were kept fixed (see Figure 5.5). However, this reduces the degrees of freedom and may limit the validity of the approach. Hence it was checked that these additional constraints do not change the shape of the surface significantly by means of additional calculations without these restrictions (see Figure 5.6).

Preliminary ground-state optimizations were performed with Møller-Plesset Perturbation Theory (MP2)[54] using the resolution of the identity approximation[299–301] as well as with the B3LYP functional[60,61,63,64] in connection with the cc-pVTZ basis sets.[302] The conductor-like screening model[192] as implemented in TURBOMOLE[193] was used to include the effect of the environment. With these calculations the bond-length alterna-

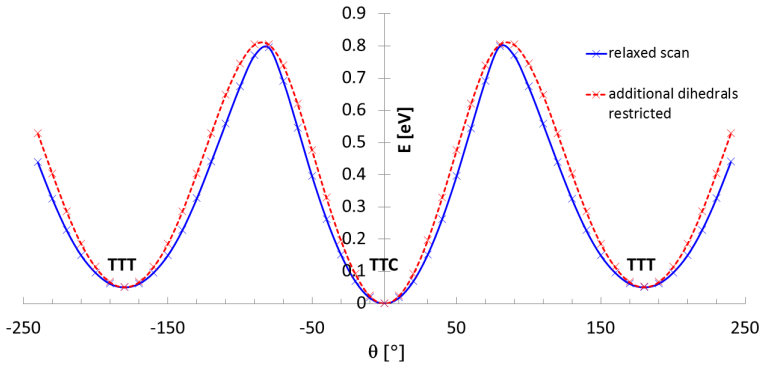

Figure 5.6: Comparison of the relaxed scan (B3LYP/cc-pVDZ with IEFPCM) with and without additional constrained dihedral angles (see Figure 5.5). *Reproduced with kind permission from AIP Publishing.*

Table 5.1: Bond length alternation pattern for TTC in Å (see Fig. 5.5 for the definition of the bond numbers)

bond	MP2/cc-pVTZ (COSMO)	B3LYP/cc-pVTZ (COSMO)	B3LYP/cc-pVDZ (IEFPCM, relaxed scan)
1	1.410	1.405	1.406
2	1.373	1.374	1.387
3	1.422	1.420	1.418

tion pattern could be obtained and the applicability of density functional methods was checked. In principle the ground state can be expected to be sufficiently well described by the B3LYP functional. However, since the bond length alternation pattern is highly important for the correct description of the barrier of the isomerization and DFT is known to have difficulties with conjugated π-systems[303] the additional MP2 calculations have been performed. For comparison also B3LYP/cc-pVDZ calculations with IEFPCM[196] have been performed using Gaussian09. The bond lengths of the bridge as predicted by the different methods are given in Table 5.1.

Since the agreement between the methods is quite satisfactory, the B3LYP functional in combination with the cc-pVDZ basis sets was chosen for the scan in the ground state. All methods predict a bond length alternation in line with the assumption of a slightly dominating ionic resonance structure.

For calculations of single points and excitation energies as well as numerical frequencies and the corresponding geometry optimization, the long-range corrected CAM-B3LYP functional[152] was applied using time-dependent density functional theory. The applicability of TDDFT was tested by benchmarking several potentially suitable functionals

against SCS-ADC(2) and experimental results[295] (see below). Unless stated otherwise all DFT calculations were performed with the Gaussian09 program package, while TURBOMOLE was used for SCS-ADC(2)[169] and TDHF computations.
For the ground- and excited state scan, a polarizable continuum model using the integral evaluation formalism (IEFPCM) was used to account for solvent effects. Vertical excitation energies were computed with non-equilibrium state-specific solvation[200] (SS-PCM). Several other approaches to include the solvent effects on the excited state have been tested, among them linear response solvation (LR-PCM)[201] as well as the corrected linear response solvation (cLR-PCM) by Mennucci et al.[199] The combination of the CAM-B3LYP functional with LR and SS solvation was also applied by Weigel et al. for a similar system.[304]
In order to investigate the possible influences of solvent reorganization, the relaxed scan in the excited state was performed using equilibrium linear response solvation (LR-PCM). State-specific solvation could not be used since analytic excited-state gradients are not available for this method.[305] However, it was shown recently that performing geometry optimizations in the excited state using the B3LYP functional in conjunction with linear response solvation combined with single-point calculations using CAM-B3LYP and equilibrium state-specific solvation yields a favorable error cancellation.[305] Hence the excited state-optimizations were also performed with B3LYP.
In order to reproduce fluorescence conditions, the ground state was calculated in the excited-state geometry with the solvation shell of the excited state as well as with an optimized solvent.
For the frequency calculations, the transition-state geometry obtained from the relaxed scan was optimized for the S_1 state in the gas phase. Unless stated otherwise, all calculations used the cc-pVDZ basis sets.[302]

5.1.2 Benchmark Calculations

The challenging properties of the system demand extensive benchmark calculations. SCS-ADC(2) is able to describe the changing amount of CT and neutral character of the first excited state accurately, but cannot be combined with a reasonable treatment of the environment for a system of this size due to its computational cost. TDDFT is the obvious choice for larger systems, but the correct functional has to be found. Due to the expected amount of charge-transfer character CAM-B3LYP might be appropriate, but

this has to be checked. Since it is well-known that the excited states of cyanines are difficult to compute accurately,[306] it is likely that the MCs pose similar problems. Hence as a first step different functionals are benchmarked against the results from SCS-ADC(2) in the gas phase and the experimental data. It is assumed that a functional that describes the system in the gas phase correctly will also make the right predictions concerning the solvent effects in acetonitrile. The different methods to include the solvent are investigated in a second step.

At first the energies and the oscillator strengths of the lowest bright excited state of TTC and TTT were computed with various methods (see Figure 5.7), since the experimental results suggest that the isomerization involves the S_1. The gas-phase SCS-ADC(2) results show an excellent agreement with the experiment values, although the latter have been obtained in solution (acetonitrile). This can either be attributed to error cancellation or to a very small solvent effect. Using the two-state model, the second assumption implies that the system is rather close to the cyanine limit. Indeed including the effect of the solvent on the excitation via LR-PCM changes the excitation energy by only 0.07 eV for TTC and 0.03 eV for TTT.

While HFB[307] and BLYP[60,61] show the closest absolute numerical agreement with the experiment for the vertical excitation energies of TTC and TTT, the difference between the two isomers is not well reproduced (Fig. 5.7). B3LYP, CAM-B3LYP and ωB97XD overestimate the excitation energies, but the relative energies as well as the oscillator strengths are well described. This overestimation is well-known for cyanine dyes.[306] It is also evident from the results that the cc-pVDZ basis is sufficiently converged. It should be noted that in order to gain insight into the photochemical isomerization, the relative energies and oscillator strengths of the two isomers are of significantly higher importance than the absolute values. As can be expected TDHF significantly overestimates the excitation energies.

In order to see if all methods predict the correct ordering of the lowest excited states, the first two excited states of TTT computed with different DFT functionals and TDHF are depicted in Figure 5.8. CAM-B3LYP predicts, in agreement with SCS-ADC(2), the S_1 to be the bright state, while it is the second excited state with the pure DFT functionals. Using B3LYP the two states are almost degenerate. TDHF also shows the correct ordering, but, as pointed out above, overestimates the excitation energy significantly. By inspecting the leading configurations, the bright state can be identified as a π-π^* excitation, while the dark state is dominated by an n-π^* excitation originating from the lone pair on the phenolate oxygen and thus exhibits charge-transfer (CT) character. This explains the

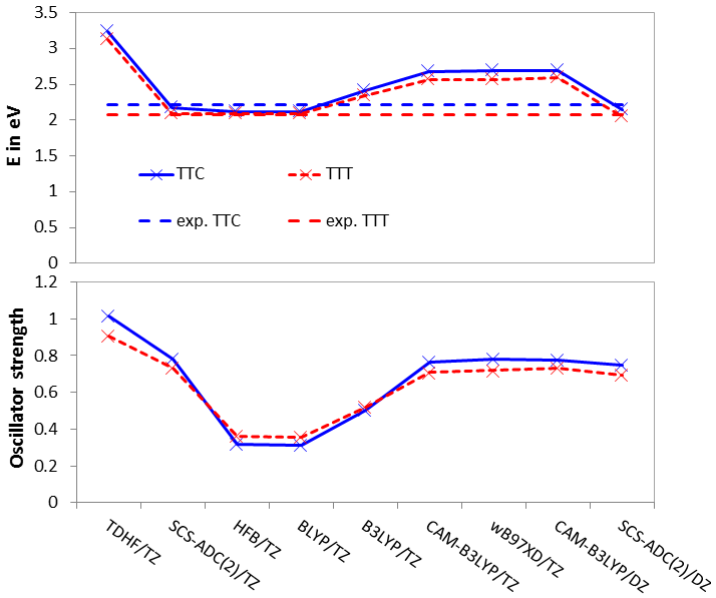

Figure 5.7: Computed vertical excitation energies and oscillator strengths (gas phase) of the lowest bright excited state for TTC and TTT with different methods (DZ ≡ cc-pVDZ, TZ ≡ cc-pVTZ). *Reproduced with kind permission from AIP Publishing.*

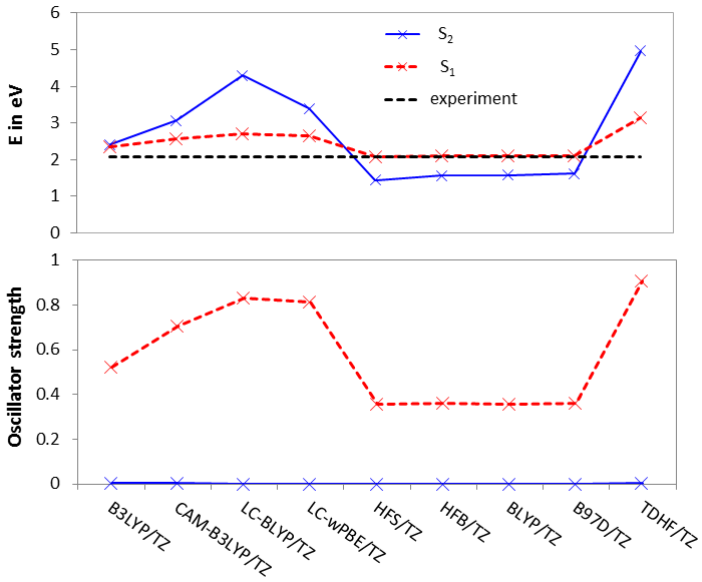

Figure 5.8: Computed vertical excitation energies and oscillator strengths (gas phase) for the first two excited states of TTT with different methods (TZ ≡ cc-pVTZ) and the experimental excitation energy of the bright state. *Reproduced with kind permission from AIP Publishing.*

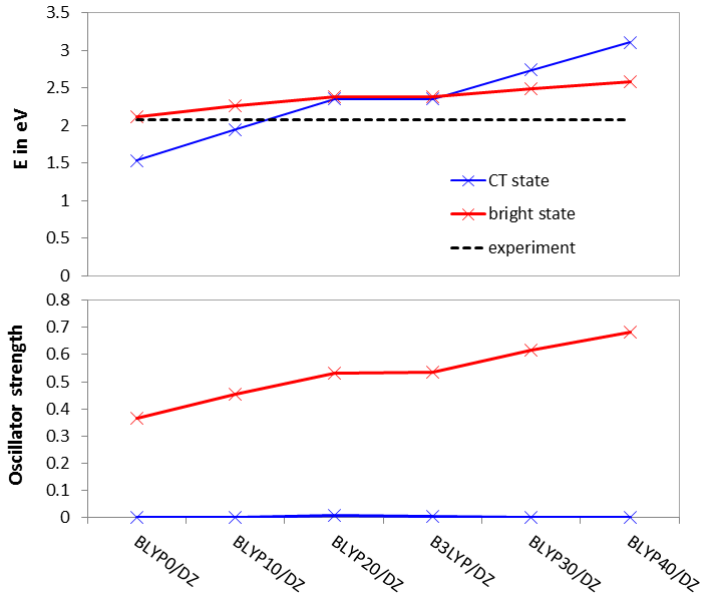

Figure 5.9: Computed vertical excitation energies and oscillator strengths for the first two excited states of TTT using functionals with different amount of exact exchange. Results for the standard B3LYP functional are also given for comparison (DZ ≡ cc-pVDZ), as well as the experimental excitation energy of the bright state. *Reproduced with kind permission from AIP Publishing.*

wrong ordering observed with the pure functionals, since they underestimate the excitation energy of CT states, as explained above. As can be expected, the underestimation is less pronounced for the hybrid functional B3LYP and even less so for the long-range corrected functionals.

The inclusion of exact exchange yields the correct order of the states, but also increases the excitation energy of the bright state. This is demonstrated in Figure 5.9 by increasing the amount of Hartree Fock exchange via a one-parameter functional

$$AE_X^{HF} + (1-A)\left(E_X^{Slater} + \Delta E_X^{non-local}\right) + \Delta E_C^{local} + \Delta E_C^{non-local} \tag{5.14}$$

using the Becke exchange[307] and the LYP[61] correlation functionals similar to the approach of Renz et al.[308] The functional with A % of exact exchange is called BLYPA. The lower the amount of HF exchange, the better the numerical agreement of the bright state with the experiment. However a significant amount of exact exchange is needed for the correct ordering of the states. Of all functionals included in the investigation, CAM-B3LYP gives the best compromise between the quantitative agreement and the correct ordering

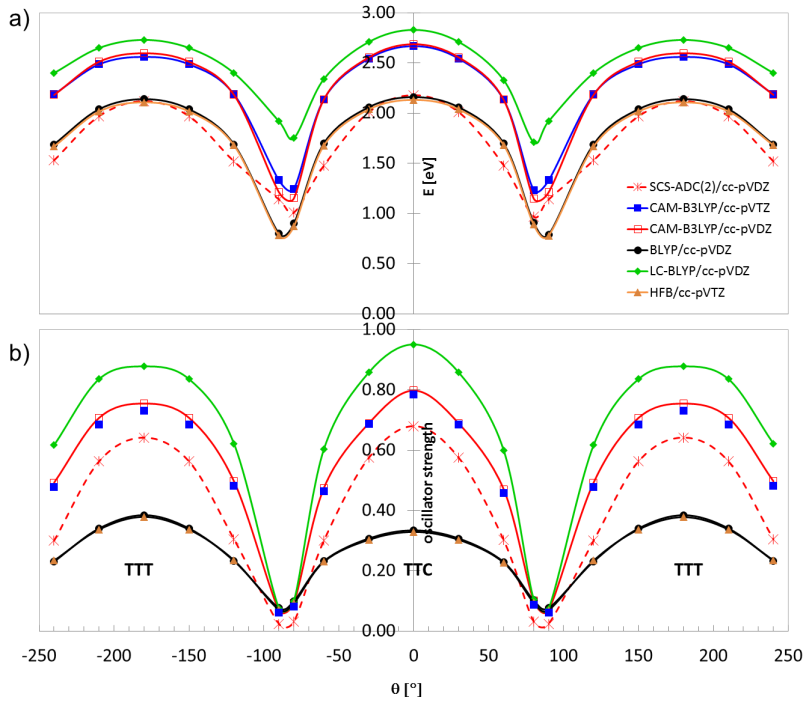

Figure 5.10: Computed vertical excitation energies (a) and oscillator strengths (b) of the first bright state for several points of the reaction coordinate with different methods. Geometries are obtained form the relaxed scan in the ground state (B3LYP/cc-pVDZ with IEFPCM). *Reproduced with kind permission from AIP Publishing.*

of the states. The fact that pure functionals provide the best numerical agreement for the absolute excitation energies is probably due to an extensive error compensation.
Using only the vertical excitation energies in the benchmark is not sufficient. The fact that a functional provides a good description at this point of the potential energy surface does not imply that this is also true for the rest of the surface. The minimal requirement for the investigation of a photochemical reaction would be that absorption and fluorescence are reproduced correctly. Since in this case the wave packet dynamic along the reaction coordinate θ is of interest, the benchmark was extended to a number of points along this coordinate. Therefore, vertical excitation energies and oscillator strengths were computed with different functionals at several points obtained from the relaxed scan in the ground state and compared to SCS-ADC(2). The results are depicted in Figure 5.10. Contrary to CAM-B3LYP, the pure functionals without long-range corrections predict a qualitatively wrong behavior of the excitation energy around the twisted geometry. The lowest excitation energy is obtained at 90° instead of 80°. Although CAM-B3LYP over-

estimates the excitation energy at the ground-state geometry more strongly than at the twisted geometry, it gives a qualitatively correct description of the shape of the potential energy curve. The cc-pVDZ basis is sufficiently converged at all points along the surface. In view of these results, the CAM-B3LYP functional was used for all further computations, although LC-BLYP also provides a good description and might also be considered for the description of merocyanine dyes.
Previous benchmark calculations[309] for related cyanine dyes came to the conclusion that the one-parameter HFB functional yields the best numerical agreement with the experiment. The investigation was focused on the vertical excitation energy of the bright state. Indeed this finding can be confirmed. However, if one takes the qualitative agreement for the complete energy profile and the position of the dark state into account, the CAM-B3LYP functional yields more reliable results.

The influence of the solvation on the vertical excitation energies was negligible. However, this fact should not lead to the conclusion that solvent effects are unimportant for the isomerization. The two-state model suggests that the solvent effect may be varying along the reaction coordinate θ, hence a reliable estimation of its influence on the shapes of the PESs of ground and excited state is crucial. This turned out to be very challenging because different approaches give very different predictions. In Figure 5.11 the results using linear response (LR-PCM),[201] state-specific solvation[200] in two variants and the corrected linear response (cLR-PCM) approach[199] are depicted.
As explained above, in the case of state-specific solvation in conjunction with TDDFT, a series of iterative TDDFT calculations is performed, where the solvent is adapted to the excited-state density. In this process the solvent is, however, also changed for the ground state. After having reached convergence, the effect of the ground-state solvation is subtracted via correction terms. In this study the excitation energies from the last TDDFT iteration (uc-SS-PCM), which are uncorrected for the effects on the ground state, as well as the final corrected ones (c-SS-PCM) are used (see below).
Figure 5.11a shows the situation for vertical absorption (ground-state structure, non-equilibrium conditions, i.e. adaption of the electronic polarization of the solvent), while Fig. 5.11b depicts the fluorescence conditions (excited state geometries, equilibrium conditions, i.e. full relaxation of the solvent). In order to illustrate the magnitude of the solvent effects, Fig. 5.11a also contains the gas phase curves. For both absorption and fluorescence conditions (5.11a, b), the solvent effects are almost negligible for the planar structures ($\theta = 0, \pm 180°$), but very pronounced for the twisted geometries ($\theta \approx 90°$),

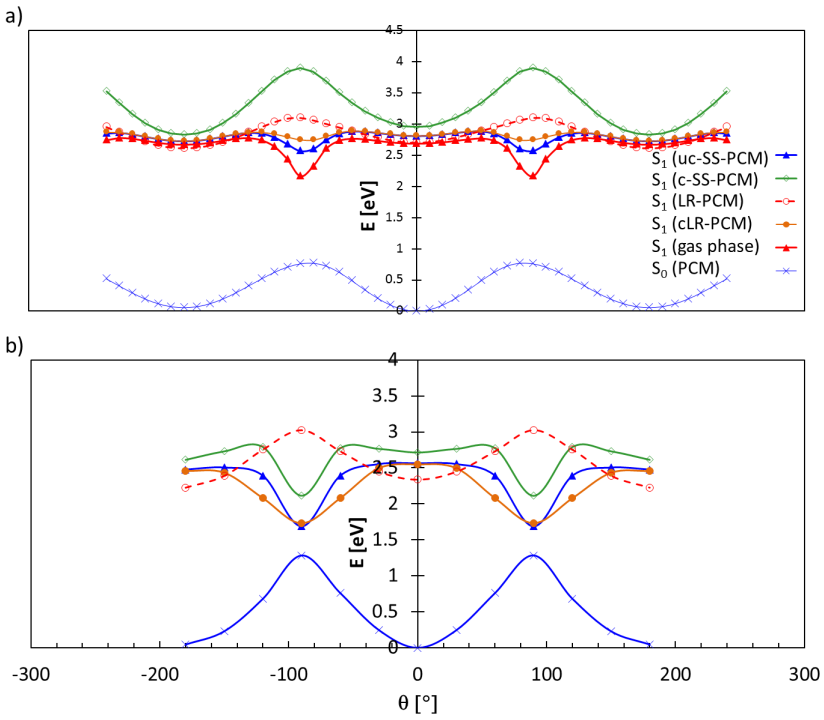

Figure 5.11: PES of S_0 and S_1 using (a) vertical conditions , i.e. ground-state geometries and non-equilibirum solvation and (b) fluorescence conditions, i.e. excited-state geometries and equilibrium solvation with different solvation methods. The ground state in (b) was calculated with the solvation shell of the excited state. *Reproduced with kind permission from AIP Publishing.*

where the rings are almost orthogonal. This is caused by the change of the weights of the two resonance structures, along the reaction coordinate. In the minimum ground-state geometry, both resonance structures are of similar importance (i.e. the MC is close to the cyanine limit), as can be deduced from the bond-length alternation pattern. Since the same is true for the S_1 state, only a minor change in character will occur upon excitation and thus only an insignificant solvatochromic shift is expected. At the transition state, however, the ground state is more or less purely zwitterionic, since the π-system is disrupted due to the orthogonality of the rings. Thus according to the two-state model, the excited state is approximately purely neutral.

For the absorption at the twisted geometry (Fig. 5.11a) a destabilization of the excited state in comparison to the gas phase can be expected, because the solvent is mainly adapted to the ionic ground state and only the fast degrees of freedom of the solvent are adapted to the neutral excited state. For the fluorescence situation (Fig. 5.11b), the opposite should be true.

Indeed, for the absorption situation (non-equilibrium solvation), all methods predict a destabilization of the excited state. However, they strongly differ in the predicted magnitude of the effects. The LR-PCM solvation scheme predicts a slight barrier in the S_1 for twisted geometries. But based on a recent paper by Pedone[305] and the work of Mennucci et al.,[199] it can be assumed to overestimate the destabilization of the solvent.
The standard SS-PCM approach (c-SS-PCM, green curve) predicts an even larger effect for this situation. Both approaches, especially the c-SS-PCM, contradict the experimental results, because such high barriers are not in line with the fast photoisomerization. The failure of the standard SS-approach seems to result from the correction terms added after the iterative TDDFT treatment,[200] because if they are neglected (uc-SS-PCM), only a moderate destabilization is predicted. Since only the dynamic part of the solvent is adapted, the effect on the ground state should be small and hence also the correction. At the planar geometry this is indeed true, with the size of the correction being around 0.1 eV. At the twisted geometry, however, the corrections are around 1 eV, which is unphysically large. In fact, it is known that the SS-PCM approach in conjunction with TDDFT can sometimes be unstable.[310] The corrected LR-PCM (cLR-PCM) approach by Mennucci et al. predicts a slightly larger destabilization of the S_1 state for twisted geometries, but nearly coincides with uc-SS-PCM for planar geometries. It is important to note that despite existing differences, the cLR-PCM and uc-SS-PCM agree in all important aspects. Both predict small barriers for the isomerization along the reaction coordinate at about $\theta = \pm 50°$and $\pm\, 130°$ and shallow minima on the S_1 surface for twisted geometries. They furthermore compute that the minima of the S_1 and the maxima of the ground state are slightly displaced. The cLR-approach was recently also successfully applied for the solvent effects on the excited states of cyanine dyes.[311] Keeping in mind that the correction terms should be small, it is not surprising that the uc-SS-PCM gives results of similar accuracy as cLR-PCM.
As discussed above, the vertical excitation energy is overestimated by the CAM-B3LYP functional calculations, but the energy difference between the two isomers is reproduced accurately. Including the solvation does not change this picture. For instance, the uc-SS-PCM calculation yields (experimental values are given in parentheses): TTC 2.81 (2.23) eV, TTT 2.67 (2.10) eV.[270,295]
In the case of fluorescence conditions (Fig. 5.11b), uc-SS-PCM, c-SS-PCM, and cLR-PCM agree in some aspects, but they also show differences. However, the uc-SS-PCM and cLR-PCM are in accord for all main aspects. Both predict that the S_1 PES possesses no barriers around $\theta = 0°$. Both also concur that the shape of the PES around $\theta = \pm 180°$

differs slightly from its behavior around $\theta = \pm 0°$. In contrast, the standard c-SS-PCM approach predicts that $\theta = \pm 180°$ as well as $\theta = 0°$ represent shallow minima with respect to the reaction coordinate. It is interesting to note that the difference between uc-SS-PCM and c-SS-PCM is much smaller than in the non-equilibrium case, despite the fact that the assumption of small correction terms is now less accurate. In the equilibrium case the total solvent contribution is adapted, which should have a larger effect on the ground state and hence the correction terms. Thus one might rather assume a larger difference instead of a smaller one. This also confirms that the huge values of the correction terms in the non-equilibrium case are unphysical and are probably caused by an instability of the method. The problem seems to be absent for equilibrium conditions.
The methods uc-SS-PCM, c-SS-PCM, and cLR all predict that the S_1 surface possesses deep minima for twisted geometries. The LR approach, however, predicts a completely different shape and hence seems to be inappropriate. The failure of the LR-PCM approach can be explained with the low oscillator strength at the twisted geometries (see below), since (as stated above) the solvent contribution to the excited state depends on the transition dipole moment in the LR approach.[198] This can lead to an artificial lack of stabilization for dark states.
Similar to the absorption, the fluorescence energy is also overestimated, but the small Stokes shift is well reproduced on the cLR- as well as the uc-SS-PCM level (experimental values again in parentheses): TTC 2.56 (2.01) eV, TTT 2.44 (1.96) eV. For the calculation of the fluorescence energy, the difference of the energy of the points with $\theta = 0, \pm 180°$ of the uc-SS-PCM excited-state curve in Fig. 5.11b and the corresponding ground state has been used.

5.1.3 Results and Discussion

The potential energy surfaces in Fig. 5.11a and b, which use the geometries from the relaxed scan in S_0 and S_1, respectively, represent two extreme cases - the absorption and fluorescence conditions. These surfaces can be used to understand the photochemical and -physical behavior of the system.
The corresponding oscillator strengths, which are given in Figure 5.12, provide a good starting point. It can be inferred that fluorescence is only efficient from either the vicinity of 0° or 180°, but not from the minima of the excited state above the transition states of the S_0, since the oscillator strength is zero at these points. The transition dipole moment vanishes due to the corresponding orbitals localizing on the orthogonal rings, thus

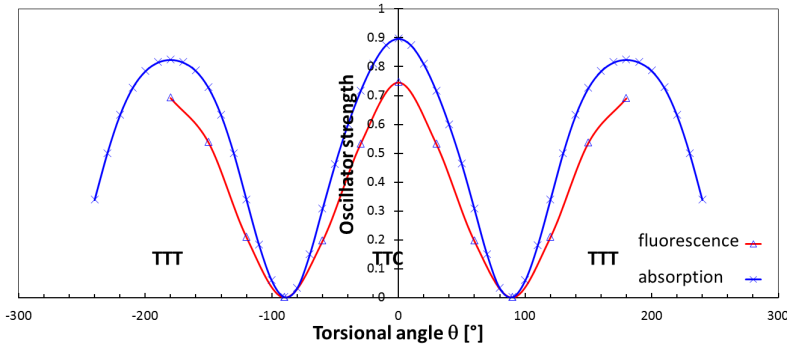

Figure 5.12: Oscillator strength for absorption and fluorescence conditions. *Reproduced with kind permission from AIP Publishing.*

reaching a non-emissive twisted intramolecular charge-transfer (TICT) state.[305] Since the PES of the ground and excited state are rather close in energy at the transition state, a non-radiative decay into S_0 might be possible (see Fig. 5.11a and b). However, a significant amount of radiationless decay would not be in line with the experimental results.[295] Thus a wave packet starting at the Franck-Condon region of TTC can either fluoresce to the ground state directly, or isomerize to TTT and fluoresce there.

The reason why this reaction is possible, but not the inverse reaction is connected to the barriers along the reaction path. The energy of the Franck-Condon region of TTC is also slightly higher than the one of TTT, which is in favor for the observed direction, but probably not sufficient for an explanation. Thus one needs to inspect the shape of the potential energy surface. The two extreme cases shown in Figure 5.11 constitute two cuts through the multidimensional surface on which the wave-packet dynamic occurs. This allows the development of a two-dimensional model in which all relaxation effects on the S_1 state (intramolecular, solvent relaxation) are combined into one effective mode, which is orthogonal to the reaction coordinate θ. One way to define and quantify this mode is the root mean square deviation for each rotational angle between the relaxed geometries of ground and excited state. Assuming a harmonic behavior of this effective mode, it is possible to analytically connect the curves for absorption and fluorescence conditions in Fig. 5.11 via parabolas, thus generating a two-dimensional PES (see Figure 5.13). For the PES in the ground state, ground-state solvation was applied for both cuts. The intersecting plane in Fig. 5.13 represents the situation before and directly after the excitation of TTC.

The time evolution of the system after photoexcitation can be understood using this model. Comparing the two surfaces in Figure 5.13 again shows that uc-SS-PCM and

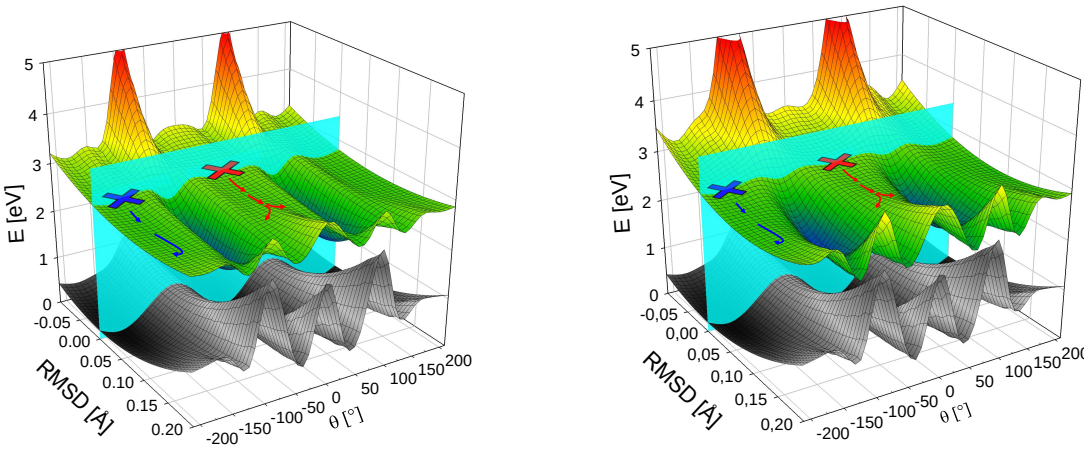

Figure 5.13: PES of S_0 and S_1, using a harmonic approximation for the effective mode orthogonal to the reaction coordinate. The intersecting plane at RMSD = 0 Å represents the points with optimized ground-state geometries, the red cross marks the Franck-Condon region of TTC and the arrows indicate the presumed wave-packet dynamic schematically. The blue cross and the blue arrows indicate the dynamic after excitation of TTT. The PES is plotted with the uc-SS-PCM results (left) and cLR-PCM (right). *Reproduced with kind permission from AIP Publishing.*

cLR-PCM give very similar results. Both surfaces allow the same interpretation of the dynamic in the excited state: After vertical excitation of TTC (red cross), the wave packet is initially accelerated perpendicular to the reaction coordinate θ, due to the small barrier in the direction of θ. During this motion, the wave packet obtains an increasing momentum in the direction of TTT, since the barrier vanishes and a gradient in this direction emerges. In order to reach the TTT-region the wave packet has to cross a "valley" in the PES. However, due to the vanishing transition dipole moment the system cannot decay radiatively to the ground state in this valley. Taking further into account that the measured time scale of 200 fs is too fast for an efficient energy dissipation, the wave packet can easily reach the TTT configuration in the S_1. Since no barrier has to be surmounted along this path, it is in line with the observed time scale.
After vertical excitation of TTT (blue cross), the wave packet is also accelerated perpendicular to the reaction coordinate, but the situation is different, since no gradient towards TTC exists. Hence, the wave packet is predicted to oscillate several times along the effective mode (blue arrows). Due to the high oscillator strength along the path of the blue arrows, fluorescence to the ground state of TTT is likely. Therefore the photoreaction will only occur to a minor extent.
Thus the shape of the PES explains the direction of the reaction. The fact that fluorescence can only occur in the region of $\theta = 0, \pm 180°$ also explains the small Stokes shift, since the energetic difference between the Franck-Condon region and the relaxed excited state geometry is rather small for these regions.
Although no fluorescence can occur from the valley in the S_1, as stated above, one might argue that a radiationless decay should be possible. Indeed the potential energy surfaces of ground and excited state become energetically very close (see Figure 5.11) and due to the depth of the valley, the wave packet should be vibrationally hot. Thus using our data there is no evidence against an efficient radiationless decay to the ground state that corroborates the experimental finding.[i] However, the displacement between the minima of the excited state and the maxima of the ground state (see Figure 5.10) suggests that the wave packet would end up in TTT anyway. Hence, if a trajectory anyhow moves towards TTC and crosses to the ground-state surface, it will not change the yield of TTT.
Using the surface calculated with the standard SS-PCM approach (c-SS-PCM), the experimentally observed photoreaction (TTC $\rightarrow$ TTT) cannot be explained. The significant barrier in the S_1 can be expected to hinder the reaction. Thus no reaction TTC $\rightarrow$ TTT

[i] Of course in order to actually estimate the efficiency of the raditionless decay a calculation of the coupling matrix elements is necessary.

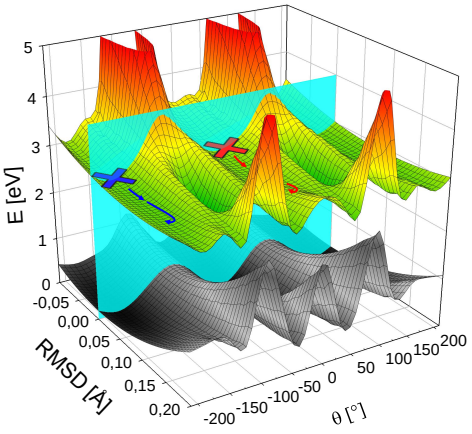

Figure 5.14: PES of S_0 and S_1, using a harmonic approximation for the effective mode orthogonal to the reaction coordinate. The intersecting plane at RMSD = 0 Å represents the points with optimized ground-state geometries, the red cross marks the Franck-Condon region of TTC and the arrows indicate the presumed wave-packet dynamics schematically. The blue cross and the blue arrows indicate the dynamics after excitation of TTT. The PES is plotted with the c-SS-PCM results. *Reproduced with kind permission from AIP Publishing.*

reaction is predicted.

The transients observed in the experiments show significant oscillations, which result from two low frequency modes. These stem from the oscillations of the wave packet on the multidimensional surface. A calculation of the normal modes in the twisted excited-state geometry revealed several modes in the experimentally observed wavenumber region. Thus a criterion, which of these are likely to become excited, is needed. The trajectory from TTC to TTT runs through the minimum of the S_1 surface, where the π-system is disrupted. This leads to a significant change of the electronic structure of the system and hence also a lot of geometric changes orthogonal to the reaction coordinate are induced. These geometric changes between the Franck-Condon region and the twisted excited-state minimum were analyzed by Stefan Rützel. He found that the corresponding vibrations should mainly possess torsional character (as had been expected), but will also contain a considerable amount of C–C stretching. These contributions arise because the disruption of the π-system leads to a significant elongation of the C–C bond at the twisted geometry ($\theta = 90°$) for the ground and excited state. Hence the bond stretching should be dominated by the C–C stretch of bond 3 in Fig 5.4 around which the isomerization is

observed.

The experimentally observed frequencies in addition to this geometric criterion can be used to identify the most probable vibrations. Assuming that the more the C–C-stretching contributes to a certain mode, the more likely this mode gets excited in the course of the isomerization, Stefan Rützel could identify two calculated modes, that also fit to the experimental values nicely.[270] The first one has a wavenumber of 185 cm^{-1} (experiment: 170 cm^{-1}) and also involves a strong tilting of the benzene ring. Therefore, it is reasonable that it is involved in the isomerization reaction. The second mode at 360 cm^{-1} almost coincides with the calculated normal mode at 362 cm^{-1}.

It is interesting to note that the present model is similar to the one devised for the 11-*cis* isomer of the retinal protonated Schiff base (PSB11) system.[312] The corresponding reaction path computations also indicate that the main isomerization reaction is overlayed by a skeletal stretching motion. Similar to the model presented here, this motion is induced by the relaxation of the system from the Franck-Condon region. In the case of retinal, however, a conical intersection is predicted. Figure 5.11 might suggest the presence of a conical intersection (CI) around $\theta = 90°$, but the molecular orbitals and the coefficients of the leading configurations show no indication for it. This is in contrast to a recent theoretical study of a related system.[313] The absence of a conical intersection is, however, in line with the experimentally observed time scale for the relaxation to the ground state. Of course, one has to keep in mind that conical intersections at other geometries cannot be excluded. Furthermore, the applicability of TDDFT for conical intersections is questionable.[47] Thus, the exclusion of a CI is mainly based on the experimental findings and can only be corroborated by the TDDFT computations.

It should be noted that the shape of the S_1 PES, on which the model is based, is rather flat. Considering the complexity of the system (variation of electronic character, strong solvent effects) in combination with the accuracy of the methods which can be employed, definitive and conclusive statements based solely on the computed values are of course difficult. However, in conjunction with the experimental results, the computed surfaces provide a reasonably accurate model, which suffciently explains and rationalizes the experimental findings.

5.1.4 Conclusions

The photochemical isomerization of the *trans-trans-cis* (TTC) to the *trans-trans-trans* (TTT) isomer of the merocyanine form of 6-nitro BIPS was studied with long-range corrected time-dependent density functional theory in conjunction with polarizable continuum models. Benchmark calculations using SCS-ADC(2) showed the applicability of the CAM-B3LYP functional. The study also contains a careful analysis of solvent effects predicted by different approaches. The results of the benchmark are also valuable for the computational characterization of the optoelectronic properties of the merocyanines in general (see next section). The theoretical results combined with the experimental findings allow a conclusive interpretation of the photochemical interconversion. The direction of the reaction can be explained using the topology of the calculated PESs, which show slight differences between the S_1 region of TTC and that of TTT. After excitation of TTC or TTT, the wave packet is accelerated perpendicular to the reaction coordinate. In the first case, however, it may partially propagate towards the other isomer, where it decays to the ground state, thus forming TTT. After excitation of TTT however, fluorescence without any isomerization is likely, thus reducing the probability of the photoreaction TTT $\rightarrow$ TTC. The acceleration perpendicular to the reaction coordinate explains the oscillations observed in the pump–probe transients. These coherent oscillations in the experimental data were assigned to the corresponding computed excited-state harmonic modes of the merocyanine. Fluorescence can occur along the cuts with $\theta = 0°$ and $\pm 180°$. The experimentally observed small Stokes shift is also corroborated by the shape of the potential energy surface.

5.2 Quantum Chemical Assessment of Merocyanines

This project was conducted in collaboration with the groups of Prof. Frank Würthner (Würzburg) and Prof. Klaus Meerholz (Cologne) and funded within the DFG priority program SPP1355 ("Elementary Processes of Organic Solar Cells"). The groups of Meerholz and Würthner have been working on the design of merocyanines for organic solar cells and transistors for several years.[273,274] Although they achieved very impressive results,[277,280] which clearly demonstrate that MCs are suitable for these applications despite their high dipolarity, a clear guideline for a rational design for the optimal merocyanine still has to be found. While some merocyanines show an excellent performance, others seem to fail completely.

The goal of this project was on the one hand to critically evaluate the experimentally applied concepts, especially the cyanine limit, with computational methods. On the other hand it was aimed at a quantum chemical characterization of different merocyanines and a comparison of the computed parameters with the experimental data measured on the molecular level (like e.g. $\tilde{c}^2$-values) as well as in the device. An emphasis of the computations was laid on the effects of the environment and aggregation. With this approach the connection between molecular (HOMO energy, VB weights, reorganization energies,...), supramolecular (couplings, diffusion constants,...) and the device properties (PCE, V_{oc},...) for the MCs should be established. Especially the effect of the crystal environment as compared to solution is of great importance. The advantage of a theoretical modeling is that the individual effects can be separated, which is often difficult to do experimentally. Furthermore, with computational methods the corresponding values are typically computed for ideal conditions. This is a drawback if one aims at a realistic modeling of a device, but it is advantageous if one is interested in the maximum performance that can principally be obtained with a certain molecule. Having identified the most important properties of an ideally suited MC, structure property relationships should be established in order to arrive at a protocol for the design of optimal MCs.
In this section an outline of the results obtained during the work on this project is presented. It includes my own calculations, but also shortly summarizes some of the results from the Bachelor thesis of Andreas Heimbeck,[289] the Diploma thesis of Anca Boariu[290] and especially the Master thesis of Charlotte Brückner.[140]
The first subsection summarizes the computational benchmarks, which were performed to ensure that the applied methodology is correct. Then the influence of the environment on the BLA and the HOMO energy is presented. The investigated MCs and their designation can be found in Figure 5.15. The choice of systems was guided by the availability of experimental data, especially X-ray structures.

5.2.1 Benchmark of Computational Methods

An extensive benchmark for the calculation of the excited states of 6-nitro BIPS and the environmental effects on them has been presented above. Another benchmark focusing on the bond length alternation of the ground state of three simple donor-bridge-acceptor model systems,

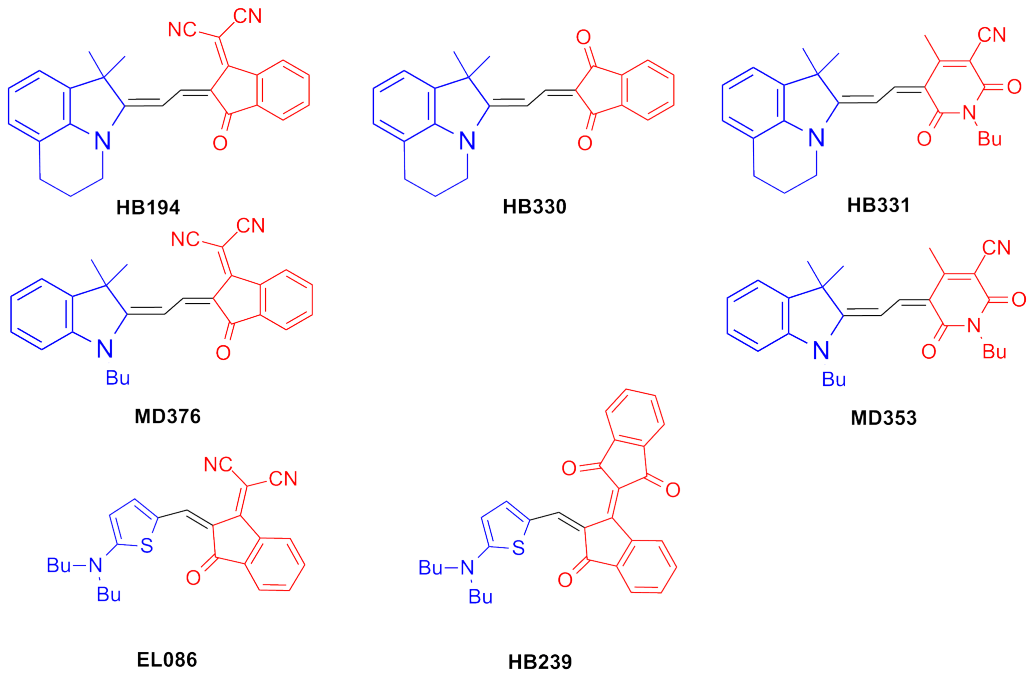

Figure 5.15: Merocyanines included in this study. The donor is given in blue, while the acceptor is depicted in red.

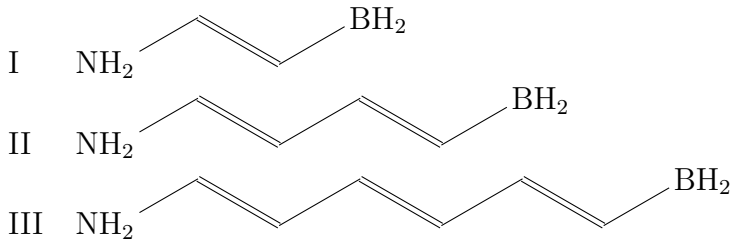

was performed using CCSD(T)/cc-pVTZ[159,314,315] as reference for system I, CCSD/cc-pVTZ for I and II and MP2/aug-cc-pVDZ for system III and included the functionals BLYP, BHLYP and B3LYP as implemented in Gaussian. The results led to the conclusion that the method dependence is not very pronounced and that B3LYP gives robust results. A benchmark against SCS-CC2 and SCS-MP2 using MD353 performed by Charlotte Brückner, which included BYLP, BHLYP, B3LYP, PBE and PBE0, also showed that B3LYP and BLYP give the most accurate results compared to the reference methods.[140] Therefore most of the calculations use the B3LYP functional.

5.2.2 Environmental Effects on the Merocyanines

Due to the high sensitivity of the MCs to the environment pure gas-phase calculations are not very meaningful if a prediction of the properties in the device is intended. Thus at first the effect of the environment has to be investigated. The influence on the excited states has already been reported above. This section deals with the environmental influence on the BLA and the HOMO energy. The latter is important, since it is supposed to be connected to the open-circuit voltage. A change in weights between the neutral and ionic resonance structure should also change the BLA, because the two resonance structures have a different bonding pattern and thus the BLA can be taken as a rough approximation for the c^2-values. Since the bond lengths in the crystal are available via X-ray spectroscopy crystallography and the bond lengths in solution can be calculated, an estimation of the effect on the crystal can be made. This also allows a discussion of the possibility to model the crystal environment with a PCM using an effective ϵ. In order to establish the connection to the measurements, a comparison between the BLA and the $\tilde{c}^2$-values is provided.

Bond Length Alternation (BLA)

In order to investigate the effect of the environment polarity on the BLA, the bond lengths of the bridge between donor and acceptor have been calculated for solvents with different ϵ. Anca Boariu performed computations on the B3LYP/cc-pVDZ level of theory with PCM for several MCs in the gas phase as well as in cyclohexane, 1-bromooctane and dichloromethane using Gaussian09.[290] The results showed that, as expected, the neutral character was decreasing with increasing ϵ. Furthermore, the higher the polarity, the higher the (qualitative) agreement with the X-ray values. However, even with the quite polar dichloromethane ($\epsilon = 8.93$) the bond lengths were not converged.
Thus calculations using an environment with larger values of ϵ were performed. In order to go to the limit of $\epsilon = \infty$ COSMO calculations using TURBOMOLE (B3LYP-D3/cc-pVDZ) have been performed together with Andreas Heimbeck. Using the COSMO approach an infinite epsilon (i.e. a conductive medium) can be used. In Figure 5.16, the bond lengths for the three bonds of the bridge for all MCs depicted in Figure 5.15 are plotted against ϵ,[i] with $\epsilon = 1$ beeing the gas-phase calculation. Bond number 1 is always

[i] Since the interaction free energy of a spherical ion inside a dielectric is proportional to $\frac{(\epsilon-1)}{\epsilon}$, which is used in the Generalized-Born models,[188] one might argue that a plot of the bond lengths against

the one closest to the donor. For HB239 and EL086 only two bond lengths could be used, while the bridge has three bonds in the other systems. The graphs in Figure 5.16 also contain the values taken from X-ray for comparison. Judging from the bond length alternation pattern, all MCs included in this study (except HB330, which is predominantly neutral even in the crystal) change from predominantly neutral to ionic at a certain value of ϵ. This is in line with the observations of Wurthner et al.[285] Hence for all MCs except for HB330, the bond length alternation pattern is predicted qualitatively wrong in the gas phase calculations as compared to the crystal, but correct if one introduces a PCM with a certain magnitude of ϵ. As can be expected HB194 and MD376 as well as HB331 and MD353 show a very similar behavior. It should be noted that the bond lengths are too large in many cases, which is at least partly connected to the size of the basis sets. Calculations using the cc-pVTZ basis sets can be found in the Bachelor thesis of Andreas Heimbeck.[289] However, the results are rather similar and as a proof of principle the calculations presented here are definitely sufficiently accurate.

Usually it is assumed that there is no sense in using higher values of ϵ then eight to ten, since the observables converge fast with increasing permittivity. This is not true for the BLA of MCs, where changes still happen at values above $\epsilon = 10$. Using values above $\epsilon = 40$, however, give reasonably converged results.

Defining a single BLA-parameter by taking the difference of the average bond length of the outer bonds and the inner one (or the difference between the two bonds lengths of the bridge in the case of HB239 and EL086) makes the comparison between the calculation and the crystal simpler (see Fig. 5.17). It is interesting to note that the value of ϵ at which the crossing from predominantly neutral to ionic occurs is (at least on this level of approximation) similar for all MCs except for HB330. Fig. 5.17 also shows that by introducing a polar environment a qualitative agreement with the crystal can be achieved. An exact numerical agreement cannot be expected. This is on the one hand due to the error of the methods and on the other hand due to the fact that the crystal environment can only approximately be modeled by a polarizable continuum. The charge distribution of the solute induces a corresponding charge distribution in the continuum, which leads to an anisotropic environment, which optimally stabilizes the solute. In the crystal, however, the surrounding charge distribution is largely defined by the neighboring molecules and

$\frac{(\epsilon-1)}{\epsilon}$ might also be sensible. This is indeed true, however, it is not expected to bring any additional information that is not provided by a plot against ϵ.

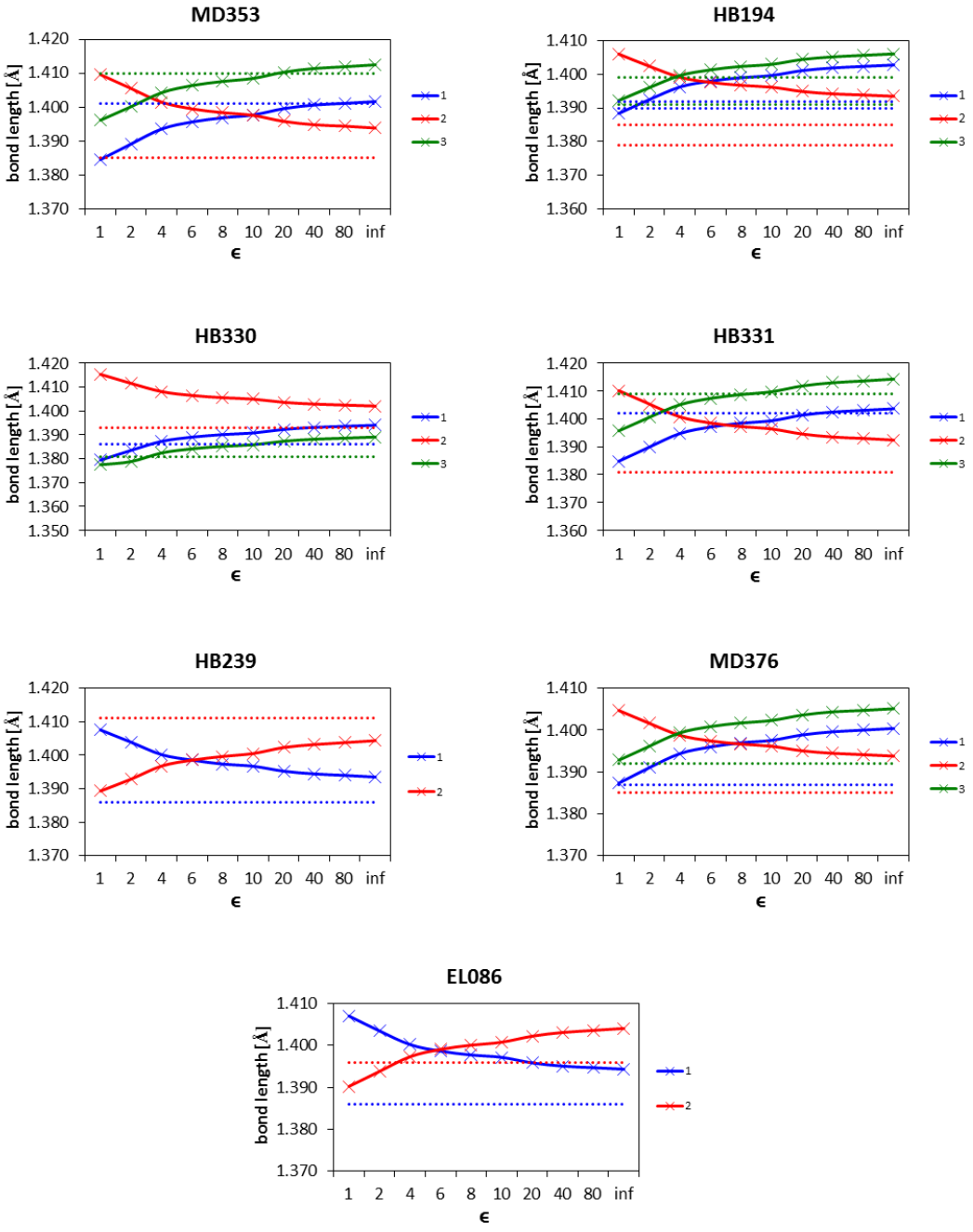

Figure 5.16: Dependence of the bond lengths of the bridge on the environment polarity (B3LYP-D3/cc-pVDZ COSMO). Bond 1 is always the one closest to the donor. The dashed lines represent the bond lengths in the crystal as obtained by X-ray spectroscopy. For HB194 there are two distinct monomers in the unit cell and hence two X-ray values are depicted. X-ray data was provided by the group of Frank Würthner.

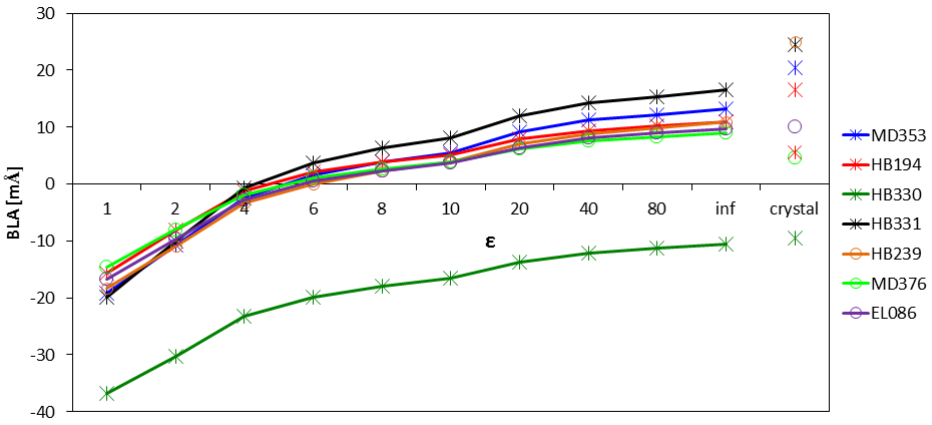

Figure 5.17: Dependence of the BLA (defined as the difference of the average bond length of the outer bonds and the inner one $BLA = \frac{BL_1+BL_3}{2} - BL_2$, with BL_1, BL_2 and BL_3 being th bond lengths of the bridge in Fig. 5.15 starting at the donor.) on the polarity of the environment (B3LYP-D3/cc-pVDZ COSMO). For comparison the BLA of the crystal is also given. For HB194 there are two distinct monomers in the unit cell and hence two X-ray values are depicted.

can only partially be influenced by the polarization due to the solute charges.[ii] Furthermore contrary to the PCM, where all points of the continuum are equally polarizable, the polarizability of the crystal environment is anisotropic.[iii] Computations on a dimer could provide the effect of the nearest neighbor in the crystal, which makes sense for the MCs, since they tend to form dimer structures in the crystal. These calculations have also been performed by Andreas Heimbeck, but turned out to be computationally very demanding.[289] Retaining the monomer as a model system and still introducing the atomistic nature of the surrounding charge distribution is for instance possible using a QM/MM approach with an electrostatic or even better a polarizable embedding. The latter also takes polarization effects into account. QM/MM calculations, however, demand

[ii] However since the molecules in the crystal usually adopt a stacking mode, which leads to the most favorable interaction between the molecules and since the interaction is dominated by electrostatics, the approximation of an optimal surrounding charge distribution has some justification.

[iii] It should be noted that even if the environment could be neglected and the computational method were exact (e.g. by using the exact functional and an infinite basis), one would not obtain a perfect agreement, since measurement and computation provide different physical quantities. While the geometry optimization yields the position of the nuclei as defined by the minimum of the potential energy surface without zero-point vibration, one measures the average of the center of electron density of the atoms with X-ray diffraction, since the X-rays are scattered by the electrons and not the nuclei.[212]

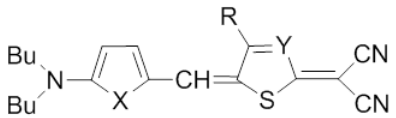

	1	2	3
X	S	S	O
Y	CH	N	N
R	H	Me	Me

Figure 5.18: The three merocyanines used in reference.[285]

a sensible choice of parameters and a careful calibration and are hence not suited for a quick prescreening of possible MCs. A first approximation for the environment of the crystal would be to use a PCM with an effective ϵ, i.e. the complex effect of the crystal environment is folded into one parameter. As a criterion for the correct value of ϵ the BLA can be used. While for most of the MCs $\epsilon = \infty$ provides the best agreement with the crystal, this not the case for all systems. A value between 10 and 20 should be used for MD376, while for HB194 it depends on which monomer of the unit cell is used. A value above 8 provides at least qualitative correct description for all systems. Hence any calculation that is aimed at making a statement about the device should use $\epsilon > 8$.

The computed BLA as well as the measured $\tilde{c}^2$ are taken as a measure of the weights of the two dominating resonance structures but both rely on heavy approximations. Thus the question arises whether the two quantities provide the same picture. In order to resolve this question, the three merocyanines that were investigated in different solvents by Würthner et al.[285] (see Figure 5.18), and for which $\tilde{c}^2$-values are consequently available were computed on the B3LYP/cc-pVDZ level of theory using COSMO by Andreas Heimbeck.[289] In order make the comparison to the experimental values clearer, a c^2-value derived from the BLA [iv] was defined as the difference between the two bond lengths of the bridge plus 0.5,

$$c^2(BLA) = BL_2 - BL_1 + 0.5, \tag{5.15}$$

thus yielding $c^2(BLA) = 0.5$ for equal bond lengths (i.e. the cyanine limit). In Fig. 5.19 the $\tilde{c}^2$-values obtained from spectroscopy (see reference[285]) are plotted against the ones defined by the BLA. Taking into account the level of the introduced approximations, the correlation is surprisingly good. Thus the results indicate that the computed BLA can be

[iv] Using this definition a difference of 0.5 Å between the bond lengths is needed to reach the limits of $c^2 = 0$ and $c^2 = 1$, which is arbitrary. However, since the focus is on the correlation between the two types of c^2-values this poses no problem.

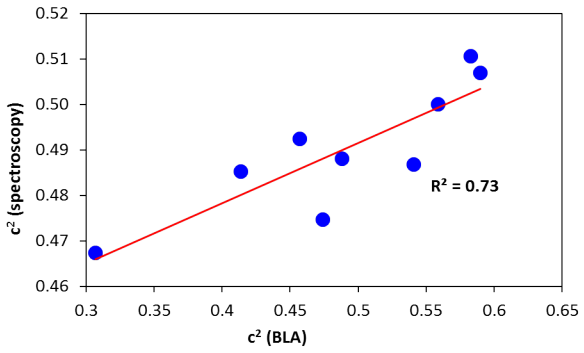

Figure 5.19: Plot of $\tilde{c}^2$-values obtained from spectroscopy (taken from reference[285]) against the ones calculated from the BLA. The linear regression is given in red.

used as a rough estimate of the $\tilde{c}^2$-value.
For the measurements, solvents in a polarity range from methylcyclohexane ($\epsilon = 2.06$) to dichloromethane ($\epsilon = 8.93$) were used. The range of solvents is limited by the solubility of the MCs. However, it is evident from Figures 5.16 and 5.17 that the crystal has a different influence than a continuum approach with a corresponding ϵ value in this polarity range. Since the difference in the BLA between typical solvents and the crystal is different for different MCs no universal rule for the extrapolation from solution data can be given. However, as a rough guideline, the following hypothesis can be proposed:

- The c^2 is typically larger in the crystal than in solution and hence MCs that are below the cyanine limit in solution should be designed in order to arrive at the cyanine limit in the crystal.
- For any merocyanine a calibration of the BLA from calculations to the measured $\tilde{c}^2$-values should be approximately possible.
- If X-ray data is available the change in BLA between solution and crystal should provide an estimation for the $\tilde{c}^2$-value in the crystal.

Of course more data is needed in order to challenge these hypotheses and to corroborate (or falsify) them. However, although lots of MCs have been designed, only for very few reliable X-ray data is published or is available from the Würthner group. Using the BLA as a measure for the weight of the different resonance structures is a crude approximation, however, due to its simplicity it might be quite suitable as design criterion, since it is not worthwhile to perform very complex calculations or measurements as preselection tools.

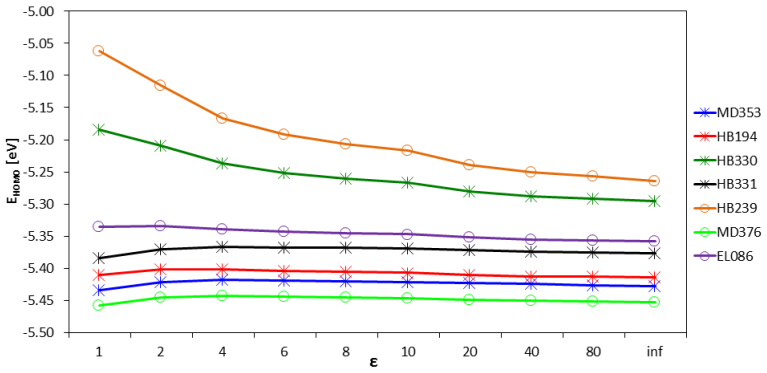

Figure 5.20: Dependence of the HOMO energy on the polarity of the environment (B3LYP-D3/cc-pVDZ COSMO).

Obviously the usefulness of this approach depends on whether the cyanine limit is a valuable criterion for the design (see below).

HOMO Energy

In the classical textbook explanation, the open-circuit voltage is directly connected to the difference between the energy of the HOMO of the donor and the LUMO of the acceptor.[3,21] However, the term "HOMO of the donor" is usually not specified explicitly. Should one use the HOMO of the molecule in the gas phase, or does one need to include the environment? Is a monomer sufficient, or is the computation of the HOMO of the crystal or a part of it necessary? Since the transition of the electron from the donor to the acceptor occurs at the interface one might also argue that the HOMO of a molecule at the interface, which experiences the electric field created by the interface dipoles,[9] might be the correct choice. These issues raise the question of the influence of aggregation and environment polarity on the HOMO energy.

The computations of the HOMO energy of several MCs as well as MC dimers taken from the crystal structure using different solvents were carried out by Anca Boariu for polarities up to $\epsilon = 8.93$.[290] Similar to the effect of the environment on the BLA, the HOMO energy was not yet converged at this polarity. The HOMO energies from the calculations presented above (B3LYP/cc-pVDZ COSMO) are depicted in Fig. 5.20. It should be noted that for the calculations of the HOMO energies the effect of the environment on the geometry as well as on the electronic structure was included, since the values were taken from the output of the geometry optimizations. Except for HB239 and HB330 the total effect of the environment is rather small. Furthermore, although the HOMO energies of several

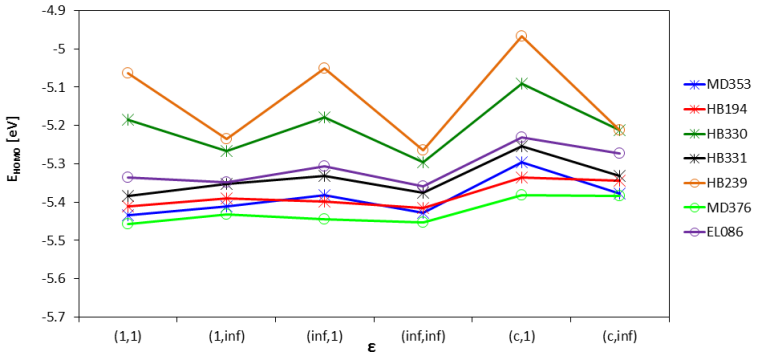

Figure 5.21: Dependence of the HOMO energy on the polarity of the environment (B3LYP-D3/cc-pVDZ COSMO) separated into contributions from the environmental effect on the geometry and the electronic structure. The first term in the brackets specifies the ϵ used in geometry optimizations (or the crystal structure, respectively), while the second one depicts the one used in the electronic structure calculation. Thus (1,inf) means that the geometry from a gas-phase calculation was used for a single-point calculation with $\epsilon = \infty$.

MCs are in the same range, the environment does not change the relative magnitude of the HOMO energies. Thus any conclusion on the relative size of the open-circuit voltage is unchanged by the environment.

Since the environment changes the geometry, especially the BLA, significantly, it is surprising that the effect on the HOMO energy is negligible for most of the MCs. In order to separate the effects on the geometry and the electronic structure, single-point calculations in the gas phase and with $\epsilon = \infty$ were performed using the structures obtained from optimizations in the gas phase and with $\epsilon = \infty$. Moreover, since the calculations concerning the BLA showed that the geometries in the crystal are still different from the ones obtained even in highly polar isotropic environments, the crystal structures were also used. The results using the cc-pVDZ basis sets are summarized in Fig. 5.21. The first term in the brackets specifies the ϵ used in the geometry optimization (or the crystal structure, c), while the second one depicts the one used in the electronic structure calculation. For HB239 and HB330 the dominating contribution on the HOMO energy seems to stem from the direct effect on the electronic structure, while the indirect environmental effect via the change in the polarity in the geometry optimization seems to be negligible. Although the BLA of HB239 changes from neutral to ionic, which is not the case for HB330, both show a very similar behavior. Using the geometry from the crystal structure leads to a

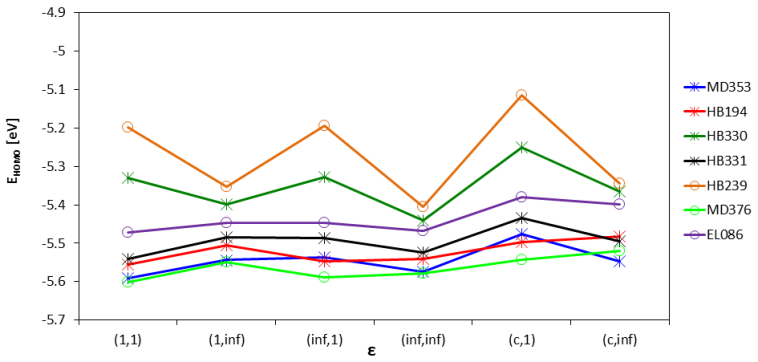

Figure 5.22: Dependence of the HOMO energy on the polarity of the environment (B3LYP-D3/cc-pVTZ COSMO) separated into contributions from the environmental effect on the geometry and the electronic structure. The first term in the brackets specifies the ϵ used in geometry optimizations (or the crystal structure, respectively), while the second one depicts the one used in the electronic structure calculation. Thus (1,inf) means that the geometry from a gas-phase calculation was used for a single-point calculation with $\epsilon = \infty$.

more significant change.

For the other MCs the effect of the geometry and the direct influence seem to be rather small and to be more canceling than enhancing each other. Going from the gas-phase to the crystal structure changes the order of the energies of HB194 and MD353 in a gas-phase calculation, but has only a small effect, when the environment is introduced in the electronic structure calculation. Again HB194 and MD376 as well as HB331 and MD353 show a very similar behavior.

Of course one might object that a basis set of double-zeta quality is insufficient to arrive at proper HOMO energies. However, additional calculations using the cc-pVTZ basis sets showed no significant change (see Figure 5.22). Hence all further calculations were performed with the smaller cc-pVDZ basis sets.

In conclusion it can be said that the effect of the environment polarity on the HOMO energy is rather small and seems to be unconnected to the change of the wave function from predominantly neutral to ionic.

A bigger effect can be expected from the aggregation, this means going beyond the monomer to a supramolecular ansatz. Anca Boariu included dimers taken form the X-ray in her studies of the HOMO energy (see[290] for details). Since the MCs tend to dimerize

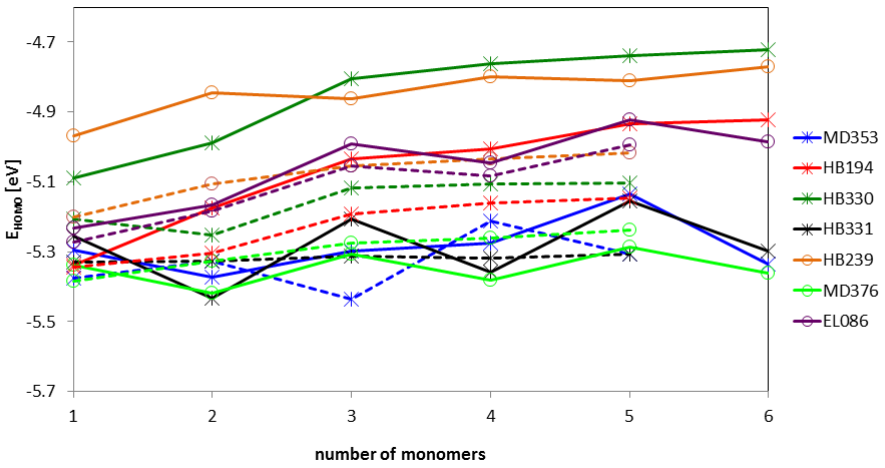

Figure 5.23: Dependence of the HOMO energy on the number of monomers in a π-stack taken from the crystal structure (B3LYP/cc-pVDZ). The dashed lines represent calculations using COSMO with $\epsilon = 50$.

a dimer is an obvious and sensible choice. However, since V_{OC} is measured in the device it cannot be excluded that the other neighbors also play an important part. Thinking in terms of FMO theory every additional monomer should lead to a splitting of the energy levels. Since the splitting is proprotional to the overlap, it should be most significant along a π-stack, since the overlap of the π-systems is bigger in the direction normal to the molecular plane.

Thus in order to investigate the effect of the aggregation π-stacks with up to six monomers were cut from the X-ray structures and used for calculations of the HOMO energy. Obviously the definition of the stack is not necessarily unambiguous, but since this sections aims at a proof of principle this poses no problems. The calculations were performed in the gas phase as well as with $\epsilon = 50$, in order to see if the PCM leads to a faster convergence with the stack size. The PCM calculations were only performed for stacks with up to five monomers for computational reasons. The results are displayed in Figure 5.23

With the dimer MOs being constructed from the ones of the monomers, one might assume that the HOMO energy of the dimer should be higher than of the monomer. However, the monomer MOs, which are used for the linear combination, are not the ones from an isolated monomer, but from the monomer in the presence of its neighbor. Due to the dipolar nature of the MCs and the formation of centrosymmetric dimers the energy levels of the monomer can be expected to be significantly lowered as compared to the gas phase,

due to the favorable electrostatic interaction. The lowering of the energy levels and the splitting are opposed effects and hence can even cancel each other. The net effect of the dimerization depends on the relative magnitude of both effects and hence on the size of the dipole moment and the MO overlap. This explains why the dimerization leads to an energy lowering for some MCs, while it raises the energy for others. Looking at Figure 5.23 it is obvious that there is no general trend for different MCs. The behavior is quite different, which is partly due to the different stacking forms. This different behavior leads to a change in the order of the HOMO energy. Furthermore there seems to be no clear convergence, even when a polarizable continuum is applied.
Thus to conclude the influence of the environment polarity on the HOMO energy is smaller than one might expect and does not necessarily affect the order of the MCs. Using the crystal structure instead of structures taken from gas-phase or COSMO calculations has a larger effect. Stacking in the crystal has also a significant influence, since it can interchanges the order of the HOMO energies of the MCs. However, no clear guideline can be presented, which stack-size might be sufficient.

5.2.3 Does a Correlation between E_{HOMO} and V_{OC} Exist?

The results of the previous section already suggest that a correlation between E_{HOMO} and V_{OC} might not be present, since the term "HOMO energy" is not really defined in a device. A further complication lies in the fact that there is no uniquely defined V_{OC} for a single MC, since it depends on the device morphology and process conditions. In collaboration with Anca Boariu experimental data received from the group of Klaus Meerholz was used to look for correlations with the calculated data. Some of the plots can be found in the diploma thesis of Anca Boariu.[290]
Before the results are discussed the question has to be addressed, whether the HOMO energy is the right quantity or if the ionization energy should be used. In exact KSDFT these two quantities are identical, while this is not the case for any approximate functionals. The HOMO energy is just an approximation for the latter. Furthermore it is not clear a priori, whether this approximation is also valid if COSMO is applied. Hence the adiabatic and vertical ionization energies have been computed (B3LYP/cc-pVDZ) in the gas phase and with $\epsilon = \infty$ using COSMO. The results are depicted in Figure 5.24. They show that the HOMO energy is a valid approximation for the ionization energy in the gas phase as well as with COSMO, at least if qualitative results are wanted.
While looking for correlations between E_{HOMO} and V_{OC}, it became apparent rather

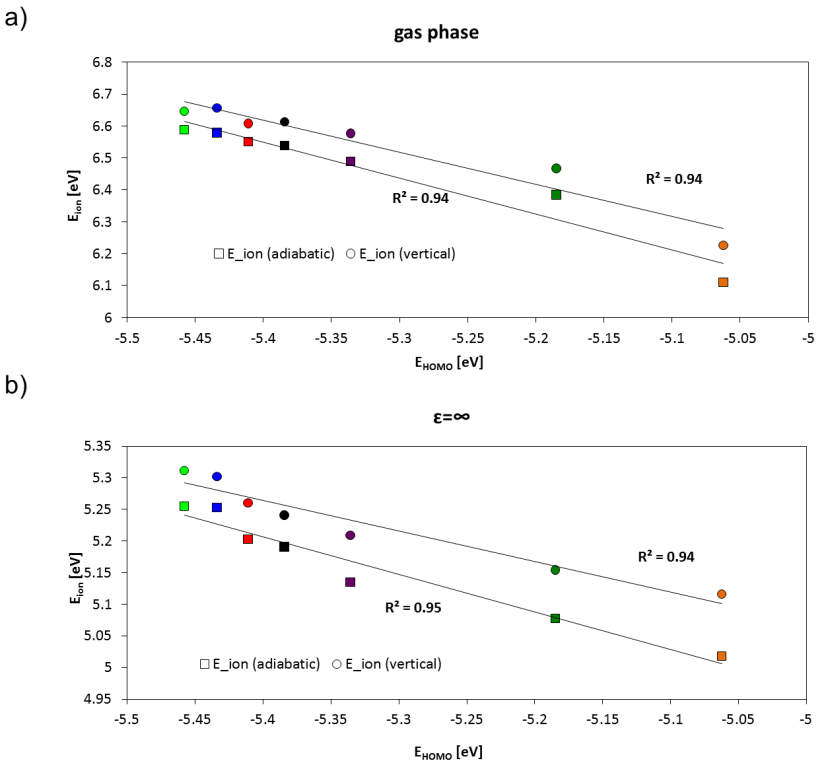

Figure 5.24: Correlation between the HOMO energy and the vertical and adiabatic ionization energy (B3LYP/cc-pVDZ) in the gas phase (a) and with $\epsilon = \infty$ using COSMO (b).

Table 5.2: R^2-value of the correlation of experimental open-circuit voltages with computed HOMO energies.

Method	R^2
(1,1)	0.85
(1,inf)	0.59
(inf,1)	0.71
(inf,inf)	0.70
(c,1)	0.68
(c,inf)	0.87

quickly that when optimized bulk heterojunction cells are used, which are typically characterized in experimental groups, no correlation can be expected. The effects due to the different morphology and the different conditions (e.g. solvents) are much bigger and hence would mask any potential correlation with the HOMO energy. Consequently, the group of Klaus Meerholz produced unoptimized (i.e. using identical process conditions) planar-heterojunction bilayer cells for five MCs. Using these data a nice correlation could be obtained, if one allows for one outlier. Since the correlation is then, however, only based on four data points, it is not statistically significant. Furthermore the group of Klaus Meerholz noticed that degradation processes might have lead to inaccurate measurements and produced encapsulated cells for four MCs. Using the open circuit voltage of these four MCs (EL086, HB331, MD353, MD376) a rough correlation can be found if the HOMO energies from the calculations in Fig. 5.21 are used. The R^2-values are depicted in table 5.2. The results show that there is some correlation, which is rather dependent on the environment, despite the small effect of the environment on the HOMO energy. By including the environment just in the electronic structure calculation the correlation coefficient changes from 0.85 to 0.59, which means that the correlation vanishes. This shows how fragile the correlation is. Furthermore due to the statistically insignificant amount of data points even the best correlation using the crystal structure and an infinite ϵ should not be overinterpreted.

As shown in the previous section, a supramolecular approach using higher oligomers might lead to different results. However, due to the unsystematic behavior of the HOMO energy on increasing the number of monomers, there is no condition to decide how to go beyond the monomer to a supramolecular approach. Due to this problems of choosing the correct zeroth-order system, one can consider to use the X-ray data and perform a calculation using periodic boundary conditions on the whole crystal. Thus the energy of the HOCO

(highest occupied crystal orbital) can be computed. Test calculations using Gaussian and the HSEH1PBE functional[316] have been performed. However, due to the size of the unit cells, converged calculations could only be obtained for few of the MCs, which makes the quest for a correlation with the open-circuit voltage impossible. Since the device is not infinite and has a clear interface, it is questionable, anyway, if the HOCO of an ideal infinite crystal has any meaning.

The results show that the connection between the HOMO energy and the open-circuit voltage is not as simple as it is suggested by the commonly used simplified scheme. Furthermore, using optimized bulk heterojunction cells the effect is completely masked. Whether a correlation is present for unoptimized bilayer cells cannot be concluded, due to insufficient experimental data. Since the cells must be produced under exactly the same conditions, one cannot simply collect data from the literature. This sensitivity of the correlation to different factors, like the process conditions or the weak influence of the environment polarity, furthermore indicates that the importance of the HOMO energy as a parameter for the suitability of an MC for organic solar cells might be overestimated. Although the rough correlation observed indeed suggests that a deeper lying HOMO should lead to a larger V_{oc}, only significant differences can be considered to be important. Small difference in the HOMO energy should hence not be overinterpreted. Therefore it does not seem sensible to put too much effort in optimizing the HOMO energy of a found target structure, since other effects are expected to be dominant.

This is in line with recent findings of Andrienko and coworkers,[317] which show that one needs to include the effect of the interface in the calculations in order to obtain optical gaps, which are meaningful. In fact the computed ionization energy at the interface is highly dependent on the interface geometry. Therefore simple measurements or calculations on the monomer can only give a rough starting point, since the device and interface morphology will change the ionization energy and hence the gap and the resulting open-circuit voltage significantly.

5.2.4 A Valence Bond Approach to the Cyanine Limit: Does a Correlation between the Cyanine Limit and the Exciton Reorganization Energy Exist?

Since the closeness of an MC to the cyanine limit and hence the measured $\tilde{c}^2$-value is one of the most important parameters for the design of new merocyanines it is of vital importance to prove if the assumed connection between the cyanine limit and the reorganization

energy really exists. Although the concept has been used for quite some time and seems to be successful, it has never been proven or been challenged theoretically. Furthermore the questions, which structural motives bring an MC close to the cyanine limit and the effect of the crystal environment, have never been elucidated computationally. Merocyanines, which are structurally rather similar can perform significantly different in the solar cell. The ideal method for this question is valence bond theory, which provides an accurate and theoretically well-grounded way of providing the weights, contrary to the BLA, which can only be considered as a rough estimation. First test calculations were performed in collaboration with Benoît Braida, which showed that an MC that is close to the cyanine limit in the gas phase can even already overshoot it when just the geometry from the crystal is used for the calculations.

The effect of the environment on the VB weights and the connection between the weights and the reorganization energy is thoroughly addressed in the master thesis of Charlotte Brückner[140] and a recent publication.[272] The weights were computed using valence bond theory (VBSCF) using block localized determinants. The definition of blocks allows to fold all possible ionic and neutral resonance structures into one determinant each.[v] Thus the VB wave functions mimics the model depicted in Figure 5.1a. Using an experimentally well-studied push-pull system based on a dithiophene unit, Charlotte Brückner showed that the applied valence bond methodology gives an excellent agreement with the measured $\tilde{c}^2$-values, although both approaches use a different ansatz (see above).

By computing the exciton reorganization energy and the weights in solvents of different polarity for systems that change from neutral to ionic in the range of the used solvents, Charlotte Brückner was indeed able to find the assumed correlation. The reorganization energy goes through a minimum, which is located roughly at the cyanine limit. Furthermore this shows that the solvent effect on the reorganization energy is definitely non-negligible. These results are the first clear indication that the main assumption on which the design of new MCs is based is valid.

The correlation is, however, only observable if the same system in different environments is used. Comparing different model systems or different MCs the effect is masked since the reorganization energy obviously depends on several factors (like the size of the system, its flexibility,...). Hence it is clear that one cannot expect a correlation using different systems.

These results confirm that the weights of the resonance structures are an important pa-

[v] Of course the choice of blocks is not unambiguous and hence extensive tests on small model systems for which full VB calculations are possible have been performed (see[140]).

rameter with respect to minimizing the exciton reorganization energy[vi] and should hence be considered when designing new MCs. Since different MCs show, however, different reorganization energies the importance of the $\tilde{c}^2$-value should also not be overestimated. Two MCs with a similar c^2-value can show quite different performances.[140]
By decomposing the different MCs into substructures, Charlotte Brückner also was able to show, which structural and environmental factors bring an MC close to the cyanine limit. This confirmed that most of the applied design strategies indeed produce MCs that can get to the cyanine limit.[140]
Sometimes it is also assumed that the charge reorganization energy is minimal at the cyanine limit although the two-state model does not give a theoretical foundation for this assumption. Indeed the results of Charlotte Brückner show that the correlation between the cyanine limit and the charge reorganization energy is less simple.[140]
Having established the connection between the cyanine limit and the exciton reorganization energy, the next question to address is the importance of the exciton reorganization energy for an organic solar cell. This is discussed in the next section.

5.2.5 Charge and Exciton Reorganization Energy and Exciton diffusion length

Considering a Marcus hopping approach for charges and excitons, the reorganization energies are important factors for the transport properties in an optoelectronic device, since they appear in the exponent of the Marcus equation.[40,41] Assuming charges and excitons are localized on a monomer, these quantities can easily be calculated. Andreas Heimbeck performed such calculations for several MCs on the (TD)B3LYP/cc-pVTZ level of theory in the gas phase as well as in solution.[289] These reorganization energies can be considered as a starting point for the classification of the transport properties of the MCs. For the results and further details see.[289]
Apart from the reorganization energies the crystal structure plays an important role for the transport, which enters the Marcus equation via the electronic couplings. Using a master-equation approach implemented by Vera Stehr[40,41] and the X-ray data, Charlotte Brückner calculated the exciton diffusion constants for several MCs.[140] These results show that the crystal structure has an important influence, since assuming an identical reorganization energy for all MCs, the diffusion constants still vary significantly. She furthermore showed that while the (for the hole-conducting merocyanines important) cationic reorga-

[vi] It is of course also of importance for an appropriate absortion behavior (see above).

nization energy varies only little between different MCs, the exciton reorganization energy shows a higher variety. In fact the variation for the charge reorganization is in the error range of the DFT methods.[140] This indicates that the exciton reorganization energy might be a more important parameter for the optimization of the transport properties than the charge reorganization energy. Nevertheless, using the computed diffusion constants leads to a different prediction of the performance of the MCs than is found experimentally. This might be due to the fact that most optoelectronic devices are constructed as thin films and it is not known if the crystal structure is a sensible approximation for the device morphology.
The experiences from the photoinduced isomerization of 6-nitro-BIPS indicate that the twist in the excited state might open the possibility for energy dissipation, thus increasing the reorganization energy dramatically. Of course the question arises if a complete twist is possible in the thin film, but also a partly twisted structure could have a massive effect. Although this isomerization is well-known in the spectroscopy community its role for exciton reorganization has so far been overlooked in the literature on optoelectronic devices. This issue is also addressed in the master thesis of Charlotte Brückner.[140] Although all studied MCs show a minimum at the twisted geometry, only for some exists a significant gradient in the Frank-Condon region (see[140] for details).

5.2.6 Excursion: Is a VB/MM approach possible?

The block-localized VB calculations including environmental effects were performed by Charlotte Brückner using a PCM approach. While this is ideally suited for calculations in solution and using an effective ϵ, one can also arrive at reasonable results for the crystal, it would be interesting to include the effect of the atomistic structure of the crystal environment. A VB/MM approach can easily be implemented, since it is based on a mechanical embedding of the structures. Therefore the interaction of the two structures has to be calculated classically and included in the Hamiltonian matrix as described above. Since the weights are included in the matrix an iterative approach has to be chosen. This is a well established ansatz, however, in block-localized determinants the charges are not clearly defined as in a standard VB calculation. In this section, an approach for a VB/MM calculations based on a block-localized VBSCF approach is suggested as a proof of principle.
As a test system for the VB/MM approach, MD376 was chosen. As a first step the results of a gas-phase VBSCF calculation are needed, which was performed by Charlotte

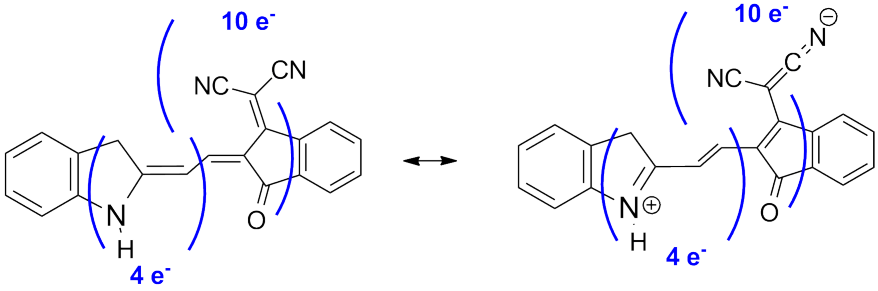

Figure 5.25: Definition of the blocks used in the gas-phase calculation by Charlotte Brückner[140]

Brückner on the VBSCF/6-31G level of theory without alkyl substituents using the blocks depicted below with a total of 14 active electrons (see Figure 5.25). The calculation was performed with Xiamen Valence Bond program XMVB.[318] The obtained weights are 0.68 and 0.32. Using matlab, a script performing the VB/MM calculation based on the gas-phase Hamiltonian matrix elements (taken from the XMVB output) was written.

If one wants to perform a VB/MM calculation based on the VB wave function depicted above the question arises on how to define the charges of the ionic and the neutral structure. In a fully localized VB calculation each atom in each resonance structure is either neutral or carries a defined charge and hence a parameterization is easy. However, due to the block-localized wave function, the charges are delocalized in each block. Therefore the ionic and the neutral structure were cut into two parts (donor and acceptor, respectively), see Figure 5.26, and the charges are calculated for the parts on the B3LYP/cc-pVDZ level of theory with the Merz-Singh-Kollman ESP fitting-scheme[221,222] as implemented in Gaussian.

Using this scheme, the only undefined part is the bridge. Simply using the standard charges for alkenes taken from a force field like OPLS-AA[214] ($\pm$0.115 e) brings two problems: a remaining net charge and a symmetrically charged bridge. Several schemes to redistribute the charges have been tested and the effect seems to be small. For a proof-of-principle calculation, these technical details are too specialized, anyway. Hence, the charges of the MM-part are simply defined by performing an ESP charge fit on the complete unconstrained monomer. Another problem arises due to the fact that the Hamiltonian matrix contains only the energy of the active electrons and thus only those "feel" the charges. This should however be a reasonable approximation.

At first the effect of a π-stack is investigated. Taking such a stack from the X-ray structure (see Figure 5.27) reveals that the distance between monomers stacked in an antiparallel

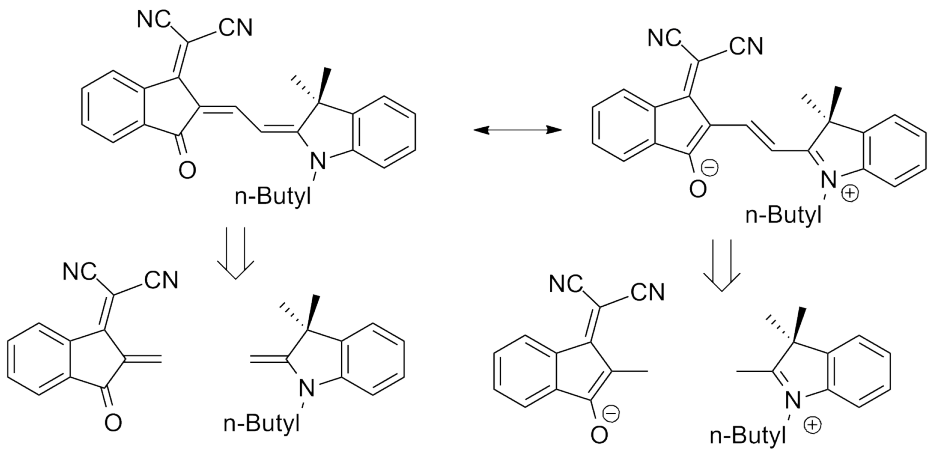

Figure 5.26: Scheme for the structures used to calculate the MM charges for the resonance structures of MD376 (right-hand side: neutral, left-hand side: ionic)

fashion is 3.38 Å, while the distance is slightly higher between these dimers (3.50 Å). The distance was calculated as the distance of the donor-N-atom from the plane formed by the 5-ring using the Hesse normal form.

The interaction energy between the QM structures and the MM-part is simply calculated as

$$E_{int} = \sum_{i}^{QM} \sum_{j}^{MM} \frac{q_{QM}(i) q_{MM}(j)}{r_{ij}} \tag{5.16}$$

The results of the VB calculations in the gas phase and with PCM (performed by Charlotte Brückner) as well as the test VB/MM computations are depicted in the table below. The numbers of the monomers in the π-stack refer to Figure 5.27 with M1 being the monomer at the bottom (red) and M6 the one at the top (purple). Two larger cuts from the crystal structure are defined in Figure 5.28. The results of the calculations are depcited in Table 5.3. The effect of the crystal is only moderate and similar to the one of the PCM with cyclohexane. Due to the high dipolar nature or the MCs one might have expected a larger effect.

The results show, however, that a VB/MM approach based on a block-localized wave function is in principle possible and gives at least not unreasonable results, if a charge fitting scheme for defined substructures is used. This approach would bring the benefit of including the molecular structure of the environment into the VB calculations. However, if the applied approximations are valid and hence the results are reasonably accurate one needs further benchmark calculations and an optimization of the methodology. This is,

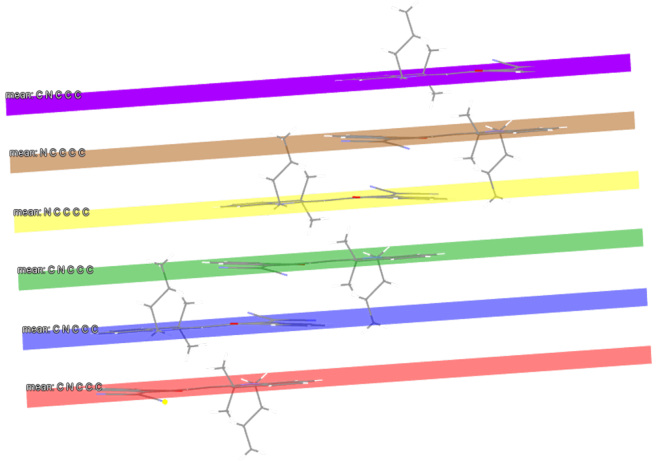

Figure 5.27: π-stack of six monomers in the crystal structure of MD376 using Mercury 3.3

Table 5.3: Results of the VB/MM calculation with different MM-parts compared to the gas-phase and VBPCM calculations. The numbers of the monomers refer to Figure 5.27 with M1 being the one at the bottom (red) and M6 the one at the top (purple). The two MM environments designated crystal 1 and crystal 2 are depicted in Figure 5.28.

	Gas phase	Cyclohexane	π-stack		crystal 1	crystal 2
QM	monomer	monomer	M3	M3	monomer	monomer
MM	-	-	M4	M1,2,4,5,6	20 monomers	141 monomers
w1	67.7	63.0	64.4	64.8	61.9	64.3
w2	32.3	37.0	35.6	35.3	38.1	35.7

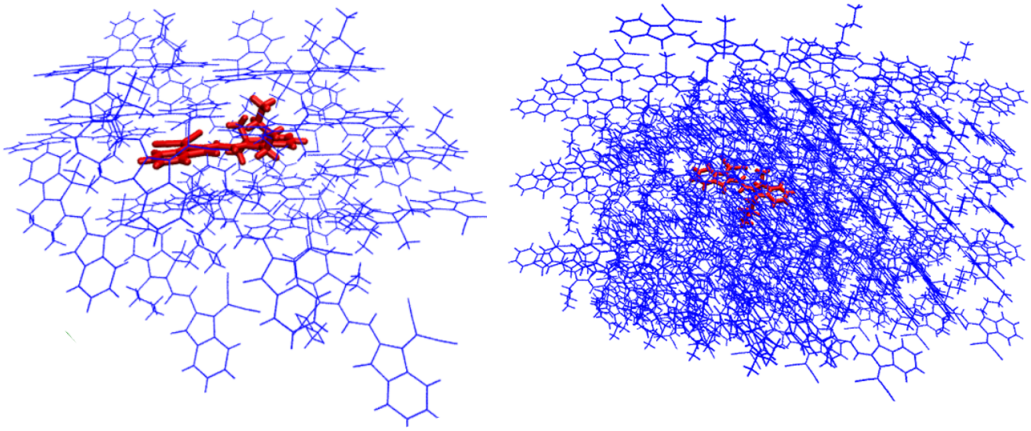

Figure 5.28: Definition of the MM part (blue) for the cuts form the crystal designated crystal 1 and crystal 2 (plotted with VMD).

however, beyond the scope of this work.

5.2.7 Conclusion

The results of this project confirmed the expectation that no single parameter provides an estimation for the performance of an MC in the device. Neither the HOMO energy of a monomer, nor the computed exciton diffusion constants or the closeness to the cyanine limit can serve as the sole basis for the prediction. This does, however, not mean that these quantities are useless, but that the question of the performance is inherently a complex multiparameter problem, which cannot be reduced to a single parameter. Furthermore the device morphology seems to be most crucial, since it influences the transport properties significantly. For instance, it is mainly governed by the morphology, whether a twist is possible, or whether the MC is even already slightly twisted in the crystal. Especially the interface seems to be important, which is emphasized by the findings of Andrienko and coworkers.[317] Thus, the currently observable focus of the research on the interface (see for instance[319] and references therein) seems to be reasonable.
While the molecular properties like the HOMO energy and the reorganization energy and the cyanine limit surely provide a starting point for the design, other factor also need to be taken into account. It is tempting to search for a single easily tunable molecular parameter, which determines the performance, but this seems to be wishful thinking.

Nevertheless, although not all goals of this ambitious project could be met, it lead to some important conclusions, which might provide useful guidelines for the future design of MCs. The most important results and conclusions are summarized below:

- The environmental effects on the geometry (especially the BLA) and the electronic structure of the MCs have been elucidated.
- Using a PCM and a standard DFT approach one can obtain a BLA that agrees qualitatively with the X-ray BLA.
- Comparing the BLA from calculations in solution with the crystal structure provides a rough estimation for the effect of the crystal environment.
- The importance of the molecular HOMO energy should not be overestimated.
- An MC that is close to the cyanine limit in solution might overshoot in the crystal.
- The cyanine limit can be reached in MCs if certain design strategies are followed.
- The cyanine limit is connected to the exciton reorganization energy.
- The device morphology seems to have a significant influence, which can be more important than purely molecular properties.
- The exciton reorganization energy seems to be more crucial than the charge reorganization energy due to different magnitudes.
- A possible twist in the excited state should be considered as a possible energy dissipation channel, which hinders the exciton transport.
- The optimization of the MCs for organic solar cells is a multiparameter problem.

6 Perylene-based dyes

Perylene-based dyes and especially PBI[i]-based colorants have been thoroughly investigated in industrial as well as academic research (see[320,321] and references therein). They have been used as versatile high-performance pigments for automotive paint, for the coloration of synthetic fibers[321] and feature excellent properties like intense colors, a high photo- and thermostability as well as chemical inertness.[320,321] Moreover, the intermolecular interactions make self-assembly into supramolecular structures possible.[320]

Perylene-based dyes are also extensively studied for the application in organic optoelectronic devices, since they are among the best n-type semiconducting materials aside from fullerene-based materials like PCBM and C_{70}-PCBM.[3,320] Among these applications are sensors,[322] transistors[323] and organic photovoltaic cells.[321,324] In fact the first bilayer organic solar cell reported by Tang used copper phthalocyanine together with perylene diamidine.[26]

Although *peri*-donor-functionalized perylene monoimides are catching up with the other sensitizer materials in dye-sensitized solar cells, the performance of PBI and its derivatives in flat and bulk heterojunctions is generally dissatisfactory and stays behind what one would expect of materials with such promising features.[321]

The low efficiencies are attributed to small exciton diffusion lengths, which are supposed to be due to exciton self-trapping in intermolecular states.[321,325,326] In a bulk heterojunction solar cell, the exciton diffusion lengths should ideally be equal or longer than the distance to the closest boundary at each point, in order to achieve a significant quantum yields. The self-trapping is related to the intrinsic properties of the dye molecules in the crystal and their intermolecular arrangement,[18,326] in contrast to the typically encountered trapping effects at grain boundaries and other defects. If the exciton reaches a trap state, it is immobilized and will eventually decay to the ground state. Hence it cannot reach the interface and does not produce charge carriers that contribute to the photocurrent.

The first section of this chapter reviews recent investigations concerning the exction trapping in perylene-based dyes based on intermolecular degrees of freedom, using a dimer

[i]Perylene bisimide

as a zeroth-order model system. In this approach, the effect of the environment was either neglected or included via mechanical embedding plus an estimation of the effect of the π-stack on the electronic splitting. Although some of the experimental results could be nicely explained using this model, it is obvious that a more realistic modeling of the exciton in the crystal necessitates a more profound inclusion of the environment. The effect of the π-stack on the excitonic state and it delocalization can be easily investigated by going to larger systems. This is, however, not possible with expensive methods like SCS-CC2 and hence the second section of this chapter deals with the performance of cheaper methods, especially TDDFT and semi-empirical methods, for the calculation of the excited states and their application to the trapping mechanism.
If a reasonable zeroth-order model system can be found, using the QM/MM methodology might be a productive approach. However, for this methodology to yield accurate results, a correct method for the QM part as well as a force field that reproduces the most important physical features of the intermolecular interactions are needed. Hence the third section of this chapter deals with the design of an appropriate force field and its application in a QM/MM framework.

6.1 Exciton Trapping in Perylene-Based Dyes

A possible exciton trapping mechanism in PBI aggregates based on intermolecular degrees of freedom was first reported by Fink et al.[18] They were able to model the absorption and emission spectra of PBI aggregates in solution using a dimer model system consisting of two π-stacked monomers. Assuming the molecular dimers are only coupled by dipole-dipole interactions in the excited state and including an intermolecular vibrational coordinate, namely the rotation of the monomers against each other, the absorption spectrum could successfully be interpreted in framework of time-dependent quantum mechanics.[327] Using a DFT-D approach the authors computed that in the minimum energy conformation in the ground state the monomers are rotated about ϕ=30° against each other (see Figure 6.1). TDHF computations predicted that photoabsorption of this H-type aggregate leads preferentially to the bright second excited state (S_2), $^1B_1$. In this model the authors discussed that after the excitation the wave packet can reach a conical intersection at ϕ=60°, where the population is transferred to the lower lying $^1B_2$ state (S_1), which has a low oscillator strength. Relaxation leads to the minimum of this state at ϕ=0°, where fluorescence is dipole-forbidden. This explains the longer fluorescence lifetime of the ag-

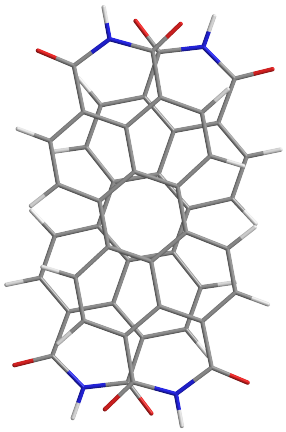

Figure 6.1: Minimum energy ground-state structure of the PBI dimer

gregates compared to the monomer.[18] The excitation is thus trapped and the excitation energy transfer (EET) can not occur efficiently anymore. The use of a dimer model system is in line with experimental results that indicate that although the exciton might be rather delocalized directly after the excitation, it quickly localizes on these subunits.[325] The role of charge-transfer states in exciton trapping processes is currently discussed in the literature (see for instance[328] and[329] and references therein). Since CT states possess a small transition dipole moment, the exciton can be trapped in such states. Assuming a dimer or oligomer as the relevant subunit, intermolecular CT states will definitely be present. However, the question arises if they are low enough in energy to be populated. Using again the dimer model system Liu et al.[329] computed the PES of the four lowest excited states using SCS-CC2 for the rotation of the monomers against each other. Their results show that the CT character of the states changes during the rotation. Nevertheless, the states with high CT character are always above the neutral states and hence no involvement of these states is predicted.[i] Furthermore, the high-level SCS-CC2 potential energy surfaces also indicate that a trapping based on an intermolecular rotation might be possible and thus confirm the TDHF results of Fink et al. Moreover, Liu et al. showed that even the long-range corrected CAM-B3LYP functional fails for this model system, although it reproduces the shape of the PES quite accurately. The character of two states is, however, interchanged compared to SCS-CC2. While the 1^1B_1 is bright and the 2^1B_1

[i] Of course one might argue that gas-phase calculations are inapt to judge the role of CT states, since their energy typically depends heavily on the environment polarity. However, the CT states are symmetric (see section 6.2.1) and hence the effect of the environment can be expected to be small.

is dark in the SCS-CC2 calculation for small angles, the opposite is predicted by CAM-B3LYP. TDHF on the other hand gives a qualitatively correct description, but as usually it overestimates the excitation energies.

Although Fink et al. could nicely explain the experimental results using their model, it is not clear whether it can be applied to the crystal, since the rotation to ϕ=60° might be hindered sterically, depending on the distance between the stacks and the size of the substituents. Furthermore, experimental results show that the initially populated excited state of PBI aggregates in solution decays with a time constant of 215 fs.[17] This fast decay is not in line with a significant intermolecular rotation of the monomers against each other due to the rather large moment of inertia and is hence more indicative of a smaller geometric change. Using the lowest-energy conformation (Fig. 6.1) Schubert et al.[17] investigated the reaction coordinate for the distortion of the monomers from the neutral geometry to the geometry of an unsymmetrical charge-separated state (M^+M^-). They could show that along this reaction coordinate the wave packet can be transferred to the lowest excited state, which is a neutral excited (Frenkel) state within approximately 200 fs. The process involves a doorway CT state. After the wave packet has reached the S_1 state it can relax with a longer timescale to the minimum of this state by rotating to ϕ=0°.

Apart from the twisted conformation, the PBIs are (depending on the substitution pattern) also found in other packing modes, where the monomers are not rotated against each other but shifted longitudinally or transversely. The correlation between molecular conformation, the crystal packing and the color of 18 different PBI molecules has been thoroughly investigated experimentally by Klebe and coworkers.[330] Zhao et al.[331] showed that the different packing modes can be reproduced by DFT-D computations on PBI dimers. They were also able to reproduce the trends in the excitation energies with TDHF calculations on these dimers. This is also a strong indication that a dimer is a sensible zeroth-order system. The computations were performed for unsubstituted PBI dimer structures. The effect of the other monomers in the π-stack on the excited states of the dimer was included by assuming that the interaction between the excited states decays according to the dipole-dipole rule. Then a series expansion of the absorption energy can be used, which leads to the inclusion of Apéry's constant (see[331] for details).

Comparing experimentally measured exciton diffusion lengths of several perylene-based dyes Settels and coworkers[326] noted that DIP[ii] has a significantly longer exciton diffu-

[ii] diindeno perylene

sion length than PTCDA[iii] or PTCBI[iv]. Hence they assumed that the proposed exciton trapping mechanism might be active in the other perylene-based dyes, but not in DIP. In order to investigate whether the absence of the trapping mechanism can be explained using molecular properties, the authors compared the electronic structure of PBI, PTCDA, perylene and DIP. However, a computation of the PES of the lowest excited states for the rotation of the monomers against each other as well as for a longitudinal displacement using SCS-CC2 showed that the shape of the potential energy surfaces and the character of the excited states are virtually identical and seem to be dominated by the perylene core. Both intermolecular motions lead to an intersection for all systems. Therefore the difference in the exciton diffusion lengths cannot be explained by the electronic structure of the systems on a molecular level.

This lead to the conclusion that the crystal structure might play an important role. Settels et al.[332] investigated possible trapping mechanisms in α-PTCDA (exciton diffusion length $L_D = 22\,nm$) and DIP ($L_D = 100\,nm$) again using the dimer as zeroth-order model system. Using a Marcus hopping approach[41] and the X-ray structures, the exciton diffusion lengths of DIP can be reproduced nicely, but the length for α-PTCDA is almost one order of magnitude too large. Since the calculated exciton diffusion lengths do not include any trapping effects, these results are another indication that a trapping mechanism might be active in α-PTCDA but not in DIP.[332] Since α-PTCDA crystallizes in parallel displaced structures, a trapping mechanism different from the one described above has to be active. Steric effects do not allow all possible conformations. Settels et al. identified a conical intersection (CI) that can be reached by a transversal and longitudinal shift of the monomers against each other. The crystal environment was included via a QM/MM approach using the AMOEBA force field and a mechanical embedding, while the electronic effect of the stack was included similar to the approach described above using Apéry's constant.

The results show that while the crystal environment of α-PTCDA allows a movement of the wave packet to the CI, this is not the case in DIP, where a huge barrier has to be surmounted. This explains nicely why no intrinsic exciton trapping mechanism is observed in DIP.

These studies summarized above indicate that the intermoelcular degrees of freedom might be quite important for the modeling of organic optoelectronic devices, since they can lead to trap states. This is especially important since most studies in the literature are based

[iii] perlyene tetracarboxylic acid dianhydride
[iv] perylene tetracarboxylic bisbenzimidazole

on monomers or model Hamiltonians that neglect these degrees of freedom. From a more technical view point, they also show that TDHF gives way to high excitation energies, while TDDFT and even CAM-B3LYP fail and hence the authors had to rely on the expensive SCS-CC2 method. The next section investigates the possibility of using cheaper methods.

6.2 Computing the Excited States of Dimers

Due to the complex mixture of charge-transfer and neutral excited states, Settels and Liu used SCS-CC2 computations. However, for the investigation of larger aggregates, which would be of interest in order to evaluate the effect of the π-stack and to investigate the delocalization of the excitonic state, this method is too expensive. Cheaper methods that also give an accurate description would be highly desirable. Hence benchmark calculations have been performed using the dimer model system. From the work of Liu et al.[329] it is known that it is not sufficient just to look at the potential energy curves, but also the character of the excitation needs to be inspected carefully. The first part of this section deals with the possible types of excitations in a homo dimer and describes one way to define the character of the states, since this approach is used in the benchmark. Then the applicability of TDDFT is discussed and potential applications are shown. The last part of this section deals with the performance of semi-empirical methods.

6.2.1 The Character of the Excitation

In order to understand the character of the lowest singly excited states in π-stacked dimer systems, one can use either localized or delocalized MOs. As a simple model system for the derivation of the important equations, the ethylene dimer in D_{2h} symmetry will be used here. The results can, however, be generalized to all π-stacks of two planar identical molecules, if the monomers are approximated as a two-level system.[i] A very similar approach was reported by Shirai et al.[333]

The localized and the delocalized orbital picture for the ethylene dimer is depicted in Figure 6.2. Constructing the delocalized orbitals from the monomer orbitals and neglecting

[i] For ethylene this means including all π-MOs and the approach is hence accurate, at least within a minimal basis set. For larger molecules the other MOs can obviously also be involved. However, the lowest excited states are typically dominated by the contributions from the minimal [2,2]-space. Hence this approximation should be valid for a qualitative discussion for the lowest excited states of most systems.

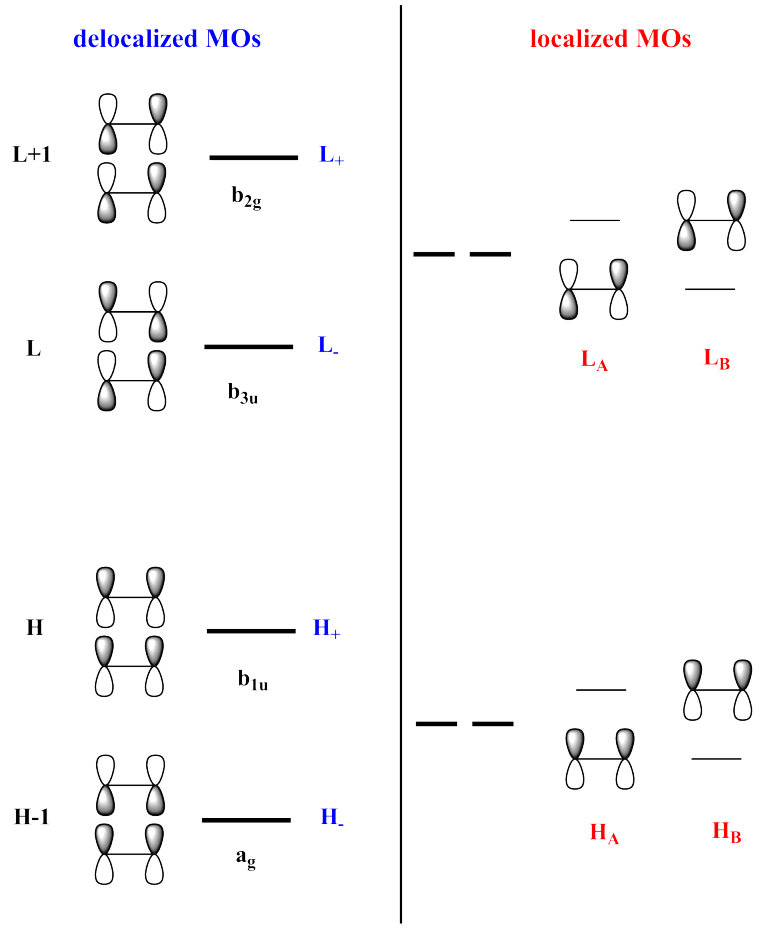

Figure 6.2: Delocalized (left-hand side) and localized (right-hand side) MOs of the ethene dimer. L_A, L_B, H_A and H_B are the localized HOMOs and LUMOs of the monomers A and B, and are pairwise equal in energy. The delocalized MOs L_+, L_-, H_+ and H_- can be constructed as a linear combination of the monomer MOs and have all different energies.

the overlap elements of the type $\langle H_A|H_B\rangle$ in the normalization, the connection between the two pictures can easily be established.[ii] The delocalized frontier dimer MOs are the plus and minus linear combinations of the monomer HOMO and LUMO,

$$H_- = \frac{1}{\sqrt{2}}(H_A - H_B), \tag{6.1}$$

$$H_+ = \frac{1}{\sqrt{2}}(H_A + H_B), \tag{6.2}$$

$$L_- = \frac{1}{\sqrt{2}}(L_A - L_B), \tag{6.3}$$

$$L_+ = \frac{1}{\sqrt{2}}(L_A + L_B). \tag{6.4}$$

A standard quantum chemical calculation of the dimer uses the delocalized MOs.[iii] Hence the excitations are also classified in terms of the configurations involving the delocalized dimer MOs L_+, L_-, H_+ and H_-. Naming the configurations after the sign of the linear combination of the MOs involved in the respective excitation (i.e. the MOs of which the population is changed due to the excitation) gives: Φ_{++}, Φ_{--}, Φ_{+-} and Φ_{-+}. The corresponding excitations are depicted in Figure 6.3. Using the symmetry of the MOs, one can easily derive that Φ_{++}, Φ_{--} belong to the B_{3u} representation, while Φ_{+-} and Φ_{-+} belong to B_{2g}. From the four configurations four excited-state wave functions can be constructed, two with B_{3u} and two with B_{2g} symmetry,

$$\Psi_{B2g,1} = c_1\Phi_{+-} + c_2\Phi_{-+}, \tag{6.5}$$

$$\Psi_{B2g,2} = \tilde{c}_1\Phi_{+-} - \tilde{c}_2\Phi_{-+}, \tag{6.6}$$

$$\Psi_{B3u,1} = c_3\Phi_{++} + c_4\Phi_{--}, \tag{6.7}$$

$$\Psi_{B3u,2} = \tilde{c}_3\Phi_{++} - \tilde{c}_4\Phi_{--}. \tag{6.8}$$

Thus the CI matrix of the system consists of two separate 2x2-blocks. Using the normalization and the orthogonality conditions $\langle\Psi_{b2g,1}|\Psi_{b2g,2}\rangle = 0$ and $\langle\Psi_{b3u,1}|\Psi_{b3u,2}\rangle$ one can

[ii] Similar to the derivation of the two-state model in the chapter 5 neglecting the overlap is an approximation. However, for a qualitative discussion, the assumption of zero overlap is justified, since the typical distances for the dimer calculations presented below is 3.3 Å.

[iii] Applying localization techniques localized MOs can be obtained (see for instance [48]), however these are not completely identical to the monomers MOs, since the transformation is typically performed with the constraint that the set of MOs should be orthogonal, which is obviously not the case for monomer MOs. However a localization should qualitatively give the same conclusions as the approach presented here.

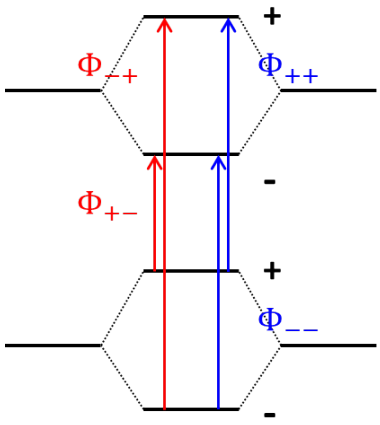

Figure 6.3: The four important configurations in the π-stacked ethylene dimer.

reduce the coefficient space to one coefficient per block,

$$\Psi_{B2g,1} = c\Phi_{+-} + \sqrt{1-c^2}\Phi_{-+}, \tag{6.9}$$

$$\Psi_{B2g,2} = \sqrt{1-c^2}\Phi_{+-} - c\Phi_{-+}, \tag{6.10}$$

$$\Psi_{B3u,1} = d\Phi_{++}\sqrt{1-d^2}\Phi_{--}, \tag{6.11}$$

$$\Psi_{B3u,2} = \sqrt{1-d^2}\Phi_{++} - d\Phi_{--}. \tag{6.12}$$

Although defining the character of an excited states in terms of the coefficient of these configurations is possible, it is not very descriptive. However using the localized picture on the other hand the interpretation is straightforward. The four excited states that can be constructed using the localized orbitals are depicted in Figure 6.4. A local excitation of one monomer leads to a neutral excited state. Since each of the monomers can be excited, a linear combination of two configuration state functions has to be used, which can pictorially be represented as $M^*M \pm MM^*$. If an electron is excited from one monomer to the other, charge-transfer states are generated, which again have to be written as a linear combination: $M^+M^- \pm M^-M^+$.
Neglecting the overlap, the NE and CT wave functions can be written as,

$$\Psi_{NE,\pm} = \frac{1}{\sqrt{2}}\left(\Phi_{NE,A} \pm \Phi_{NE,B}\right), \tag{6.13}$$

$$\Psi_{CT,\pm} = \frac{1}{\sqrt{2}}\left(\Phi_{CT,1} \pm \Phi_{CT,2}\right). \tag{6.14}$$

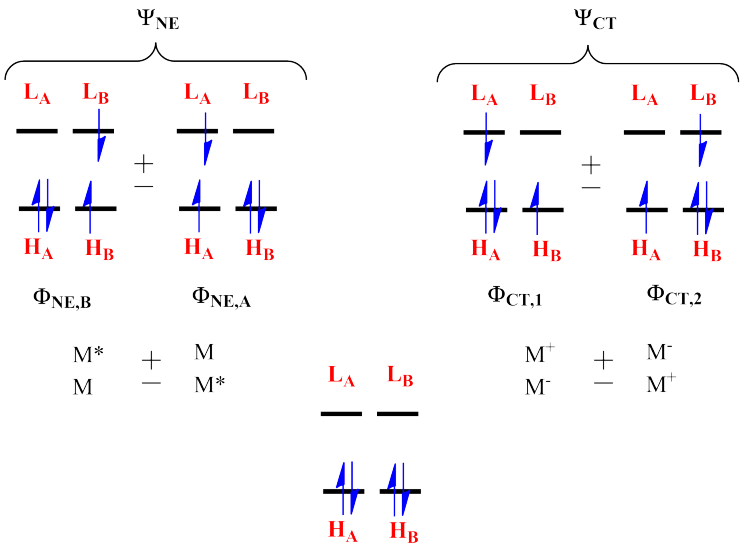

Figure 6.4: Upper panel: possible excitations in the localized picture. The neutral excited (NE) states are depicted on the left-hand side, while the charge-transfer (CT) states are shown on the right-hand side. Lower panel: ground state.

For homodimers the contribution of the two configurations has to be equal in both cases, due to symmetry.

For an interpretation of the results of quantum chemical calculations of the excited states, which typically give the state or excitation energies and the coefficients c, a transformation from the delocalized to the localized picture is thus needed, which means expressing Ψ_{B2g} and Ψ_{B3u} in terms of $\Psi_{NE,\pm}$ and $\Psi_{CT,\pm}$.

In order to establish the connection, one can use the transformation of the orbitals (equations 6.1-6.4). At first the localized configuration state functions are written in terms of the corresponding orbitals. In order to arrive at a proper spin eigenfunction, each has to be constructed from two determinants,

$$\Phi_{NE,A} = \frac{1}{\sqrt{2}}\left[|H_B\overline{H}_BH_A\overline{L}_A| - |H_B\overline{H}_B\overline{H}_AL_A|\right] = \frac{1}{\sqrt{2}}[\phi_1 - \phi_2], \tag{6.15}$$

$$\Phi_{NE,B} = \frac{1}{\sqrt{2}}\left[|H_A\overline{H}_AH_B\overline{L}_B| - |H_A\overline{H}_A\overline{H}_BL_B|\right] = \frac{1}{\sqrt{2}}[\phi_3 - \phi_4], \tag{6.16}$$

$$\Phi_{CT,1} = \frac{1}{\sqrt{2}}\left[|H_A\overline{H}_AH_B\overline{L}_A| - |H_A\overline{H}_A\overline{H}_BL_A|\right] = \frac{1}{\sqrt{2}}[\phi_5 - \phi_6], \tag{6.17}$$

$$\Phi_{CT,2} = \frac{1}{\sqrt{2}}\left[|H_B\overline{H}_BH_A\overline{L}_B| - |H_B\overline{H}_B\overline{H}_AL_B|\right] = \frac{1}{\sqrt{2}}[\phi_7 - \phi_8]. \tag{6.18}$$

The same can be done for the delocalized configuration state functions,

$$\Phi_{++} = \frac{1}{\sqrt{2}}\left[|H_-\overline{H}_-H_+\overline{L}_+| - |H_-\overline{H}_-\overline{H}_+L_+|\right] = \frac{1}{\sqrt{2}}[\chi_1 - \chi_2], \tag{6.19}$$

$$\Phi_{--} = \frac{1}{\sqrt{2}}\left[|H_+\overline{H}_+H_-\overline{L}_-| - |H_+\overline{H}_+\overline{H}_-L_-|\right] = \frac{1}{\sqrt{2}}[\chi_3 - \chi_4], \tag{6.20}$$

$$\Phi_{+-} = \frac{1}{\sqrt{2}}\left[|H_-\overline{H}_-H_+\overline{L}_-| - |H_-\overline{H}_-\overline{H}_+L_-|\right] = \frac{1}{\sqrt{2}}[\chi_5 - \chi_6], \tag{6.21}$$

$$\Phi_{-+} = \frac{1}{\sqrt{2}}\left[|H_+\overline{H}_+H_-\overline{L}_+| - |H_+\overline{H}_+\overline{H}_-L_+|\right] = \frac{1}{\sqrt{2}}[\chi_7 - \chi_8]. \tag{6.22}$$

By plugging into equations 6.19-6.22 the definition of the delocalized MOs (equations 6.1-6.4), the connection between the determinants χ_i and ϕ_i can be established,

$$\chi_1 = \frac{1}{2}\left[\phi_1 + \phi_3 + \phi_5 + \phi_7\right], \tag{6.23}$$

$$\chi_2 = \frac{1}{2}\left[\phi_2 + \phi_4 + \phi_6 + \phi_8\right], \tag{6.24}$$

$$\chi_3 = \frac{1}{2}\left[\phi_1 + \phi_3 - \phi_5 - \phi_7\right], \tag{6.25}$$

$$\chi_4 = \frac{1}{2}\left[\phi_2 + \phi_4 - \phi_6 - \phi_8\right], \tag{6.26}$$

$$\chi_5 = \frac{1}{2}\left[\phi_1 - \phi_3 + \phi_5 - \phi_7\right], \tag{6.27}$$

$$\chi_6 = \frac{1}{2}\left[\phi_2 - \phi_4 + \phi_6 - \phi_8\right], \tag{6.28}$$

$$\chi_7 = \frac{1}{2}\left[\phi_1 - \phi_3 - \phi_5 + \phi_7\right], \tag{6.29}$$

$$\chi_8 = \frac{1}{2}\left[\phi_2 - \phi_4 - \phi_6 + \phi_8\right]. \tag{6.30}$$

Using these relations, the delocalized configuration state function can be written in terms of the localized ones,

$$\Phi_{++} = \frac{1}{2}\left[\Phi_{NE,A} + \Phi_{NE,B} + \Phi_{CT,1} + \Phi_{CT,2}\right], \tag{6.31}$$

$$\Phi_{--} = \frac{1}{2}\left[\Phi_{NE,A} + \Phi_{NE,B} - \Phi_{CT,1} - \Phi_{CT,2}\right], \tag{6.32}$$

$$\Phi_{+-} = \frac{1}{2}\left[\Phi_{NE,A} - \Phi_{NE,B} + \Phi_{CT,1} - \Phi_{CT,2}\right], \tag{6.33}$$

$$\Phi_{++} = \frac{1}{2}\left[\Phi_{NE,A} - \Phi_{NE,B} - \Phi_{CT,1} + \Phi_{CT,2}\right]. \tag{6.34}$$

Finally with these relations it is possible to express the delocalized excited state wave functions in terms of the localized interpretable wave functions,

$$\begin{aligned}
\Psi_{B2g,1} &= c_1\Phi_{+-} + c_2\Phi_{-+} \\
&= \frac{c_1+c_2}{\sqrt{2}}\Psi_{NE,-} + \frac{c_1-c_2}{\sqrt{2}}\Psi_{CT,-} && (6.35)\\
&= \frac{c+\sqrt{1-c^2}}{\sqrt{2}}\Psi_{NE,-} + \frac{c-\sqrt{1-c^2}}{\sqrt{2}}\Psi_{CT,-} && (6.36)\\
\Psi_{B2g,2} &= \tilde{c}_1\Phi_{+-} - \tilde{c}_2\Phi_{-+}, \\
&= \frac{\tilde{c}_1-\tilde{c}_2}{\sqrt{2}}\Psi_{NE,-} + \frac{\tilde{c}_1+\tilde{c}_2}{\sqrt{2}}\Psi_{CT,-} && (6.37)\\
&= \frac{\sqrt{1-c^2}-c}{\sqrt{2}}\Psi_{NE,-} + \frac{\sqrt{1-c^2}+c}{\sqrt{2}}\Psi_{CT,-} && (6.38)\\
\Psi_{B3u,1} &= c_3\Phi_{++} + c_4\Phi_{--}, \\
&= \frac{c_3+c_4}{\sqrt{2}}\Psi_{NE,+} + \frac{c_3-c_4}{\sqrt{2}}\Psi_{CT,+} && (6.39)\\
&= \frac{d+\sqrt{1-d^2}}{\sqrt{2}}\Psi_{NE,+} + \frac{d-\sqrt{1-d^2}}{\sqrt{2}}\Psi_{CT,+} && (6.40)\\
\Psi_{B3u,2} &= \tilde{c}_3\Phi_{++} - \tilde{c}_4\Phi_{--}, \\
&= \frac{\tilde{c}_3-\tilde{c}_4}{\sqrt{2}}\Psi_{NE,+} + \frac{\tilde{c}_3+\tilde{c}_4}{\sqrt{2}}\Psi_{CT,+} && (6.41)\\
&= \frac{\sqrt{1-d^2}-d}{\sqrt{2}}\Phi_{NE,+} + \frac{\sqrt{1-d^2}+d}{\sqrt{2}}\Psi_{CT,+}. && (6.42)
\end{aligned}$$

The results are in line with the ones obtained by Shirai et al.[333] Using these equations and the coefficients from the output of a quantum chemical calculation, it is possible to compute the character of the excitation in terms of neutral or charge-transfer excited states. The weight of the CT or NE character is then simply defined as the square of the coefficients, e.g. $\frac{(c_3-c_4)^2}{2}$.

It can easily be seen from the equations that a 1:1 mixing of the delocalized configurations implies a pure state in terms of the CT or NE character.[iv] Furthermore since both irreducible representations form a 2x2-block, the higher the CT character in one state, the lower it is in the other. This is shown in Figure 6.5 for the states of B_{3u} symmetry. The sum of the CT-weights in both states always has to be unity. For systems with more π-electrons than ethene, this is of course only approximately true, since higher states

[iv] This is similar to the expansion of the minimal CI wave function of the H_2 molecule in neutral and ionic resonance structures (see for instance[96]).

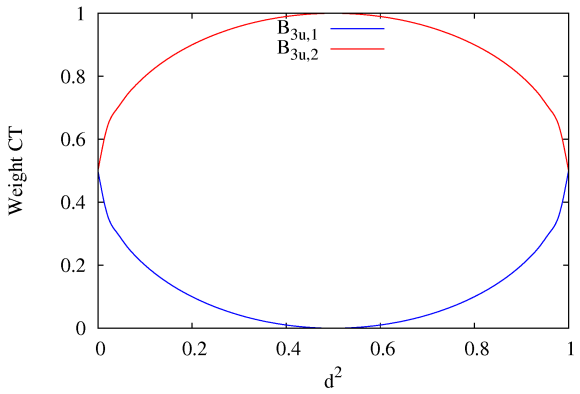

Figure 6.5: Amount of charge-transfer character in the states with B_{3u} symmetry as a function of the coefficent of the delocalized configurations d^2.

of the same irreducible representation will participate. For a qualitative discussion the results obtained here should however be valid.

Of course it is also possible to work the other way round and to write the localized wave functions in terms of their delocalized counterparts. This can be exploited to express the energy expectation values of the pure CT and NE states in terms of the energy of the delocalized excited state wave functions. This can be considered as diabatization.[v] Subtracting equation 6.41 multiplied by (c_3+c_4) from equation 6.39 multiplied by $(\tilde{c}_3-\tilde{c}_4)$ and rearranging gives

$$\Psi_{CT,+} = \frac{\tilde{c}_3 - \tilde{c}_4}{K}\Psi_{B3u,1} - \frac{c_3 + c_4}{K}\Psi_{B3u,2}, \tag{6.44}$$

with

$$K = \frac{1}{\sqrt{2}}\left[(c_3 - c_4)(\tilde{c}_3 - \tilde{c}_4) - (c_3 + c_4)(\tilde{c}_3 + \tilde{c}_4)\right]. \tag{6.45}$$

[v] A strictly diabatic basis Φ_i should fulfill the condition that the nonadiabatic coupling elements are zero,

$$\left\langle \Phi_i \middle| \frac{\partial}{\partial \mathbf{R}} \Phi_j \right\rangle = 0. \tag{6.43}$$

However, it can be shown that this is only possible in rare cases, like diatomic states of the same symmetry, because the necessary so-called curl condition is typically not satisfied for Born-Oppenheimer states of real molecules (see[334,335] for details). Hence one has to look for a basis that approximately fulfills this condition. Often a basis is used that keeps the "character" of a state as constant as possible along a certain coordinate. One example for this are for instance individual VB structures.[96] Using this definition the CT and NE states can also qualify as diabatic.

An analogous expression can be obtained for $\Psi_{NE,+}$. Calculating the energy expectation value yields,

$$E_{CT,+} = \langle \Psi_{CT,+} | H | \Psi_{CT,+} \rangle = \frac{(\tilde{c}_3 - \tilde{c}_4)^2}{K^2} E_{B3u,1} + \frac{(c_3 + c_4)^2}{K^2} E_{B3u,2}, \quad (6.46)$$

$$E_{NE,+} = \langle \Psi_{NE,+} | H | \Psi_{NE,+} \rangle = \frac{(\tilde{c}_3 + \tilde{c}_4)^2}{K^2} E_{B3u,1} + \frac{(c_3 - c_4)^2}{K^2} E_{B3u,2}. \quad (6.47)$$

Due to the applied approximations one cannot expect to obtain diabatic energies of high accuracy from these equations, but they should suffice to reproduce the qualitative behavior of the states and their relative ordering.
The approach presented in this section can hence be used to interpret quantum chemical computations in terms of CT and NE character. Furthermore approximate diabatic states can be constructed.

6.2.2 TDDFT

In order to be able to compute bigger systems than dimers, TDDFT is one obvious choice. Another advantage of TDDFT is that a geometry optimization in the excited state of the dimer should be feasible. This is not possible with SCS-CC2, because the gradients are computationally very demanding. Furthermore any standard optimization without constraints leads to deformed monomers. This deformation maximizes the interaction between the monomers, but lowers the applicability of the model to the crystal, where the monomers are restricted by the stack and can therefore not deform. Thus Settels and Liu had to compute potential energy surfaces for all degrees of freedoms they anticipated to be important. An optimization that only involves the degrees of freedom between the monomers and keeps the monomer geometries fixed would directly yield the relaxed excited state geometry and hence reveal the important degrees of freedom. Such an optimization is possible with Gaussian using dummy atoms and TDDFT and a Z-matrix approach. Hence there are several reasons, why a sufficiently accurate functional is highly desirable.
Keeping in mind that Liu et al.[329] showed that even CAM-B3LYP fails for the dimer model system it does not seem to be too promising to find applicable functionals. However, the authors attributed the failure to the fact that the diabatic CT and NE states are very close in energy and hence small changes in the excitation energies predicted by the functionals can have dramatic effects. Therefore a functional that leads to slightly different diabatic energies might yield the correct results.

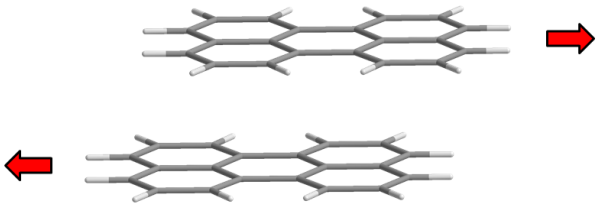

Figure 6.6: Definition of the longitudinal displacement.

An obvious candidate is ωB97XD,[154] a widely used long-range corrected hybrid functional. Test calculations on the PBI dimer, built up from monomers with the geometry taken from the work of Settels and Liu (BLYP-D/TZV(P)), showed that ωB97XD/cc-pVDZ also gives the wrong character of the B_u states, since the oscillator strengths are incorrect. The $2B_u$ state is predicted to be brighter than the 1 B_u state in the eclipsed geometry. The same was observed by Liu et al.[329] for CAM-B3LYP. However, a recent study by Casanova on the excited states of the perylene dimer[336] relied on the ωB97XD/6-31+G(d)[337] level of theory. The resulting potential energy surfaces look reasonable compared to the SCS-CC2 results. Nevertheless, similar to PBI the character could be incorrect. Since Settels showed that the excited states of several perylene-based dyes behave quite similar,[326] this is not unlikely. Hence the applicability of ωB97XD was checked carefully.
Since perylene is the smallest of the perylene-based dyes it is a reasonable starting point for a thorough investigation of the performance of TDDFT. The longitudinal displacement was chosen as a coordinate for the potential energy surfaces (see Figure 6.6), with a distance between the molecular planes of 3.3 Å, similar to Settels et al.[326] The monomer was optimized on the ωB97XD/cc-pVTZ level of theory. Settels and Liu used SCS-CC2 as a benchmark method, which was also used here together with SCS-ADC(2) in conjunction with the cc-pVDZ basis sets.[vi] ADC(2) has the advantage that the computation of the oscillator strengths is significantly faster (see section 3.3.4). The ground-state surface was computed on the ωB97XD/6-31+G(d) level of theory[vii], while the excitation energies of the respective method were added to these values to generate the excited-state potential energy surfaces. In the dimer system several low-lying states exist. For this investigation, the two B_u and A_g states that arise from the splitting of the monomer frontier MOs (see

[vi] All DFT calculations were performed with Gaussian, while TURBOMOLE was used for SCS-ADC(2) and SCS-CC2.
[vii] The basis was chosen in order to be comparable to the results of Casanova[336].

section 6.2.1) were chosen, since they are the states expected to contribute to the exciton trapping.[viii] The results of the *ab initio* reference methods SCS-CC27cc-pVDZ and SCS-ADC(2)/cc-pVDZ are depicted in Figure 6.7.

Apart from the potential energy surfaces and the oscillator strengths also the character in terms of the delocalized determinants (square of the coefficients) and the amount of charge-transfer character is given. The latter was computed using the equations derived in section 6.2.1.[ix] Whether the plus or the minus linear combination of the monomer frontier MOs is lower in energy depends on the relative displacement of the monomers and hence their order changes along the chosen coordinate. Therefore, the MOs have to be inspected visually in order to decide which of the coefficients are the correct ones.[x]

Before the results are discussed it should be noted that the *ricc2* module of TURBOMOLE only prints coefficients above a certain threshold. Whenever a coefficient became smaller than the threshold, it was set to zero in the character calculation, which leads to discontinuities in the curves. For instance the fact that the CT character of the two A_g states is almost completely identical for the first 0.75 Å can be attributed to some coefficients being smaller than the threshold. The same is true for the hump in the 1 B_u character curve. The dashed line, which is more realistic, was computed using the additivity of the weights in the two B_u curves.

From Figure 6.7 it is evident that SCS-CC2 and SCS-ADC(2) yield almost identical results. The potential energy surfaces and the character of the states are in agreement to the computations of Settels et al.,[16,326] which used an approach based on a Löwdin localization proposed by Liu[338] for obtaining the character. Moreover the behavior of the character of the bright states is in line with the behavior of the oscillator strengths.

[viii] It should be noted that depending on the system and the method these states are not the four lowest excited states along the complete surface. B_g and A_u states are sometimes among the lowest four states, however, they have been omitted for the sake of clarity.

[ix] It should be noted that the equations have been derived for the coefficients of a CI. Although these are not identical to the coefficients taken from a linear-response method like TDDFT or CC2 a qualitative agreement is usually observed.

[x] When applying the equations of section 6.2.1 another problem arises: The signs of the coefficients of the CI-type expansion are not unambiguous and can hence also be different for different points of the PES, which leads to unphysical fluctuations in the curves. In order to circumvent this problem the absolute values were used, e.g. $\omega_{CT} = \frac{(|c_3|-|c_4|)^2}{2}$. Of course this has the disadvantage that it can artificially prevent the character of two states from interchanging. Therefore a careful inspection is needed whenever the character of two states becomes identical, or the transition moments or other properties indicate a crossing of the character curves. Using absolute values also introduces an ambiguity in the choice of the sign between the coefficients, which determines which state is which. For the B_u states the oscillator strength clearly defines which state has a dominating CT and which a dominating NE character and for the A_g states the results of Settels and Liu were used as reference.

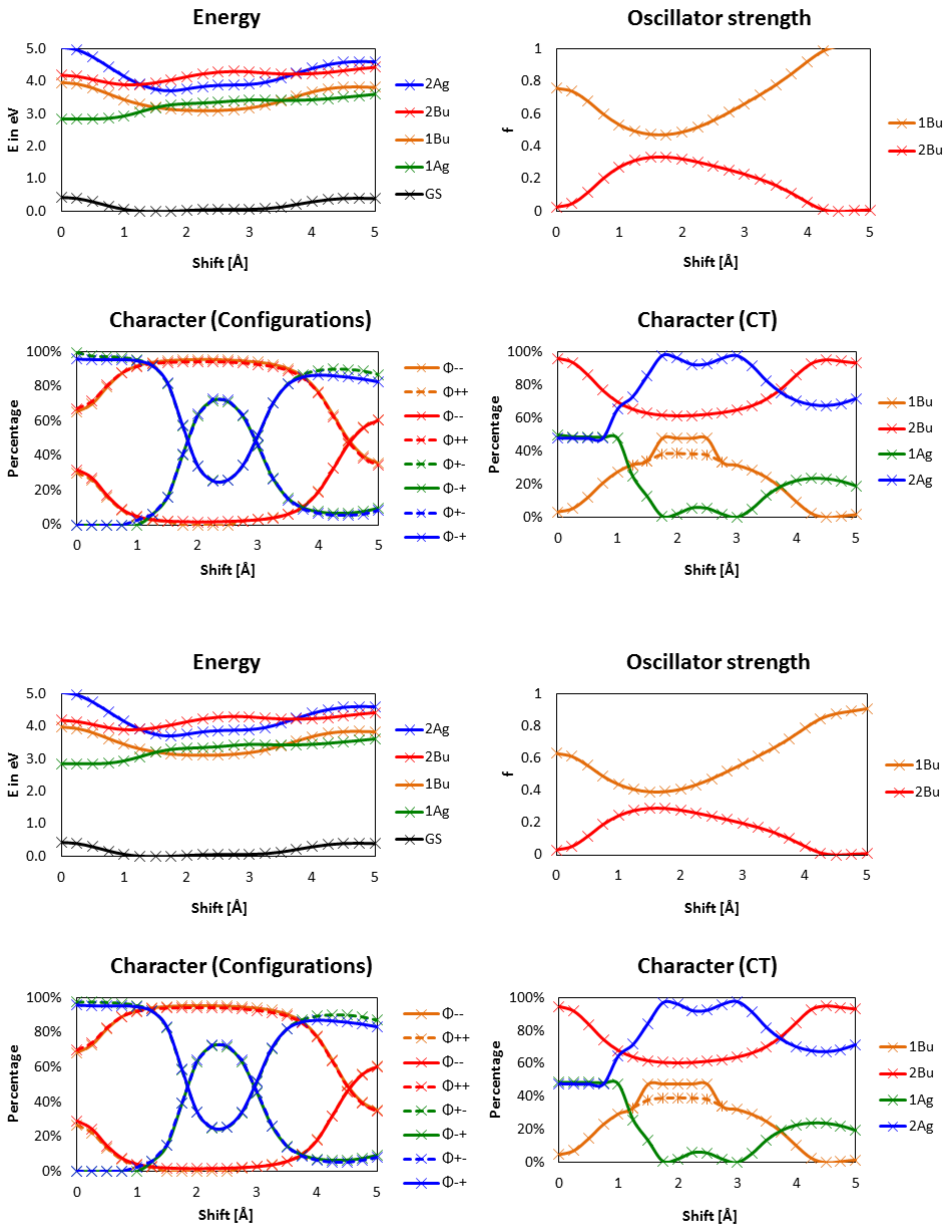

Figure 6.7: *Ab initio* results for the longitudinal shift in the perylene dimer. Upper panel: SCS-ADC(2)/cc-pVDZ, lower panel: SCS-CC2/cc-pVDZ. Ground state surface: ωB97XD/6-31+G(d), monomer geometry: ωB97XD/cc-pVTZ

These results show that either method, SCS-CC2 or SCS-ADC(2), can can be used as a reference.
The TDDFT calculations were performed with the ωB97XD functional and for comparison also with CAM-B3LYP. In order to be able to compare the computations to the ones of Casanova, the 6-31+G(d) basis sets[337] were used. The results are depicted in Figure 6.8.
The potential energy curves as well as the character of the DFT methods [xi] are in agreement with the *ab initio* results. Qualitatively CAM-B3LYP shows minor deviations in the oscillator strength. While 1 B_u is always predicted to be brighter than 2 B_u by ωB97XD and the *ab initio* methods, there is a small region where CAM-B3LYP predicts it to be the other way round. The character of the two states is also more similar in CAM-B3LYP. The PES of the TDDFT methods are shifted to lower energies compared to the *ab initio* methods. However, for ωB97XD this shift is roughly constant and around 0.2 eV, while it is slightly bigger and less constant for CAM-B3LYP (see Figure 6.9). However, the differences are within the margin of accuracy that can be expected for TDDFT and hence both methods can be considered to be reasonably accurate.

These results are not in line with the results reported above for PBI, where CAM-B3LYP as well as ωB97XD failed. This is surprising, since the excited states of the perylene and PBI dimer were shown to be very similar.[326] Therefore the same procedure was repeated for PBI. However, since PBI is larger only SCS-ADC(2) was used as reference to reduce the computational costs. The SCS-ADC(2) results[xii] for the PBI dimer are depicted in Figure 6.10. By comparing with the results in Figure 6.7 it is evident that the excited states and their character are indeed very similar to perylene.
The TDDFT results are shown in Figure 6.11. The oscillator strengths of the two bright

[xi] TDDFT also contains de-excitations, which influence the norm. The general excitation/de-excitation operator for TDHF/TDDFT can be written in a basis of one-particle/one-hole excitation and de-excitation operators,[68]

$$\hat{\mathcal{O}}^\dagger = \sum_{i,a} a^\dagger i X_{ia} + \sum_{i,a} i^\dagger a Y_{ia}. \tag{6.48}$$

Hence the norm is defined as

$$\langle \hat{\mathcal{O}}^\dagger | \hat{\mathcal{O}}^\dagger \rangle = \vec{X}^\dagger \vec{X} - \vec{Y}^\dagger \vec{Y}, \tag{6.49}$$

However, since these de-excitations are typically very small, they have been neglected in the analysis of the character.

[xii] The discontinuities in the graphs describing the CT character are again due to the threshold for the printing of the coefficients. If the magnitude of the coefficient was below the threshold for only a single shift distance, the neighboring points were used to extrapolate its value.

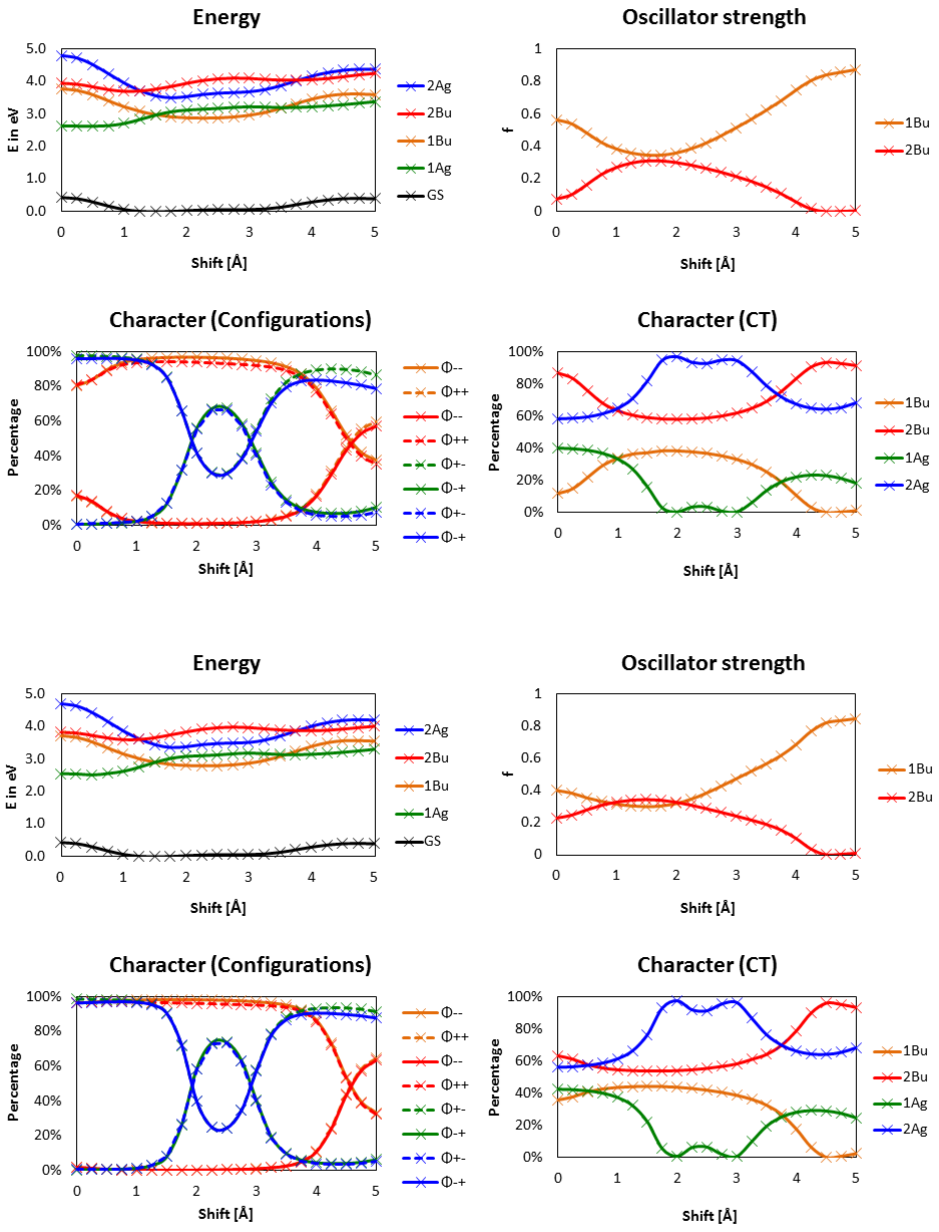

Figure 6.8: TDDFT results for the longitudinal shift in the perylene dimer. Upper panel: ωB97XD/6-31+G(d), lower panel: CAM-B3LYP/6-31G(d). Ground state surface: ωB97XD/6-31+G(d), monomer geometry: ωB97XD/cc-pVTZ

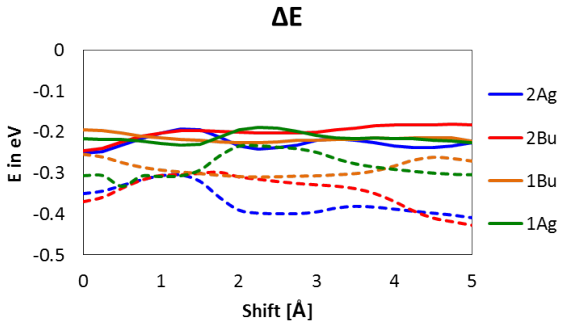

Figure 6.9: Energy difference to SCS-ADC(2)/cc-pVDZ for the perylene dimer. Continuous lines: ωB97XD/6-31+G(d), dashed lines: CAM-B3LYP/6-31+G(d)

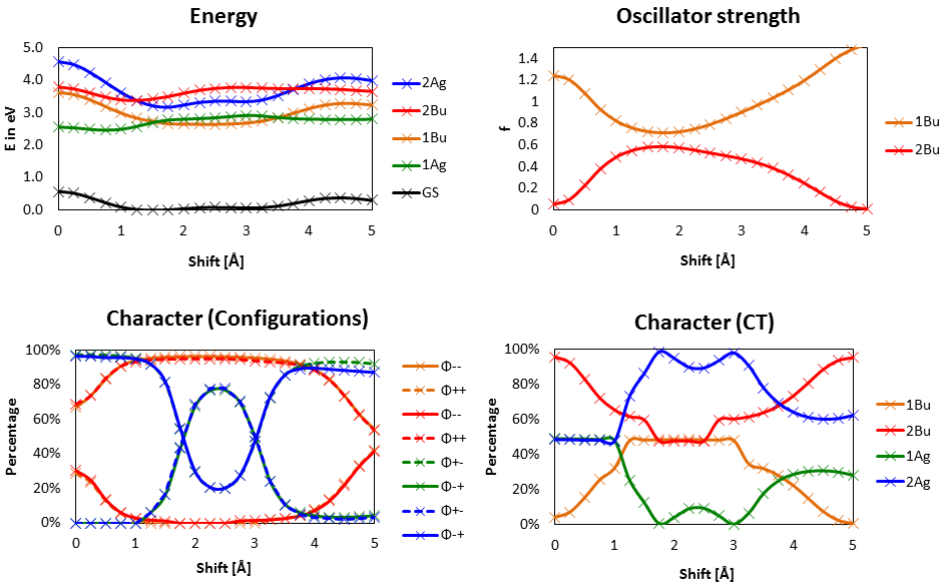

Figure 6.10: SCS-ADC(2)/cc-pVDZ results for the longitudinal shift in the PBI dimer. Ground state surface: ωB97XD/6-31+G(d), monomer geometry: ωB97XD/cc-pVTZ

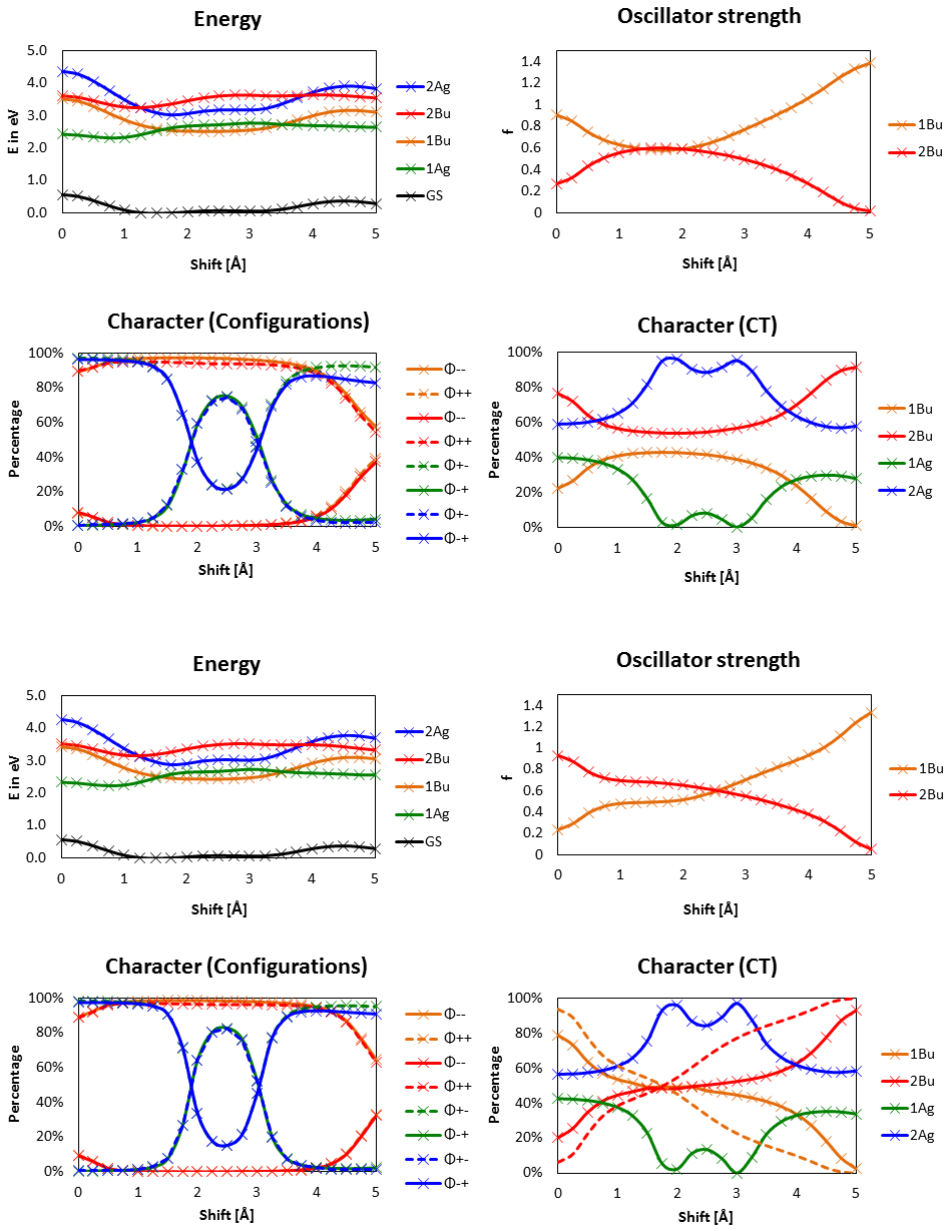

Figure 6.11: TDDFT results for the longitudinal shift in the PBI dimer. Upper panel: ωB97XD/6-31+G(d), lower panel: CAM-B3LYP/6-31G(d). Ground state surface: ωB97XD/6-31+G(d). Monomer geometry: ωB97XD/cc-pVTZ. The dashed lines in the plots for the character in the lower panel have been obtained using the transition dipole moments (see text).

states are predicted to be less different by ωB97XD than by SCS-ADC(2), but apart from that the functional again yields correct results. The CAM-B3LYP results, however, now show the incorrect behavior already observed by Liu et al. At smaller shift distances the 2 B_u state is predicted to be brighter than the 1 B_u state. This order interchanges for distances larger than 2.5 Å, where the predictions are qualitatively correct. This is in line with a strong CT character in the 1 B_u state at 0 Å that decreases along the reaction coordinate and an inverse behavior for the 2 B_u state.[xiii] Assuming that the transition moment for the diabatic CT state is zero, the character can also be derived from the transition dipole moments of the two adiabtatic states μ_1 and μ_2.[329] The amount of CT character obtained using this scheme[xiv] is plotted as dashed lines for CAM-B3LYP (Fig. 6.11). These curves support the crossing obtained from the character analysis based on the coefficients.

In order to understand why the character of the two B_u states is predicted to be different by two functionals, which typically yield results of similar accuracy, the energies of the diabatic CT and NE states, from which the two B_u states can be constructed, were calculated using the formulas derived in section 6.2.1.[xv] The energy of the diabats is plotted next to the potential energy curves in Figure 6.12. It has to be stressed that due to the approximations, the diabats can only be expected to be qualitatively correct. Since the formulas involve the total energy, the total energies of the adiabatic states, i.e. the energy of the ground state energy curve (wB97XD/6-31+G(d)) plus the excitation energy computed on the respective level were used. Thus the calculation involves results from the ground and excited state calculation and hence in the case of CAM-B3LYP from different methods, which introduces further errors.

[xiii] Plotting the curves without the absolute values suggested a crossing of the B_u states between 1.75 and 2 Å. Hence the sign between the absolute values of the coefficients was changed at 2 Å. Due to the uncertainty in the sign of the coefficients, the behavior of the two dark A_g states could in principle also be the other way round, however, there is no indication to assume that their behavior is the inverse of the previous calculations.

[xiv] The CT character of the 2 B_u state is given by[329]

$$\frac{\mu_2^2}{\mu_2^2 + \mu_1^2}, \tag{6.50}$$

while the character of the 1 B_u stat is simply calculated as

$$1 - \frac{\mu_2^2}{\mu_2^2 + \mu_1^2}. \tag{6.51}$$

[xv] Similar to the computation of the character the absolute values of the coefficients were used. The sign was chosen to be consistent with the calculation of the character.

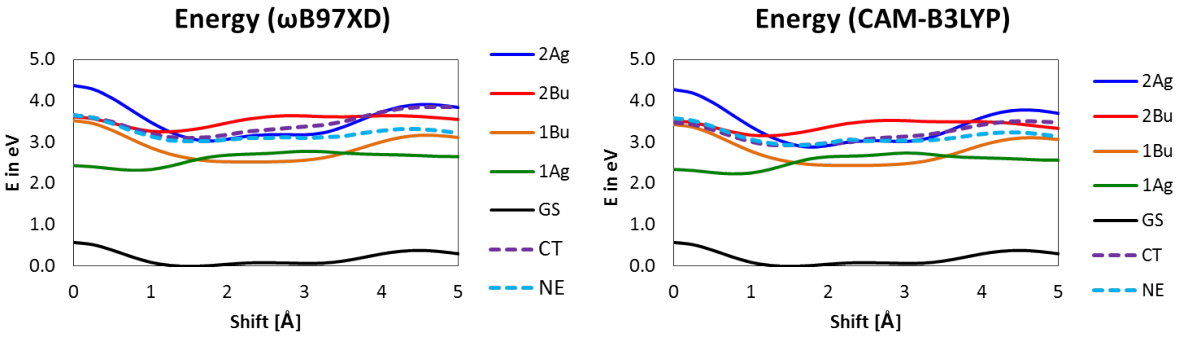

Figure 6.12: Diabatic energies of the CT and NE states forming the two B_u states and the adiabatic PES.

From Figure 6.12 it is obvious that the diabats are indeed rather close in energy, especially at the eclipsed geometry. Furthermore the CT curve is predicted to be slightly lower in energy than the NE curve for small shifts by CAM-B3LYP, contrary to ωB97XD. For 0 Å ωB97XD predicts the diabats to have the same energy within the accuracy of the methods, while the CT state is 0.10 eV below the NE state in CAM-B3LYP. Hence the mixing of the two states will give adiabatic states with an inverted character by CAM-B3LYP compared to ωB97XD.
Since the energetic splitting due to the mixing of the diabatic states is apparently rather small and the states are very close in energy this wrong ordering has only a limited influence on the energy of the adiabatic states. For larger shift distances the diabats are sufficiently separated and thus this problem does not arise. Close to the eclipsed geometry, however, small changes can indeed have a dramatic effect on the character and the oscillator strengths.
Hence the relative order of the diabats explains why the two functionals predict very different results. The relative energy of the NE and CT diabatic states on the other hand can be expected to be highly dependent on the amount of HF exchange. In the short-range limit both functionals contain around 20 % HF exchange, however, in the long-range limit the amount of HF reaches a limit at around 65 % in CAM-B3LYP, while it becomes 100 % in ωB97XD (see below). Due to the significant distance of 3.3Å between the monomers this difference in the amount of long-range HF exchange might be responsible for the different prediction of the order of the states of the functionals.

The fact that ωB97XD failed in the test calculations, but gives a correct description

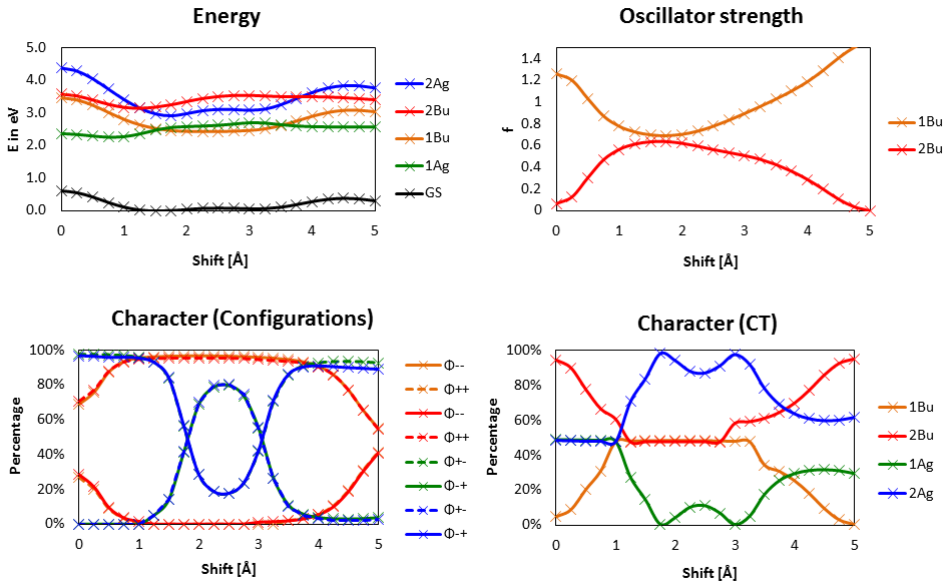

Figure 6.13: SCS-ADC(2)/cc-pVDZ results for the longitudinal shift in the PBI dimer. Ground state surface: ωB97XD/6-31+G(d) Monomer geometry: taken from Settels et al.

here is rather surprising. This can either be attributed to the different basis sets applied or the different monomer geometries. Since cc-pVDZ and 6-31G+(d) are both polarized split-valence basis sets of double-zeta quality it is unlikely that significantly different results are obtained when the basis is changed. This was also confirmed by corresponding calculations. Hence the geometry of the monomer seems to be crucial. In order to verify this the computations were repeated using the monomer geometry of Settels et al.,[326] which was originally computed on the BLYP-D/TZV(P)[339,340] level of theory.

The SCS-ADC(2) results using this geometry (see Figure 6.13) are quite similar to the ones with the ωB97XD/cc-pVTZ geometry. The ground state PES is scarcely changed, but the excitation energies are lowered roughly constantly by around 0.2 eV. Inspecting the two geometries shows that the one used by Settels et al. has longer bond lengths and seems to be connected qualitatively to the ωB97XD/cc-pVTZ geometry by a breathing motion.

As a reference, an SCS-MP2/cc-pVTZ optimization was performed. In Figure 6.14 the distortion of the two other geometries relative to the SCS-MP2/cc-pVTZ geometry is depicted in an exaggerated form to visualize the effect, while table 6.1 provides the SCS-MP2/cc-pVTZ single-point energies for geometries optimized on different levels of theory.

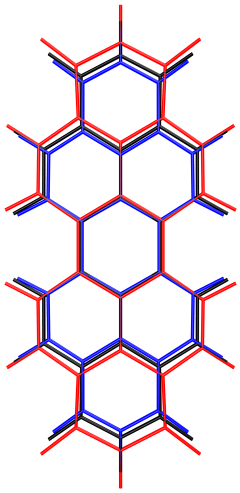

Figure 6.14: The reference SCS-MP2/cc-pVTZ geometry is shown in black, while the ωB97XD/cc-pVTZ (blue) geometry and the one of Settels et al. (red) are plotted in an exaggerated form, i.e. the distortion relative to the reference is scaled with a factor of 10.

Table 6.1: Energetic differences of structures optimized on different levels of theory.

Geometry	E(SCS-MP2/cc-pVTZ) [kcal/mol]
SCS-MP2/cc-pVTZ	0.0
SCS-MP2/cc-pVDZ	3.00
ωB97XD/cc-pVDZ	0.53
ωB97XD/cc-pVTZ	1.46
Settels et al.	2.95

The single-point energies show that the geometry of Settels et al. as well as the ωB97XD geometry are energetically not very close to the one predicted by SCS-MP2. Furthermore Figure 6.14 shows that while one is more extended than the reference the other is more contracted, which means that the difference between them is even larger than suggested by the single-point energies, which are relative to the reference. Assuming that the structure predicted by SCS-MP2/cc-pVTZ is closest to the truth, the geometry obtained by ωB97XD and the one taken from Settels et al. are ideal test cases, since they deviate in two different direction from the reference and present thus two extreme cases.
The results of the TDDFT calculations are given in Figure 6.15. Both functionals predict the excitation energies to be lower in energy for the geometry of Settels et. al. by around 0.2 eV, in line with SCS-ADC(2) results. CAM-B3LYP again predicts the wrong character of the B_u states for small shift distances. A computation of the diabats reveals

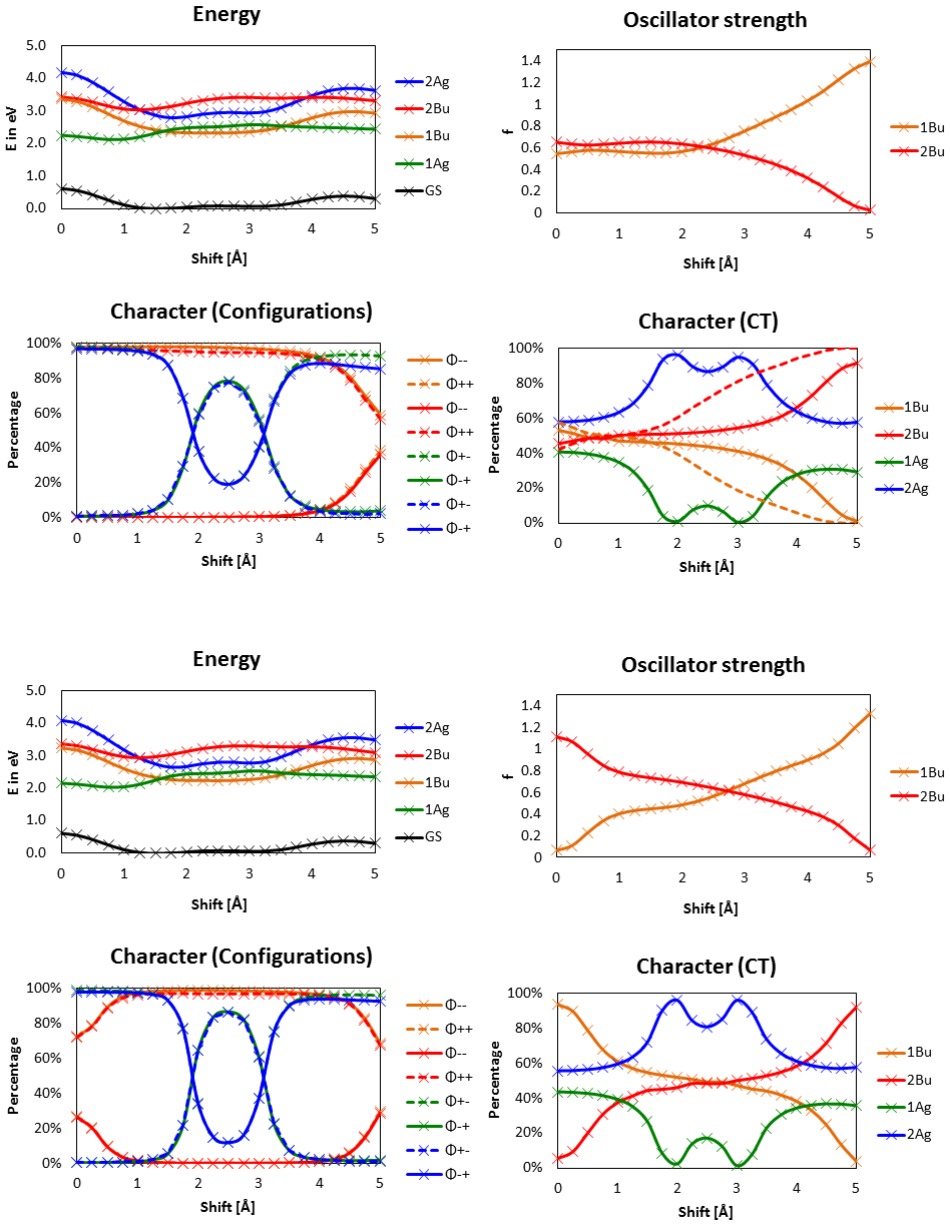

Figure 6.15: TDDFT results for the longitudinal shift in the PBI dimer. Upper panel: ωB97XD/6-31+G(d), lower panel: CAM-B3LYP/6-31G(d). Ground state surface: ωB97XD/6-31+G(d), monomer geometry: taken from Settels et al. The dashed lines in the plots for the character in the upper panel have been obtained using the transition dipole moments.

that at 0 Å the CT state is now 0.15 below the NE state. The same trend is observable for ωB97XD. While both diabats were equal in energy using the ωB97XD geometry, the CT state is now slightly lower in energy than the NE state by 0.05 eV. Thus ωB97XD now also predicts a wrong character of the states at small shift distances. The change of geometry seems to stabilize the CT state slightly more than the NE state, which has a significant effect for ωB97XD, due to the two states being extremely close in energy. This sensitivity of ωB97XD using this system explains why it sometimes gives correct and sometimes incorrect results.
To summarize the results obtained so far, both functionals work well for the perylene dimer, but CAM-B3LYP fails for the PBI dimer, while the reliability of ωB97XD depends on the geometry.

In order to obtain a reliable functional for this system (i.e. a functional that reproduces the SCS-ADC(2) results) one should make sure that the diabatic CT state is energetically above the NE state. As already mentioned the relative energy of the two states should depend critically on the amount of exact HF exchange. Hence an applicable functional should have a slightly higher amount of HF exchange than the functionals used above. While it might be possible for a standard hybrid functional to increase the amount of exact exchange until the correct order of the states is obtained, this not the best way, since it will not necessarily lead to physically very grounded results. Furthermore simply increasing the HF exchange will eventually lead to an overestimation of the excitation energy, as it is observed for TDHF.[329]
In order to describe CT and NE states on a similar, theoretically more founded level a long-range corrected functional should be used. However, these functionals do not use a fixed amount of HF exchange and thus the question arises what a higher amount of HF exchange means in this context. Therefore before the results of calculations with other possible functionals are reported, a short excursion on the HF exchange in long-range corrected functionals is given.

Excursion: The amount of HF exchange in different long-range corrected functionals

In the simplest case of a pure density functional, the exchange of the long-range corrected functional is written as a sum of the long-range exchange from HF and the short-range exchange from DFT. The latter is often denoted as DFA (density functional approxima-

tion),[150,151,341]

$$E_x^{HF} = E_x^{LR-HF}(\mu) + E_x(\mu)^{SR-DFA}, \tag{6.52}$$

with μ (which is often also denoted as ω) being the range separation parameter of the Ewald split. The long-range contribution is simply given by

$$E_x^{LR-HF} = -\frac{1}{2}\sum_{\sigma}\sum_{ij}^{occ}\int\int \phi_{i\sigma}^*(\mathbf{r}_1)\phi_{j\sigma}^*(\mathbf{r}_1)\frac{\mathrm{erf}(\mu r_{12})}{r_{12}}\phi_{i\sigma}(\mathbf{r}_2)\phi_{j\sigma}(\mathbf{r}_2)d\mathbf{r}_1 d\mathbf{r}_2, \tag{6.53}$$

with $\phi_{i\sigma}$ being the occupied spin orbitals with spin σ. The short-range DFA part is scaled accordingly. Hence this approximation leads to zero HF exchange at short distances and 100 % at the limit $r_{12} \to \infty$. The value of μ defines the steepness of the transition. LC-BLYP as implemented in Gaussian uses $\mu = 0.47\,\mathrm{bohr}^{-1}$, although $\mu = 0.33\,\mathrm{bohr}^{-1}$ is also often used.[342,343] LC-ωPBE[153] uses PBE exchange and a range-separation parameter of $\mu = 0.4\,\mathrm{bohr}^{-1}$[344]

As in standard DFT it is beneficial to also include some HF exchange in the short-range limit. Hence Chai and Head-Grodon proposed to add a short-range HF term to the exchange functional,[341]

$$E_x^{HF} = E_x^{LR-HF}(\mu) + c_x E_x^{SR-HF}(\mu) + E_x(\mu)^{SR-DFA}. \tag{6.54}$$

E_x^{SR-HF} is simply defined by

$$E_x^{SR-HF} = -\frac{1}{2}\sum_{\sigma}\sum_{ij}^{occ}\int\int \phi_{i\sigma}^*(\mathbf{r}_1)\phi_{j\sigma}^*(\mathbf{r}_1)\frac{\mathrm{erfc}(\mu r_{12})}{r_{12}}\phi_{i\sigma}(\mathbf{r}_2)\phi_{j\sigma}(\mathbf{r}_2)d\mathbf{r}_1 d\mathbf{r}_2. \tag{6.55}$$

For ωB97X[341] the parameters are $\mu = 0.3\,\mathrm{bohr}^{-1}$ and $c_x = 0.17$, while they are $\mu = 0.2\,\mathrm{bohr}^{-1}$ and $c_x = 0.22$ for ωB97XD.[154] It is important to note that ωB97XD is not just ωB97X plus an added empirical dispersion, but a reparameterized version order to yield optimal results with dispersion. With these functionals the amount of exact exchange is non-zero for $r_{12} = 0$ and rises to 100% at $r_{12} = \infty$.

The exchange correlation potential of a hybrid functional a decays asymptotically as $-a/r$, with a being the fraction of exact exchange, while the exact behavior would be $-1/r$, which is recovered by all of the range-separated hybrids that use 100 % HF exchange in the long-range limit.[341]

The Coulomb-attenuating method (CAM-B3LYP) uses, apart from the range-separation parameter μ, two additional parameters and is also bound at the long-range limit (see

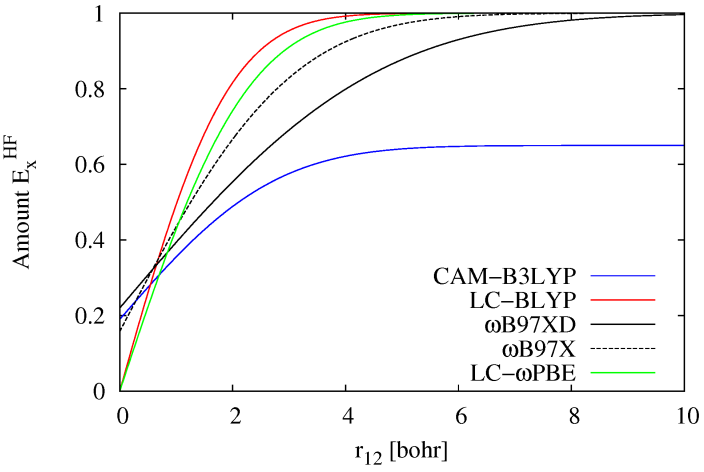

Figure 6.16: Schematic plot of the amount of exact exchange against r_{12} for different functionals.

section 3.3.2). For $r_{12} = \infty$ the amount of exact exchange reaches 65 %.
The behavior of the amount of exact exchange for different range-separated functionals is given schematically in Figure 6.16. The graphs were obtained by plotting the error function with the corresponding parameters.[xvi]

From Fig. 6.16 it is clear that CAM-B3LYP should always contain less HF-exchange than ωB97XD. Hence it makes sense that it is more prone to underestimate the energy of the CT state. While ωB97X contains slightly less exact exchange than ωB97XD at short distances, the amount of HF exchange becomes significantly larger in the medium- and long-range region. Since the dispersion is of no relevance for the calculation of the excitation energy it might be a promising approach to add ωB97X excitation energies to the ωB97XD ground state curve. The results using the more problematic monomer geometry of Settels et al. are depicted in Fig. 6.17. Contrary to ωB97XD the character of the two states is now predicted correctly. This is due to the fact that the CT state is now 0.25 eV above the NE state at 0 Å. The functionals LC-BLYP and LC-ωPBE also predict the correct character and give qualitatively correct results. The CT state is computed to

[xvi] In order to sketch the behavior of ωB97X and ωB97XD simply the weighted sum of the two range-separation functions is plotted, i.e.

$$c_x \mathrm{erfc}(\mu r_{12}) + \mathrm{erf}(\mu r_{12}). \tag{6.56}$$

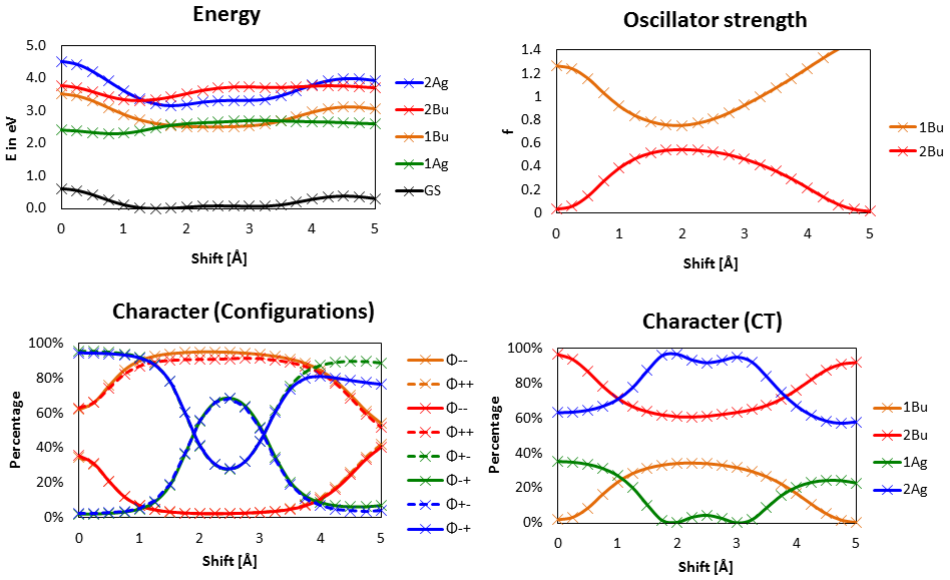

Figure 6.17: ωB97X/6-31+G(d) results for the longitudinal shift in the PBI dimer. Ground state surface: ωB97XD/6-31+G(d), monomer geometry: taken from Settels et al.

be 0.47 and 0.37 eV above the NE state.

In order to compare the accuracy of the methods, the energetic difference of the state energies with respect to SCS-ADC(2) are plotted in Fig. 6.18 (left-hand side).

As can be expected the functionals with a high amount of HF exchange like LC-ωPBE and LC-BYLP significantly overestimate the excitation energy, while ωB97XD and CAM-B3LYP underestimate it. ωB97X also slightly overestimates the excitation energy, but gives overall a nice agreement. Hence to add ωB97X excitation energies to the ωB97XD ground-state curve seems to be a sensible protocol, which should enable the calculation of bigger systems, e.g. tetramers (see below).

Another possibility is to make ωB97XD more robust by tuning the range-separation parameter ω. This was done in collaboration with Charlotte Brückner. Typically the parameters are tuned until the HOMO energy or the HOMO-LUMO gap reproduces an observable correctly, like the ionization or excitation energy. This is physically grounded, since the HOMO energy should be equal to the ionization energy in exact KSDFT. Here we used a more pragmatic approach and varied ω for the PBI dimer in the eclipsed configuration using the monomer geometry of Settels et al. until the agreement with the SCS-ADC(2) excitation energies (and oscillator strength) was optimal. The best result

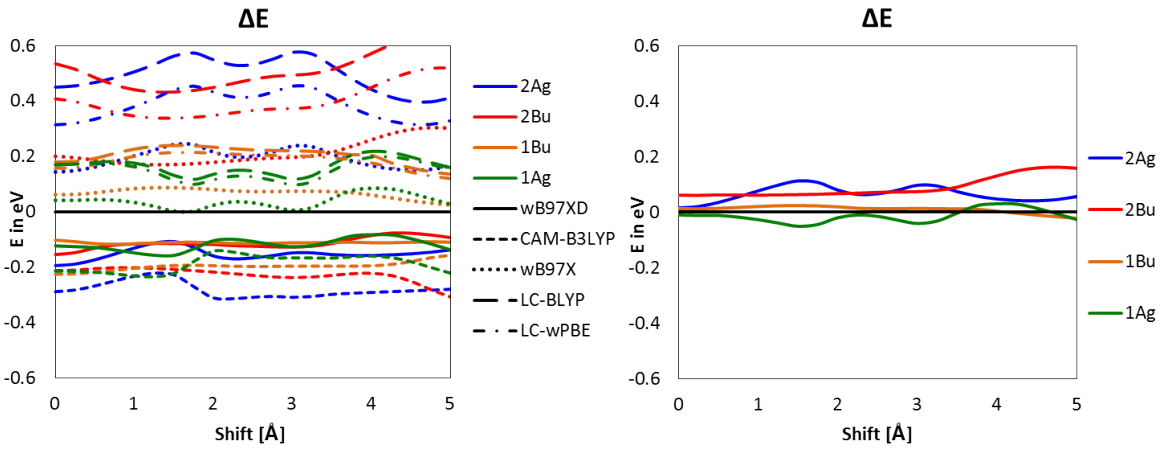

Figure 6.18: Energy difference to SCS-ADC(2)/cc-pVDZ. Left-hand side: various functionals, right-hand side: ωB97XD25/6-31+G(d) ($\omega = 0.25$)

was obtained with $\omega = 0.25\,\mathrm{bohr}^{-1}$. The corresponding method was called ωB97XD25. The difference in energy to SCS-ADC(2) along the potential energy surface is depicted in Fig. 6.18 (right-hand side). The agreement is excellent and the character is also reproduced correctly (see Figure 6.19). The CT state is predicted to be 0.15 eV above the NE state at 0 Å.

The result of the tuning process is illustrated in Fig. 6.20, where the difference to the SCS-ADC(2) results for the excitation energies and the oscillator strengths is plotted against ω. The oscillator strengths seem to be more or less converged above $\omega = 0.24\,\mathrm{bohr}^{-1}$, while the excitation energies rise continuously, which is quite is to be expected due to the increasing amount of HF exchange at intermediate distances. The slope of the curves agrees nicely with the amount of CT character computed for 0 Å, with the states with a larger CT character increasing more steeply than the ones, which are predominantly neutral.

Of course for results of high accuracy (e.g. for thermochemistry) all DFT parameters should be balanced and hence be reoptimized if one parameter is changed. This is one disadvantage of this approach. However, since the range separation parameter is changed only moderately (from $\omega = 0.2\,\mathrm{bohr}^{-1}$ to $\omega = 0.25\,\mathrm{bohr}^{-1}$) the description can be expected to be still sufficiently balanced to give reasonable results.

The mean error and the root mean square deviation of all investigated functionals with respect to SCS-ADC(2) are given in Table 6.2 for each state for the whole PES. The values again show that ωB97XD underestimates the excitation energies, but less than

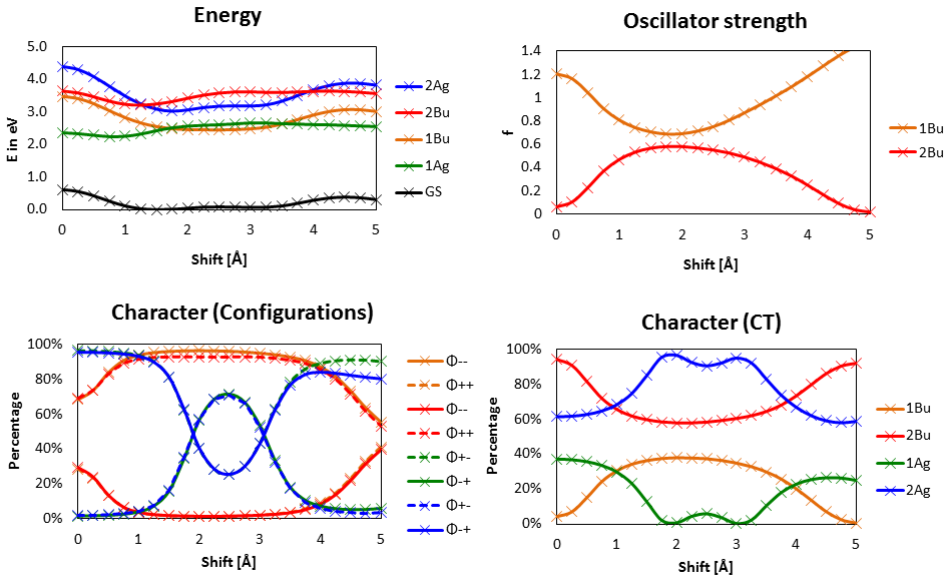

Figure 6.19: ωB97X25/6-31+G(d) results for the longitudinal shift in the PBI dimer. Ground state surface: ωB97XD/6-31+G(d), monomer geometry: taken from Settels et al.

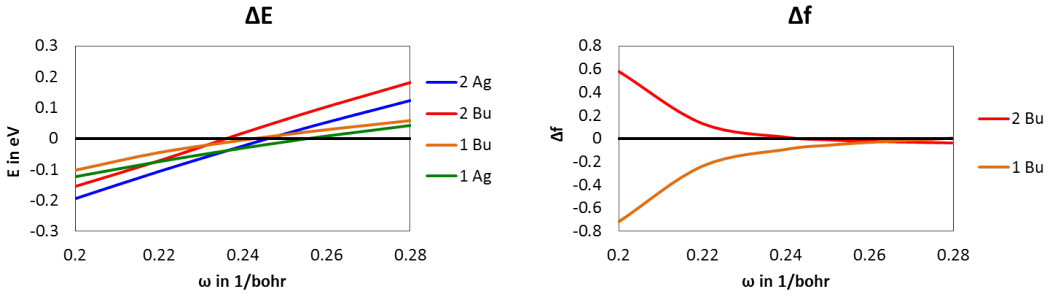

Figure 6.20: Energy difference of the excitation energies of ωB97XD(ω) and SCS-ADC(2)/cc-pVDZ (left-hand side) and the difference of the corresponding oscillator strengths (right-hand side) plotted against ω (shift distance 0 Å).

Table 6.2: The mean error (ME) and the root mean square deviation (RMSD) of different functionals with respect to SCS-ADC(2) (in eV) for the whole PES using the monomer geometry of Settels et al.

functional		1 A_g	1 B_u	2 B_u	2 A_g
ωB97XD	ME	-0.12	-0.11	-0.11	-0.15
	RMSD	0.12	0.11	0.12	0.15
CAM-B3LYP	ME	-0.19	-0.20	-0.23	-0.28
	RMSD	0.19	0.20	0.23	0.28
ωB97X	ME	0.04	0.07	0.21	0.19
	RMSD	0.04	0.07	0.22	0.19
LC-BLYP	ME	0.16	0.20	0.51	0.50
	RMSD	0.17	0.21	0.52	0.50
LC-ωPBE	ME	0.15	0.18	0.40	0.38
	RMSD	0.15	0.19	0.40	0.39
ωB97XD25	ME	-0.01	0.01	0.09	0.06
	RMSD	0.03	0.02	0.10	0.07

CAM-B3LYP, while LC-ωPBE overestimates the excitation energies, which is even more the case for LC-BLYP. ωB97X is only slightly overestimating. The excitation energies predicted by ωB97XD25 are very close to the reference. The RMSD of this method is greatest for the 2 B_u with 0.1 eV. All methods give a larger error for the 2 B_u and 2 A_g states than the 1 A_g and 1 B_u states.
It should be noted that the relative energy of the CT and the NE state will also depend on the intermolecular distance between the monomers. Hence it is likely that also for the functionals with a higher amount of HF exchange, there will be a certain distance where the NE and CT are so close that slight differences can change the character of the sates completely. However, for these functionals this can be expected to occur for distances between the π planes significantly smaller than 3.3 Å, which are usually not observed.

In this section it was demonstrated that it is in principle possible to describe the excited states of perylene and PBI dimers with TDDFT. However, care must be taken since due to the closeness of the CT and NE state minor changes can have a dramatic effect. For instance, when the excited states of standard molecules are computed, it is usually observed that the method applied for the geometry optimization is of minor importance. This is not the case for the dimers.

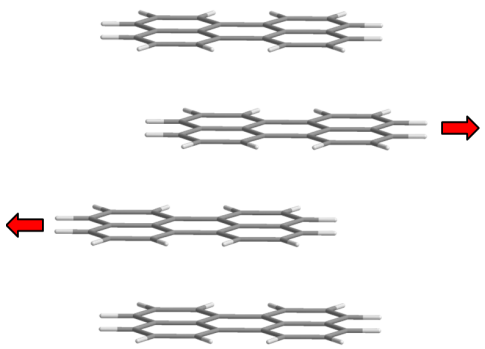

Figure 6.21: Definition of the longitudinal displacement in the perylene tetramer.

Applications using TDDFT

It was shown that ωB97X as well as ωB97XD25 give a very good description of the dimer system. Also LC-BLYP and LC-ωPBE give a qualitatively correct description, but overestimate the excitation energies. The failure of CAM-B3LYP observed by Settels and Liu was confirmed and could be rationalized by the amount of HF exchange. The fact that TDDFT can be used opens new possibilities for the description of these systems. In the last part two applications of TDDFT, which are not possible with SCS-CC2, are discussed as a proof of principle, using the results of the previous benchmark of DFT functionals. The first one extends the system from a dimer to a tetramer. Since all perylene-based dyes show similar potential energy surfaces perylene itself was chosen due to computational reasons. Following the approach described above, the ground state surface was calculated with ωB97XD while the excitation energies were computed using ωB97X both in conjunction with the 6-31G+(d) basis sets. For the potential energy surface of the longitudinal shift, the two inner monomers were shifted against each other, while the two outer monomers were kept fixed (see Fig. 6.21).

This models the situation of a dimer in a perfectly eclipsed π-stack that becomes distorted, e.g. due to an excitation. Obviously this model is artificial since an eclipsed stack is typically not observed. However, using this model one can most easily evaluate the effect of the next neighbors in the stack and check whether an exciton trap state is still present, or whether it is just an artifact of the dimer model. Furthermore the calculations can give hints if the exciton is localized on the dimer or delocalized over the whole

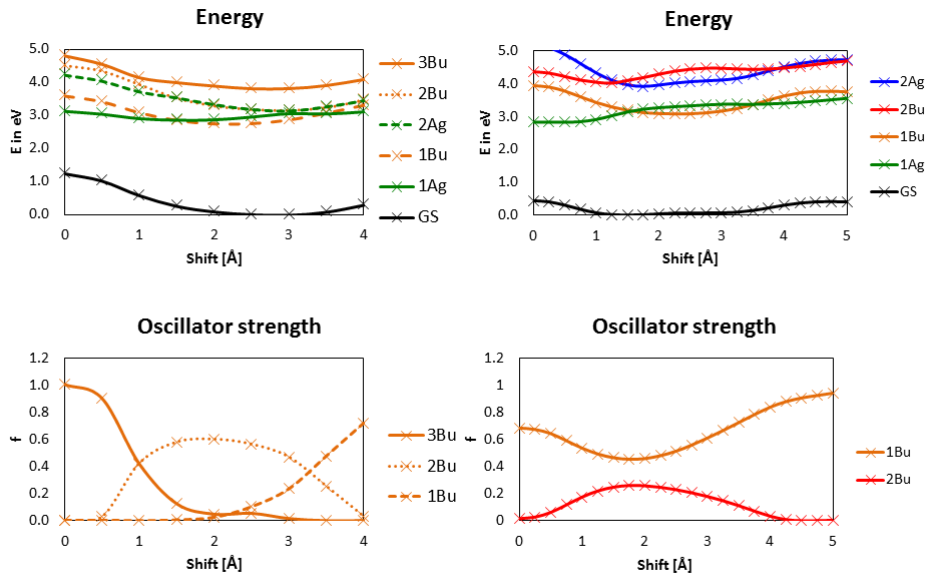

Figure 6.22: ωB97X/6-31+G(d) results for the longitudinal shift in the Perylene tetramer (left-hand side). Ground state surface: ωB97XD/6-31+G(d). For comparison the results for the dimer are given on the same level of theory (right-hand side)

tetramer.[xvii] The two A_g states and the three B_u states lowest in energy were chosen for this investigation.

The results are depicted in Fig. 6.22. For comparison the PES of the dimer are also given (right-hand side). Assuming the (artificial) eclipsed stack as a starting point (shift distance $r = 0$ Å), the trapping process in the dimer could work as follows: An excitation will lead to the bright 1 B_u state, from which it can reach the crossing with the 1 A_g state, where a part of the population can switch to the lower lying state (probably after a few back and forth vibrations). Moving on the 1 A_g surface to its minimum at 0 Å the exciton is trapped, since the state is dark and the Stokes shift is significant (1.1 eV), which makes an efficient excitation energy transfer impossible.

Starting from the ground state minimum at around 1.5 Å the wave packet will be transferred to the excited state in the region of crossing right away, where it is likely that a significant part of the population crosses directly to the trap state. Now the Stokes shift is obviously less pronounced, but still significant.

[xvii] Obviously a calculation, which neglects the rest of the environment as well as vibrations and defects can be expected to overestimate the delocalization of the exciton compared to the real system in the crystal.

Obviously the tetramer is more complex since more states arise. Furthermore already the ground state PES is quite different. At 0 Å the MOs are more or less localized on the inner and outer dimer and hence transitions can be classified according to this scheme. Hence this is a good (even though artificial) starting point to discuss the photochemistry of the system. The transition that contributes most strongly to the 1 A_g and the 3 B_u state at this conformation (c^2= 86% and 38%, respectively) is localized on the inner dimer. Thus these states can directly be compared to the ones of the dimer, while the other states contain transitions within the outer two monomers or between the inner and outer dimer. An excitation of the system at 0 Å will lead to the bright 3 B_u state and hence be mainly localized on the inner dimer. The excitation energy is predicted to be only 0.06 eV larger than in the dimer. The wave packet then experiences a gradient towards larger shift distances. Along this coordinate the MOs become more delocalized and the classification of the states is less obvious. The 3 B_u and the 2 B_u are rather close in energy and become very similar in character, which makes a population transfer to the 2 B_u state likely, presumably via an avoided crossing. The part of the population that stays in the 3 B_u state will have a rather long fluorescence life time, since the oscillator strength of this state decreases along the shift coordinate. The other part of the population moves to the minimum of the 2 B_u states at around 3 Å. Here it can either fluoresce to the ground state, since the 2 B_u has aquired a significant oscillator strength along the coordinate, which leads to a Stokes shift of 0.39 eV, or switch to the lowest B_u state. At distance between 2 and 3.5 Å the MOs are again rather localized and from the coefficients it can be inferred that the 2 B_u is dominated by transitions between the inner and outer dimer in this regions. Since the states are very close in energy and similar in character, the transition to the 1 B_u surface is quite likely. Here the wave packet can move to the minimum at around 2-2.5 Å. The fluorescence will occur with a rather long life time, due to the low oscillator stength. Around its minimum the 1 B_u state it is dominated by a transition in the inner dimer (75%) and hence the dimer fluorescence should be observed. The Stokes shift is predicted to be 0.60 eV. This state can also be considered to be a trap state, however, contrary to the dimer model this time the trap state is of B_u symmetry. In the dimer the 1 A_g state at 0 Å was the lowest excited state, while the minimum of the 1 B_u state is predicted to be lower than the one of the $1A_g$ state in the tetramer. Although the excitation energy of the 1 A_g state is significantly lower in the tetramer than the dimer (1.89 vs. 2.39 eV) this is overcompensated by the rise of ground state PES (1.26 vs. 0.44 eV compared to the dimer). Hence the minimum of the 1 A_g is shifted to 1.5 Å and is now higher in energy than the one of the 1 B_u state. However, since this depends crucially

on size of the dispersion it should be interpreted with care. Furthermore one has to keep in mind that the model system is artificial and does not represent an actual part of the crystal structure. Assuming the wave packet reaches the 1 A_g state in the tetramer it is less likely to move to 0 Å (as in the dimer), where a very long living fluorescence with a Stokes shift of 1.68 eV would be observed, but rather moves towards the crossing with the 1 B_u state.
Starting at the minimum of the ground state surface means starting from a significantly more shifted structure than in the dimer (3 Å vs. 1.5 Å). Here the excitation will dominantly lead to the 2 B_u state and the exciton will be delocalized over all four monomers. Since the wave packet is close to the crossing point a part will switch to the 1 B_u surface and be trapped at its minimum, where again a long-lived dimer fluorescence will be observed.
Thus also using the tetramer a trapping mechanism can be proposed. However, it is more complex than the one active in the dimer and there are also differences in the nature of the trap state.
The eclipsed tetramer system used here can serve as a proof of principle. In order to make a statement about an actual material one should start from actual stacks taken from the X-ray structure. Since PBI is well-studied in this respect it might be more suitable than perylene, although the computational cost will be much higher.

The second application uses a Z-matrix approach. As already mentioned above a direct geometry optimization is a much more elegant tool to explore the excited state surface and to find the relevant degrees of freedom than to conduct scans along all plausible coordinates and thus to construct several PES explicitly. In order to separate external and internal degrees of freedom the monomer geometry was built up relative to a cross of five dummy atoms in the middle of the central PBI ring. The monomer was optimized with the constriction that the dummy atoms are fixed and that the optimization yields D_{2h} symmetry on the ωB97XD/cc-pVTZ level of theory. The existence of a minimum within these constraints was confirmed with a frequency calculations. The dimer was constructed using the monomer with the dummy atoms in a way that all intermolecular degrees of freedom are defined between the dummy atoms on the different monomers (see Fig. 6.23). Using the Z-matrix of this dimer, the 6 intermolecular degrees of freedom can easily be separated from the internal degrees of freedom.
As a test the ground state of the dimer was optimized on the ωB97XD/cc-pVDZ level of theory with all internal degrees of freedoms kept fixed. The optimization yielded a

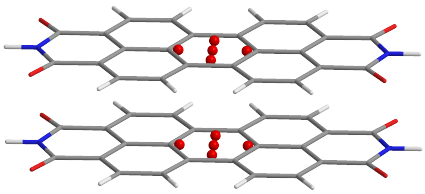

Figure 6.23: Dimer for the Z-Matrix approach. The dummy atoms are depicted in red.

conformation in which the monomers are rotated 29° against each other. Using a shifted starting structure another stationary point was found, where the monomers are longitudinally and transversally shifted against each other. This is in line with the results of Fink et al.[18,331]

For the optimization of the excited states, the use of ωB97XD seems unadvisable due to its insufficient robustness for this system. However, keeping the results presented above in mind there are two possibilities: either ωB97XD25 or ωB97X could be used. Since the latter lacks dispersion an empirical correction has to be included. Gaussian09 offers the possibility to add Grimme's D3 dispersion correction, however, due to the existence of the ωB97XD functional no parameters for ωB97X are defined. Since the coefficients of similar functionals should also be similar, using the factors defined for LC-ωPBE (sr: 1.0, sr,6: 1.355, s8: 1.297) should give a reasonable approximation. This method will be called ωB97X+D.

However, because both methods use altered parameters, it should be checked whether the description of the intermolecular interaction is still balanced. While an optimization in the ground state starting from the eclipsed conformation yields the rotated structure, when ωB97XD and ωB97X+D are used, the optimization with ωB97XD25 ends up in the shifted conformation. However, commencing from appropriate starting structures both ωB97X+D/cc-pVDZ and ωB97XD25/cc-pVDZ predict a rotated and a shifted stationary point, with the rotated structure being 1.5 kcal/mol lower in energy. ωB97XD/cc-pVDZ predicts the rotated structure to be 2.1 kcal/mol lower in energy. This indicates that both methods are still well balanced, despite the modified parameters.

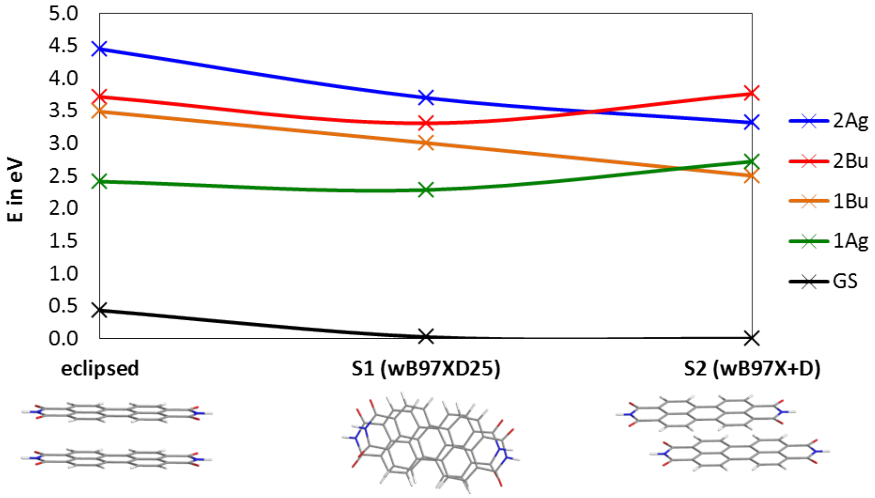

Figure 6.24: Ground and excited state for the eclipsed geometry and the optimized S_1 and S_2 state (the level for the optimization is given in brackets). Ground state: ωB97XD/6-31+G(d), excited states: ωB97XD25/6-31+G(d)

Due to the high computational cost the excited states were preoptimized with the 6-31G basis and the obtained structure subsequently reoptimized with the 6-31G* sets. Using ωB97X+D starting from the eclipsed geometry leads to a stationary point, where the monomers are shifted about roughly 2.5 Å against each other in line with the computed potential energy surfaces presented above (see for instance 6.10). In the S_1 state no convergence could be achieved.[xviii]

With ωB97XD25 the optimization in the S_1 led to a longitudinally twisted and slightly rotated structure, indicating that more than one single coordinate could be important. With this method the optimization in the S_2 starting from the eclipsed conformation did not converge directly. However using an already shifted starting structure also leads to the shifted stationary point.

Single points of the ground and excited states of the optimized structures were computed with ωB97XD/6-31+G(d) for the ground state and ωB97XD25/6-31+G(d) for the excited states and compared to the eclipsed conformation (see Fig. 6.24).

Obviously the inverse procedure would also be possible, i.e. to keep the intermolecular degrees of freedom fixed and to optimize the internal ones. This might also be interesting keeping in mind that Schubert and Settels proposed a distortion towards a zwitterionic (M^+M^-) structure. However, due to the high amount of degrees of freedom this is com-

[xviii] The optimization leads to a shifted and rotated geometry, where it oscillates between two structures.

putationally more demanding.

6.2.3 Semi-Empirical Methods

Electronic structure calculations of large systems often rely on semi-empirical methods. For the calculation of excited states especially the OMx methods by Thiel and coworkers (see section 3.2.4) have been proven to be quite successful. With these methods the excited states of systems containing dozens of perylene-based monomers can easily be calculated. However, usually the performance of these methods is evaluated for single molecules and hence it is uncertain whether they yield satisfactory results for excited states that arise primarily from the intermolecular interaction such as Förster transfer[345] etc. Therefore the performance of the semi-empirical methods was investigated carefully for the dimer model system of PBI.[xix] A significant part of the results presented in this section were obtained by Veronika Krämer in the framework of her Bachelor thesis.[347]
In her thesis she first evaluated the performance for the monomer. The lowest excited states of PBI are reproduced with reasonable accuracy by the OMx methods as compared to ADC(2)/cc-pVTZ, when a [12,12] active space[xx] is used.[347] The difference between the three individual methods is rather small.
The results of OM1 and OM3 calculations on the dimer can be found elsewhere,[347] here the results of an OM2 CISDT calculation with a large [16,16]-active space are exemplarily discussed (see Figure 6.25). Keeping in mind the approximations involved in the methods, OM2 can be expected to yield the best results. In the upper panel the ωB97XD/cc-pVTZ geometry was used for the monomer, while the geometry taken from Settels et al. was used in the lower panel. It is important to note that only the excitation energies and properties were taken from the GUGA CI calculation, while the results of the ωB97XD/6-31+G(d) calculation (with the corresponding monomer geometry) were used for the ground-state surface.
The excitation energies are in the correct order of magnitude, but otherwise the deviations to SCS-ADC(2) are large. Similar to ωB97XD the character of the B_u states for smaller shift distances is seriously dependent on the monomer geometry. While the 1 B_u state is correctly predicted to be the brighter state using the ωB97XD/cc-pVTZ geometry, this is not the case for small shift distances with the geometry taken from Settels et al. However, contrary to ωB97XD the shape of the potential energy surfaces is qualitatively

[xix] Some of the results concerning the ground state have already been published in reference.[346]
[xx] The active space used in the GUGA CI treatment was enlarged stepwise until a reasonable convergence was achieved.

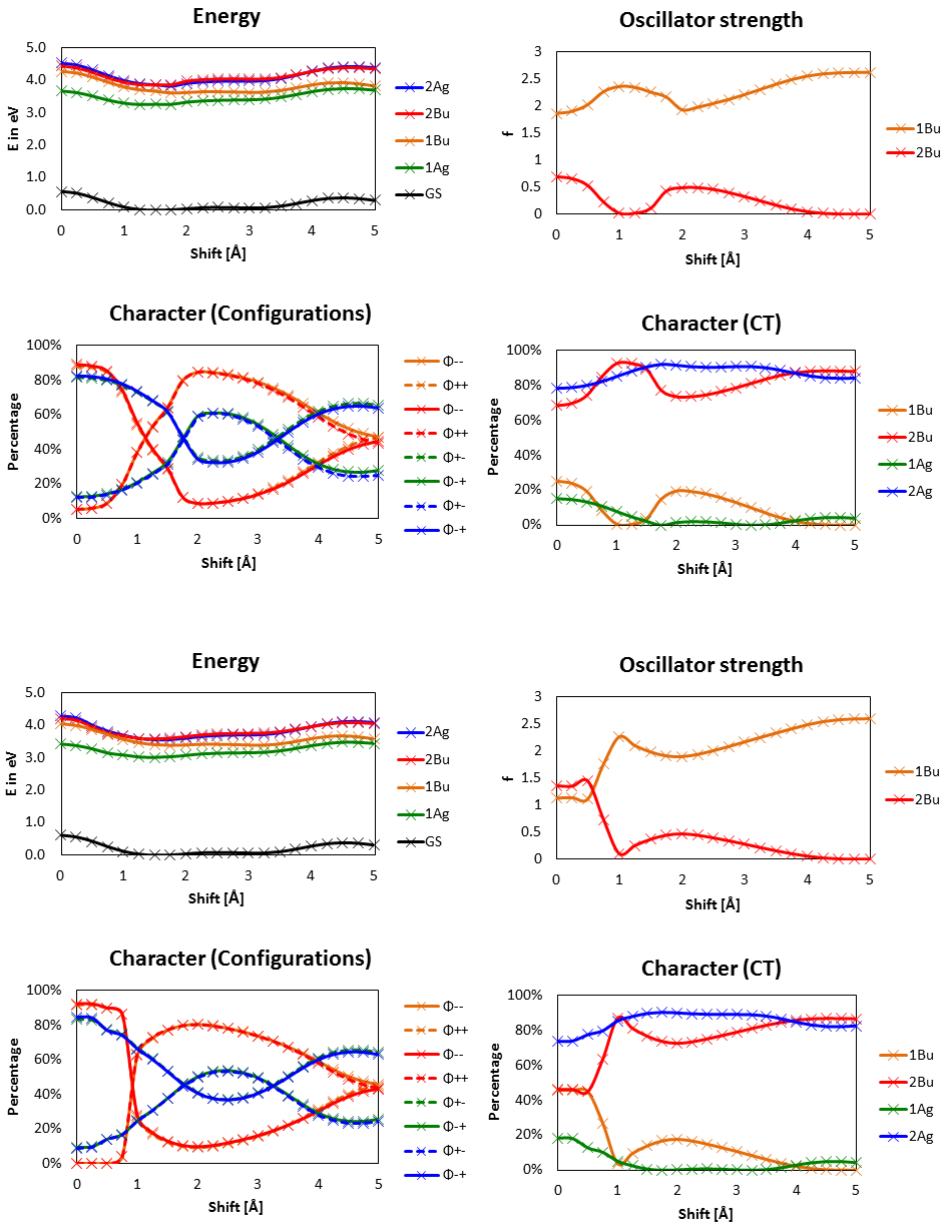

Figure 6.25: OM2[16,16] CISDT results for the longitudinal shift in the PBI dimer. Upper panel: ωB97XD/cc-pVTZ monomer geometry, lower panel: monomer geometry taken from Settels et al. Ground state surface: ωB97XD/6-31+G(d). For accurate results, see Fig. 6.10

wrong, regardless of the monomer geometry (see Fig.6.10 for comparison).
The most striking difference is that the crossing between the 1 B_u and the 1 A_g state is missing and hence no trapping is predicted. Apart from the fact that the excitation energies are quite far from the reference (Mean error: 1 A_g 0.75 eV, 1 B_u 0.81 eV, 2 B_u 0.48 eV, 2 A_g 0.43 eV) the shape of the potential energy surfaces is different and lacks features. The splitting between the states is also incorrect, which is of significant importance for optoelectronic applications. The importance roots in the fact that the rate for the excitation energy transfer is proportional to the square of the coupling constant J according to Fermi's golden rule.[348,349] Very often a supermolecular approach is used to compute the coupling constant, which is then given as one half of the splitting between the two lowest excited states that arise from the dimerization (see[350] and references therein for details).
The lacking features of the PES and the fact that the splitting is quite small at smaller shift distances leads to the assumption that the interaction between the molecules is underestimated by the semi-empirical method. This can either be attributed to the neglect (or approximation) of terms in the semi-empirical Hamiltonian or to the fact that a minimal basis set is used, which is inherently not well suited for the description of intermolecular interactions, or both effects might play a role. It is plausible that due to the very contracted basis functions the molecules do not "feel" the presence of each other correctly, since all interaction terms involving orbital overlap will be close to zero.
In order to investigate the reasons behind the failure of OM2 the energetic splitting between the 1 A_g and the 1 B_u state (i.e. twice the coupling constant J) has been computed with different methods and for different distances between the monomer planes. If the too small overlap is the root of the problem, then diminishing the distance between the monomers should overcome this deficiency, make the features appear and lead to an improved splitting. If on the other hand only the neglect of terms is responsible no significant change is expected. Another possibility to gain insight is to copute the excited states with TDDFT and a minimal basis, which should also lead to diminished features if the basis set size is of significant importance. Furthermore, assuming that the intermolecular overlap is the root of the problem implies that for large distances (where the overlap can be neglected) OM2 should agree with the high-level methods.
The results of the corresponding calculations can be found in Fig. 6.26. First of all it is evident that for the standard distance between the molecular planes of 3.3 Å the coupling constant predicted by OM2 indeed significantly lacks features, which are present when using SCS-ADC(2)/cc-pVDZ or ωB97XD/6-31+G(d). However, the features appear when

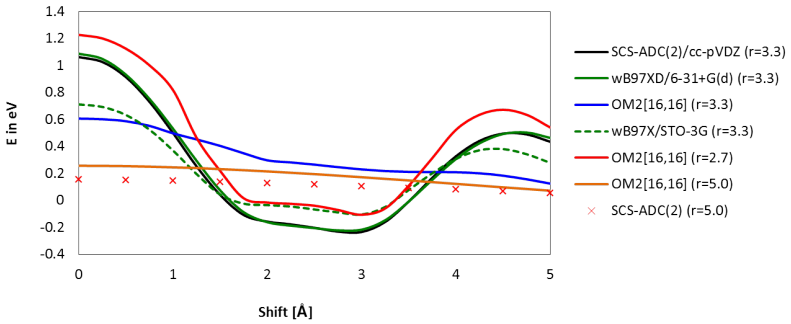

Figure 6.26: The energetic splitting between the 1 A_g and the 1 B_u state ($2J$) computed with different methods and for different distances between the molecular planes (monomer geometry: ωB97XD/cc-pVTZ).

the distance between the monomer planes in the OM2 calculation is diminished. At 2.7 Å the crossing between the 1 A_g and $1B_u$ state is also predicted by OM2, which is apparent form the slightly negative values of the splitting in Figure 6.26. Hence the assumption that the overlap is involved is corroborated. Comparing the curves at 3.3 Å, it seems that OM2 only predicts some part of the coupling constant correctly, but lacks a term that is oscillating along the coordinate.

Using ωB97XD with a minimal STO-3G[351] basis[xxi] the coupling is underestimated at the eclipsed conformation and the features are significantly reduced. However, less than with OM2, which shows that the basis set size is not solely responsible for the failure of OM2. Going to a larger intermolecular separation OM2 gives results, which are very well in accord with the SCS-ADC(2) results. This is again indicative that a wrong description of the orbital overlap is involved, since at r = 5 Å the overlap should be negligible.

In order to understand and rationalize these findings one needs to inspect which terms are responsible for the splitting between the states. Since the two lowest excited states belong to different irreducible representations the matrix elements are less easily derived in the delocalized picture using the CI approach than in the localized diabatic picture. The latter picture also has the advantage of being directly related to the transport integrals. Assuming the states to be completely neutral[xxii] the splitting will depend on

[xxi] This procedure was not possible with SCS-ADC(2) since no corresponding auxiliary basis, which is needed for the *ricc2* module, is implemented in TURBOMOLE.

[xxii] Since these two states have the least CT character along the whole PES this approximation seems justified.

the matrix element $\langle \Phi_{NE,A} | \hat{H} - E_{NE,A} | \Phi_{NE,B} \rangle$. However, keeping in mind that $\Phi_{NE,A}$ describes a local excitation on the monomer A, while $\Phi_{NE,B}$ describes an excitation on monomer B (see Fig. 6.4) this integral is also the electronic transfer matrix element. Using again the simple four electron/four orbital model from section 6.2.1 and a few further approximations the coupling constant can be written as (see[350] for details)

$$J \approx 2(H_A L_A | H_B L_B) - (L_A L_B | H_B H_A) = J_F - J_D. \tag{6.57}$$

The first term can be seen as the Coulomb interaction between two transition densities and represents the so-called Förster transfer, while the second term depends on the orbital overlap and is connected to the so-called Dexter transfer.[350]
Scholes, Harcourt and Ghiggino also included the CT determinants and derived the following formula for the electronic transfer element T_{RP} between two identical molecules[352–354]

$$T_{RP} \approx 2(H_A L_A | H_B L_B) + 2\beta_{H_A H_B}\beta_{L_A L_B}/A \tag{6.58}$$

with A beeing the energy difference between the local NE and CT states (i.e. M^+M^- and M^*M) and $\beta_{H_A H_B}$ and $\beta_{L_A L_B}$ are the reduced resonance integrals,

$$\beta_{H_A H_B} = h_{H_A H_B} - S_{H_A H_B} h_{H_A H_A}, \tag{6.59}$$

$$\beta_{L_A L_B} = h_{L_A L_B} - S_{L_A L_B} h_{L_A L_A}. \tag{6.60}$$

Again the matrix element contains the Förster integral and an orbital overlap dependent part $2\beta_{H_A H_B}\beta_{L_A L_B}/A$.
The reduced resonance integrals β are dependent on the two-center one-electron integrals, which are not neglected in the MNDO-based methods, but due to the approximations the evaluation involves the explicit calculation of the overlap matrix elements (see section 3.2.4). Due to the rather contracted basis it is likey that these terms will be highly underestimated. Because of the anisotropy of the p-functions of the interacting π-MOs it is not unlikely that these overlap-dependent terms are responsible for the oscillations along the shift coordinate (see below), while the Förster-type term can be expected to decrease steadily with increasing shift distances, since it can be approximated as dipole-diplole interaction.[350] Thus the underestimation of the overlap-dependent terms explains why the OM2 curve lacks features. The fact that the one-electron two-center hamiltonian elements are computed directly in DFT and not approximated by terms involving the

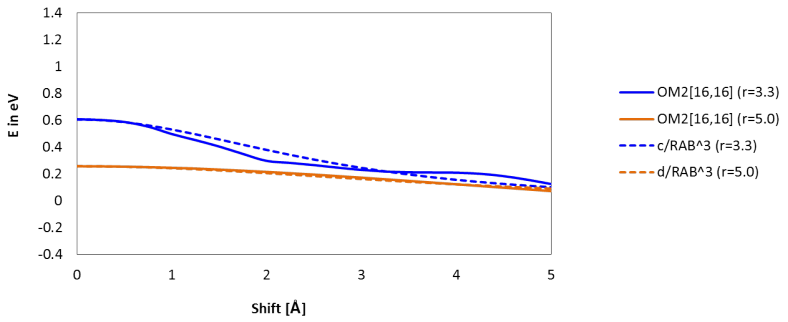

Figure 6.27: The distance dependence of the interaction between two point dipoles ($(const/R_{AB}^3)$) plotted for the longitudinal shift for two different distances between the molecular planes. For comparison the splitting predicted by OM2 is also given. The constant was chosen so that the interaction energy reproduces the OM2 value at the eclipsed geometry.

overlap explicitly might also explain, why the basis set size is less problematic for DFT. While it is logical to assume that the OMx methods will have problems with the overlap-based terms, there is no inherent reason why the Förster-type integral should be computed with a significant error. Thus in the long-range limit, where the overlap-depending, Dexter-type terms vanish and only the Förster-type term survives, it can be assumed that OM2 will give a reasonable description, which is in line with the results presented above. In Fig. 6.27 the distance dependence of the interaction between two point dipoles ($1/R_{AB}^3$), which are shifted against each other is fitted to the splitting predicted by OM2 using a single parameter. At 5.0 Å the splitting predicted by OM2 can be almost perfectly modeled by assuming a dipole-dipole interaction. This is not too surprising at an intermolecular distance of this size. However at 3.3 Å OM2 shows only some minor features, which are not present in the dipole-dipole interaction, but apart from that, the agreement is excellent. This is also in line with an underestimation of the overlap-dependent parts.
Hence all the results presented so far can be rationalized by assuming that a too contracted basis set leads to an underestimation of the intermolecular overlap. This is especially severe, since these overlap terms are explicitly calculated and used to approximate the two-center one-electron integrals in MNDO-based methods.

In section 4.2.3 it was shown that the repulsion between two closed-shell molecules is also dependent on two-center one-electron integrals (the reduced resonance integrals) and

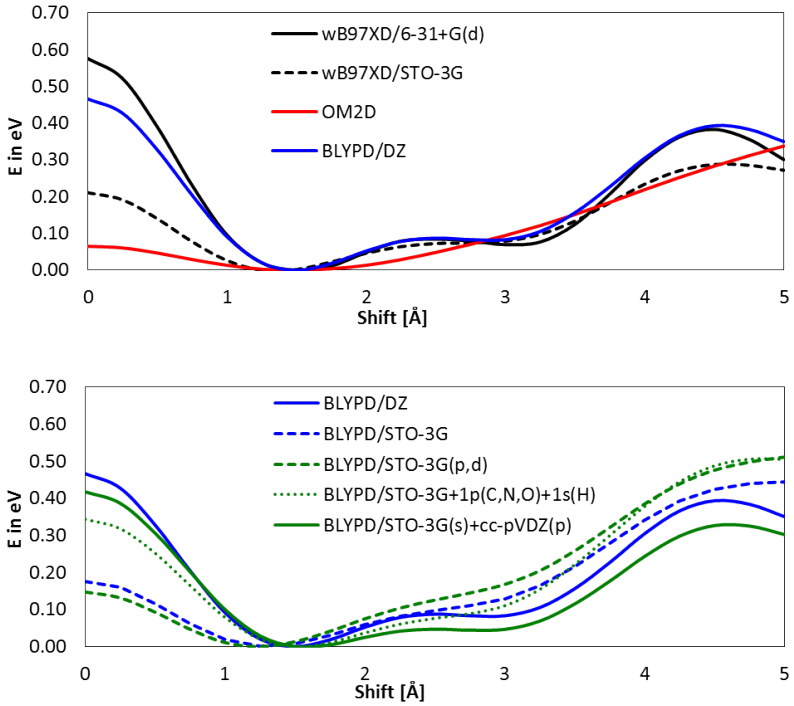

Figure 6.28: Ground state potential energy surface for the longitudinal shift in the PBI dimer (monomer geometry: ωB97XD/cc-pVTZ) computed with different methods (upper panel) and different basis sets (lower panel). For the description of the specialized basis sets see text.

hence also on the orbital overlap. Thus if the orbital overlap is small this should also have an influence on the repulsion and therefore on the ground state potential energy surface. Indeed comparing the ground state surface predicted by OM2D and ωB97XD/6-31+G(d) (see Fig. 6.28, upper panel) it is evident that OM2D underestimates the repulsion at the eclipsed conformation and lacks features similar to the coupling in the excited state. Using a minimal basis (STO-3G) also ωB97XD underestimates the repulsion and the features significantly, albeit less than OM2D. As already seen above, this indicates that the basis set effect plays an important part, but also that the approximation involved in the calculation of the matrix elements, especially the use of overlap integrals has an impact.[xxiii] On the one hand due to the approximations, the overlap is directly involved in the corresponding matrix elements and on the other hand the one-electron two-center

[xxiii] For *p*-type functions it is not very straightforward to compare STO and GTO basis functions, due to the rather complex normalization process and the fact that the former are usually given in polar coordinates, while the latter are typically implemented in Cartesian coordinates. Writing both in

integrals involve parameters, which are typically not fitted to reproduce intermolecular interactions and hence this failure is not completely surprising.
In order to investigate which basis functions are most important for the accurate shape of the PES several different basis sets have been constructed (see Fig. 6.28, lower panel) and used with BLYP-D3 as implemented in TURBOMOLE. As can be seen this pure DFT functional predicts a similar ground state PES as ωB97XD, when a sufficiently large basis set is used.
In the STO-3G(p,d) basis set a single Gaussian polarization function was added for H (p) and C,N,O (d) to the STO-3G function. The exponent was taken from the cc-pVDZ basis. Obviously the polarization function has only a minor effect. Hence instead an additional single *p*-function was added for C,N,O and an *s*-function for H, and the resulting basis set was named STO-3G+1p(C,N,O)+1s(H). The coefficients were taken from the uncontracted functions of the cc-pVDZ basis sets. The inclusion of this single basis function on each atom has a significant effect and produces a qualitatively correct result for the

---

polar coordinates and just looking at the radial part one obtains[50]

$$R_{\zeta,l}^{STO} = \frac{(2\zeta)^{3/2}}{\sqrt{(2l+2)!}}(2\zeta r)^l \exp(-\zeta r) \tag{6.61}$$

$$R_{\boldsymbol{\alpha},\mathbf{c},l}^{STO-3G} = N\sum_{i=1}^{3} c_i \frac{2\alpha_i^{(3/4)}}{\pi^{1/4}}\sqrt{\frac{2^l}{(2l+1)!!}}(\sqrt{2\alpha_i}r)^l \exp(-\alpha_i r^2). \tag{6.62}$$

The normalization constant can most simply be obtained by numerically integrating

$$\int_0^\infty (R_{\boldsymbol{\alpha},\mathbf{c},l}^{STO-3G})^2 r^2 dr \tag{6.63}$$

using gnu octave.[355] Taking the values for a 2p-basis functions on carbon used in the STO-3G[351] basis and the Slater-type functions of OM2 (1.420)[127] the following graph was obtained.

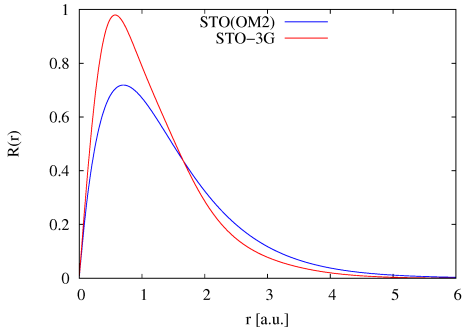

From the Figure it is evident that the basis used in OM2 is similar to the STO-3G basis set. The probability density is even a bit higher in the long range region.

ground-state PES. A further improvement is obtained if all the *s*-functions are taken from the STO-3G basis, while all *p*-functions for C,N and O are taken from the cc-pVDZ basis sets (STO-3G(s)+cc-pVDZ(p)).
Hence adding an additional *p*-type function to the minimal basis improves the description significantly and it can hence be assumed that adding an additional function to the semi-empirical methods with subsequent reparameterization might also lead to improved results. However, this procedure is very time-demanding and therefore it is questionable if the benefit makes it worthwhile.
Of course one could also argue that the monomer charge distribution, the core-core repulsion, or the dispersive part are incorrectly described by the semi-empirical methods, which leads to the observed lack of features in the ground-state PES. However, Veronika Kramer computed Mulliken charges of the monomers and calculated the PES with different dispersion corrections and methods with different core-core repulsions and found that neither of these is responsible for the problems with the ground state.[347] The underestimation of the overlap is the only assumption that is in line with all observed results. In the next section it will consequently be shown that the shape of the ground state PES can be modeled by using an overlap-based repulsion.

The results presented in this section show that the semi-empirical methods investigated here are inapt for the description of the excited states and even the ground state potential energy surface of perylene-based dimers, at least as long as their intermolecular distance is in a range, where the orbital overlap still plays a role. Since this is to a significant extent due to the small basis it can be assumed that the other semi-empirical methods will have the same problem. Veronika Krämer investigated the performance of several other methods and indeed found a similar failure.[347]

6.3 Designing a Force Field for Perylene-Based Dyes: OPLS-AA$_O$

For the modeling of excitonic states in organic semiconductors consisting of small prganic molecules, QM/MM methods are a promising approach. A small part of the system can be calculated with a high-level method (e.g. *ab inito* or DFT methods), while the environment is treated on the MM level. Since the systems under consideration consist of

separate molecules, the boundary can be easily defined without cutting through covalent bonds, thus making no link-atom scheme necessary, which simplifies the approach.
While the results presented above indicate that a dimer should be a sensible starting point for the QM system and show furthermore that an appropriate TDDFT approach can be found, the MM-system still has to be defined. Since the molecular morphology of the films in organic solar cells is difficult to predict theoretically and to determine experimentally, a common assumption is that the system has a microcrystalline structure, where each domain can be modeled by the crystal structure. Whether this assumption is justified or not, the ideal crystal structure is a sensible starting point, anyway. In a second step, disorder can easily be generated, for instance by using a molecular-dynamics approach.
However, a force field is needed that describes the intermolecular interaction accurately. Especially for the intermolecular motions involved in the trapping mechanism the interaction of the π-densities is crucial. In this section, it is shown that standard force fields do not perform well in this respect and an ansatz for an anisotropic repulsion energy is presented that gives significantly improved results.

6.3.1 The Failure of Standard Force Fields

In order to be able to easily adjust the different terms in the force field, the non-bonded interaction between two monomers[i] was implemented using an octave script.[355] The non-bonded interaction terms of OPLS-AA[213,214] consist of the Coulomb interaction between point charges and the Lennard-Jones potential, which are both easy to implement and to parameterize. Therefore, this energy expression is a convenient choice. Moreover, parameters for substituted organic aromatic systems are already defined.[214] Since it is designed to model the behavior of organic liquids and was shown to yield good results,[356,357] OPLS-AA can be assumed to describe the intermolecular interactions reasonably well, despite the simple functional form.
Therefore the energy expression

$$E_{ab} = \sum_{i}^{i\in a} \sum_{j}^{j\in b} \left[\frac{q_i q_j e^2}{r_{ij}} + 4\epsilon_{ij} \left(\frac{\sigma_{ij}^{12}}{r_{ij}^{12}} - \frac{\sigma_{ij}^{6}}{r_{ij}^{6}} \right) \right], \tag{6.64}$$

[i] Since only the intermolecular interactions are of interest, implementing just the terms describing the non-bonded interactions suffices.

was implemented, with q_i being the atomic charges and σ_{ij} and ϵ_{ij} being the parameters of the Lennard-Jones potential.[ii] Using the parameters defined for OPLS-AA, the interaction energy can easily be calculated along the longitudinal shift (see Figure 6.29). For comparison the shift was also calculated with AMOEBA using TINKER[358] by Maxim Tafipolsky. OPLS-AA predicts the minimum to be located at a too large shift distance and lacks features similar to OM2-D. Furthermore, the repulsion at the eclipsed geometry seems to be significantly underestimated. AMOEBA predicts the position of the minimum roughly correctly, but similar to OPLS-AA, the underestimated repulsion and the lack of features is irrefutable.
In order to understand the failure of OPLS-AA, one can analyze the different contributions,

$$E_{ab} = E_q + E_{rep} + E_{disp} = \sum_{i}^{i\in a}\sum_{j}^{j\in b}\frac{q_i q_j e^2}{r_{ij}} + \sum_{i}^{i\in a}\sum_{j}^{j\in b} 4\epsilon_{ij}\frac{\sigma_{ij}^{12}}{r_{ij}^{12}} - 4\epsilon_{ij}\sum_{i}^{i\in a}\sum_{j}^{j\in b}\frac{\sigma_{ij}^{6}}{r_{ij}^{6}}, \qquad (6.65)$$

along the PES, which are depicted in Figure 6.30.[iii] E_q is the electrostatic interaction, which is modeled as the Coulomb interaction of atomic point charges, E_d is the dispersive and E_{rep} the repulsive part of the van der Waals energy E_{vdw}. Thus, E_{rep} can be be

[ii] Technical details of the implementation: The standard combination rules were applied, e.g. $\sigma_{ij} = \sqrt{\sigma_{ii}\sigma_{jj}}$. In order to be able to easily check the choice of the atom type, a subroutine was written that plots the atoms and their positions along with the atom type and saves it as a PNG file. For convenient in- and output, own file types were defined and corresponding subroutines were written. The coordinates plus the atom type are defined in a *.ct* file, while the parameters (atomic charges and Lennard-Jones parameters) are stored in a *.prm* file. Functions handling the output of the potential energy surfaces and *.xyz* files were also written. The main script performing the OPLS-AA calculation reads in the coordinates of the monomer and generates a dimer with the desired displacement of the monomers. It then calls subroutines for the different energy contributions or the complete OPLS-AA energy, respectively. The loop over different shift distances (e.g. the longitudinal displacement) was also directly implemented into the script. Since the main function expects the input structure to lie in the xy-plane, a preconditioning function was designed that beforehand aligns the monomer. The latter is defined by two vectors (see Figure).

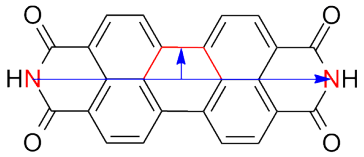

At first, the function aligns the vector defined by the two nitrogen atoms along the x-axis, with the origin being exactly in the middle between the two atoms. Then, a second orthogonal vector is defined by searching the four atoms closest to the origin, choosing two of them and adding their position vectors. The resulting vector is projected onto the zy-plane and rotated to the x-axis.

[iii] In this Figure, as well as in the following graphs, the range for the shift was enlarged to 8 Å.

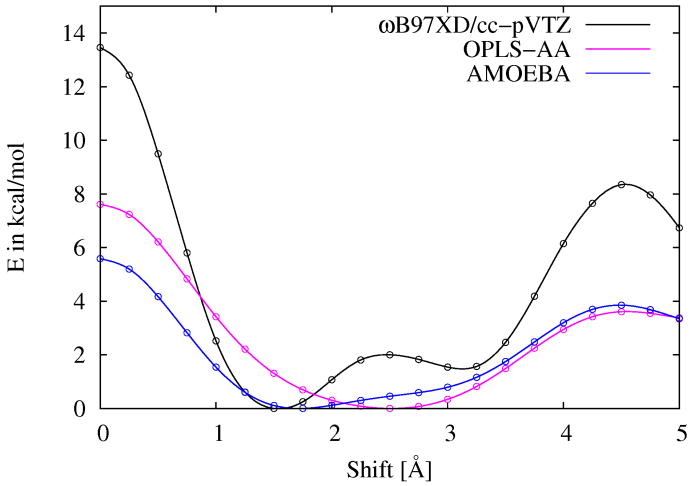

Figure 6.29: Ground-state potential energy surface of the longitudinal shift in the PBI dimer computed with OPLS-AA,AMOEBA as well as ωB97XD/cc-pVTZ

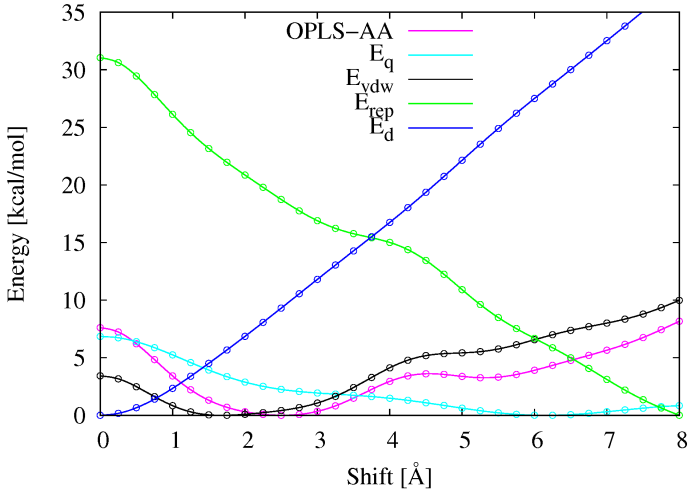

Figure 6.30: Different energy contributions along the longitudinal shift. With E_q being the Coulomb, E_d the dispersive and E_{rep} the repulsive part of the van der Waals energy E_{vdw}. The minimal value of all energy contributions has been set to zero. It should be noted that the shift distance was enlarged to 8 Å.

identified with the closed-shell repulsion, which is also sometimes called Pauli-repulsion.[238] As can be expected for systems with a moderate polarity, the van der Waals energy is already a reasonable approximation for the total energy. Both curves show roughly the same behavior. The Coulomb energy mainly leads to an increase close to the eclipsed conformation, since the charge repulsion is maximal here. Along the shift the Coulomb interaction deceases, but rises again for distances above 7 Å, since the two polar bisimide groups become spatially close again. It seems rather unlikely that the missing features are caused by an error in the coulomb interaction, especially since AMOEBA with its more involved handling of the electrostatic interaction also lacks features. However, at least the underestimation of the repulsion close to the eclipsed conformation could be corrected by increasing the charge repulsion. Therefore, the quality of the corresponding parameters (i.e. the atomic charges) has to be checked.

Among the two components of the van der Waals energy, the repulsion is much more likely to be responsible for the lacking features of the potential energy curve than the dispersion. The dispersion energy curve is rather continuously increasing as one might expect and since an almost identical approach is used in the DFT-D methodology, where the problem does not arise,[iv] it can be assumed that the dispersive part is not responsible for the failure of the force field.[v] Furthermore, the repulsive part of the van der Waals interaction can also be used to correct the underestimation of the repulsion. Therefore, the repulsive interaction also needs to be inspected carefully.

The Electrostatic Interaction

In order to investigate the quality of the OPLS-AA charge parameters, atomic charges have been calculated with different schemes (Mulliken, NBO, Hirshfeld and ESP) using BLYP, B3LYP and different basis sets as implemented in Gaussian09. Instead of comparing the charges itself, the Coulomb energy along the shift computed with different charges was compared.

The energy computed with Mulliken charges was not surprisingly found to be extremely basis set dependent. The STO-3G, cc-pVDZ and cc-pVTZ basis sets yield completely different results and hence a judgment of the quality of the OPLS-AA charges is not possible

[iv] The accuracy of the DFT-D approach for the ground state can be confirmed by comparing the potential energy surfaces to the results of calculation with SCS-MP2, see[326]

[v] Plotting the dispersion correction from a BLYP-D3/cc-pVTZ computation performed with TURBOMOLE for the longitudinal shift reveals that it has a smaller slope than the dispersion energy of OPLS-AA, but the same shape. Plotting the two dispersion energies against each other and performing a linear regression analysis gives a correlation coefficient of $R^2 = 0.99$.

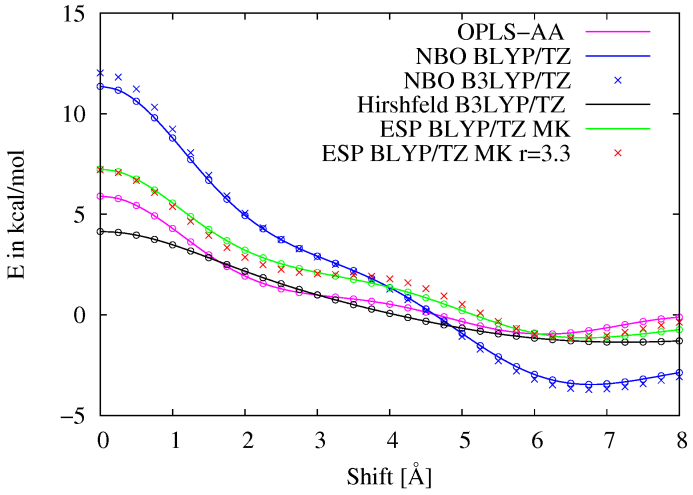

Figure 6.31: Coulomb energy along the longitudinal displacement calculated with different sets of atomic charges. TZ ≡ cc-pVTZ, MK ≡ Merz-Kollman scheme

with this approach. Since this was expected, the Mulliken charges were only computed for the sake of completeness. Using NBO, Hirshfeld or ESP[vi] charges, there is a significant change when going form STO-3G to cc-pVZD, but the difference between cc-pVDZ and cc-pVTZ is rather small. Some exemplary results are presented in Fig. 6.31. The results obtained with Hirshfeld as well as with ESP agree well with the ones obtained using the OPLS-AA charges. The implementation of the ESP scheme in Gaussian allows to enter alternative radii and hence it was checked if changing the radii of all elements to the distance between the monomers (r = 3.3 Å) gives a significant improvement. However, although the curve shows slightly more features, the effect of the radius seems (at least in this range) to be of minor importance. With the NBO charges the magnitude of the Coulomb interaction is higher than with the other charges. The NBO results also show that the choice functional, which is used for the calculation, is not crucial.
Since ESP charges actually reproduce the electrostatic potential, which is the important physical quantity for the charge-charge interaction between the monomers, they can be assumed to provide the best results. Following this assumption the OPLS-AA charges are also quite accurate. Nevertheless, it was tested whether using a different charge scheme gives improved results. In Fig. 6.32 the total energy along the shift is plotted using OPLS-AA, NBO and ESP charges and compared to the DFT results. Using the ESP charges with the altered radii changes the total energy only negligibly compared to the

[vi]For the calculation of the ESP charges the Merz-Kollman scheme was used, but it was checked that the charge fitting method of Hu, Lu, and Yang[359] does not yield significantly different results.

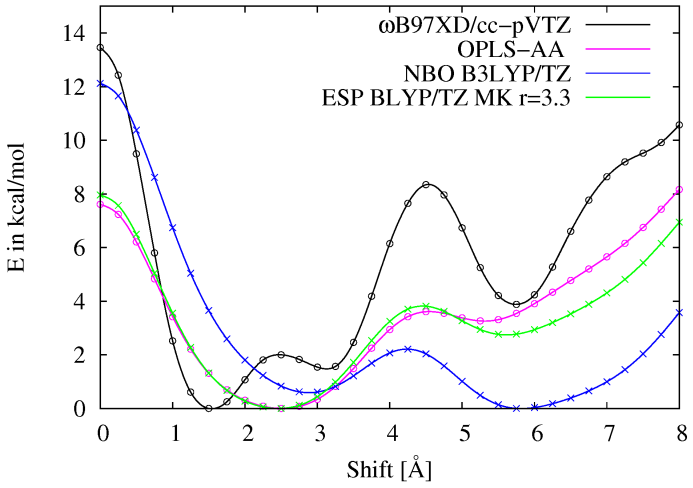

Figure 6.32: Total energy along the longitudinal displacement calculated with different atomic charges. TZ ≡ cc-pVTZ, MK ≡ Merz-Kollman scheme

standard OPLS-AA charges. As can be expected, the NBO charges lead to a stronger repulsion at the eclipsed conformation, but otherwise do not improve the shape of the curve. Moreover, the global minimum (along this coordinate) is now predicted to be around 6 Å, which is definitely incorrect.
Thus, one can conclude that the OPLS-AA charges seem to be well-suited and that the electrostatic interaction is not the main reason for the failure of the force field. This is corroborated by the fact that even AMOEBA, which relies on multipoles and includes polarization, gives incorrect results.[vii]

The Closed-Shell Repulsion

In section 4.2.3, it was shown that the repulsion between two closed-shell molecules is connected to the molecular overlap or overlap between the densities, respectively. In section 6.2.3, it was derived that the underestimation of overlap-dependent terms is responsible for the missing features in the ground-state curve predicted by the semi-empirical methods. In the case of the longitudinal motion of two PBI monomers against each other, the closed-shell repulsion arises due to the interaction of two π-densities (see Fig. 6.33). In the spirit of molecular mechanics, this repulsive interaction can be decomposed into contributions from atom pairs. The interaction between the atomic centers, however, can

[vii] Although the PES computed with AMOEBA shows a lack of features and underestimates the repulsion close to the eclipsed geometry, it provides a better description in the region from 1Å to 3.5 Å, which indicates that the higher-order multipoles and/or the polarization are nevertheless also important.

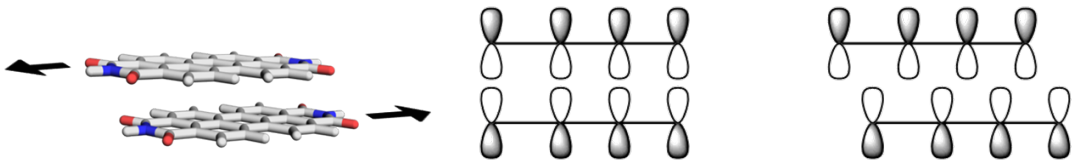

Figure 6.33: Schematic representation of the interaction of the two π-densities at different points of the PES.

be expected to be inherently anisotropic due to the shape of the p-orbitals. However, since the repulsion is modeled via an $\frac{1}{r_{ij}}^{12}$-term in the Lennard-Jones potential in OPLS-AA, which assumes a completely isotropic interaction between each pair of atoms, it is not surprising that the description is erroneous. Hence, an anisotropic modeling of the repulsion would be needed for an accurate description. However, whether this assumption is grounded has to be verified.

The energy of a DFT-D calculation is naturally partitioned into the part of the electronic structure calculation and the empirical dispersion correction. The latter is basically the same as in molecular mechanics. Thus, in the spirit of the partitioning of a force field, the pure DFT contains the electrostatic plus the closed-shell repulsion. Comparing the sum of the electrostatic energy and the repulsion energy of the force field with the pure DFT energy should be instructive. This approach definitively rules out any contributions from the dispersive part. Since the electrostatic interaction was already cleared from the suspicion of being responsible for the failure, any significant differences can be attributed to an error in the closed-shell repulsion.[viii]

In order to check if the problem really lies in the functional form of the repulsion term (e.g. the isotropy) and not just in a simple underestimation, a fit can be performed, where the repulsion energy is fitted linearly to the difference of the DFT energy and the electrostatic interaction,

$$E_{Diff} = E_{DFT} - E_q \tag{6.66}$$

$$E_{Diff} \approx p_1 E_{rep} + p_2. \tag{6.67}$$

[viii] Obviously, small differences will occur due to the fact that modeling the electrostatic interaction via point charges is an approximation.

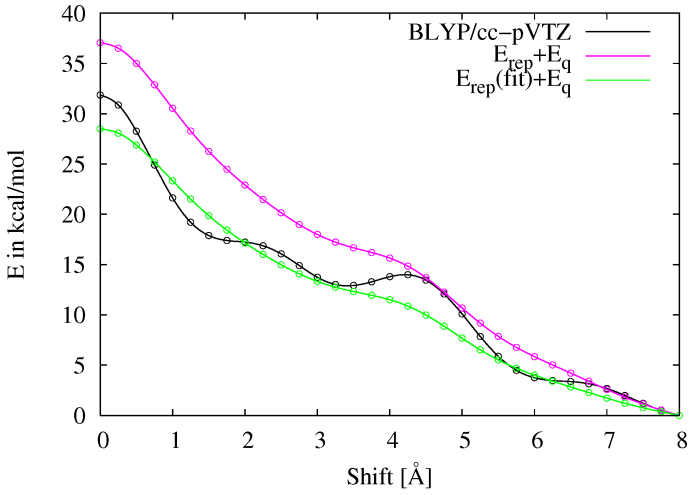

Figure 6.34: Comparison of the pure DFT energy along the shift with the sum of electrostatic and repulsion energy with and without fit.

p_1 and p_2 are the fit parameters. With this fit the repulsion is simply scaled.[ix] The results of a BLYP/cc-pVTZ calculation performed with Gaussian09 are depicted in Figure 6.34.[x] It is evident that the sum of electrostatic and repulsion energy is indeed approximately comparable to the DFT energy, but lacks features. As can be expected, the fit shifts the curve, so that it is closer to the DFT energy, however, the features are obviously still missing and hence the curve looks similar to a moving average of the DFT curve.
This again indicates that the way the repulsion is modeled is physically incorrect. Of course, it is possible that with a different set of parameters, a better agreement could be obtained. However, several test calculations were performed, which did not yield any significant improvement. Thus the assumption that the functional form of the repulsive term is incorrect is quite likely. However, the hypothesis that an anisotropic repulsion (albeit physically more grounded) leads to a better performance has to be tested and critically challenged.

6.3.2 An Anisotropic Repulsion

An anisotropic repulsion can of course be generated in several different ways of varying complexity. In order to test the assumption at first, a simple proof of principle approach

[ix] The DFT energy values were shifted so that the minimal value of the PES is zero prior to the fit. The fit was performed using the *fit* function implemented in gnu octave.
[x] In the Figures presented in this and the following sections, the minimum of each PES has been set to zero, unless stated otherwise.

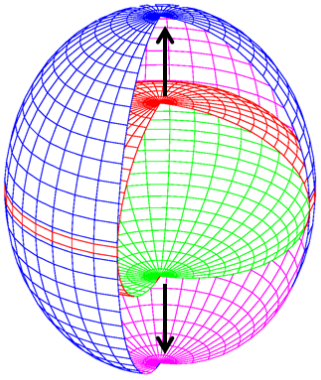

Figure 6.35: Effect of the anisotropy parameter: the interaction sphere becomes an ellipsoid

can be used. The Lennard-Jones repulsion is isotropic since all atoms j around a certain atom i, which are on the surface of a sphere with the radius r_{ij}, give the same energy contribution. There is thus no angular dependence. In order to distort the "interaction sphere" into an ellipsoidal shape and hence to introduce an angular dependence, one can simply introduce a parameter λ,

$$r_{ij} = \sqrt{(x_i - x_j)^2 + (y_i - y_j)^2 + \lambda(z_i - z_j)^2}, \tag{6.68}$$

which results in a simple anisotropic repulsion model. The effect of the anisotropy parameter is schematically depicted in Figure 6.35. Here, the z-component is scaled by the parameter in order to mimic the anisotropy of the p_z-functions.
In order to evaluate the performance of the ansatz, the same approach as above was used, i.e. a linear fit of the repulsion energy to the difference between the DFT and the electrostatic energy for all points of the PES. The value of λ was varied in a loop in steps of 0.05 until the RMSD between the DFT and the force field potential energy curve was minimal. Of course, by introducing an anisotropic repulsion, one should reconsider the choice of parameters ($\{\sigma\}$,$\{\epsilon\}$) because the OPLS-AA parameters were optimized for an isotropic repulsion. Since finding the correct parameter set involves an optimization with several degrees of freedom, which is at this proof of principle stage not worth the effort, the parameters used for the repulsion were simply set to $\epsilon = 1$ and $\sigma = 3$ for all atoms. Thus, one can differentiate the effects due to the anisotropy and due to the different parameters.

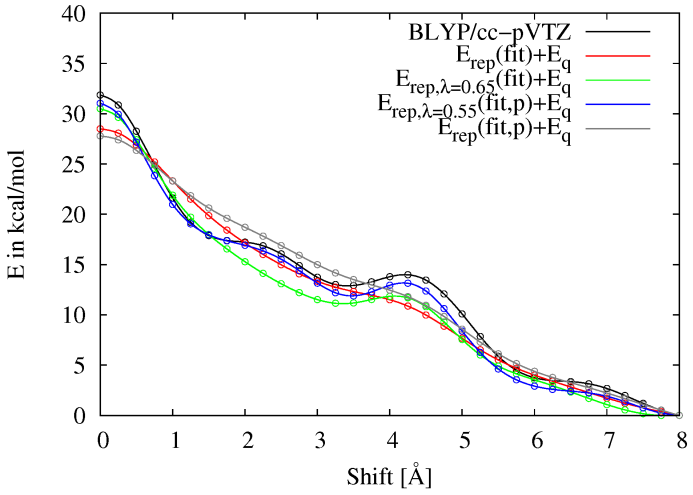

Figure 6.36: Comparison of the pure DFT energy with the sum of electrostatic and repulsion energy using an isotropic (E_{rep}) as well as an anisotropic repulsion ($E_{rep,\lambda}$). For E_{rep}(fit,p) and $E_{rep,\lambda}$(fit,p) the "p" indicates that different parameters were used ($\epsilon = 1$ and $\sigma = 3$ for all atoms)

The complete equation for the interaction energy can then be be written as

$$\begin{aligned} E_{ab} &= E_q + E_{rep}(\lambda) + E_{disp} \\ &= E_q + p_1 \tilde{E}_{rep}(\lambda) + p_2 + E_{disp} \\ &= \sum_i^{i\in a}\sum_j^{j\in b} \frac{q_i q_j e^2}{r_{ij}} + p_1 \sum_i^{i\in a}\sum_j^{j\in b} 4\tilde{\epsilon}_{ij} \frac{\tilde{\sigma}_{ij}^{12}}{r_{ij,\lambda}^{12}} + p_2 - 4\epsilon_{ij} \sum_i^{i\in a}\sum_j^{j\in b} \frac{\sigma_{ij}^6}{r_{ij}^6} \end{aligned} \tag{6.69}$$

At first, only the sum $E_q + E_{rep}(\lambda)$ is compared to the DFT energy, as in the last section. The results are depicted in Fig. 6.36. For comparison, also the fitted curve with the isotropic repulsion from Fig. 6.34 is given. With the standard values for ϵ and σ the optimal value for the anisotropy parameter is $\lambda = 0.65$ ($E_{rep,\lambda}(fit)$). Introducing the anisotropy reduces the RMSD of the force field compared to the DFT curve from 1.43 kcal/mol to 0.96 kcal/mol. One can also see that some of the features appear. There are only some minor deviations in the range from 1 to 3 Å. This can be resolved by changing the parameters to $\epsilon = 1$ and $\sigma = 3$ for all atoms ($E_{rep,\lambda}(fit, p)$). The optimal value of the anisotropy is $\lambda = 0.55$, the RMSD is 0.42 kcal/mol and the agreement is now excellent. In order to understand the effect of the changed parameters, the isotropic repulsion is also plotted using $\epsilon = 1$ and $\sigma = 3$ ($E_{rep}(fit, p)$). As one can see, the curve is flatter in the range from 1 to 3 Å, which diminishes the deviation. It seems that the anisotropy covers

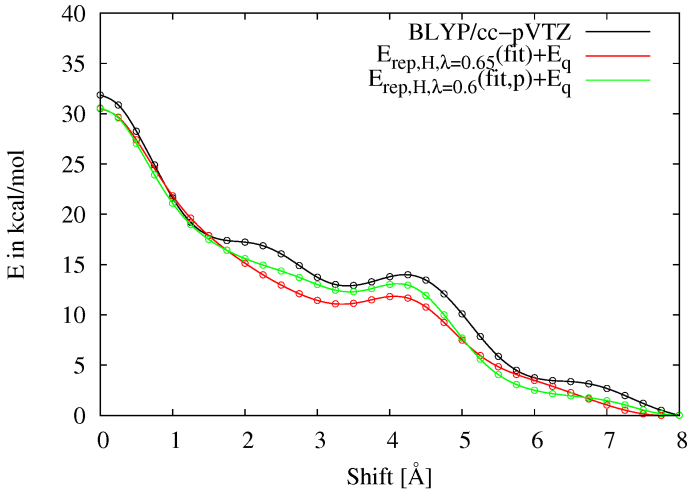

Figure 6.37: E_{rep}+E_q with anisotropic repulsion without a (repulsion) contribution from the hydrogen atoms.

all main effects of the repulsion energy and does not need very different parameters for the different atoms.

The results demonstrate nicely that introducing the anisotropy clearly leads to an improved description. The features in the PES appear naturally by switching on the anisotropy. Hence it can be assumed that in order to obtain a physically grounded description of the intermolecular interactions, an anisotropic repulsion is needed, at least for intermolecular distances where the overlap is non-negligible.

However, at the current point, the implementation has one unphysical aspect. For the computation of the interaction energy a subroutine *distancematrix* is called, which calculates the distance between two atoms on different monomers with the coordinate vectors $\vec{v}_1$ and $\vec{v}_2$. Since the anisotropy parameter is introduced in this subroutine, all intermolecular interactions are made anisotropic, even those between hydrogen atoms. Especially if the parameters $\epsilon = 1$ and $\sigma = 3$ are used for all atoms, the hydrogen atoms have a significant effect, which makes not much sense, if one assumes that the repulsion stems from the interaction of the π-densities.

In order to eliminate the repulsion contributions of the hydrogen atoms one can simply choose $\epsilon = 0$ for all hydrogen atoms. The results are depicted in Figure 6.37. Using standard parameters for ϵ and σ the PES is quite similar to the one with hydrogen contributions (RMSD = 0.97 kcal/mol). If the modified parameters ($\epsilon = 1$ and $\sigma = 3$) are used the curve is slightly worse (RMSD=0.58 kcal/mol) than the one with H contribution.

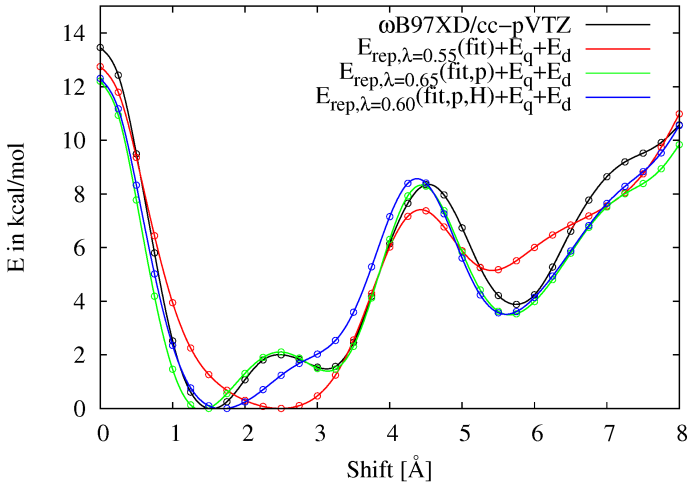

Figure 6.38: E_{rep}+E_q+E_d with anisotropic repulsion with ($E_{rep,\lambda=0.55}(fit)$, $E_{rep,\lambda=0.65}(fit,p)$) and without ($E_{rep,\lambda=0.65}(fit,p,H)$) a contribution from the hydrogen atoms. The letter "p" indicates that different parameters were used in the computation of the repulsion ($\epsilon = 1$ and $\sigma = 3$ for all atoms).

Hence one plausible assumption is that the anisotropic repulsion on the hydrogen atoms compensates the neglect of other effects, e.g. higher electrostatic moments. Since the repulsion contribution from the hydrogen atoms leads to better results, the pragmatic approach is chosen and it is kept in the implementation unless noted otherwise.
In order to complete the approach and to obtain the total energy, the dispersion interaction has to be added. The repulsion energy can then be fitted to the difference $E_{DFTD} - E_q - E_d$. For the calculation of the dispersion contribution, the standard OPLS-AA parameters were used.[xi] ωB97XD/cc-pVTZ was chosen as reference method. The results are depicted in Fig. 6.38 Using the anisotropic repulsion with standard parameters for the repulsion leads to a shifted minimum, but otherwise gives a quite satisfactory result (RMSD = 1.0 kcal/mol). Using the altered parameters ($\epsilon = 1$ and $\sigma = 3$) gives an accurate description (RMSD = 0.58 kcal/mol). Neglecting the hydrogen atoms in the repulsion treatment again slightly worsens the results (RMSD = 0.71 kcal/mol).[xii]

[xi] That means that even if the parameters are altered in the repulsion term, the standard ones are still used in the dispersion term (see eq. 6.69).

[xii] Of course, it is also possible to use the standard isotropic Lennard-Jones repulsion for the interaction between the hydrogen atoms (i.e. $\lambda = 0$), which seems physically more grounded. However, then the question remains how to treat the interaction between the hydrogen atoms and the second-row elements. Test calculations revealed that keeping the anisotropy for the latter interactions, but using the isotropic repulsion for the interactions between the hydrogens also gives quite accurate results.

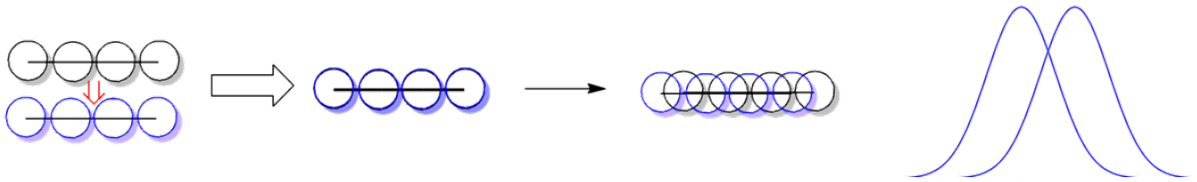

Figure 6.39: Using an s-type primitive Gaussian overlap in two dimensions as a basis for an anisotropic repulsion.

To summarize the results obtained in this section so far, one can clearly state that introducing the anisotropy in the repulsion significantly improves the description. Even the proof-of-principle model with a simple anisotropy parameter can accurately reproduce the DFT curve.

Using a simple anisotropy parameter is a very simple ansatz. A more subtle approach is to use an overlap-based model. Obviously p-type functions seem to be most suitable for the problem and a corresponding ansatz is giving in the next section. Since the implementation of the overlap integrals of p-type functions is much more demanding than for s-type functions, at first a test implementation using s-type primitive Gaussians is presented to see if an overlap approach gives an improved result. Using the formula for the integral derived in reference[49] the ansatz for the repulsion can be written as,[xiii]

$$E_{rep} \propto \sum_{i,j} \langle s_i | s_j \rangle = \sum_{i,j} N \frac{\pi}{\beta_i + \beta_j}^{3/2} e^{-\frac{\beta_i \beta_j}{\beta_i + \beta_j} r_{ij}^2}. \tag{6.70}$$

Since Gaussian functions are spherically symmetric, the question arises how this ansatz can be used to introduce anisotropy. This can be achieved by projecting the problem into two dimensions, see Fig. 6.39. If only the x- and y-coordinate are used in the subroutine that calculates the distance matrix, the overlap is calculated in two dimensions. At 0 Å, all corresponding pairs of Gaussians are hence on top of each other and the overlap is maximal.[xiv] For small displacements, the overlap between these corresponding pairs decreases similar to the overlap between the two two-dimensional Gaussians, which are sketched on the right-hand side of Fig. 6.39. This has the consequence that the interaction between any atom pair is significantly stronger if they are on top each other than if they

However, since the ansatz with a simple anisotropy parameter is only meant to serve as a proof of principle, this approach was not further pursued.

[xiii] The justification for such an ansatz is given in the next section, here it is justed tested as a proof of principle.

[xiv] Since there are 40 pairs of corresponding Gaussians, whose overlap integrals are all one, the total overlap is 40 plus the contribution from all other pairs.

are displaced, more than this would be the case for an isotropic repulsion. Hence this ansatz also introduces anisotropy.
The implementation of the subroutine in octave is simply given as:[xv]

```
function [S]=S_Overlap(n,coord,Beta,d)

#n:    number of atoms in one monomer (read from xyz)
#coord: matrix of the coordinates of the dimer
#Beta: exponent of the Gaussians

S=0;
   for i=1:n
      for j=1:n
        v1=coord(i,1:3);
        v2=coord(j+n,1:3);
        rij=distancematrix_xy(v1,v2)/0.529;

        #normalisation
        N=(4*Beta(i)*Beta(j)/pi()^2)^(3/4);

        Int(i,j)=(pi()/(Beta(i)+Beta(j)))^(3/2)
        *e^(-Beta(i)*Beta(j)/(Beta(i)+Beta(j))*(rij)^2);

        #sum up and multiply with contraction coefficents:
        S=S+d(i)*d(j)*Int(i,j)*N;


       endfor;
     endfor;

end;
```

For this ansatz the contraction coefficients can be used to switch off the contribution of certain atoms. The subroutine *distancematrix_xy* computes the distance in the xy-plane (i.e. by neglecting the z-coordinate).
The repulsion energy is again fitted to the difference with the DFT energyy. The total

[xv] The implementation follows the description in reference [49] and the subroutine was already used in the well-tested "Hercules program", a code developed in collaboration with Johannes Becker for teaching purposes. Hercules computes the energy and several important matrix elements and properties using HF, VBSCF, MP2 and CISD for the H_2 molecule with a minimal STO-3G basis for different intermolecular distances.

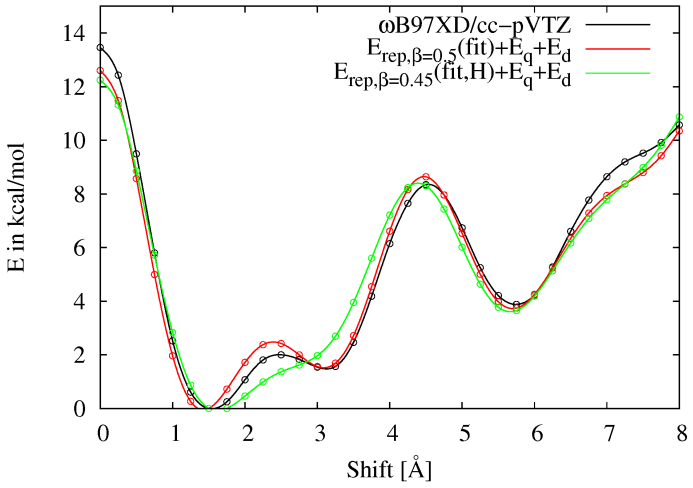

Figure 6.40: E_{rep}+E_q+E_d using an anisotropic repulsion based on the overlap of s-type Gaussian functions in two dimensions, with ($E_{rep,\beta=0.5}(fit)$) and without ($E_{rep,\beta=0.45}(fit,H)$) a contribution from the hydrogen atoms.

energy can then be written as

$$\begin{aligned} E_{ab} &= E_q + p_1\tilde{E}_{rep}(\beta) + p_2 + E_{disp} \\ &= \sum_i^{i\in a}\sum_j^{j\in b}\frac{q_i q_j e^2}{r_{ij}} + p_1\sum_i^{i\in a}\sum_j^{j\in b} S_{ij}(\beta) + p_2 - 4\epsilon_{ij}\sum_i^{i\in a}\sum_j^{j\in b}\frac{\sigma_{ij}^6}{r_{ij}^6}, \end{aligned} \tag{6.71}$$

with

$$S_{ij}(\beta) = \langle s_i(\beta)|s_j(\beta)\rangle. \tag{6.72}$$

The results are depicted in Fig. 6.40. Similar to the anisotropy parameter λ, β is also varied until the RMSD is minimal. The obtained results are comparable to the ones with the anisotropy parameter. With the s-overlap, an RMSD value of 0.49 kcal/mol is obtained. Excluding the contribution from the hydrogen atoms decreases the accuracy to RMSD = 0.69 kcal/mol. As already stated above, the inclusion of the anisotropy on the hydrogen atoms might compensate the lack of higher multipole moments. Another possibility is that it partly compensates that all atoms have the same parameter β. Since the ground-state surfaces of different perylene-based dyes are quite similar, it can be assumed that the perylene core is very important and hence that its contribution might be higher than the one of the bisimide. This is furthermore corroborated by the fact that the HOMO is also mainly localized on the perylene unit. Therefore, introducing different

parameters for different atom types might lead to a further improvement.
The results presented in this section demonstrate that using an overlap-based ansatz of the repulsion energy can give correct results. Even the simple overlap of s-type Gaussian functions in two dimensions leads to a significant improvement of the PES and introduces the features missing in standard force-field calculations. Hence a more formal derivation and justification of this overlap-based approach is given in the next section and the ansatz is extended to p-type functions, which should provide a more realistic model for the π-densities.

6.3.3 A Density-Based Overlap Approach Using Primitive Gaussian p-type Functions

In section 4.2.3 different approaches to calculate the intermolecular repulsion using overlap-dependent terms were discussed. On the one hand there are orbital-overlap approaches, where the overlap integrals of the MOs on the different monomers are used. On the other hand, there are methods based on the density overlap. If all MOs and their overlap integrals have to be calculated, much of the cost-effectiveness of force fields is lost. Using the density overlap fewer integrals have to be evaluated, but a converged SCF calculation is still needed. Hence, the approach used in this work is to use a simple approximation for the density overlap integral, which can be parameterized in the spirit of a force field, similar to Söderhjelm et al.[215]
Since the π-density can eventually be broken down to contributions of p-type Gaussian functions in any standard quantum-chemical calculation,[xvi] the most straightforward approach is to write the monomer density directly as a linear combination of atom-centered p-type Gaussian functions $\rho_A = \sum_i^A p_i$.[xvii] The density overlap can then be decomposed into a sum of overlap integrals over primitive Gaussians,

$$S_\rho = \int \rho_A(\mathbf{r})\rho_B(\mathbf{r})d^3\mathbf{r} = \int \left(\sum_i^A p_i(\mathbf{r})\right)\left(\sum_j^B p_j(\mathbf{r})\right) d(\mathbf{r}) = \sum_i^A \sum_j^B \langle p_i|p_j\rangle. \qquad (6.73)$$

Due to the shape of the p-type functions this ansatz introduces an anisotropy to the atom-atom interaction. The implementation follows two scripts of Valeev and coworkers,[360,361]

[xvi] Polarization functions are neglected, since a simple and efficient approach is needed.
[xvii] As already mentioned, this is similar to the ansatz followed by Söderhjelm et al.,[215] who expanded the density using Slater functions and approximated the resulting integrals with an exponential function (see section 4.2.3).

which cover the computation of the overlap integrals of primitive Cartesian Gaussian functions with an arbitrary orbital angular momentum. A basis function is given as

$$\phi = x^l y^m z^n e^{-\alpha r^2}. \tag{6.74}$$

The normalization constant is given by

$$N = \left[\left(\frac{2}{\pi} \right)^{3/4} \frac{2^{(l+m+n)} \alpha^{(2l+2m+2n+3)/4}}{\sqrt{(2l-1)!!(2m-1)!!(2n-1)!!}} \right]. \tag{6.75}$$

If one p-function is localized on atom **A** and the other on atom **B**, then the overlap integral is given as

$$\int \phi_1(\alpha_1, \mathbf{A}, l_1, m_1, n_1) \phi_2(\alpha_2, \mathbf{B}, l_2, m_2, n_2) d\mathbf{r} = N_1 N_2 e^{-\alpha_1 \alpha_2 (\overline{\mathbf{AB}})^2 / \gamma} I_x I_y I_z, \tag{6.76}$$

with $\gamma = \alpha_1 + \alpha_2$. The Gaussian function in equation 6.76 covers the radial dependence, while the angular dependence is covered by the contribution for the different spatial coordinates, which are given by

$$I_x = \sum_{i=0}^{(l_1+l_2)/2} f_{2i}(l_1, l_2, \overline{\mathbf{PA}}_\mathbf{x}, \overline{\mathbf{PB}}_\mathbf{x}) \frac{(2i-1)!!}{(2\gamma)^i} \left(\frac{\pi}{\gamma} \right)^{1/2}, \tag{6.77}$$

with

$$P = \frac{\alpha_1 \mathbf{A} + \alpha_2 \mathbf{B}}{\gamma} \tag{6.78}$$

and

$$f_k(l_1, l_2, \overline{\mathbf{PA}}_\mathbf{x}, \overline{\mathbf{PB}}_\mathbf{x}) = \sum_{i=\max(0,k-l_2)}^{\min(l_1,k)} (\overline{\mathbf{PA}})_x^{l_1-i} \binom{l_1}{i} (\overline{\mathbf{PB}})_x^{l_2-k+i} \binom{l_2}{k-i}. \tag{6.79}$$

The implementation is given as follows:

```
function [S]=P_Overlap(no,coord,_alpha)

#no:    number of data points (read from xyz)
#coord: matrix of the coordinates
#_alpha: exponent of the Gaussians

#Debug value:
```

```
#two centres coord=[0 0 0; 0 0 0.74], alpha=1.1, <pz|pz>=-0.392647

S=0;
S12=0;
bohr=0.529177;

        #-----------------------------------------------------------------
        #angular moments
        l(1)=0;
        l(2)=0;
        m(1)=0;
        m(2)=0;
        n(1)=1;
        n(2)=1; #--> n=0,1 s,pz orbital

        alpha(1)=_alpha;
        alpha(2)=_alpha;
        gamma=alpha(1)+alpha(2);

        #-----------------------------------------------------------------
        #Building Normalization constants
        for p=1:2
                N(p)=(2/pi())^(3.0/4.0)*2^(l(p)+m(p)+n(p))
                *alpha(p)^((2*l(p)+2*m(p)+2*n(p)+3)/4)/sqrt(sequence(2*l(p)-1)
                *sequence(2*m(p)-1)*sequence(2*n(p)-1));
        end

 for i=1:no
    for j=1:no

        A=coord(i,1:3)/bohr;
        B=coord(j+no,1:3)/bohr;
        RAB=norm(A-B);

        #-----------------------------------------------------------------
        #Definition of auxiliary quantities
        P=(alpha(1)*A+alpha(2)*B)/gamma;
        PA=P-A;
        PB=P-B;

        #-----------------------------------------------------------------
        #Building of the x,y,z-integrals
```

```
        Ix=0;
        for p=0:(l(1)+l(2))/2
          Ix=Ix+func(2*p,l,(PA(1)),(PB(1)))*sequence(2*p-1)/(2*gamma)^p
          *(pi/gamma)^0.5;
        endfor;

        Iy=0;
        for p=0:(m(1)+m(2))/2
          Iy=Iy+func(2*p,m,(PA(2)),(PB(2)))*sequence(2*p-1)/(2*gamma)^p
          *(pi/gamma)^0.5;
        endfor;

        Iz=0;
        for p=0:(n(1)+n(2))/2
          Iz=Iz+func(2*p,n,(PA(3)),(PB(3)))*sequence(2*p-1)/(2*gamma)^p
          *(pi/gamma)^0.5;
        endfor

        #-------------------------------------------------------------
        # Calculation of the actual overlap integral

        S12=N(1)*N(2)*exp(-alpha(1)*alpha(2)*RAB^2/gamma)*Ix*Iy*Iz;

        S=S+S12;

      endfor;
endfor;

end;
```

The two subroutines that compute the sequences are given by

```
#=============================================================#
#  Function that computes the sequence                        #
#  f_k=sum_{max(0,k-l_2)}^{min(l1,k)}PA_{x}^{l_1-i}#
#  \binom{l_1}{i}PB_{X}^{l_2-k+i}\binom{l_2}{k-i}  #
#=============================================================#
function f=func(k,ang,PA,PB)
  start=max(0,k-ang(2));
  limit=min(ang(1),k);
```

```
  f=0;
  for i=start:limit
    f=f+PA^(ang(1)-i)*nchoosek(ang(1),i)*PB^(ang(2)-k+i)
    *nchoosek(ang(2),k-i);
  endfor;

end;

#=============================================#
#  Function that computes the sequence        #
#  (2l-1)!!=1*3*5...(2l-1)                    #
#=============================================#
function product=sequence(x)
  product=1;
  n=1;

  while n <= x
    product=product*n;
    n=n+2;
  endwhile;

end;
```

The implementation was first tested for s-functions against the s-overlap subroutine. Furthermore, as a debug-value, the overlap between two p-functions separated by a distance of 0.74 Å with an exponent of $\alpha = 1.1$ was calculated with Gaussian09.
Obviously, script languages like octave do not yield very fast programs, since they are not compiled. The function was hence subsequently optimized for efficiency (*P_overlap_fast*), for instance by precomputing the results of the subroutine *sequence* before the double loop over the atoms and by restricting the generality to p-functions. Nevertheless, computing the overlap of a PBI dimer takes around 3.1 s on a 3 GHz processor. Computing the whole PES (33 data points) takes around 105 s. For the purpose of this work, this performance is sufficient, however, for a broader application an implementation using a language like C++ or Fortran should be used.

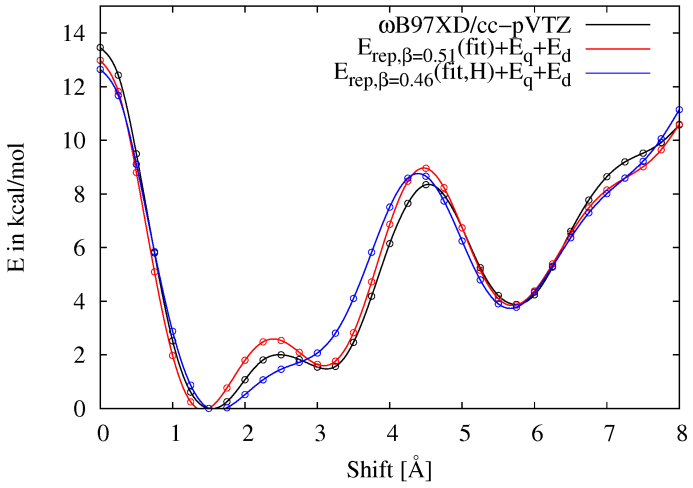

Figure 6.41: E_{rep}+E_q+E_d using an anisotropic repulsion based on the overlap of p-type Gaussian functions, with ($E_{rep,\beta=0.51}(fit)$) and without ($E_{rep,\beta=0.46}(fit,H)$) a contribution from the hydrogen atoms.

Fitting the repulsion energy again to the DFT PES gives the results presented in Fig. 6.41. β is taken as a parameter, similar to the approaches presented above and was first screened in steps of 0.05 and then in a second sweep in steps 0.01. The optimal value for β was found to be 0.51, which gives an RSMD of 0.46 kcal/mol. Deleting the basis functions on the hydrogen atoms leads to a worse result (RMSD=0.67 kcal/mol). The results are astonishingly similar to the s-overlap approach. This can be explained by the fact that the distance dependence of the $\langle s|s\rangle$ overlap integral in two dimensions and the $\langle p|p\rangle$ overlap integral both have a Gaussian distance term and hence basically the same distance dependence for the longitudinal shift. The significant difference in the prefactor is covered by the fit. Thus one might argue that the s-overlap, with its much easier implementation is the better choice. However, although it is not clear whether it is possible to find parameters of a certain generality using the p-overlap approach, it is very likely that very different parameters are needed for different intermolecular distances with the s-overlap approach. Hence the p-overlap approach seems to be more promising.
Although the agreement between the DFT and the fitted force-field curve is excellent, the significant contribution of the H-atoms is not completely satisfactory. The density overlap contains the complete density and hence also contributions from the σ-system and therefore also from the hydrogen atoms. However, p-functions are not the appropriate basis functions for the hydrogen atoms and hence it was tested whether it leads to an improved description if p-functions are only used for the second row elements, while s-functions are

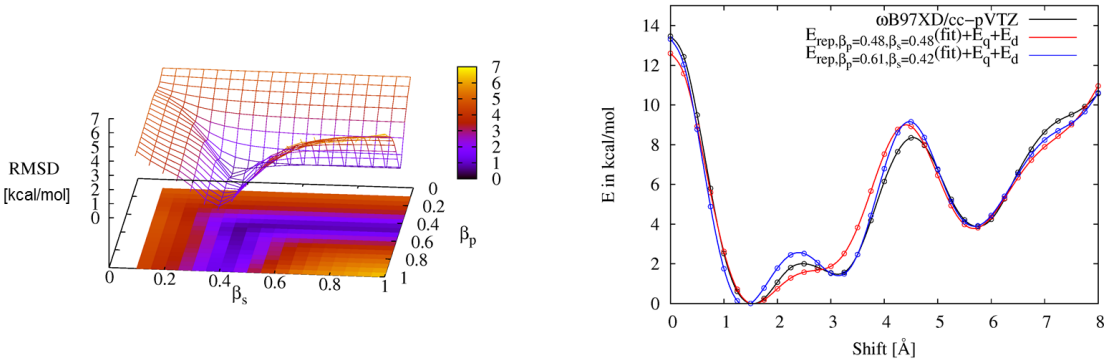

Figure 6.42: Left-hand side: Optimization of two different exponential parameters for s- and p-type Gaussian functions. Right-hand side: E_{rep}+E_q+E_d using an anisotropic repulsion based on the overlap of p-type Gaussian functions on second-row elements and s-type functions on all hydrogen atoms with identical and different parameters.

used for the hydrogen atoms. This is easily possible, since the function *P_overlap* can in principle handle any type of orbital. It is also easily possible to implement a computation of the percentage of $\langle s|s\rangle$, $\langle s|p\rangle$ and $\langle p|p\rangle$-overlap. In order to ensure positive $\langle s|p\rangle$-overlap a phase factor had to be introduced.[xviii] However, using the same β-value for H-atoms and second row atoms, this approach did not yield results of a significantly higher accuracy than without hydrogen atoms (RSMD = 0.63 kcal/mol, see Figure 6.42). Hence, two separate parameters were introduced and optimized separately. The optimization in the two-dimensional parameter space yielded $\beta_p = 0.61$ and $\beta_s = 0.42$. With these parameters an excellent agreement (RMSD = 0.46 kcal/mol) could be obtained. For higher values for β_s the contribution of the hydrogen atoms decreases and becomes eventually close to zero. Thus above a certain value the magnitude of β_s has no effect anymore (see Fig. 6.42, left-hand side).

The percentage of $\langle s|s\rangle$, $\langle s|p\rangle$ and $\langle p|p\rangle$-overlap at 0 Å is given as 26%, 18% and 56%. Using this overlap scheme is more physical than using p-functions also on the hydrogen atoms, but it is still questionable if such a high contribution of the hydrogen atoms is reasonable or if it is an artefact.[xix]

[xviii] Otherwise positive and negative contributions of the $\langle s|p\rangle$-overlap cancel each other.

[xix] In principle one might argue that as long as the ansatz works it does not matter if the amount of s-contribution allows any physical interpretation. However, arriving at an accurate description, which is general and uses transferable parameters, is obviously more likely using a physically grounded description.

Table 6.3: Exponential parameters and RMSD values for shifts with different distances between the intermolecular planes (in Å) using different methods.

Method		3.0	3.3	3.6
p(C,N,O)	β	0.47	0.46	0.45
	RMSD	1.54	0.67	0.32
p(C,N,O,H)	β	0.52	0.51	0.50
	RMSD	0.87	0.46	0.25
s(C,N,O)s(H)	β_s	0.41	0.42	0.43
	β_p	0.61	0.61	0.62
	RMSD	0.89	0.46	0.26

6.3.4 Generality of the Density-Based Overlap Approach

The results presented so far show that it is possible to derive a force field that accurately describes the intermolecular interactions between PBI monomers along the longitudinal shift. However, it is doubtful whether the parameters are general. Since this work is aimed at the modeling of excitonic states in perylene-based dyes with a focus on certain intermolecular degrees of freedom, which are important for a potential exciton trapping, it is sufficient if accurate parameters can be found for each system/degree of freedom. However, for broader applications, a certain generality and transferability of the parameters would be desirable. Therefore, this is also briefly investigated here. A complete survey of the generality against test sets is, however, beyond the scope of this work. Furthermore, for a general force field, different parameters for different atom types should be introduced. Optimizing this parameter space for a larger set of molecules is not feasible with the current implementation.

As a simple test, the shift is calculated for three different distances between the molecular planes: 3.0, 3.3 and 3.6 Å. The calculation is performed with p-functions on all atoms, p(C,N,O,H), p-functions only on the second row elements, p(C,N,O), as well as with p-functions on second row elements and s-functions on the hydrogen atoms, p(C,N,O)s(H). The results for the exponential parameter β are given in Table 6.3. As one can see, the value of β does not change dramatically and hence seems to be fairly transferable for different shift distances. However, the fit parameters are much more problematic, see Table 6.4. The fit parameters, especially the important scaling factor,[xx] seems to depend

Table 6.4: Fit parameters shifts with different distances between the intermolecular planes (in Å) using different methods.

Method		3.0	3.3	3.6
p(C,N,O)	p_1	-378.6	-518.8	-832.8
	p_2	7.8	23.0	24.3
p(C,N,O,H)	p_1	-548.3	-889.8	-1718.497
	p_2	12.8	25.1	25.175
p(C,N,O)s(H)	p_1	1832.5	4366.1	15029.4
	p_2	15.7	27.0	26.7

crucially on the interplane distance.[xxi] One way to remedy this might be to introduce a distance dependence into the scaling factor. In fact, there are approaches, where the density overlap is scaled by an exponential term.[215] This distance dependence could either be introduced for the complete system (i.e. $p_1 \rightarrow p_1(r)$), with r being the distance between the monomer centers) or for the interaction between each atom pair.

Since the density is calculated with just one Gaussian function on each atom with the same parameters for all atom types, it is possible that the distance dependence of the density is not accurately reproduced. A distance dependent scaling factor might be able to compensate for this. Furthermore, the approach can only be a sensible approximation for large distances[215] and hence might fail for 3.0 Å.

In order to visualize the effect of the different parameters, the results of calculations with distances of 3.0 Å and 3.6 Å, but using the parameters optimized for 3.3 Å, are shown in Figure 6.43. For 3.0 Å, the repulsion is dramatically overestimated at small shift distances, but the features of the PES are roughly correct, albeit also overestimated. For OPLS-AA, the opposite is true. Since the curve without a repulsion contribution of the hydrogens shows the least severe overestimation, especially the contributions of the hydrogen atoms seem to be problematic. Using a shift distance of 3.6 Å, the repulsion is underestimated for smaller and overestimated for larger shift distances, but not dramatically. The features are slightly underestimated. The PES predicted by OPLS-AA is overall closer to the DFT curve (and hence has a smaller RMSD), but lacks the features. Furthermore, the curves with the overlap approach predict the correct minimum, contrary to OPLS-AA. Hence, the parameters for 3.3 Å seem to be at least transferable to larger distances. The

[xx] The additive parameter is not important, since it only shifts the whole PES, which is shifted, anyway, when the minimum of the different energy contributions is set to zero.

[xxi] The different sign in the ansatz using s-functions on the hydrogen atoms is due to the phase factors, which were introduced to ensure positive $\langle s|p\rangle$-overlap .

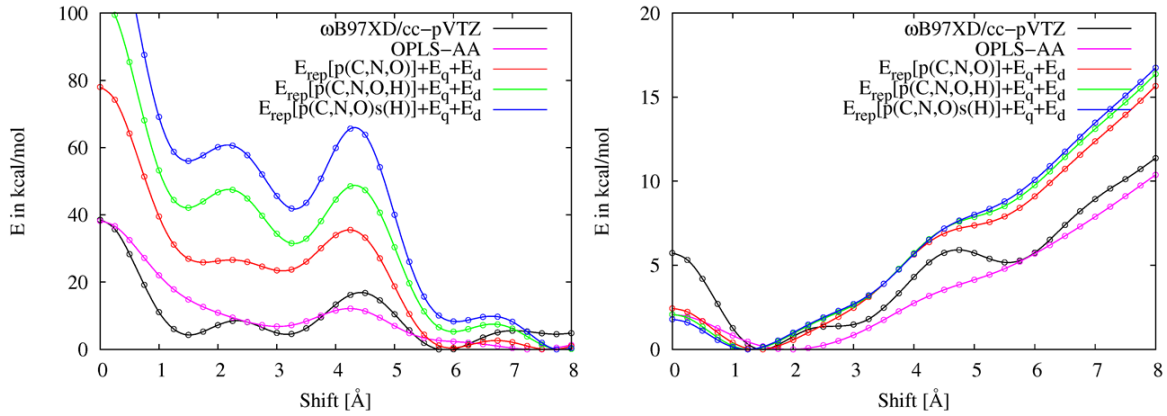

Figure 6.43: PES of the longitudinal shift with 3.0 and 3.6 Å distance between the intermolecular planes using the parameters obtained for 3.3 Å.

failure at the smaller interplane distance is not so problematic, since these distances will typically not be encountered.
However, if a general force field is desired it should be investigated, whether an additional distance dependence needs to be introduced or/and whether the description of the density should be improved, e.g. by introducing different parameters.
Another possibility is to introduce a factor c that adds a certain percentage of isotropic Lennard-Jones repulsion,

$$E = E_q + E_d + c \cdot E_{rep\_LJ} + E_{rep}. \tag{6.80}$$

E_{rep} is then fitted to the difference of the DFT energy and the sum of E_q, E_d and $\cdot E_{rep\_LJ}$. With this approach, the overlap-based repulsion could also be applied as a correction to any force field using a Lennard-Jones potential. Several test calculations with different scaling factors were performed, but no benefit was observed. For medium values (e.g. $c = 0.5$) the results are qualitatively identical and for higher values the PES becomes closer to the OLS-AA curve. One might also consider to use a distance-dependent mixing coefficient $c \to c(r)$ in the spirit of the range-separated functionals, but this is beyond the scope of this work.

Another question is the transferability of the problem to different systems, especially other perylene-based dyes like perylene or PTCDA. Exemplary results are given in Fig. 6.44. The approach clearly also works for these compounds. For PTCDA, the exponential

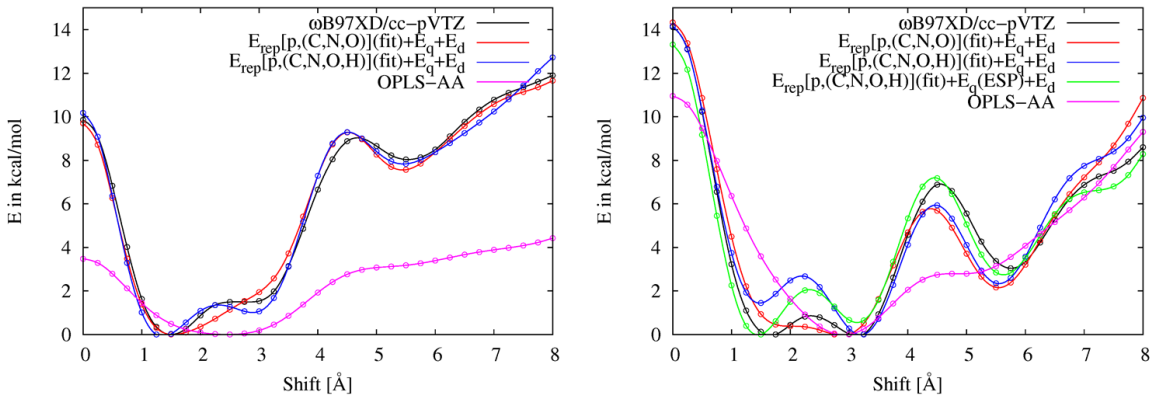

Figure 6.44: PES of the longitudinal shift for perylene (left-hand side) and PTCDA (right-hand side) with different methods. $E_q(ESP)$ refers to the interaction between atomic point charges taken from an ESP fit (ωB97XD/cc-pVTZ)

parameter is 0.45 without a repulsion contribution from the hydrogen atoms, while it is 0.48 with p-functions at the hydrogen atoms, which is rather close to the results for PBI.[xxii] For perylene, however, the parameter is 0.65 with and 0.67 without a contribution of the hydrogen atoms. This shows that for a generalizable force field, different β-values for different atom types have to be defined. In the case of PTCDA, DFT predicts two minima, which are almost equal in energy, while the force field predicts the second minimum to be significantly lower in energy. This might be due to an incorrect charge-charge interaction, since the choice for the parameters on the anhydride group is ambiguous. Consequently, another computation was performed with charges taken from an ESP fit (ωB97XD/cc-pVTZ) performed with Gaussian09. The optimal exponential parameter is now $\beta = 0.51$. From Fig. 6.44, it is evident that with the optimized charges, the first minimum is lower (in agreement with DFT) and that the energetic difference between the minima is reduced.

The results presented in this section show that although the overlap approach works in principle also for different distances and different systems, the parameters are not directly transferable. However, due to the simplicity of the ansatz (all atoms are identical in their repulsion contribution), it could not be expected that the resulting force field is very general. With this approach the properties of the whole system are folded into one sin-

[xxii] Due to a lack of parameters for an anhydride group, the parameters for the imide group were used, except for the bridging oxygen atoms. Here, the sum of the charges of the nitrogen and the hydrogen atom of the imide group and the Lennard-Jones parameters of an ester oxygen were used.

gle parameter, which makes the parameter only suitable for this system. Using different β-parameters for different atom types as in any standard force field might significantly improve the transferability of this approach. This is, however, beyond the scope of this work.

As stated above, the force field in its current state is sufficient for the modeling of the longitudinal displacement in perylene-based dyes, if the parameters are defined for the model system in question. Since it is based on OPLS-AA and uses an overlap approach, the force field will be called **OPLS-AA**$_O$ in the following. Of course, the different flavors (p-type, s-type, or no basis function on the hydrogen atoms) have to be specified additionally.

6.3.5 Excursion: Using a Simplified MO-Based Overlap Approach?

Apart from the density-based ansatz, often the MO-overlap is used for the modeling of the repulsion (see section 4.2.3). As mentioned above, a computation of the monomer MOs and the subsequent calculation of all overlap integrals is quite demanding. Although the MOs have to be calculated only once, the overlap integrals have to be computed for each point of the PES. Because MM calculations should be fast and efficient, it is hence questionable if this ansatz is worth pursuing if one considers the limitations for potential applications. However, despite this limitation, from a more fundamental point of view, it is interesting to see whether the approach brings any benefits. Hence, a simplified test implementation was devised.

In order to save time in the computation as well as for the implementation, several approximations were introduced. At first, only the π-MOs were used. Furthermore, they were modeled by a single p-type Gaussian function on each second-row atom, using the same exponential parameter for all atoms, which was again optimized to fit to yield the best agreement with the DFT curve. The relative phase and the coefficients were taken from a HF/STO-3G calculation performed with Gaussian09. The different MOs were added separately to investigate whether all MOs are needed or if some of the higher lying orbitals suffice, which would obviously reduce the computational cost significantly. The repulsion energy is thus expressed as

$$E_{rep} = p_1 \sum_i^A \sum_j^B \langle \psi_i | \psi_j \rangle^2 + p_2, \tag{6.81}$$

with ψ_i and ψ_j being the occupied MOs on monomers A and B, which are expanded in the basis of the primitive Gaussian functions p_i,

$$\psi_i = \sum_{\nu}^{N} c_{\nu i} p_{\nu i}. \tag{6.82}$$

Thus it follows,

$$E_{rep} = p_1 \sum_{i}^{A} \sum_{j}^{B} \left[\sum_{\nu}^{N} \sum_{\mu}^{N} c_{\nu i} c_{\mu j} \langle p_{\nu i} | p_{\mu j} \rangle \right]^2 + p_2. \tag{6.83}$$

From this equation, it is obvious that this ansatz is significantly more expensive than the density-overlap approach, since the double sum over all used MOs has to be evaluated. The implementation is given as

```
for i=1:mi # sum over MOs
    for j=i:mi # sum over MOs

      # Calculation of the overlap intergal between
      # the MOs with coefficients i and j
      # The coefficients are stored in the matrix d
        ER(i,j)=P_Overlap_fast_d_MO(n,coordn,_Beta,d(i,1:n),d(j,1:n));

        # Output of invidual overlap
      fprintf(fid1,"<%i|%i> = %8.4e",i,j,ER(i,j));
      fflush(fid1);


      ER(i,j)=ER(i,j)^2;
      ER(j,i)=ER(i,j);

    endfor
  endfor

  # summing up the different contributions
  Erep(shiftcount)=0;
  for i=1:mi
    for j=1:mi
            Erep(shiftcount)=Erep(shiftcount)+ER(i,j);
    endfor
 endfor
```

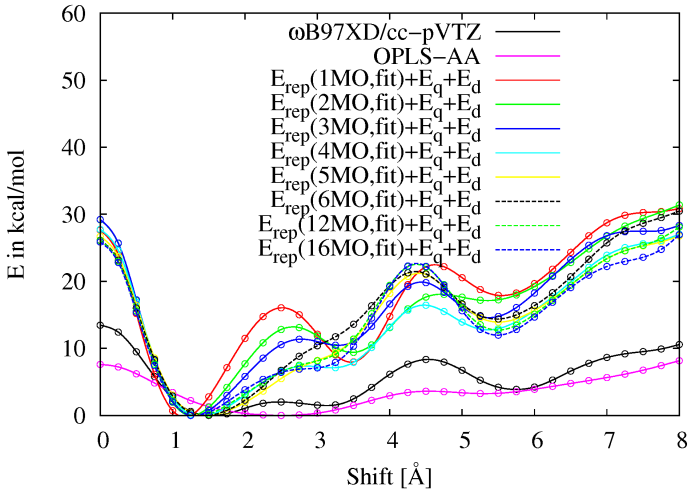

Figure 6.45: E_{rep}+E_q+E_d using an anisotropic repulsion based on the overlap of the molecular orbitals with $\beta = 0.5$ and different numbers of MOs. "1MO" means that just the HOMO is included, while "2MO" means that the HOMO and the HOMO-1 is used and so on.

Calculations with one up to 16 π-MOs were performed. In order to see the dependence of repulsion energy on the number of used MOs, the PESs with one to 16 MOs and an intermediate value for the exponential parameter ($\beta = 0.5$) are at first plotted in Figure 6.45. From the Figure, it is evident that already just with the HOMO the shape of the curve is similar to the DFT PES. However, the repulsion is overestimated for small as well as for high shift distances. The latter could be rooted in the fact that the overlap does not decrease as fast as the density overlap due to the nodal structure of the MOs. With the intermediate value of β, using more MOs does not change the picture significantly. One possible remedy would be to use only the first few MOs and to introduce an additional distance-dependent damping factor (see[215]). Some test calculations were performed, however, since the results were not very satisfactory, this ansatz was not further pursued.

As a next step, the value of β was varied in steps of 0.1 from 0.1 to 1.0. While the fitting procedure in the case of the density overlap yielded a clear optimal value for β, the optimal value is not so clearly defined here, depending on the number of MOs. Up to three MOs, there is no clear minimum and the RMSD is always well above 10 kcal/mol. Using four MOs, the optimal value is found at the lower boundary of the chosen interval, $\beta = 0.1$ with an RSMD of 4.73 kcal/mol. From five to nine MOs, $\beta = 0.1$ remains the optimal value, but the RMSD is again larger (above 6 kcal/mol). Using 10 to 13 MOs, the

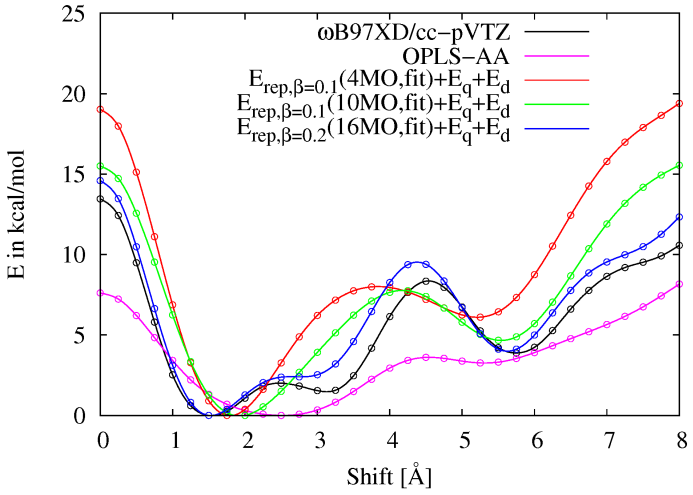

Figure 6.46: E_{rep}+E_q+E_d using an anisotropic repulsion based on the overlap of the molecular orbitals with optimized β.

optimal value is still the same but the RMSD is smaller (2.59, 1.46 , 1.72, 1.57 kcal/mol). Using 14 to 16 MOs, the optimal value is $\beta = 0.2$ with also rather small RMSD values (1.82, 1.26, 1.08 kcal/mol).

Only the calculations with 10 or more MOs as well as the one with four MOs yielded reasonably small RMSD values. The PESs using 4, 10 and 16 MOs are plotted in Fig. 6.46. The agreement with four and even ten MOs is rather poor. With 16 MOs, the PES can be described quite accurately, similar to the density-overlap approach. However, since even 10 MOs are not sufficient for a satisfactory description, this ansatz is much more expensive than the density-overlap approach.[xxiii]

6.3.6 The Density-Based Repulsion as Correction for OM2-D

Since the ground-state PES of OM2-D underestimates the repulsion at small shift distances as well as the features similar to OPLS-AA, it is conceivable that the overlap-based repulsion could also be used as a correction for the semi-empirical method. This is also physically grounded, since it was derived that the lack of features is due to an underestimation of the overlap-dependent terms (see section 6.2.3 and equation 4.43) and hence adding an overlap-dependent correction makes sense. Fitting the repulsion to the difference of the DFT-D and OM2-D energy produces the results given in Figure 6.47. Adding

[xxiii] Some additional test calculations with an energy-weighted overlap model (see section 4.2.3) were performed. However, since the results were not significantly different, this ansatz was not further pursued.

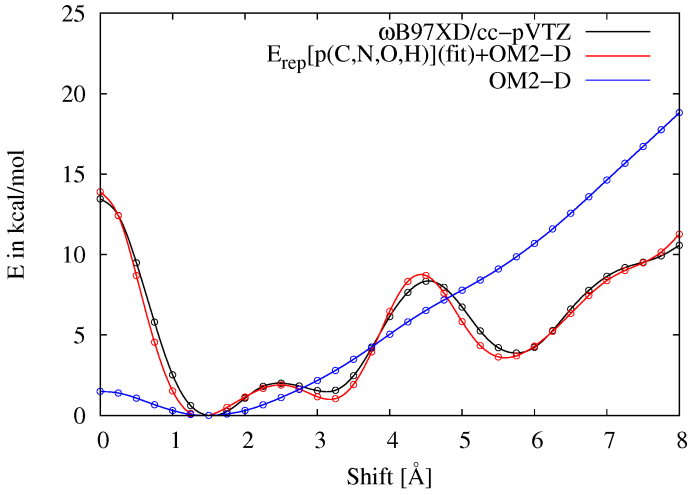

Figure 6.47: PES for the longitudinal shift in the PBI dimer computed with OM2-D with and without an overlap-based correction

the overlap-based repulsion to the OM2-D energy clearly leads to an improvement in the description.[xxiv] The optimal value for β is 0.77 and the RSMD value is 0.5 kcal/mol. This corroborates the theory that the underestimation of the intermolecular overlap is responsible for the failure of OM2-D for the ground-state PES and shows that using an additive correction term is possible.

6.3.7 Using OPLS-AA$_O$ in a QM/MM Framework

In the previous sections, a force field based on OPLS-AA with a density-based overlap ansatz for the closed-shell repulsion term was introduced, which is called OPLS-AA$_O$. In this section, the force field is applied to a tetramer, in order to test its applicability and to demonstrate its possible use in a QM/MM framework. The tetramer test system was chosen identical to the perylene tetramer used in section 6.2.2 (Figure 6.21). The only difference is that here PBI is used. As reference the ground-state surface was calculated on the ωB97XD/cc-pVDZ level of theory as implemented in Gaussian09.
At first, a pure MM description is tested. In order to use the subroutine presented above, which calculates the interaction energy of a dimer, the total interaction is calculated as a sum of dimer contributions. With this ansatz it is easy to implement that the overlap-based repulsion is used between next neighbors, while the standard Lennard-Jones repulsion is applied for the other interactions. The parameters p_1 and β were taken

[xxiv] For the sake of clarity only the version with p-type Gaussian functions on all atoms was used, however, the other approaches are of course applicable, too.

from the dimer calculation. In this case OPLS-AA$_O$ with p(C,N,O,H) was used[xxv] and hence $p_1 = -889.8$ and $\beta = 0.51$ were used, see Tables 6.3 and 6.4. Since p_2 is just an additive contribution to the total energy that is unimportant (the minimum of the whole PES is set to zero, anyway) the constant was omitted. The details of the implementation, especially the double loop over the monomers and the generation of the six distinct dimers, is given below:

```
Etot=0;
Etot_O=0;
#Double sum over all monomers
for i=1:NofM
  for j=(i+1):NofM

    #Bulding pair coordinate matrices
    coord_pair=[coord((i-1)*n+1:i*n,1:3);coord((j-1)*n+1:j*n,1:3)];

    #Calling energy subroutines:
    [Eq, Erep_LJ, Ed]=EOPLS_components(n,coord_pair,epsilon,sigma,q);

    #Define Repulsion energy
    if (abs(i-j)==1)
      Erep(i,j)=p(1)*P_Overlap_fast(n,coord_pair,Beta);
    else
      Erep(i,j)=Erep_LJ;
    endif;

    #Summing up the different contributions
    E(i,j)=Eq+Erep_LJ+Ed;
    EO(i,j)=Eq+Ed+Erep(i,j);

    #Summing up the contribution of the dimers
    Etot=Etot+E(i,j);   #OPLS-AA
    Etot_O=Etot_O+EO(i,j); #OPLS-AA_O

  endfor;
endfor;
```

Since the interactions is calculated as dimer contributions, one can easily analyze the total energy in terms of these contributions. There are 6 dimers: 1-1, 1-3, 1-4, 2-3, 2-4 and 3-4. Obviously the interaction energies of 1-2, 2-3 and 3-4 (next neighbors) are identical

[xxv] For the sake of clarity again only this version of OPLS-AA$_O$ was used, however, the other approaches are of course applicable, too.

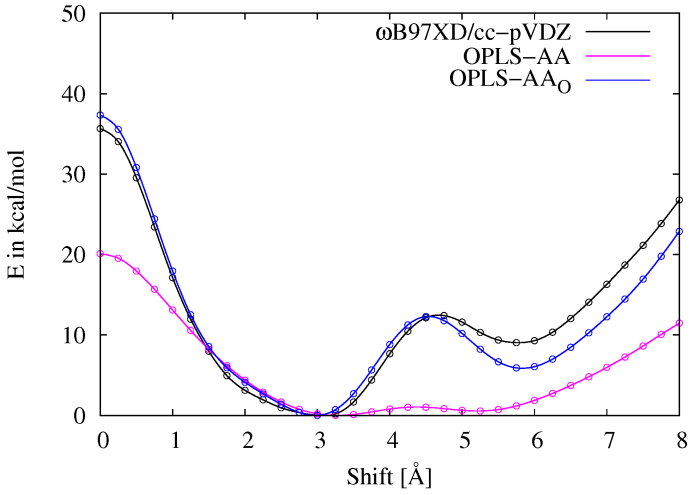

Figure 6.48: Force-Field calculation of the longitudinal shift in the tetramer with OPLS-AA and OPLS-AA$_O$ (p[C,N,O,H]). The PES predicted on the ωB97XD/cc-pVDZ level of theory is given as reference.

and the same is true for 1-3 and 2-4 (next but one). At 0 Å the contribution of the 1,3-interaction is about 12% and the 1,4-interaction about 1% of the 1,2-interaction for OPLS-AA$_O$. Hence, if larger molecular cluster are to be calculated, one might consider using a cut-off at a certain distance. The PES predicted by the force-field calculation is shown in Figure 6.48. Similar to the case in the dimer, OPLS-AA lacks features, while OPLS-AA$_O$ gives an excellent agreement. This is entirely due to the next-neighbor interaction, since all other interactions are identical for both methods. Since the energy can be decomposed into dimer contributions, it is not surprising that the quality of the results is similar to the dimer case.

Although the force field alone already provides a good description of the system, it is of interest to test its applicability in a QM/MM framework. For the modeling of excitonic states a quantum mechanical method has to be applied. The force field can only be used for the surrounding environment. As a model system the tetramer is used, with the inner dimer being the QM system and the outer dimer being the MM system. An electrostatic embedding is chosen. The charges of the outer dimer are included in the QM Hamiltonian.[xxvi] This is schematically depicted in Figure 6.49. Since the carbon atoms

[xxvi] Thinking in terms of an application to excited states a mechanical embedding is not suitable, since in this scheme the excited states are not influenced by the environment. A polarized embedding would obviously be best, but is not possible using the OPLS-AA-based force field.

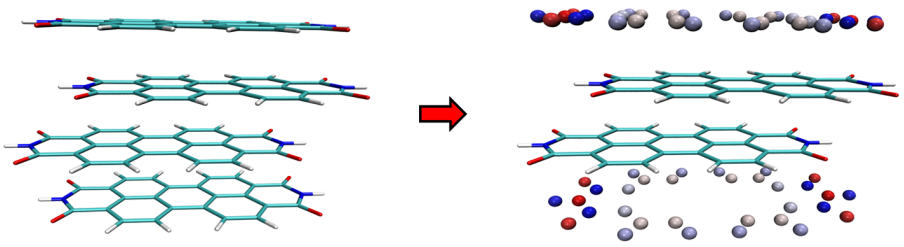

Figure 6.49: The tetramer (left-hand side) and its representation in the QM Hamiltonian (right-hand side). The position of the charges is represented by the dots and their magnitude and sign is represented by the color.

of the type "naphthalene fusion C" have zero atomic charges, they do not contribute to the Hamiltonian and are thus omitted in Figure 6.49.
For the QM calculation, the ωB97XD/cc-pVDZ level of theory with external charge distribution[362] was chosen as implemented in Gaussian09. The energy of the MM system is simply given by the 1,4-interaction as implemented above and is identical for OPLS-AA and OPLS-AA$_O$. The QM/MM interface contains the 2-4, 1-3, 1-2 and 3-4 dimer. The latter two are responsible for the difference between OPLS-AA and OPLS-AA$_O$, since in the overlap-based repulsion is only active between next neighbors. The energy contribution of the interface only consists of E_{rep} and E_d, since the complete charge interaction is included in the QM part. The results of the QM/MM calculation with OPLS-AA and OPLS-AA$_O$ as well as the pure QM calculation in the gas phase and with external charges are given in Figure 6.50.

The charge distribution of the outer dimer is stabilizing the inner dimer for larger shift distances, but destabilizing for small shift distances. This can be rationalized by the fact that identical charges are lying right on top of each other at the beginning of the PES. The relative energy of the minima is also changed by the charges, with the second minimum being the global one with the external charge distribution.
The QM/MM PES using OPLS-AA is not too far from the reference, but basically has the same shape as the QM curve, which is not surprising, since it was shown that OPLS-AA does not add any features. Therefore the shape of the curve is not correct. OPLS-AA$_O$, on the other hand, provides an accurate description within the QM/MM framework.
This QM/MM approach can easily be extended to the excited states simply by perform-

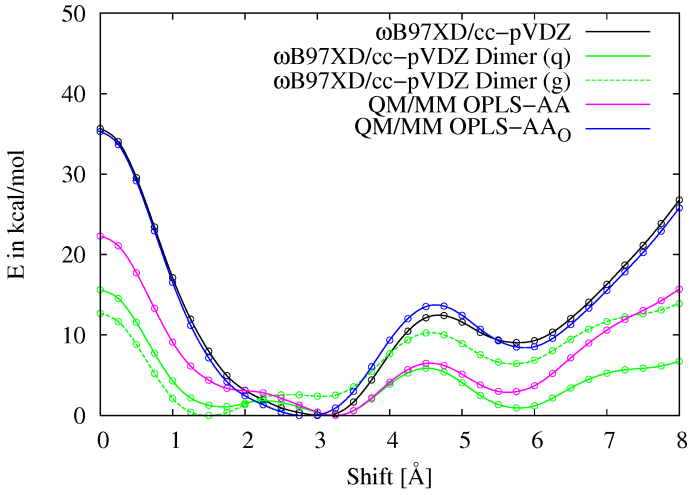

Figure 6.50: QM/MM calculation of the longitudinal shift in the tetramer using ωB97XD/cc-pVDZ OPLS-AA and OPLS-AA$_O$ (p[C,N,O,H]). The PES of the pure QM calculation in the gas phase (g) and with external charges (q) is also plotted. The PES predicted on the ωB97XD/cc-pVDZ level of theory is given as reference. For the definition of QM and MM-part and the shift, see 6.49.

ing an excited-state calculation of the QM system including the charge distribution of the MM part and adding the excitation energies on the ground-state QM/MM potential energy surface. Following the recipe devised in section 6.2.2 the excitation energies are calculated with the ωB97X functional in conjunction with the cc-pVDZ basis sets.[xxvii] The result of the QM/MM description of the excited states are depicted in Fig. 6.51 The effect of the point charges on the excitation energies seems to be very small (only a few meV) and hence the differences to a pure QM calculation stem mainly from the effect on the ground-state surface, which consequently shifts all PES. The main features, like the absorption and emission wave lengths and especially the possible exciton trapping mechanism, are hence similar to the dimer calculations presented above. However, similar to the case of the perylene tetramer, the minimum of the 1 A_g state is shifted to larger shift distances, which changes the preferred geometry in the trap state.

The results presented on the simple tetramer model system show that using a QM/MM approach with OPLS-AA$_O$ for the description of excitonic states in perylene-based dyes is possible. Furthermore, it is evident that the inclusion of the environment is important, since it changes the shape of the PES. For a thorough description of the exciton trapping

[xxvii] The 6-31+G(d) basis sets could not be used due to convergence problems.

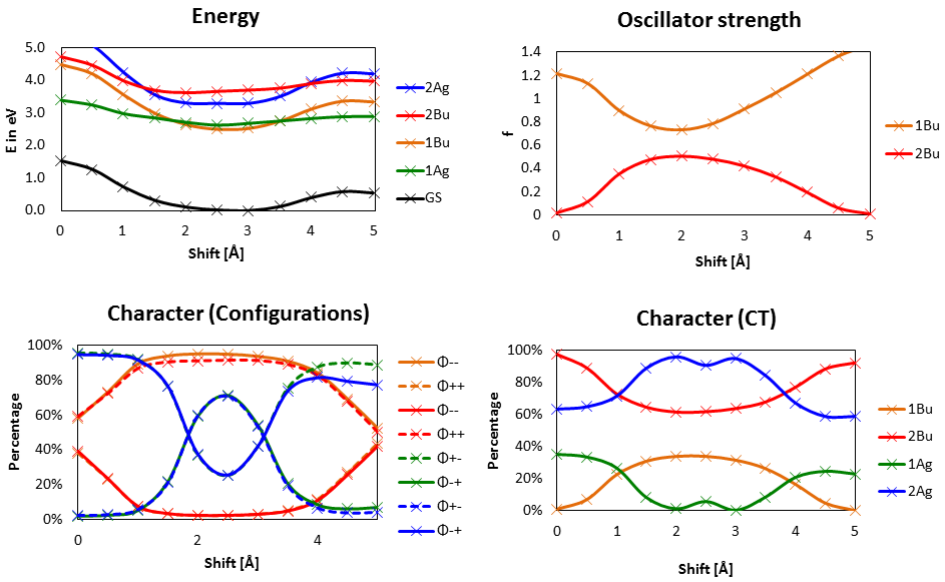

Figure 6.51: QM/MM results for the longitudinal shift in the PBI dimer. Ground-state surface: ωB97XD/cc-pVDZ + OLPS-AA$_o$ with electrostatic embedding. The excited state surfaces were generated by adding excitation energies (ωB97X/cc-pVDZ + MM charges) to the ground state surface. Monomer geometry: taken from Settels et al.[326]

mechanism, QM/MM calculations should be performed for all relevant intermolecular degrees of freedom. The results obtained for the model system indicate that for the calculation of the excitation energies, a gas-phase calculation might be reasonably accurate, however, this needs further testing.

6.3.8 Outlook

In order to improve the quality and especially the generality of the OPLS-AA$_O$ force field, different parameters for different atom types should be defined in the future. Since this needs an optimization within a rather large parameter space, the implementation of the force filed should be ported to a programming language such as C++ or Fortran. One might also consider using Slater-type functions instead of Gaussian functions, since a single Slater function should be a better-suited basis function than a single Gaussian function. Furthermore, instead of the rather simple model for the electrostatic interactions relying on point charges, a more involved treatment could be used in conjunction with the anisotropic repulsion. For instance, using AMOEBA instead of OPLS-AA as the underlying force field might be interesting.

At the moment, gradients are also missing, which need to be included to make several important applications possible. For instance for a relaxed scan in an QM/MM framework, an optimization of the environment is crucial. In the current implementation, where only the intermolecular interactions are included, standard atomic gradients cannot be used directly.[xxviii] This is only possible if the intramolecular interactions are also taken into account. Since the latter can be expected to be less important for some of the applications, using a rigid body optimization might be of interest. Using the anisotropy parameter, the implementation of a gradient is straightforward, while the gradient of the p-overlap is more involved.

One of the current limitations is given by the fixed coordinate frame of the p-functions. If p_z-orbitals are used, the ansatz only works if the molecules are located parallel to the xy-plane. Hence, if any molecule is rotated out of the xy-plane, the results of the calculation will be meaningless. One possible remedy would be to rotate the p-orbitals together with the molecule, this is, however, not trivial.

Currently, OPLS-AA$_O$ was designed to include the effects of a π-stack. A movement like the longitudinal displacement in a real system involves of course also interactions between

[xxviii] Without intramolecular interactions the molecule is obviously not stable. An implementation that projects the atomic gradients of OPLS-AA onto the intermolecular distance was tested and yielded quite nice results. However, this ansatz neglects the important rotational degrees of freedom.

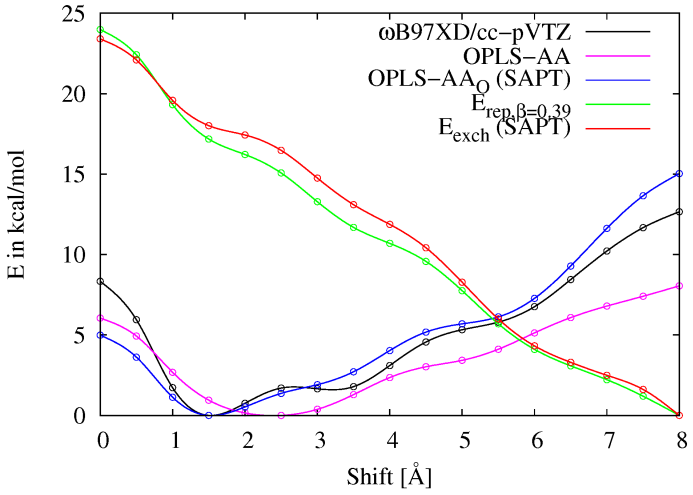

Figure 6.52: Fitting the repulsive part of OPLS-AA$_O$ (p[C,N,O,H]) to the exchange-repulsion obtained from a SAPT calculation for the longitudinal shift in the NDI dimer.

the stacks. Since it can be assumed that the anisotropic repulsion is less important for these interactions, the standard isotropic repulsion should be applicable. Therefore, the implementation needs to be extended to differentiate between interactions within the stack and between stacks.

Following the ansatz of a physically-motivated intermolecular force field from symmetry-adapted perturbation theory (FF-SAPT)[217,261] pursued by Maxim Tafipolsky, it is also possible to fit the anisotropic repulsion to the exchange-repulsion term from a SAPT computation. The results of a test calculation on the NDI[xxix] dimer can be found in Figure 6.52.[xxx] Keeping in mind that only the repulsion energy was fitted to the SAPT curve, while all other terms are taken from the standard OPLS-AA force field, the agreement between DFT and OPLS-AA$_O$-SAPT is quite good. Using a more involved model for the charge interaction and also parameterizing it using the corresponding SAPT term should significantly improve the result. Hence this ansatz seems quite promising.

The force field in its current state can be used to compute the excitonic states in stacks of perylene-based dimers in a QM/MM framework. In order to test if the Apéry constant should be included to account for the orbital interaction with the other monomers one could perform QM/MM calculations on the perylene tetramer and compare the results with the TDDFT calculations presented above.

[xxix] naphthalene diimide

[xxx] The SAPT calculation was performed by Maxim Tafipolsky.

6.4 Summary and Conclusion

In this chapter, the description of excitonic states in perylene-based dyes was discussed with a special focus on a possible exciton-trapping mechanism involving the intermolecular motion between two monomers. In this work, the longitudinal shift in the dimer was taken as coordinate for the investigation. At first it was shown how the character of an excited state in the dimer can be defined in terms of charge-transfer and neutral excitations. A simple approximative way to extract the character of the states and the energy of the diabats (pure CT and NE states) from a standard quantum-chemical calculation was derived.

While SCS-CC2 and SCS-ADC(2) should provide an accurate description, cheaper methods are needed to extend the investigation of the trapping mechanism to larger aggregates, as well as for excited states optimization, which are useful to explore the important degrees of freedom for the wave packet dynamic. SCS-ADC(2) and SCS-CC2 were used as reference to evaluate the performance of cheaper methods.

At first, the performance of TDDFT was investigated by benchmarking several functionals. It was shown that for perylene ωB97XD as well as CAM-B3LYP give good results. In the case of PBI, CAM-B3LYP fails and gives a qualitatively incorrect description of the character of the excited states of B_u symmetry for a major part of the PES, although the shape of the excited state surfaces is roughly correct. This is in agreement with the observations of Liu and Settels. The performance of ωB97XD depends crucially on the monomer geometry. Following an assumption of Settels and Liu, it could be shown that the diabats are so close in energy in the case of ωB97XD that small effects like the monomer geometry can have a significant influence. In order to arrive at a more reasonable energetic distance between the diabatic states, long-range corrected functionals with a higher amount of exact exchange were used (ωB97X, LC-BLYP, LC-ωPBE). While LC-BLYP and LC-ωPBE give qualitatively correct results but tend to overestimate the excitation energies, ωB97X was shown to give quite accurate excitation energies. For the calculation of excited-state potential energy surfaces, it was recommended to compute the ground-state surface with ωB97XD and to add excitation energies computed with ωB97X. This approach was then applied to the perylene tetramer. Differences to the dimer calculations and their implication on potential trapping mechanisms are discussed. In order to be able to perform excited state optimizations, dispersion is needed. Thus, the range separation parameter of ωB97XD was optimized for the excited states of the dimer system, which yielded the tuned functional ωB97XD25. The latter provides results

of high accuracy. With this functional the excited states of the PBI dimer were optimized using only the intermolecular degrees of freedom.

It was shown that although semi-empirical methods, like the OMx methods, are very efficient and hence interesting for the computation of the excited states of larger aggregates, they do not give an accurate description of the excited states of the dimer. The potential energy curves of the ground and excited states lack features. The same is true for the dependence of the coupling constant on the shift coordinate. This behavior was attributed to an underestimation of the overlap-dependent terms due to the contracted basis sets. This is corroborated by the fact that decreasing the distance between the molecular planes makes the features appear. For larger distances, where the overlap-dependent terms are close to zero anyway, the prediction of the coupling of OM2 are almost in line with SCS-ADC(2) results. It could be shown that DFT with a minimal basis also predicts a ground-state curve with a lack of features, although this lack is not as severe as in the OMx methods. This could be explained by the fact that the overlap is explicitly used in the computation of two-center one-electron integrals in MNDO-based methods. Adding single basis functions in the DFT calculation, it could be shown that an additional p-function would improve the results significantly.

For a description of perylene-based dyes in a QM/MM framework, an appropriate force field is needed. It was shown that neither OPLS-AA nor AMOEBA give a satisfactory description of the ground-state surface for the longitudinal shift. Similar to the semi-empirical methods, the important features are completely missing. This failure was attributed to the isotropic form of the atom-atom interaction in the repulsion term. It was shown that neither the charge-charge, nor the dispersion interaction are responsible for this, at least not to a significant extent.
In order to investigate possible ways to include anisotropy, the non-bonded interactions of OLPS-AA were implemented in an octave script. It was shown that already by introducing a simple anisotropy parameter the features arise naturally. By fitting the repulsion contribution to the difference of the other energy components and the DFT energy, a very accurate description of the ground-state surface is possible. It was demonstrated that this is also true for an s-type Gaussian overlap model in two dimensions. Using a density-based overlap and decomposing the density into p-type Gaussian functions on each atom led to the design of the OPLS-AA$_O$ force field. The implementation involves the calculation of the overlap integral between p-functions on different centers. This force

field yields best results if p-functions are also added to hydrogen atoms, but neglecting the contribution of the hydrogen atoms also gives satisfactory results. Using s-type functions on the hydrogen atoms is also possible and yields accurate results. OPLS-AA$_O$ provides a very accurate description for the system and the intermolecular motion for which it was parameterized, which indicates that the description is physically correct, but the parameters do not seem to be very general. Changing the distance between the molecular planes or the perylene-based dye leads to a significant change especially in the multiplicative fit parameter. It was discussed that this could be due to the fact that currently the same exponential parameter for all atoms is used. The properties of the whole system are folded into this parameter, making it only suitable for this system. Introducing different parameters for different atom types in the future should significantly increase the generality.
In a short excursion, it was shown that a simplified MO-based overlap approach can also be used, which is, however, much more demanding computationally and hence less efficient.
It was further demonstrated that the density-based repulsion can be used as a correction for OM2-D.
In the last section, OPLS-AA$_O$ was used to describe the longitudinal shift of the inner dimer in a PBI tetramer. The anisotropic repulsion was applied for next neighbors, while the standard isotropic repulsion was used for all other interactions. The fit parameters were taken from the previous dimer calculation. It was shown that OPLS-AA$_O$ when fitted to the dimer also gives a very good description of the tetramer. In order to be able to model the excited states of this system, a QM/MM approach relying on an electrostatic embedding was used, with the inner dimer being the QM system. It was shown that using OPLS-AA$_O$ a very good description of the ground-state surface can be obtained in the QM/MM framework. By adding the excitation energies obtained for the QM system with ωB97X to the ground-state surface (following the recipe devised in section 6.2.2) a QMM/MM description of the excited states could be obtained and the differences to pure dimer calculations were discussed.

7 Bis(borolyl)thiophene and Pyracene

> And now for something
> completely different.
>
> *(Monty Python)*

Besides the merocyanines and the perylene-based dyes two other π-conjugated compounds with an interesting electronic structure were investigated and the applicability of the methods of computational chemistry was evaluated in collaboration with experimentally working groups. These projects were focused on gaining insight into the electronic structure of these compounds, which can ultimately also help to gain a better understanding of the suitability of different compounds for optoelectronic applications. A fundamental knowledge of the electronic structure enables one to make a prediction on the efficiency of the compounds in at least some of the elementary processes of organic electronics.

7.1 The Electronic Structure of a Bis(borolyl)thiophene and the Corresponding Dianion

The results presented in this section have been obtained in close collaboration with Christan Hörl and Zarah Falk and have partially been published in reference.[363]

Bis(triarylamine)thiophene compounds are known to form so-called positive bipolarons, which are basically delocalized dications. A doubly charged system can either exhibit two separated polarons with two corresponding geometric distortions or one bipolaron with a single geometric distortion.[364,365] These bipolarons are believed to play an important role in conducting polymers and there has been consequently an increasing interest in these compounds (see[363,366] and references therein). However, not much is known about negative bipolarons.[363]

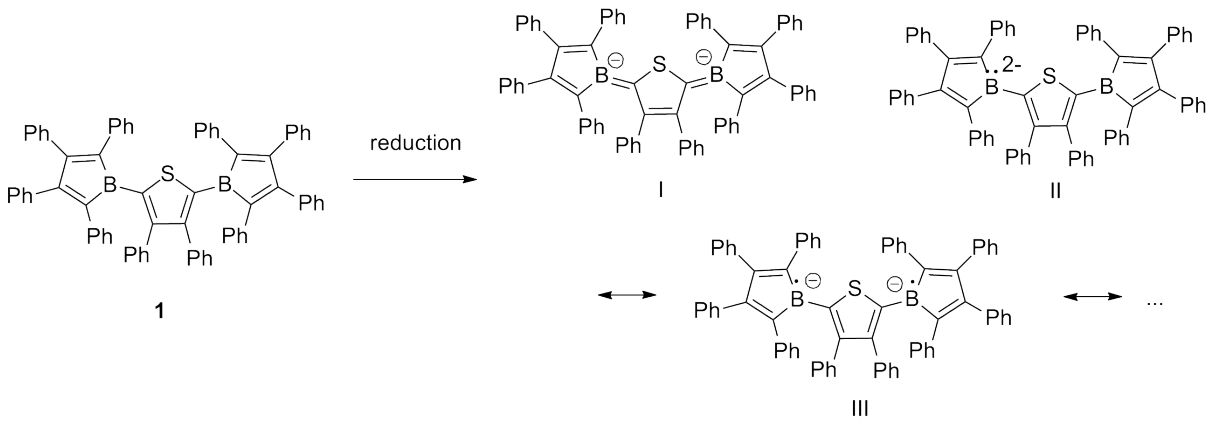

Figure 7.1: Preparation of a 2,5-Bis(borolyl)thiophen dianion from its neutral precursor.

Aiming at the preparation of such a negative bipolaron, a 2,5-Bis(borolyl)thiophen dianion $[\mathbf{1}]^{\mathbf{2}-}$ was obtained via reduction of the neutral precursor with decamethylcobaltocene ($[CoCp^*_2]$) in the research group of Holger Braunschweig (see Fig. 7.1). Similar to the positive bipolarons the dianion can be represented by several resonance structures. Especially the closed-shell quinoidal (I) and the open-shell biradical (III) structure are of interest, since they present the two extreme cases.[366] The closed-shell structure can be expected to be dominating if the two rings "communicate", i.e., if the coupling between the borole rings across the thiophene ring is significant.[366] If on the other hand the coupling is small, the biradical structure dominates and the question about the multiplicity arises, since III can either be an open-shell singlet or a triplet biradical. Hence it is of interest whether the system's ground state is of singlet multiplicity and if this is the case, whether the amount of biradical character is of importance.

Indeed, EPR measurements showed a signal and hence suggested a triplet ground state. However the X-ray data (see[363]) is more in line with a quinoidal structure. In order to understand the nature of the ground state and to rationalize the experimental findings quantum chemical calculations were performed. At first, the phenyl rings were substituted by hydrogen atoms ($[\mathbf{1'}]^{\mathbf{2}-}$) and all calculations were first performed on this model system. Apart from kinetically stabilizing the system, the phenyl rings surely also influence the electronic structure of the molecule and hence the results obtained for the model system may not compare to the experiment directly. However we could use them to evaluate the methodology and to get some fundamental insight into the electronic structure of the parent compound.

At first the quality of the singlet-triplet gap predicted by B3LYP was benchmarked on

Table 7.1: Singlet-triplet gap of $[\mathbf{1}']^{\mathbf{2-}}$ predicted by CASPT2

Active Space	[2,2]	[10,10]	[10,10]	[10,10]	[12,12]
Basis	cc-pVDZ	cc-pVDZ	aug-cc-pVDZ	cc-pVTZ	cc-pVDZ
vertical gap [eV]	0.65	0.62	0.59	0.61	0.56

the model system against CASPT2 results using different active spaces and basis sets (see Table 7.1). The CASSCF/CASPT2 calculations were performed using a Cholesky[367] decomposition scheme and the neutral SCF orbitals as starting guess for the CASSCF treatment with MOLCAS 7.4.[368–370] The vertical gap of $[\mathbf{1}']^{\mathbf{2-}}$ is predicted to be around 0.6 eV. Using this value it could be shown that UB3LYP underestimates the gap by around 0.2 eV (see[363] for details). This is sufficiently accurate to assume that a computation of the gap in $[\mathbf{1}]^{\mathbf{2-}}$ with UB3LYP makes sense.[i] The vertical gap is predicted to be 0.26 eV by UB3LYP. Assuming the error of the DFT approach is similar for the model system and the substituted system, the ground state is definitely predicted to be singlet (vertical gap 0.4 - 0.5 eV). The adiabtic singlet-triplet gap of $[\mathbf{1}]^{\mathbf{2-}}$ is predicted to be around 0.1 eV, which is not large, but not so small that a significant thermal population of the triplet state is likely. This is especially true if one assumes that the adiabatic gap is also underestimated. Hence the triplet state cannot be responsible for the observed EPR signal.

Due to the presence of sulfur some amount of spin-orbit coupling[ii] should occur and hence the ground-state wave function might have significant triplet contributions.[iii] The admixture of the triplet state could in principle be responsible for the experimentally observed EPR signal. In order to estimate the amount of triple contribution the following eigenvalue equation can be solved,

$$\begin{pmatrix} E_s & V \\ V & E_T \end{pmatrix} \begin{pmatrix} c_1 \\ c_2 \end{pmatrix} = E \begin{pmatrix} c_1 \\ c_2 \end{pmatrix}, \tag{7.2}$$

[i] The calculations on the substituted system $[\mathbf{1}]^{\mathbf{2-}}$ were performed by Zarah Falk.

[ii] The Hamiltonian for the spin-orbit coupling is given by

$$\hat{H}_{so} = \sum_i \zeta_i(r) \mathbf{l}_i \cdot \mathbf{s}_i. \tag{7.1}$$

With the coupling constant ζ being highly dependent on the atomic number, $\zeta(r) \propto Z^4$, spin-orbit coupling is only expected for heavier elements (see[371] for details).

[iii] Since the quantum chemical calculations used in this work are all non-relativistic, they do not incorporate these effects. Using a relativistic pseudopotential is of course possible but would only take care of scalar relativistic effects.[48]

with E_S and E_T being the energy of the singlet and the triplet state and V being the spin-orbit coupling element. An estimation for the latter was obtained using data for thiophene taken from the literature.[372] The coupling element between the singlet ground state of thiophene and the triplet state with the most similar occupation[iv] to the one of the triplet state of $[\mathbf{1'}]^{\mathbf{2}-}$ was used. The estimation revealed that the triplet contribution will be well below 0.05 % and is hence too small to explain the EPR signal (see[363] for details).

Using Ockham's razor[373] the most plausible explanation should be used and that is that the EPR signal is caused by a remaining contamination of the monoanion. This could indeed be confirmed experimentally, since preparing the dianion via comproportionation led to a product without any EPR signal.

Having resolved the question of the multiplicity the electronic structures of the bipolaron and of its precursor were further investigated. Since the coupling and hence the delocalization between the rings is of interest for these systems, the barrier for the rotation of one borole ring was calculated with a relaxed scan for the neutral precursor, the dianion in its singlet and triplet state and the monoanion on the UB3LYP/6-311++G** level of theory with Gaussian09 using the model system (see Fig. 7.2). A high barrier indicates a high contribution of the quinoidal structure, while a lower barrier is expected if the biradical structure has a significant weight. Using the model system without the substituents has (apart from the reduced computational cost) the advantage that one obtains the pure effect of the electronic structure without the influence of steric effects. All states are predicted to be planar with a significant barrier for the rotation. The barrier of the neutral precursor is lower than the one of the singlet dianion. For the latter the amount of spin contamination increases along the PES (at least before the annihilation of the first spin-contaminant), which indicates that the open-shell biradical character increases upon twisting. The monanion has the highest and the triplet dianion the lowest barrier.

These results can be explained by inspecting the MO-scheme (Fig. 7.3) and taking the charge repulsion into account. Going from the neutral precursor to the singlet dianion, the MO π_7 is filled, which is bonding between the thiophene ring and borole rings. This overcompensates the increased charge repulsion, which would favor a rotation of the rings and hence the barrier is increased. This indicates that the quinoidal resonance structure has a significant weight. If the biradical resonance contributor had a high weight the barrier should be more similar to the one of the triplet state. The monoanion has a reduced

[iv] This means the coefficients of the singly occupied MOs of $[\mathbf{1'}]^{\mathbf{2}-}$ on the thiophene ring are most similar to the ones in thiophene itself.

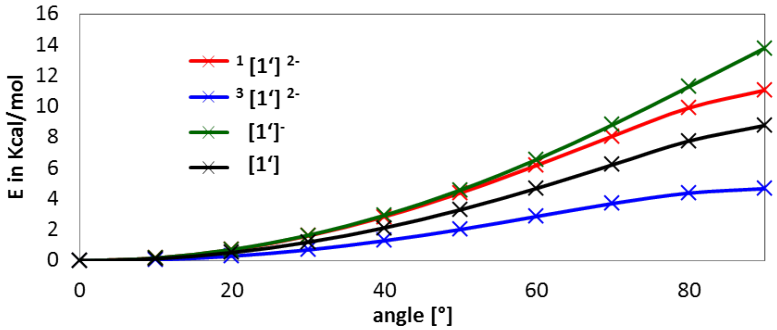

Figure 7.2: Profile for the rotation of one borole ring out of the plane for different states of [**1′**] (UB3LYP/6-311++G**)

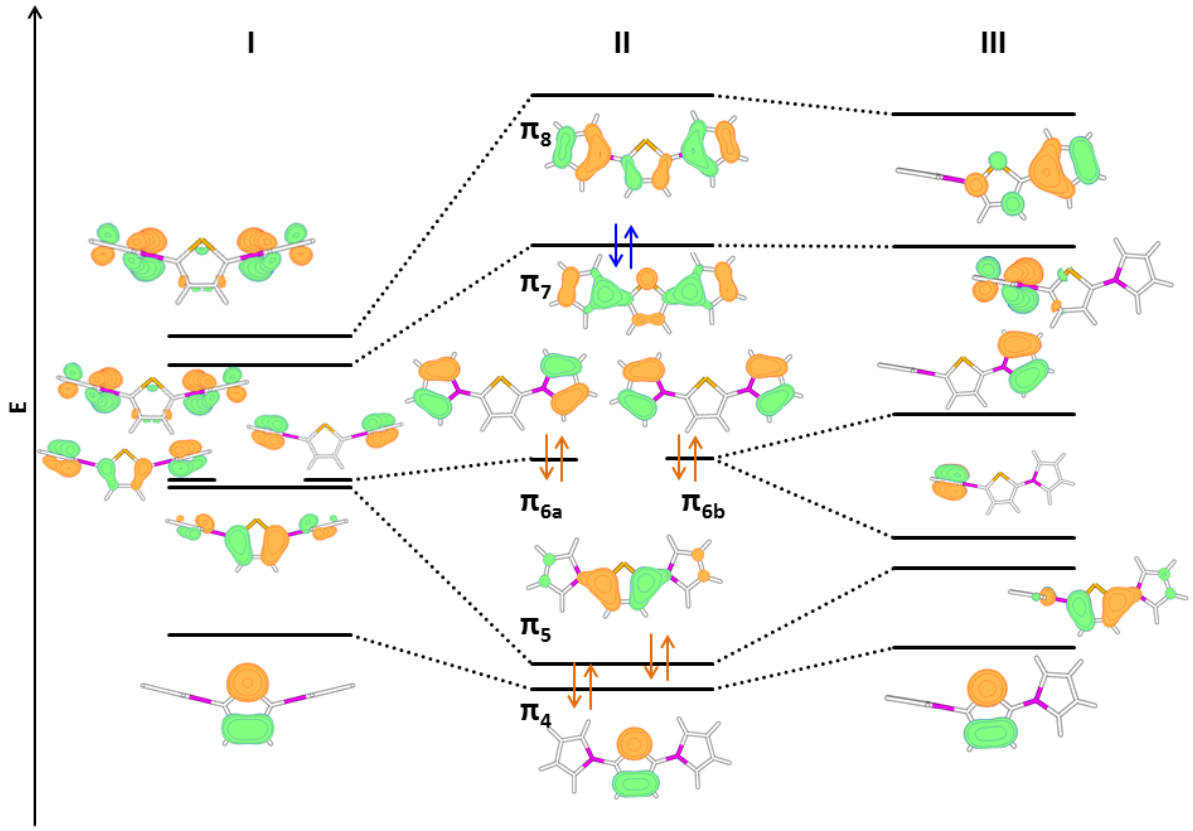

Figure 7.3: MO-Scheme of [**1′**]/[**1′**]$^{2-}$ (BLYP/6-31G). On the left-hand side (I) both borole rings are rotated out of the thiophene plane, while on the right-hand side (III) only one ring is rotated. The MOs are plotted with molden.[374]

repulsion but also a reduced bonding between the ring systems compared to the dianion. It is difficult to predict *a priori* which effect will be dominating, but the calculations show that the barrier is even higher than for the singlet dianion. The triplet dianion has the lowest barrier, since it has the same charge repulsion as the singlet state, but thinking in terms of VB theory it cannot benefit from covalent bonding between the rings in the presumably dominating biradical structure III in Fig. 7.1. In the MO picture, this can also be rationalized, since π_8 is populated, which does not exhibit any bonding between the thiophene and the borole rings.

These results indicate that a significant amount of delocalization is present in the singlet ground state of $[\mathbf{1'}]^{\mathbf{2-}}$, which shows that the system is mainly closed-shell in nature, with only a modest open-shell singlet biradical contribution. Only a VB calculation could provide a clearly defined weight of the biradical structure. However, apart from the singlet-triplet gap, the population numbers of a minimal CASSCF calculation and the weight of the doubly excited determinant can also give a very good indication. For a pure biradical structure the population numbers of HOMO and LUMO should both be one and the weights of the doubly excited determinant and the ground state determinant should be equal (i.e. 50:50). A minimal [2,2]-CASSCF calculation gave population numbers of the HOMO (1.65) and the LUMO (0.35) and a weight of the doubly excited configuration of 18% and hence confirms a moderate biradical character of $[\mathbf{1'}]^{\mathbf{2-}}$. This is also in line with the magnitude of the singlet-triplet gap.

The substituted system will have a larger biradical weight, which is indicated by the smaller singlet-triplet gap, but it can still be expected to be mainly closed-shell in character. $[\mathbf{1}]^{\mathbf{2-}}$ is slightly twisted, which is probably due to the interaction with the larger substitutents. Since the rotational profile of the model system $[\mathbf{1'}]^{\mathbf{2-}}$ is very flat for small angles a small twist is easily possible. The barrier to planarity of $[\mathbf{1}]^{\mathbf{2-}}$ is predicted to be quite small (around 0.5 kcal/mol, see[363] for details).

It might be surprising that the neutral precursor is also planar, since one might expect a free rotation around the axis between the rings. However, the MO π_5 shows some bonding between the rings. On the VB level this can be explained using a resonance structure of the type given in Fig. 7.4.

In order to explain the UV/VIS spectra CAM-B3LYP/6-31G** computations were benchmarked against SCS-ADC(2) with the cc-pVDZ and the aug-cc-pVDZ basis sets in the gas phase for the model system of the precursor and the dianion. Since the agreement was quite satisfactory (see[363] for details), the DFT approach was also applied to [**1**] and $[\mathbf{1}]^{\mathbf{2-}}$ using the IEFPCM approach. In line with the experiment one strongly absorbing

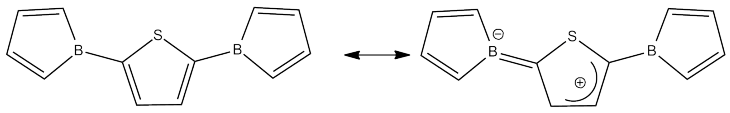

Figure 7.4: Resonance structure explaining the barrier for the rotation in the neutral precursor.

band is predicted for both systems, which is significantly red-shifted in the dianion (395 vs. 800 nm).[363] The neutral precursor additionally features a weakly absorbing band at 566 nm. The latter is predicted by the computations to consist of two close-lying excited states formed by the two configurations arising from the excitation from the almost degenerate HOMO and HOMO-1 to the LUMO. The first excitation has a higher oscillator strength ($\pi_{6b} \rightarrow \pi_7$, $\lambda = 620$ nm, $f = 0.007$) than the second ($\pi_{6a} \rightarrow \pi_7$, $\lambda = 617$ nm, $f = 0.001$). Both have minor contributions from the excitation $\pi_{6a} \rightarrow \pi_8$ and $\pi_{6b} \rightarrow \pi_8$, respectively. The strongly absorbing band of the neutral precursor is dominated by the excitation $\pi_5 \rightarrow \pi_7$ in the model system. With the substituents the assignment of the MOs is less clear ($\lambda = 383$ nm, $f = 1.45$).
The band of the dianion could be clearly assigned to the HOMO→LUMO transition ($\pi_7 \rightarrow \pi_8$, $\lambda = 1142$ nm, $f = 1.31$). It is red-shifted compared to the experiment, which might be due to more involved solvent effects or the interaction with the counter ions.

In this project it could be shown that the Bis(borolyl)thiophene has a singlet ground state with a moderate biradical contribution. On the basis of the results of the quantum chemical computations the correct multiplicity of the ground state of the bipolaron could be predicted and consequently additional experiments were prompted. Furthermore the electronic structure of the bipolaron could be elucidated and the experimental spectra interpreted. Calculations on the parent compound made it possible to obtain information of the electronic structure itself without steric effects, which is not possible experimentally.

7.2 The Electronic Structure of Pyracene

The results presented in this section have been obtained in close collaboration with the group of Ingo Fischer and have partially been published in reference.[375]

Polycyclic aromatic hydrocarbons (PAHs) are among the most fundamental representatives of the large class of organic semiconducting materials. To understand their op-

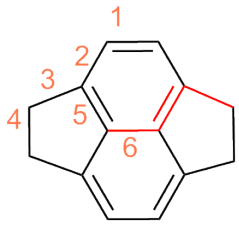

Figure 7.5: The structure of pyracene. Some important bond lengths and one dihedral angle are marked.

toelectronic properties, their electronic structure and the interplay between the effects of the σ- and the π-system on the geometry (see below) is hence of vital importance, in order to gain a fundamental understanding. PAHs are investigated due to their application in thin films,[376] but also due to the fact that they can be considered as the smallest building blocks of graphene nano-flakes and ribbons[377] and their properties are therefore important for the rising field of graphene-based optoelectronics.[378]

Pyracene (see Figure 7.5) is an especially interesting case since the five-membered rings induce a considerable strain upon the naphthalene core, which leads to distortions, affecting the π-system. The question whether the π-electrons prefer a highly symmetric environment or are themselves distortive was answered by Shaik and Hiberty, who showed that the σ-system of benzene prefers the D_{6h} geometry, while the π-system is distortive.[379] In pyracene this interplay is further complicated by the induced strain, which makes it a very interesting model compound. Furthermore apart from the distortion in the π-plane a distortion out of the plane has to be discussed in pyracene, which is definitely not preferred by the aromatic system.

Upon electronic excitation mainly the π-system will be weakened and the interesting question arises, whether this leads to a different balance between the strain and the electronic effects of the π-system and hence to a change in geometry.[i]

The investigation of this balance was the aim of this project. Pyracene was prepared in the group of Anke Krüger and IR, Raman and REMPI spectra were measured in the group of Ingo Fischer. The measurements were aimed at elucidating the electronic structure of pyracene in the ground and excited state, especially the interplay between ring strain and aromaticity. The computations were performed to complement the data obtained from the experiment, to help in the assignment of the bands in the spectra and to explain and

[i]The question of geometric change upon excitation is of course also of vital importance for exciton transport properties, namely the reorganization energy.

Table 7.2: Vertical excitation energies (eV) and oscillator strength at the ground-state equilibrium geometry

State	E_{vert} SCS-CC2	E_{vert} SCS-ADC(2)	$f_{SCS-CC2}$	$f_{SCS-ADC(2)}$
S_1 $^1B_{3u}$	4.16	4.17	0.01	0.02
S_2 $^1B_{1u}$	4.60	4.59	0.12	0.14
S_3 ^1A_u	5.03	5.09	0.00	0.00

rationalize the experimental results.

At first, some preliminary studies to evaluate the methodology using ADC(2) and CASPT2 were performed on naphthalene, where a significant amount of data from the literature exists.[113,380] These studies were also important to be aware of similarities and differences of pyracene and naphthalene. Then the ground and several excited states of pyracene were computed. The ground state geometry was optimized using spin-component scaled Møller-Plesset perturbation theory[54] in combination with a polarized valence triple zeta basis (SCS-MP2/cc-pVTZ) as implemented in TURBOMOLE using the resolution of the identity approximation.[299,300] Frequency calculations on the same level were performed to ensure the existence of a minimum and to make an assignment of the peaks in the experimental ground state IR spectrum possible.

Geometry optimizations in the excited state were performed on the SCS-CC2 level of theory. Single points were calculated on the SCS-CC2 and SCS-ADC(2) level of theory. Absolute state energies were obtained by adding the excitation energies to the corresponding SCS-MP2 ground-state energies. For the geometry optimizations in the excited state the aug-cc-pVDZ basis sets were used. Since the states are very close in energy additional single-point calculations using the aug-cc-pVTZ basis sets were performed. The vibrational frequency calculations in the excited states[163,164] were performed with the cc-pVDZ basis sets using reoptimized geometries due to the computational cost of the numerical evaluation of second derivatives.

The computations predict in line with the results from vibrational spectroscopy (IR and RAMAN) the ground state to be D_{2h} symmetric, which is not self-evident due to the considerable ring strain.

The vertical excitation energies are given in table 7.2. The agreement between SCS-CC2 and SCS-ADC(2) is excellent. Both methods predict the first excited state to be almost dark, while the second excited state is bright. This is similar to the situation in naphthalene.[380]

The S_1 consists of a linear combination of the HOMO $\rightarrow$ LUMO+1 and the HOMO-1 $\rightarrow$

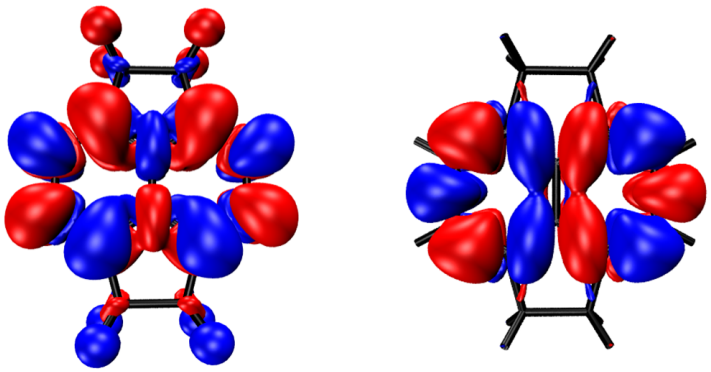

Figure 7.6: Transition densities for the transition $S_0 \rightarrow S_1$ (left-hand side) and $S_0 \rightarrow S_2$ (right-hand side), SCS-CC2/cc-pVDZ, plotted with VMD

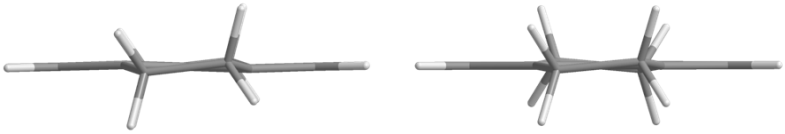

Figure 7.7: Optimized geometries in the S_2. Left-hand side: C_{2h}, right-hand side: D_2

LUMO transition, while the S_2 is dominated by the HOMO $\rightarrow$ LUMO transition. The corresponding transition densities are plotted in Fig 7.6.

The geometry optimizations in the excited state were partly quite dependent on the starting structure. Starting from the D_{2h}-symmetric ground-state minimum energy structure, the optimization in the S_1 led to a stationary point, which is also of D_{2h} symmetry. The frequency analysis confirmed that it is indeed a minimum. Following the same procedure in the S_2, however, yielded a D_{2h}-symmetric stationary point with two imaginary frequencies. Using distorted starting structures yielded two minima of C_{2h} and two of D_2 symmetry. One of each is depicted in Fig. 7.7. In these distorted structures the C_2-bridges are slightly twisted out of planarity. Hence the potential energy surface of the S_2 is of quadruple-well form. The four minima can interconvert via the D_{2h}-symmetric transition state.

The adiabatic excitation energies are given in Table 7.3. The agreement between SCS-CC2 and SCS-ADC(2) is again excellent[ii] and the difference with respect to the experimental

[ii] It should be stressed that the optimization was performed with SCS-CC2 in both cases and only the single-point calculation were performed with different methods.

Table 7.3: Adiabatic excitation energies (eV) including zero-point correction.

State	E_{adia} SCS-CC2	E_{adia} SCS-ADC(2)	Exp.
S_1 $^1B_{3u}$	3.97	3.98	3.819
S_2 $^1B_{1u}$ (D_2)	4.28	4.25	
S_2 $^1B_{1u}$ (C_{2h})	4.26	4.23	

Table 7.4: Bond lengths (in Å) and dihedral angles (in °)of pyracene for different states. For the definition, see Fig. 7.5

parameter	S_0	S_1 D_{2h}	S_2 D_{2h}	S_2 D_2	S_2 C_{2h}
1	1.438	1.463	1.410	1.410	1.411
2	1.386	1.435	1.457	1.457	1.455
3	1.524	1.530	1.527	1.527	1.526
4	1.579	1.590	1.592	1.590	1.587
5	1.400	1.403	1.403	1.404	1.404
6	1.380	1.438	1.406	1.406	1.405
Dihedral	180	180	180	177	176

value is also within the typical error margin for adiabatic excitation energies.[381] The energetic difference, as well as the barrier for the inversion[iii] between the two pairs of minima is very small. Since the energy differences are well below the accuracy of the method it can only be stated that the potential energy surface is quite flat in the S_2 and the molecule is thus floppy with respect to the distortion of the bridges out of planarity.

Some geometrical parameters (bond lengths and the dihedral angle, for the definition see Fig. 7.5) are given in Table 7.4. Apart from the dihedral angle there is no clear trend observable. Computing the PES of the S_1 for the same distortions as in the S_2 shows that the potential energy surface is also quite flat in the S_1 (see[375] for details). The energies of the states with the different minimum energy geometries are depicted in Fig. 7.8. At the minimum energy structure of the S_2 state the energetic difference between the excited states is quite small, which was demanding for the computations because the calculations frequently converged on the wrong root. Furthermore, this makes a vibronic coupling between the states likely, which also influences the spectra.

The results of the computations suggest the following interpretation: In the ground state the aromaticity is stronger than the ring strain and hence the ring stays planar. In the S_1 the aromaticity of the π-system is weakened, but not enough to change the balance. In the S_2, however, the balance is changed, which leads to a slight distortion. The bond

[iii] The barrier for the distorted D_2 minima is about $20 cm^{-1}$, while the C_{2h}-symmetric minima are more or less isoenergetic with the transition state.

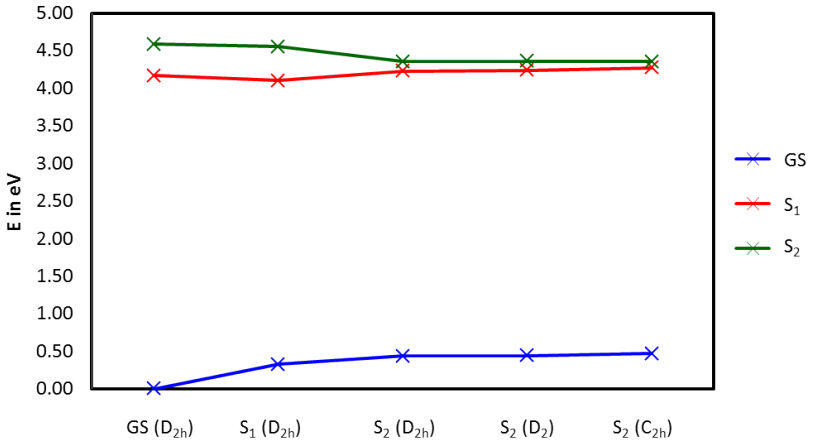

Figure 7.8: Energy of the ground and the first two excited states using the minimum-energy geometries of the different states (SCS-ADC(2)/aug-cc-pVDZ)

lengths, however, are not significantly distorted, which might be due to the fact that the σ-system, which is not notably affected by the excitation also plays an important role for the existence or non-existence of the bond length alternation in aromatic systems.
The computed frequencies of the S_1 state could be used in the assignment of the experimentally derived bands. The agreement between theory and experiment is quite good (see[375] for details).
In the experimental set-up of the REMPI the ions were detected in a time-of-flight mass spectrometer. Since the pyracene dimer appeared quite prominently the question of the shape of the dimer arose. The dimers are especially interesting due to potential excimer formation.[375] For an estimation of the lowest energy structure of the dimers six potential conformations were optimized on the B3LYP-D3/cc-pVDZ level of theory using the Gaussian program package. The dimer structures and their relative energies are given in Fig. 7.9. The lowest energy structure is the crossed one and hence it is most likely the one observed experimentally.

In this project the computations elucidated the PES of the S_1 and S_2 state of pyracene and were hence able to provide the basis for an estimation of the balance between aromaticity and ring strain. The computed frequencies furthermore helped in assigning the bands and interpreting the experimental spectra. The most likely conformations of the pyracene dimer could also be predicted.

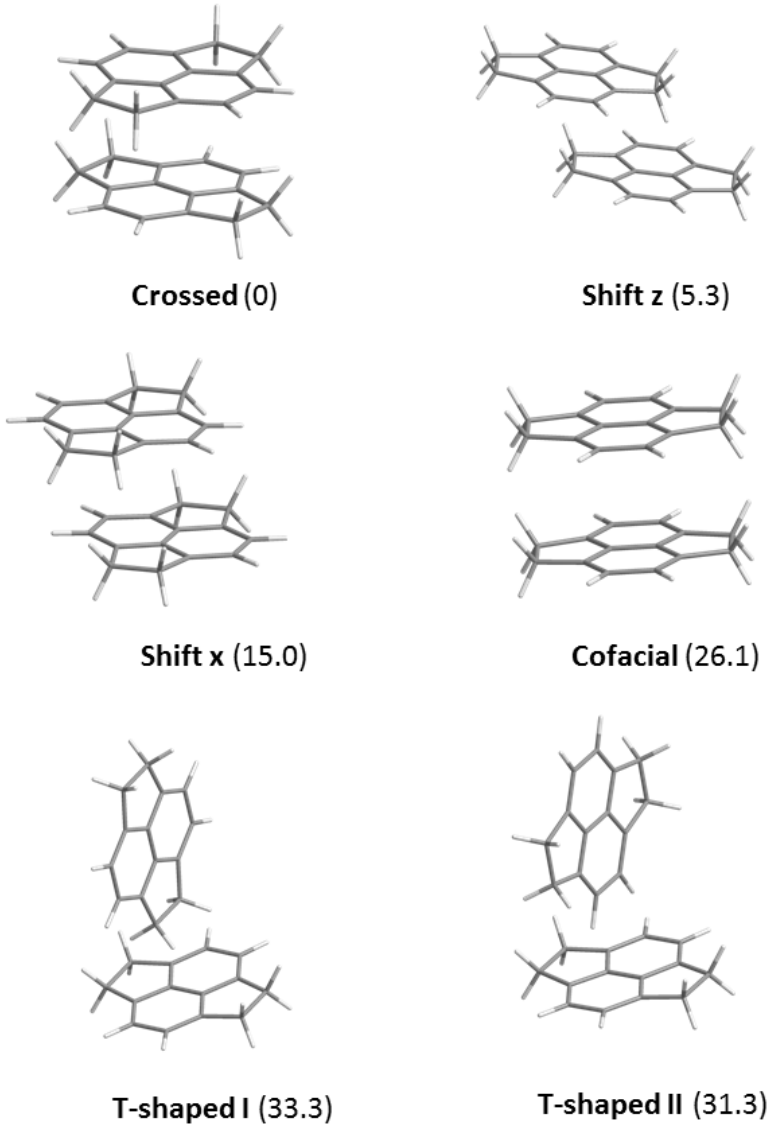

Figure 7.9: Optimized structures of pyracene dimers and their relative energies (in kJ/mol).

8 Summary

The scope of computational chemistry can be broadened by developing new methods and more efficient algorithms. However, the evaluation of the applicability of the methods for the different fields of chemistry is equally important. In this thesis systems with an unusual and complex electronic structure, such as excitonic states in organic semiconductors, a boron-containing bipolaron and the excited states of pyracene were studied and the applicability of the toolkit of computational chemistry was investigated. Concerning the organic semiconductors the focus was laid on organic solar cells, which are one of the most promising technologies with regard to satisfying the world's need for cheap and environmentally sustainable energy. This is due to the low production and material costs and the possibility of using flexible and transparent devices. However, their efficiency does still not live up to the expectations. Especially the exciton diffusion lengths seem to be significantly too short. In order to arrive at improved modules, a fundamental understanding of the elementary processes occurring in the cell on the molecular and supramolecular level is needed. Computational chemistry can provide insight by separating the different effects and providing models for predictions and prescreenings. In this thesis, the focus was laid on the description of excitonic states in merocyanines and perylene-based dyes taking the influence of the environment into account.

At first, the photochemical isomerization between two configurations of 6-nitro BIPS observed experimentally was studied by first benchmarking several functionals against SCS-ADC(2) in the gas phase and subsequently calculating the excited-state potential energy surface. The geometries obtained from a relaxed scan in the ground state as well as from a scan in the excited state were used. The environment was included using different polarizable continuum models. It was shown that the choice of the model and especially the question of the state specificity of the approach is of vital importance. Using the results of the calculations, a two-dimensional potential energy surface could be constructed that could be used to explain the experimental findings. Furthermore, the importance of the excited-state isomerization as a potential deactivation channel in the

exciton transport was pointed out.

Then the assessment of the suitability of different merocyanines for optoelectronic applications with quantum-chemical methods was discussed. At first, the effect of the environment on the geometry, especially on the bond length alternation pattern, was investigated. It was shown that the environment changes the character of the ground-state wave function of several merocyanines qualitatively, which means that the results of gas-phase calculations are meaningless - at least when a comparison with solution or device data is desired. It was demonstrated that using a polarizable continuum model with an effective ϵ, a qualitative agreement between the calculated geometry and the geometry in the crystal structure can be obtained. Therefore, by comparing the bond length alternation in solution and in the crystal, a rough estimate of the effect of the crystal environment can be made.
It was further shown that the connection between the HOMO energy and the open-circuit voltage is not as simple as it is often implied in the literature. It was discussed that it is not clear whether the HOMO of a single molecule or a π-stack containing several monomers should be used and if the environmental charges of the bulk phase or the interface should be included. Investigating the dependence of the HOMO energy on the stack size yielded no definitive trend. Furthermore, it was discussed that the effect due the optimization of the modules (solvent, bulk heterojunction) during the production masks any potential correlation between the HOMO energy and measured open-circuit values. Therefore, a trend can only be expected for unoptimized bilayer cells. It was concluded that ultimately, the importance of the HOMO energy should not be overestimated.
The correlation between the exciton reorganization energy and the so-called cyanine limit, which is predicted by a simple two-state model, was also discussed. By referring to the results of VB calculations, it was discussed that the correlation indeed exists and is non-negligible, although the effect is not as strong as one might have expected. In this context, a potential application of a VB/MM approach was covered briefly. The importance of the molecular reorganization energy and the device morphology was also discussed.
It was concluded that the optimization of merocyanines for organic optoelectronic devices is inherently a multiparameter problem and one cannot expect to find one particular parameter, which solely controls the efficiency.

The perylene-based dyes were studied with a focus on the description of a potential trapping mechanism involving an intermolecular motion in a dimer. The aim was to find

methods which can be applied to larger model systems than a dimer and take the effect of the environment into account. As a test coordinate the longitudinal shift of two monomers against each other was used. At first, it was demonstrated how the character of an excited state in a dimer can be defined and how it can be extracted from a standard quantum-chemical calculation. Then several functionals were benchmarked and their applicability or failure was rationalized using the character analysis. Two recipes could be proposed, which were applied to a constraint optimization (only intermolecular degrees of freedom) in the excited states of the PBI dimer and to the description of the potential energy surfaces of ground and excited states along a longitudinal displacement in the perylene tetramer, respectively.

It was further demonstrated that the semi-empirical OMx methods fail to give an accurate description of the excited-state potential energy surfaces as well as the ground-state surface along the test coordinate. This failure could be attributed to an underestimation of overlap-dependent terms. Consequently, it could be shown that the methods are applicable to large intermolecular distances, where the overlap is negligible. The results of DFT calculations with differently composed basis sets suggested that adding an additional single p-function for each atom should significantly improve the performance.

QM/MM methods are ideally suited to take the effect of the environment on a a dimer model system into account. However, it was shown that standard force fields also give an incorrect description of the interaction between the monomers along the intermolecular coordinate. This failure was attributed to the isotropic atom-atom interaction in the repulsion term of the Lennard-Jones potential. This was corroborated using two simple proof-of-principle anisotropy models. Therefore, a novel force field called OPLS-AA$_O$ was presented that is based on OPLS-AA, but uses an anisotropic model for the repulsion. The model involves the overlap integral between the molecular densities, which are modeled as a sum of atom-centered p-type Gaussian functions. It was shown that using this force field an excellent agreement with the DFT results can be obtained when the correct parameters are used. These parameters, however, are not very generalizable, which was attributed to the simplicity of the model in its current state (using the same exponential parameter for all atoms). As a short excursion, the applicability of an MO-based overlap model was discussed.

It was demonstrated that the repulsion term based on the density overlap can be used to correct the failure of the OMx methods for the ground states. This is in accord with the assumption that an underestimation of the overlap terms is responsible for the failure.

It was shown that OPLS-AA$_O$ also gives an excellent description of the longitudinal shift

in a PBI tetramer. Using the tetramer as a test system and applying the recipe obtained in the TDDFT benchmark for the QM-part and OPLS-AA$_O$ for the MM-part in conjunction with an electrostatic embedding scheme, a QM/MM description of the excited states of the PBI dimer including the effect of the environment could be obtained.

In the last chapter the theoretical description of the Bis(borolyl)thiophene dianion and the excited states of pyracene were discussed. The electronic structure of the Bis(borolyl)thiophene dianion - a negative bipolaron - was elucidated using DFT and CASPT2 methods. Furthermore, an estimation of the extent of triplet admixture to the ground state due to spin-orbit coupling was given.
In the second project the S_1 and S_2 states of pyracene were computed using SCS-CC2 and SCS-ADC(2) and an estimation for the balance between aromaticity and ring strain was given. This also involved computing the vibrational frequencies in the excited states. In both studies the results of the computations were able to rationalize and complete experimental results.

9 Zusammenfassung

Die Anwendungsmöglichkeiten der Methoden der theoretischen Chemie können erweitert werden, indem neue Methoden und effizientere Algorithmen entwickelt werden. Es ist jedoch ebenso wichtig die Anwendbarkeit der Methoden für die verschiedenen Felder der Chemie zu evaluieren. In dieser Arbeit wurden Systeme mit einer komplexen und ungewöhnlichen Struktur, wie exzitonische Zustände in organischen Halbleitern, ein borbasiertes Bipolaron und die angeregten Zustände von Pyracen untersucht und die Anwendbarkeit der verschiedenen Methoden evaluiert. Im Bezug auf die organischen Halbleiter wurde der Fokus auf organische Solarzellen gelegt, welche zu den vielversprechendsten Technologien gehören, um dem weltweiten Bedarf an billiger und ökologisch nachhaltiger Energie zu begegnen. Dies liegt an den niedrigen Produktionskosten und der Möglichkeit flexible und transparente Module zu verwenden. Ihre Wirkungsgrade werden den Erwartungen jedoch noch nicht gerecht. Vor allem die Exzitonendiffusionslängen scheinen deutlich zu gering zu sein. Um verbesserte Module zu erhalten ist ein fundamentales Verständnis der Elementarprozesse in der Zelle auf molekularem und supramolekularem Level vonnöten. Die theoretische Chemie kann dabei helfen dies zu erreichen, indem sie die verschiedenen Effekte separiert und Modelle für Vorhersagen und zur Vorauswahl geeigneter Verbindungen bereitstellt. In dieser Arbeit wurde der Fokus auf die Beschreibung von exzitonischen Zuständen in Merocyaninen und perylenbasierten Farbstoffen unter Berücksichtigung von Umgebungseinflüssen gelegt.

Zunächst wurde die experimentell beobachtete photochemische Isomerisierung zwischen zwei Konfigurationen von 6-nitro BIPS untersucht, indem zuerst die Anwendbarkeit verschiedener Funktionale im Vergleich zu SCS-ADC(2) in der Gasphase überprüft wurde und anschließend die Potentialfläche des angeregten Zustands berechnet wurde. Es wurden sowohl die Geometrien aus einem *relaxed scan* im Grundzustand als auch von einem *scan* im angeregten Zustand verwendet. Umgebungseffekte wurden unter Verwendung verschiedener Kontinuumsansätze (*polarizable continuum models*) berücksichtigt. Es konnte gezeigt werden, dass die Wahl des Ansatzes und vor allem die Frage nach der Zu-

standsspezifizität des Kontinuumsansätze sehr entscheidend ist. Mit den Ergebnissen der Berechnungen konnte eine zweidimensionale Potenzialfläche konstruiert werden, mittels welcher die experimentellen Beobachtungen erklärt werden konnten. Außerdem wurde auf die Bedeutung der Isomerisierung im angeregten Zustand als einem potenziellen Deaktivierungskanal für den Exzitonentransport hingewiesen.

Anschließend wurde die Möglichkeit einer Bewertung der Eignung verschiedener Merocyanine für optoelektonische Fragestellungen mit quantenchemischen Methoden diskutiert. Zunächst wurde der Einfluss der Umgebung auf die Geometrie und insbesondere auf die Bindungslängenalternanz untersucht. Es wurde gezeigt, dass die Umgebung die Wellenfunktion mehrerer Merocyanine qualitativ verändert, was bedeutet, dass Berechnungen in der Gasphase keinen Sinn machen - zumindest nicht, wenn die Ergebnisse mit Daten, die in Lösung oder in der Zelle erhalten wurden, verglichen werden sollen. Es konnte gezeigt werden, dass unter Verwendung eines Kontinuumsansatzes mit einer effektiven Dielektrizitätskonstante ϵ eine qualitative Übereinstimmung zwischen der berechneten Geometrie und der Geometrie in der Kristallstruktur erzielt werden kann. Dies ermöglicht es, durch einen Vergleich der Bindungslängenalternanz in Lösung und im Kristall eine grobe Abschätzung für den Einfluss der Kristallumgebung zu erhalten.
Es wurde außerdem dargelegt, dass der Zusammenhang zwischen der Energie des HOMOs und der Leerlaufspannung nicht so eindeutig ist, wie es oft in der Literatur suggeriert wird. Es stellte sich die Frage, ob die HOMO-Energie eines einzelnen Moleküls oder eines Stapels bestehend aus mehreren Monomeren verwendet werden sollte und ob der Umgebungseffekt der Ladungen der Bulkphase oder der Grenzfläche berücksichtigt werden sollte. Die Untersuchung der Abhängigkeit der HOMO-Energie von der Anzahl der Monomere ergab keinen klaren Trend. Die Tatsache, dass die Optimierung des Moduls während des Produktionsprozesses (Solvent, Bulk-Hereojunction-Konzept) eine potenzielle Korrelation zwischen der HOMO-Energie und der Leerlaufspannung maskiert, wurde ebenfalls diskutiert. Deshalb kann eine Korrelation nur für nicht optimierte Zweischichtzellen erwartet werden. Es wurde der Schluss gezogen, dass die Bedeutung der HOMO-Energie letztendlich nicht überbewertet werden sollte.
Der Zusammenhang zwischen der Exzitonenreorganisationsenergie und dem sogenannten Cyaninlimit, welcher von einem einfachen Zwei-Zustands-Model vorhergesagt wird wurde diskutiert. Unter Verweis auf die Ergebnisse von VB-Berechnungen konnte diskutiert werden, dass der Zusammenhang in der Tat existiert und nicht vernachlässigbar, aber auch nicht so groß ist, wie man vermutet haben könnte. In diesem Kontext wurde die potenzielle

Anwendbarkeit eines VB/MM-Ansatzes kurz besprochen. Die Bedeutung der molekularen Reorganisationsenergie und der Morphologie der Zelle wurden ebenfalls diskutiert. Es wurde das Fazit gezogen, dass die Optimierung der Merocyanine für die Anwendung in organischen Halbleitern inhärent ein Multiparameterproblem ist und man nicht erwarten kann, einen einzelnen Parameter zu finden, der allein die Effizienz kontrolliert.

Die perylenbasierten Farbstoffe wurden mit dem Fokus auf der Beschreibung eines potenziellen Exzitoneneinfangmechanismus, untersucht, welcher auf der intermolekularen Bewegung in einem Dimer basiert. Das Ziel war es Methoden zu finden, die auf größere Systeme anwendbar sind und den Umgebungseinfluss berücksichtigen können. Als Testkoordinate wurde die longitudinale Verschiebung der Monomere gegeneinander verwendet. Zunächst wurde gezeigt, wie der Charakter eines angeregten Zustandes in einem Dimer definiert werden kann und wie ein Maß für den Charakter ausgehend von einer normalen quantenchemischen Berechnung erhalten werden kann. Anschließend wurden verschiedene Funktionale evaluiert und ihre Anwendbarkeit beziehungsweise ihr Versagen mittels der Charakteranalyse rationalisiert. Zwei Ansätze konnten vorgeschlagen werden, welche auf eine Optimierung in den angeregten Zustände des Dimers mit Nebenbedingung (nur intermolekulare Freiheitsgrade) beziehungsweise auf eine Beschreibung der Potenzialflächen des Grundzustandes und der angeregten Zustände für die longitudinale Verschiebung in einem Perylentetramer angewendet wurden.
Es wurde außerdem gezeigt, dass die semiempirischen OMx Methoden keine akkurate Beschreibung der Potenzialflächen der angeregten Zustände sowie des Grundzustandes für die Testkoordinate liefern. Dies konnte mit der Unterschätzung der intermolekularen Überlappterme begründet werden. Folglich war es möglich zu zeigen, dass die Methoden für intermolekulare Abstände, bei denen der Überlapp vernachlässigbar ist, anwendbar sind. Die Ergebnisse von DFT-Rechnungen mit unterschiedlich zusammengesetzten Basissätzen ließen ferner den Schluss zu, dass das Hinzufügen einer einzelnen p-Funktion an jedem Atom eine deutliche Verbesserung bringen sollte.
QM/MM-Methoden sind ideal geeignet, um den Einfluss der Umgebung auf ein Dimer-Modellsystem zu berücksichtigen. Es wurde jedoch gezeigt, dass gängige Kraftfelder ebenfalls eine inkorrekte Beschreibung der Wechselwirkung zwischen den Monomeren entlang der intermolekularen Koordinate liefern. Dies wurde mit der isotropen Beschreibung der Atom-Atom-Wechselwirkung im Repulsionsterm des Lennard-Jones-Potenzials begründet. Diese Annahme wurde durch die Anwendung zweier Proof-of-Principle-Ansätze untermauert. Folglich wurde ein neues Kraftfeld, genannt OPLS-AA$_O$, eingeführt, wel-

ches auf OPLS-AA basiert, aber eine anisotrope Modellierung der Repulsion verwendet. Diese anisotrope Repulsion basiert auf dem Überlappintegral der molekularen Elektronendichten, welche als Summe aus atomzentrierten p-artigen Gaußfunktionen modelliert wird. Es wurde gezeigt, dass mit diesem Kraftfeld eine hervorragende Übereinstimmung mit den DFT-Ergebnissen erhalten werden kann, wenn die richtigen Parameter verwendet werden. Diese Parameter sind jedoch nicht sehr generalisierbar, was mit der Einfachheit des Models zu seinem momentanen Stand begründet wurde (Verwendung desselben Parameters im Exponenten bei allen Atomen). Als kurzer Exkurs wurde die Anwendbarkeit eines MO-basierten Überlappmodells diskutiert.
Es konnte nachgewiesen werden, dass der Repulsionsterm, der auf der Dichteüberlappung basiert, auch als Korrekturterm für die Anwendbarkeit der OMx-Methoden bezüglich des Grundzustandes verwendet werden kann. Dies deckt sich mit der Annahme, dass eine Unterschätzung von Überlapptermen für das Versagen der semiempirischen Methoden verantwortlich ist.
Es wurde gezeigt, dass OPLS-AA$_O$ die Potenzialfläche für die longitudinale Verschiebung in einem PBI Tetramer exzellent beschriebt. Unter Verwendung des Tetramers als Testsytem und unter Anwendung eines der vorgeschlagenen TDDFT-Ansätze für den QM-Teil und OPLS-AA$_O$ für den MM-Teil in Verbindung mit einem *electrostatic embedding*-Ansatz konnte eine QM/MM-Beschreibung der angeregten Zustände des PBI Dimers unter Berücksichtigung des Umgebungseinfluss erhalten werden.

Im letzten Kapitel wurde die theoretische Beschreibung des Bis(borolyl)thiophendianions und von Pyracen diskutiert. Die elektronische Struktur des Bis(borolyl)thiophendianions wurde beschrieben unter Verwendung von DFT- und CASPT2-Methoden. Außerdem wurde eine Abschätzung des Ausmaßes der Triplettbeimischung zum Grundzustand durch die Spin-Bahn-Kopplung gegeben.
Im zweiten Projekt wurden der S_1- und S_2- Zustand des Pyracens unter Verwendung von SCS-CC2 und SCS-ADC(2) berechnet und eine Abschätzung des Verhältnisses von Aromatizität und Ringspannung gegeben. Dies beinhaltete auch die Berechnung der Schwingungsfrequenzen im angeregten Zustand.
In beiden Studien konnten die Ergebnisse der Berechnungen die experimentellen Daten vervollständigen und rationalisieren.

10 Acknowledgments

First of all, I would like to thank my supervisor Prof. Bernd Engels for giving me the opportunity to work in his group on this interesting topic, for his support, for providing a relaxed working atmosphere and especially for allowing me the freedom to develop my own ideas. Furthermore he provided the financial possibilities to attend several international conferences, thus allowing me to broaden my expertise and to discuss my results with scientists from all over the world.

When I started working in this field, many people helped me to get a grip on theoretical chemistry and its methods. Prof. Reinhold Fink helped me with many fruitful discussions and by answering all my questions. Dr. Volker Settels introduced me to the calculation of excited states with CC2 and TDDFT and shared with me a lot of his insight into organic electronics. I want to thank both of them for their help and their patience. I also would like to thank Dr. Vera Stehr, Dr. Alexander Schubert and Dr. Klaus Renziehausen for many interesting discussions and for helping me with the more physics-related aspects of the field.

In computational chemistry often technical issues annoyingly delay the progress. Many thanks go to Thomas Schmidt, Daniel Bellinger, Daniel Weber and Johannes Becker, who always provided support when problems with the cluster, the software or the desktop computers occurred. Thomas Schmidt furthermore introduced me to VMD and showed me several tricks how to master it.

During my PhD thesis I was involved in different projects with the groups of Prof. Braunschweig, Prof. Fischer, Prof. Engel, Prof. Lambert, Prof. Würthner, Prof. Brixner, Prof. Dyakonov and Prof. Schirmeister and I am grateful for the interesting and challenging problems they provided. This allowed me to apply the tools of computational chemistry to very different chemically relevant problems. Special thanks deserve Dr. Christian Hörl, Dr. Stefan Rützel and Dr. Matthias Stolte. Their high expertise combined with

their modesty and the fact that they are excellent team players made the collaborations very enjoyable and at the same time very efficient and target-oriented.
The same is true for the collaboration with many people within our institute, who contributed with ideas and a lot of work. Many thanks go to Dr. Vera Stehr, Zarah Falk, Anna Heilos, Eileen Welz, Charlotte Brückner, Dr. Maxim Tafipolsky and Christoph Brüning.

I had the fortune to supervise several excellent Bachelor, Master and Diploma candidates and to introduce them to the field of computational chemistry. Their contribution to this work is quite significant and I hope I succeeded in always making clear, whose work was involved. Many thanks go to Marco Schmid, Veronika Krämer, Andreas Heimbeck, Anca Boariu, Simon Schmitt and Charlotte Brückner.

Many thanks go to the whole Engels group as well as the Engel group for creating a great atmosphere of tolerance in the institute and for all the fun they provided. Many thanks go to Uschi Rüppel for excellently organizing all administrative work, as well as the leisure activity of the group.

I would also like to thank Prof. Fédéric Castet for accepting to be a reviewer of my thesis.

I also want to thank my parents for all the help and support during my studies, as well as during the time as a PhD student and of course also for financially funding my studies. Finally I want to thank Charlotte for proofreading my lengthy thesis, for writing an excellent master thesis that finally provided most satisfyingly all the answers to the questions related to the merocyanines I have been struggling with for so so long without progress and of course most importantly for making my life so rich by allowing me to spend it with her.

If to do were as easy as to know what were good to do, chapels had been churches and poor men's cottages princes' palaces.

(William Shakespeare, The Merchant of Venice)

La lutte elle-même vers les sommets suffit à remplir un cœur d'homme. Il faut imaginer Sisyphe heureux.

(Albert Camus, Le Mythe de Sisyphe)

11 Bibliography

[1] Thiel, W. Angew. Chem. **2011**, 123, 9382–9384.

[2] Deglmann, P.; Schäfer, A.; Lennartz, C. Int. J. Quantum Chem. **2015**, 115, 107–136.

[3] Mishra, A.; Bäuerle, P. Angew. Chem. Int. Ed. **2012**, 51, 2020–2067.

[4] Pagliaro, M.; Ciriminna, R.; Palmisano, G. ChemSusChem **2008**, 1, 880–891.

[5] Heliatek press release. 2013.

[6] Baumeier, B.; May, F.; Lennartz, C.; Andrienko, D. J. Mater. Chem. **2012**, 22, 10971–10976.

[7] Shang, Y.; Li, Q.; Meng, L.; Wang, D.; Shuai, Z. Theor. Chem. Acc. **2011**, 129, 291–301.

[8] Ortmann, F.; Bechstedt, F.; Hannewald, K. Phys. Status Solidi B **2011**, 248, 511–525.

[9] Linares, M.; Beljonne, D.; Cornil, J.; Lancaster, K.; Brédas, J.-L.; Verlaak, S.; Mityashin, A.; Heremans, P.; Fuchs, A.; Lennartz, C.; Idé, J.; Méreau, R.; Aurel, P.; Ducasse, L.; Castet, F. J. Phys. Chem. C **2010**, 114, 3215–3224.

[10] Verlaak, S.; Beljonne, D.; Cheyns, D.; Rolin, C.; Linares, M.; Castet, F.; Cornil, J.; Heremans, P. Adv. Funct. Mater **2009**, 19, 3809–3814.

[11] Brédas, J.-L.; Norton, J. E.; Cornil, J.; Coropceanu, V. Acc. Chem. Res. **2009**, 42, 1691–1699.

[12] Thompson, N. J.; Hontz, E.; Congreve, D. N.; Bahlke, M. E.; Reineke, S.; Van Voorhis, T.; Baldo, M. A. Adv. Mater. **2014**, 26, 1366–1371.

[13] Savoie, B. M.; Jackson, N. E.; Chen, L. X.; Marks, T. J.; Ratner, M. A. Acc. Chem. Res. **2014**, 47, 3385–3394.

[14] Nelson, J.; Kwiatkowski, J. J.; Kirkpatrick, J.; Frost, J. M. Acc. Chem. Res. **2009**, 42, 1768–1778.

[15] O'Boyle, N. M.; Campbell, C. M.; Hutchison, G. R. J. Phys. Chem. C **2011**, 115, 16200–16210.

[16] Settels, V. Quantum chemical description of ultrafast excitonic self-trapping in perylene based materials. Ph.D. thesis, Julius-Maximilians-Universität Würzburg, 2012.

[17] Schubert, A.; Settels, V.; Liu, W.; Würthner, F.; Meier, C.; Fink, R. F.; Schindlbeck, S.; Lochbrunner, S.; Engels, B.; Engel, V. J. Phys. Chem. Lett. **2013**, 4, 792–796.

[18] Fink, R. F.; Seibt, J.; Engel, V.; Renz, M.; Kaupp, M.; Lochbrunner, S.; Zhao, H.-M.; Pfister, J.; Würthner, F.; Engels, B. J. Am. Chem. Soc. **2008**, 130, 12858–12859.

[19] Bredas, J.-L.; Durrant, J. R. Acc. Chem. Res. **2009**, 42, 1689–1690.

[20] Armaroli, N.; Balzani, V. Energy for a Sustainable World; Wiley-VCH Verlag & Co. KGaA: Weinheim, 2011.

[21] Brabec, C., Scherf, U., Dyakonov, V., Eds. Organic Photovoltaics; Wiley-VCH Verlag & Co. KGaA: Weinheim, 2014.

[22] Hush, N. S. Ann. N. Y. Acad. Sci. **2003**, 1006, 1–20.

[23] Müllen, K., Ed. Organic Light Emitting Devices: Synthesis, Properties and Applications.; Wiley-VCH Verlag & Co. KGaA: Weinheim, 2006.

[24] Klauk, H. Chem. Soc. Rev. **2010**, 39, 2643–2666.

[25] Heckmeier, M.; Heider, U.; Maisch, R. Physik Journal **2015**, 14, 33–38.

[26] Tang, C. W. Appl. Phys. Lett. **1986**, 48, 183–185.

[27] Grätzel, M. J. Photochem. Photobiol. C **2003**, 4, 145–153.

[28] Burschka, J.; Pellet, N.; Moon, S.-J.; Humphry-Baker, R.; Gao, P.; Nazeeruddin, M. K.; Gratzel, M. Nature **2013**, 499, 316–319.

[29] Hodes, G. Science **2013**, 342, 317–318.

[30] Bach, U. Nat. Chem. **2015**, 7, 616–617, News and Views.

[31] Lee, J.; Vandewal, K.; Yost, S. R.; Bahlke, M. E.; Goris, L.; Baldo, M. A.; Manca, J. V.; Voorhis, T. V. J. Am. Chem. Soc. **2010**, 132, 11878–11880.

[32] Ohkita, H.; Cook, S.; Astuti, Y.; Duffy, W.; Tierney, S.; Zhang, W.; Heeney, M.; McCulloch, I.; Nelson, J.; Bradley, D. D. C.; Durrant, J. R. J. Am. Chem. Soc. **2008**, 130, 3030–3042.

[33] Nan, G.; Zhang, X.; Lu, G. J. Phys. Chem. C **2015**, 119, 15028–15035.

[34] Shockley, W.; Queisser, H. J. J. Appl. Phys. **1961**, 32, 510–519.

[35] Giebink, N. C.; Wiederrecht, G. P.; Wasielewski, M. R.; Forrest, S. R. Phys. Rev. B **2011**, 83, 195326.

[36] Tayebjee, M. J. Y.; McCamey, D. R.; Schmidt, T. W. J. Phys. Chem. Lett. **2015**, 6, 2367–2378.

[37] Van Voorhis, T. Nat. Phys. **2015**, 11, 300–301.

[38] Congreve, D. N.; Lee, J.; Thompson, N. J.; Hontz, E.; Yost, S. R.; Reusswig, P. D.; Bahlke, M. E.; Reineke, S.; Van Voorhis, T.; Baldo, M. A. Science **2013**, 340, 334–337.

[39] Ojala, A.; Petersen, A.; Fuchs, A.; Lovrincic, R.; Pölking, C.; Trollmann, J.; Hwang, J.; Lennartz, C.; Reichelt, H.; Höffken, H. W.; Pucci, A.; Erk, P.; Kirchartz, T.; Würthner, F. Adv. Func. Mat. **2012**, 22, 86–96.

[40] Stehr, V.; Pfister, J.; Fink, R. F.; Engels, B.; Deibel, C. Phys. Rev. B **2011**, 83, 155208.

[41] Stehr, V.; Fink, R. F.; Engels, B.; Pflaum, J.; Deibel, C. J. Chem. Theory Comput. **2014**, 10, 1242–1255.

[42] Diermann, R. Süddeutsche Zeitung **2015**,

[43] Katz, E. A.; Faiman, D.; Tuladhar, S. M.; Kroon, J. M.; Wienk, M. M.; Fromherz, T.; Padinger, F.; Brabec, C. J.; Sariciftci, N. S. J. Appl. Phys. **2001**, 90, 5343–5350.

[44] He, T.; Stolte, M.; Burschka, C.; Hansen, N. H.; Musiol, T.; Kälblein, D.; Pflaum, J.; Tao, X.; Brill, J.; Würthner, F. Nat. Commun. **2015**, 6.

[45] Völker, S. F.; Dellermann, T.; Ceymann, H.; Holzapfel, M.; Lambert, C. J. Polym. Sci. A Polym. Chem. **2014**, 52, 890–911.

[46] Xu, T.; Yu, L. Mater. Today **2014**, 17, 11–15.

[47] González, L.; Escudero, D.; Serrano-Andrés, L. ChemPhysChem **2012**, 13, 28–51.

[48] Jensen, F. Introduction to Computational Chemistry: Second Edition; John Wiley & Sons LTD.: Chichester, 2007.

[49] Szabo, A.; Ostlund, N. S. Modern Quantum Chemistry; Dover Publications, 1996.

[50] Helgaker, T.; Jørgensen, P.; Olsen, J. Molecular Electronic-Structure Theory; John Wiley & Sons LTD.: Chichester, 2000.

[51] McWeeny, R. Methods of Molecular Quantum Mechanics, Second Edition; Academic Press Limited: London, 1989.

[52] Löwdin, P.-O. In On the Nonorthogonality Problem; Löwdin, P.-O., Ed.; Adv. Quantum Chem.; Academic Press, 1970; Vol. 5; pp 185–199.

[53] Becke, A. D. J. Chem. Phys. **2014**, 140, 18A301.

[54] Møller, C.; Plesset, M. S. Phys. Rev. **1934**, 46, 618–622.

[55] Burke, K. J. Chem. Phys. **2012**, 136, 150901.

[56] Slater, J. C. Phys. Rev. **1951**, 81, 385–390.

[57] Hohenberg, P.; Kohn, W. Phys. Rev. **1964**, 136, B864–B871.

[58] Kohn, W.; Sham, L. J. Phys. Rev. **1965**, 140, A1133–A1138.

[59] Koch, W.; Holthausen, M. C. A Chemist's Guide to Density Functional Theory; Wiley-VCH Verlag GmbH: Weinheim, 2001.

[60] Becke, A. D. Phys. Rev. A **1988**, 38, 3098–3100.

[61] Lee, C.; Yang, W.; Parr, R. G. Phys. Rev. B **1988**, 37, 785–789.

[62] Zhao, Y.; Truhlar, D. G. Acc. Chem. Res. **2008**, 41, 157–167.

[63] Vosko, S. H.; Wilk, L.; Nusair, M. Can. J. Phys. **1980**, 58, 1200–1211.

[64] Becke, A. J. Chem. Phys. **1993**, 98, 5648–5652.

[65] Burke, K.; Ernzerhof, M.; Perdew, J. P. Chem. Phys. Lett. **1997**, 265, 115–120.

[66] Tozer, D. J.; Handy, N. C. J. Chem. Phys. **1998**, 109, 10180–10189.

[67] Savin, A.; Umrigar, C.; Gonze, X. Chem. Phys. Lett. **1998**, 288, 391–395.

[68] Casida, M.; Huix-Rotllant, M. Annu. Rev. Phys. Chem. **2012**, 63, 287–323.

[69] van Meer, R.; Gritsenko, O. V.; Baerends, E. J. J. Chem. Theory Comput. **2014**, 10, 4432–4441.

[70] Steinmann, S. N.; Corminboeuf, C. J.Chem. Phys. **2011**, 134, 044117.

[71] Becke, A. D.; Johnson, E. R. J. Chem. Phys. **2005**, 122, 154104.

[72] Grimme, S.; Antony, J.; Ehrlich, S.; Krieg, H. J. Chem. Phys. **2010**, 132, 154104.

[73] Cohen, A. J.; Mori-Sánchez, P.; Yang, W. Chem. Rev. **2012**, 112, 289–320.

[74] Goerigk, L.; Grimme, S. J. Chem. Theory Comput. **2011**, 7, 291–309.

[75] Shaik, S. New J. Chem. **2007**, 31, 2015–2028.

[76] Hollas, J. M. Modern Spectroscopy; John Wiley & Sons Ltd: Chichester, 2004.

[77] Dreuw, A.; Head-Gordon, M. Chem. Rev. **2005**, 105, 4009–4037.

[78] Martin, R. L. J. Chem. Phys. **2003**, 118, 4775–4777.

[79] Plasser, F.; Lischka, H. J. Chem. Theory and Comput. **2012**, 8, 2777–2789.

[80] Peach, M. J. G.; Benfield, P.; Helgaker, T.; Tozer, D. J. J. Chem. Phys. **2008**, 128, 044118.

[81] Guido, C. A.; Cortona, P.; Mennucci, B.; Adamo, C. J. Chem. Theory Comput. **2013**, 9, 3118–3126.

[82] Etienne, T.; Assfeld, X.; Monari, A. Journal of Chemical Theory and Computation **2014**, 10, 3896–3905.

[83] Slater, J. C.; Wood, J. H. Int. J. Quantum Chem. **1970**, 5, 3–34.

[84] Ziegler, T.; Rauk, A.; Baerends, E. Theor. Chim. Acta **1977**, 43, 261–271.

[85] Kowalczyk, T.; Yost, S. R.; Voorhis, T. V. J. Chem. Phys. **2011**, 134, 054128.

[86] Besley, N. A.; Gilbert, A. T. B.; Gill, P. M. W. J. Chem. Phys. **2009**, 130, 124308.

[87] Gilbert, A. T. B.; Besley, N. A.; Gill, P. M. W. J. Phys. Chem. A **2008**, 112, 13164–13171.

[88] Gaudoin, R.; Burke, K. Phys. Rev. Lett. **2004**, 93, 173001.

[89] Ziegler, T.; Krykunov, M.; Autschbach, J. J. Chem. Theory Comput. **2014**, 10, 3980–3986.

[90] Ziegler, T.; Seth, M.; Krykunov, M.; Autschbach, J.; Wang, F. J. Chem. Phys. **2009**, 130, 154102.

[91] Walter, C. Multi-Reference Methods for the Description of Molecules with a Complex Electronic Structure. Diploma thesis, Julius-Maximilians Universität Würzburg, 2011.

[92] Bytautas, L.; Henderson, T. M.; Jiménez-Hoyos, C. A.; Ellis, J. K.; Scuseria, G. E. J. Chem. Phys. **2011**, 135, 044119.

[93] Ridley, J.; Zerner, M. Theor. Chim. Acta **1973**, 32, 111–134.

[94] Silva-junior, M. R.; Thiel, W. J. Chem. Theory Comput. **2010**, 6, 1546–1564.

[95] Miralles, J.; Castell, O.; Caballol, R.; Malrieu, J.-P. Chem. Phys. **1993**, 172, 33–43.

[96] Shaik, S. S.; Hiberty, P. C. A chemist's guide to valence bond theory; JohnWiley and Sons, Inc., 2008.

[97] Merer, A.; Watson, J. K. J. Mol. Spectrosc. **1973**, 47, 499–514.

[98] Roos, B. O.; Taylor, P. R.; Siegbahn, P. E. Chem. Phys. **1980**, 48, 157–173.

[99] Banerjee, A.; Grein, F. Int. J. Quantum Chem. **1976**, 10, 123–134.

[100] Roos, B. r. O. Int. J. Quantum Chem. **1980**, 18, 175–189.

[101] Levy, B.; Berthier, G. Int. J. Quantum Chem. **1968**, 2, 307–319.

[102] Ruedenberg, K.; Cheung, L. M.; Elbert, S. T. Int. J. Quantum Chem. **1979**, 16, 1069–1101.

[103] Veryazov, V.; Malmqvist, P. r. A. k.; Roos, B. O. Int. J. Quantum Chem. **2011**, 111, 3329–3338.

[104] Pulay, P. Int. J. Quantum Chem. **2011**, 111, 3273–3279.

[105] Olsen, J. Int. J. Quantum Chem. **2011**, 111, 3267–3272.

[106] Truhlar, D. G. J. Comput. Chem. **2007**, 28, 73–86.

[107] Szalay, P. G.; Müller, T.; Gidofalvi, G.; Lischka, H.; Shepard, R. Chem. Rev. **2012**, 112, 108–181.

[108] Langhoff, S. R.; Davidson, E. R. Int. J. Quantum Chem. **1974**, 8, 61–72.

[109] Hanrath, M.; Engels, B. Chem. Phys. **1997**, 225, 197–202.

[110] Andersson, K.; Malmqvist, P. A.; Roos, B. O.; Sadlej, A. J.; Wolinski, K. J. Phys. Chem. **1990**, 94, 5483–5488.

[111] Andersson, K.; Malmqvist, P. A.; Roos, B. O. J. Chem. Phys. **1992**, 96, 1218–1226.

[112] Finley, J.; Malmqvist, P.-A.; Roos, B. O.; Serrano-Andrés, L. Chem. Phys. Lett. **1998**, 288, 299–306.

[113] Schreiber, M.; Silva-Junior, M. R.; Sauer, S. P. A.; Thiel, W. J. Chem. Phys. **2008**, 128, 134110.

[114] Lyakh, D. I.; Musial, M.; Lotrich, V. F.; Bartlett, R. J. Chem. Rev. **2012**, 112, 182–243.

[115] Thiel, W. NIC Series **2000**, 3, 261–283.

[116] Dewar, M. J. S.; Thiel, W. J. Am. Chem. Soc. **1977**, 99, 4899–4907.

[117] Fleming, I. Molecular Orbitals and Organic Chemical Reactions, Student Edition; John Wiley & Sons: Chichester, 2009.

[118] Dewar, M. J. S.; Zoebisch, E. G.; Healy, E. F.; Stewart, J. J. P. J. Am. Chem. Soc. **1985**, 107, 3902–3909.

[119] Rocha, G. B.; Freire, R. O.; Simas, A. M.; Stewart, J. J. P. J. Comput. Chem. **2006**, 27, 1101–1111.

[120] Stewart, J. J. P. J. Comput. Chem. **1989**, 10, 209–220.

[121] Stewart, J. J. Mol. Model **2007**, 13, 1173–1213.

[122] Kolb, M.; Thiel, W. J. Comput. Chem. **1993**, 14, 775–789.

[123] Weber, W.; Thiel, W. Theor. Chem. Acc. **2000**, 103, 495–506.

[124] Scholten, M. Semiempirische Verfahren mit Orthogonalisierungskorrekturen: Die OM3 Methode. Ph.D. thesis, Heinrich-Heine-Universitat Düsseldorf, 2003.

[125] Korth, M.; Thiel, W. J. Chem. Theory Comput. **2011**, 7, 2929–2936.

[126] Koslowski, A.; Beck, M. E.; Thiel, W. J. Comput. Chem. **2003**, 24, 714–726.

[127] MNDO V7.2
By Walter Thiel, Max-Planck-Institut fuer Kohlenforschung,
Kaiser-Wilhelm-Platz 1, D-45470 Muelheim, Germany.

[128] Kubo, R. J. Phys. Soc. Jpn. **1957**, 12, 570–586.

[129] Kuypers, F. Klassische Mechanik; Wiley-VCH: Weinheim, 2010.

[130] Rugh, W. J. Nonlinear system theory: the Volterra/Wiener approach; Johns Hopkins University Press: Weinheim, 1981.

[131] Greiner, W.; Reinhardt, J. Field Quantization; Springer-Verlag: Berlin Heidelberg, 1996.

[132] Wormit, M. Development and Application of Reliable Methods for the Calculation of Excited States: From Light-Harvesting Complexes to Medium-Sized Molecules. Ph.D. thesis, Johann Wolfgang Goethe-Universität in Frankfurt am Main, 2009.

[133] Oddershede, J. Int. J. Quantum Chem. **1982**, 22, 583–589.

[134] Kreyszig, E. Advanced Engineering Mathematics, 9^{th} edition; John Wiley & Sons, Inc.: Hoboken, 2006.

[135] Gross, E. K. U.; Maitra, N. T. Fundamentals of Time-Dependent Density Functional Theory; Springer-Verlag, Berlin-Heidelberg, 2011.

[136] van Leeuwen, R. Phys. Rev. Lett. **1999**, 82, 3863–3866.

[137] Brändas, E. J., Kryachko, E. S., Eds. Fundamental World of Quantum Chemistry, Volume III; Kluwer Academic Publishers: Dordrecht, 2004.

[138] Casida, M. E. In Recent Advances in Density Functional Methods, Part I; Chong, D. E., Ed.; World Scientific, Singapore, 1995.

[139] Schwabl, F. Statistical Mechanics; Springer Verlag: Berlin Heidelberg New York, 2002.

[140] Brückner, C. Theoretical Characterization of the Optoelectronic Properties of Merocyanines. Master thesis, Julius-Maximilians Universität Würzburg, 2014.

[141] Hirata, S.; Head-Gordon, M. Chem. Phys. Lett. **1999**, 314, 291–299.

[142] Laurent, A. D.; Jacquemin, D. Int. J. Quantum Chem. **2013**, 113, 2019–2039.

[143] Renz, M.; Theilacker, K.; Lambert, C.; Kaupp, M. J. Am. Chem. Soc. **2009**, 131, 16292–16302.

[144] Ziegler, T.; Seth, M.; Krykunov, M.; Autschbach, J.; Wang, F. J. Mol. Struct. **2009**, 914, 106–109.

[145] Cullen, J.; Krykunov, M.; Ziegler, T. Chem. Phys. **2011**, 391, 11–18.

[146] Savin, A. In Recent Developments and Applications of Modern Density Functional Theory; Seminario, J., Ed.; Elsevier, Amsterdam, 1996.

[147] Leininger, T.; Stoll, H.; Werner, H.-J.; Savin, A. Chem. Phys. Lett. **1997**, 275, 151–160.

[148] Gill, P. M. W.; Adamson, R. D.; Pople, J. A. Mol. Phys. **1996**, 88, 1005–1009.

[149] Dombroski, J. P.; Taylor, S. W.; Gill, P. M. W. J. Phys. Chem. **1996**, 100, 6272–6276.

[150] Iikura, H.; Tsuneda, T.; Yanai, T.; Hirao, K. J. Chem. Phys. **2001**, 115, 3540–3544.

[151] Tawada, Y.; Tsuneda, T.; Yanagisawa, S.; Yanai, T.; Hirao, K. J. Chem. Phys. **2004**, 120, 8425–8433.

[152] Yanai, T.; Tew, D. P.; Handy, N. C. Chem. Phys. Lett. **2004**, 393, 51–57.

[153] Vydrov, O. A.; Scuseria, G. E. J. Chem. Phys. **2006**, 125, 234109.

[154] Chai, J.-D.; Head-Gordon, M. Phys. Chem. Chem. Phys. **2008**, 10, 6615–6620.

[155] Körzdörfer, T.; Brédas, J.-L. Acc. Chem. Res. **2014**, 47, 3284–3291.

[156] Stein, T.; Kronik, L.; Baer, R. J. Am. Chem. Soc. **2009**, 131, 2818–2820.

[157] Karolewski, A.; Kronik, L.; Kümmel, S. J. Chem. Phys. **2013**, 138, 204115.

[158] Elliott, P.; Goldson, S.; Canahui, C.; Maitra, N. T. Chem. Phys. **2011**, 391, 110–119.

[159] Bartlett, R. J. J. Phys. Chem. **1989**, 93, 1697–1708.

[160] Christiansen, O.; Koch, H.; JÃ¸rgensen, P. Chem. Phys. Lett. **1995**, 243, 409–418.

[161] Hättig, C.; Weigend, F. J. Chem. Phys. **2000**, 113, 5154–5161.

[162] Hättig, C.; Köhn, A. J. Chem. Phys. **2002**, 117, 6939–6951.

[163] Köhn, A.; Hättig, C. J. Chem. Phys. **2003**, 119, 5021–5036.

[164] Hättig, C. In Response Theory and Molecular Properties (A Tribute to Jan Linderberg and Poul Jørgensen); Jensen, H., Ed.; Adv. Quantum Chem.; Academic Press, 2005; Vol. 50; pp 37–60.

[165] Grimme, S. J. Chem. Phys. **2003**, 118, 9095–9102.

[166] Fink, R. F. J. Chem. Phys **2010**, 133, 174113.

[167] Hellweg, A.; Grun, S. A.; Hättig, C. Phys. Chem. Chem. Phys. **2008**, 10, 4119–4127.

[168] Winter, N. O. C.; Graf, N. K.; Leutwyler, S.; Hättig, C. Phys. Chem. Chem. Phys. **2013**, 15, 6623–6630.

[169] Trofimov, A. B.; Schirmer, J. J. Phys. B: At., Mol. Opt. Phys. **1995**, 28, 2299.

[170] Schirmer, J. Phys. Rev. A **1982**, 26, 2395–2416.

[171] Schirmer, J.; Trofimov, A. B. J. Chem. Phys. **2004**, 120, 11449–11464.

[172] Starcke, J. H.; Wormit, M.; Schirmer, J.; Dreuw, A. Chem. Phys. **2006**, 329, 39–49.

[173] Harbach, P. H. P.; Wormit, M.; Dreuw, A. J. Chem. Phys. **2014**, 141, 064113.

[174] Nakatsuji, H. Chem. Phys. Lett. **1979**, 67, 329–333.

[175] Geertsen, J.; Rittby, M.; Bartlett, R. J. Chem. Phys. Lett. **1989**, 164, 57–62.

[176] Krylov, A. I. Annu. Rev. Phys. Chem. **2008**, 59, 433–462.

[177] Packer, M. J.; Dalskov, E. K.; Enevoldsen, T.; Jensen, H. J. r. A.; Oddershede, J. J. Chem. Phys. **1996**, 105, 5886–5900.

[178] van Setten, M. J.; Weigend, F.; Evers, F. J. Chem. Theory Comput. **2013**, 9, 232–246.

[179] Baumeier, B.; Andrienko, D.; Rohlfing, M. J. Chem. Theory Comput. **2012**, 8, 2790–2795.

[180] Moritz, G.; Hess, B. A.; Reiher, M. J. Chem. Phys. **2005**, 122, 024107.

[181] Marti, K. H.; Reiher, M. Phys. Chem. Chem. Phys. **2011**, 13, 6750–6759.

[182] Marti, K. H.; Reiher, M. Z. Phys. Chem. **2011**, 224, 583–599.

[183] Chan, G. K.-L.; Head-Gordon, M. J. Chem. Phys. **2002**, 116, 4462–4476.

[184] White, S. R. Phys. Rev. B **1993**, 48, 10345–10356.

[185] Neese, F. J. Chem. Phys. **2003**, 119, 9428–9443.

[186] Brøndsted Nielsen, S., Wyer, J. A., Eds. Photophysics of Ionic Biochromophores; Springer: Heidelberg, 2013.

[187] Chalasinski, G.; Szczesniak, M. M. Chem. Rev. **2000**, 100, 4227–4252.

[188] Tomasi, J.; Mennucci, B.; Cammi, R. Chem. Rev. **2005**, 105, 2999–3094.

[189] Humphrey, W.; Dalke, A.; Schulten, K. J. Mol. Graphics **1996**, 14, 33–38.

[190] Tomasi, J.; Persico, M. Chem. Rev. **1994**, 94, 2027–2094.

[191] Miertus, S.; Scrocco, E.; Tomasi, J. Chem. Phys. **1981**, 55, 117–129.

[192] Klamt, A.; Schuurmann, G. J. Chem. Soc., Perkin Trans. 2 **1993**, 799–805.

[193] TURBOMOLE V6.5 2013, a development of University of Karlsruhe and Forschungszentrum Karlsruhe GmbH, 1989-2007, TURBOMOLE GmbH, since 2007; available from
`http://www.turbomole.com`.

[194] Cossi, M.; Rega, N.; Scalmani, G.; Barone, V. J. Comput. Chem. **2003**, 24, 669–681.

[195] Frisch, M. J. et al. Gaussian 09 Revision D.01. Gaussian Inc. Wallingford CT 2009.

[196] Cancés, E.; Mennucci, B.; Tomasi, J. J. Chem. Phys. **1997**, 107, 3032–3041.

[197] Cammi, R.; Mennucci, B. J. Chem. Phys. **1999**, 110, 9877–9886.

[198] Cammi, R.; Corni, S.; Mennucci, B.; Tomasi, J. J. Chem. Phys. **2005**, 122, 104513.

[199] Caricato, M.; Mennucci, B.; Tomasi, J.; Ingrosso, F.; Cammi, R.; Corni, S.; Scalmani, G. J. Chem. Phys. **2006**, 124, 124520.

[200] Improta, R.; Barone, V.; Scalmani, G.; Frisch, M. J. J. Chem. Phys. **2006**, 125, 054103.

[201] Cossi, M.; Barone, V. J. Chem. Phys. **2000**, 112, 2427–2435.

[202] Corni, S.; Cammi, R.; Mennucci, B.; Tomasi, J. J. Chem. Phys. **2005**, 123, 134512.

[203] Press release, Royal Swedish Academy of Sciences. October 9, 2013.

[204] Warshel, A.; Levitt, M. J. Mol. Biol. **1976**, 103, 227–249.

[205] Field, M. J.; Bash, P. A.; Karplus, M. J. Comput. Chem. **1990**, 11, 700–733.

[206] Senn, H. M.; Thiel, W. Angew. Chem. Int. Ed. **2009**, 48, 1198–1229.

[207] Gao, J. Acc. Chem. Res. **1996**, 29, 298–305.

[208] Lin, H.; Truhlar, D. Theor. Chem. Acc. **2007**, 117, 185–199.

[209] Schmidt, T. C.; Paasche, A.; Grebner, C.; Ansorg, K.; Becker, J.; Lee, W.; Engels, B. In Electronic Effects in Organic Chemistry; Kirchner, B., Ed.; Top. Curr. Chem.; Springer Berlin Heidelberg, 2014; Vol. 351; pp 25–101.

[210] Zhang, R.; Lev, B.; Cuervo, J. E.; Noskov, S. Y.; Salahub, D. R. In Combining Quantum Mechanics and Molecular Mechanics. Some Recent Progresses in QM/MM Methods; Sabin, J. R., Brändas, E., Eds.; Adv. Quantum Chem.; Academic Press, 2010; Vol. 59; pp 353–400.

[211] Svensson, M.; Humbel, S.; Froese, R. D. J.; Matsubara, T.; Sieber, S.; Morokuma, K. J. Phys. Chem. **1996**, 100, 19357–19363.

[212] Allinger, N. L. Molecular Structure Understanding Steric and Electronic Effects from Molecular Mechanics; John Wiley & Sons, Inc.: Hoboken, 2010.

[213] Jorgensen, W. L.; Tirado-Rives, J. J. Am. Chem. Soc. **1988**, 110, 1657–1666.

[214] Jorgensen, W. L.; Maxwell, D. S.; Tirado-Rives, J. J. Am. Chem. Soc. **1996**, 118, 11225–11236.

[215] Söderhjelm, P.; Karlström, G.; Ryde, U. J. Chem. Phys. **2006**, 124, 244101.

[216] Engkvist, O.; Åstrand, P.-O.; Karlström, G. Chem. Rev. **2000**, 100, 4087–4108.

[217] Tafipolsky, M.; Engels, B. J. Chem. Theory Comput. **2011**, 7, 1791–1803.

[218] Ponder, J. W.; Wu, C.; Ren, P.; Pande, V. S.; Chodera, J. D.; Schnieders, M. J.; Haque, I.; Mobley, D. L.; Lambrecht, D. S.; DiStasio, R. A.; Head-Gordon, M.; Clark, G. N. I.; Johnson, M. E.; Head-Gordon, T. J. Phys. Chem. B **2010**, 114, 2549–2564.

[219] Stone, A. J. The Theory of Intermolecular Interactions, Second Edition; Clarendon Press: Oxford, 1996.

[220] Grimme, S. J. Chem. Theory Comput. **2014**, 10, 4497–4514.

[221] Besler, B. H.; Merz, K. M.; Kollman, P. A. J. Comput. Chem. **1990**, 11, 431–439.

[222] Singh, U. C.; Kollman, P. A. J. Comput. Chem. **1984**, 5, 129–145.

[223] Hirshfeld, F. Theor. Chim Acta **1977**, 44, 129–138.

[224] Glendening, E. D.; Landis, C. R.; Weinhold, F. WIREs Comput Mol Sci **2012**, 2, 1–42.

[225] Stone, A. Chem. Phys. Lett. **1981**, 83, 233–239.

[226] Wheatley, R. J.; Price, S. L. Mol. Phys. **1990**, 69, 507–533.

[227] Sokalski, W. A.; Lowrey, A. H.; Roszak, S.; Lewchenko, V.; Blaisdell, J.; Hariharan, P. C.; Kaufman, J. J. J. Comput. Chem. **1986**, 7, 693–700.

[228] Corner, J. Proc. R. Soc. A **1948**, 192, 275–292.

[229] Berne, B. J.; Pechukas, P. J. Chem. Phys. **1972**, 56, 4213–4216.

[230] Stone, A. Mol. Phys. **1978**, 36, 241–256.

[231] Price, S.; Stone, A. Mol. Phys. **1980**, 40, 805–822.

[232] Margenau, M.; Kestner, M. R. Theory of Intermolecular forces; Pergamon Press: Oxford, 1969.

[233] Murrell, J. N.; Randic, M.; Williams, D. R. Proc. R. Soc. A **1965**, 284, 566–581.

[234] Jensen, J. H.; Gordon, M. S. Mol. Phys. **1996**, 89, 1313–1325.

[235] Kutzelnigg, W. Einführung in die Theoretische Chemis; Wiley-VCH Verlag GmbH: Weinheim, 2002.

[236] Murrell, J.; Teixeira-Dias, J. Mol. Phys. **1970**, 19, 521–531.

[237] Gresh, N.; Claverie, P.; Pullman, A. Int. J. Quantum Chem. **1986**, 29, 101–118.

[238] Kim, Y. S.; Kim, S. K.; Lee, W. D. Chem. Phys. Lett. **1981**, 80, 574–575.

[239] Kita, S.; Noda, K.; Inouye, H. J. Chem. Phys. **1976**, 64, 3446–3449.

[240] Gavezzotti, A. J. Phys. Chem. B **2003**, 107, 2344–2353.

[241] Brdarski, S.; Karlström, G. J. Phys. Chem. A **1998**, 102, 8182–8192.

[242] Meier, K.; Thiel, W.; van Gunsteren, W. F. J. Comput. Chem. **2012**, 33, 363–378.

[243] Altun, A.; Shaik, S.; Thiel, W. J. Comput. Chem. **2006**, 27, 1324–1337.

[244] Lennartz, C.; Schäfer, A.; Terstegen, F.; Thiel, W. J. Phys. Chem. B **2002**, 106, 1758–1767.

[245] Sumowski, C. V.; Ochsenfeld, C. J. Phys. Chem. A **2009**, 113, 11734–11741.

[246] Kumbhar, S.; Fischer, F. D.; Waller, M. P. J. Chem. Inf. Model. **2012**, 52, 93–98.

[247] Albu, T. V.; Corchado, J. C.; Truhlar, D. G. J. Phys. Chem. A **2001**, 105, 8465–8487.

[248] Bernardi, F.; Olivucci, M.; Robb, M. A. J. Am. Chem. Soc. **1992**, 114, 1606–1616.

[249] Warshel, A.; Weiss, R. M. J. Am. Chem. Soc. **1980**, 102, 6218–6226.

[250] Aaqvist, J.; Warshel, A. Chem. Rev. **1993**, 93, 2523–2544.

[251] Shurki, A.; Crown, H. A. J. Phys. Chem. B **2005**, 109, 23638–23644.

[252] Gordon, M. S.; Freitag, M. A.; Bandyopadhyay, P.; Jensen, J. H.; Kairys, V.; Stevens, W. J. J. Phys. Chem. A **2001**, 105, 293–307.

[253] Gao, J.; Zhang, J. Z. H.; Houk, K. N. Acc. Chem. Res. **2014**, 47, 2711–2711.

[254] Pruitt, S. R.; Bertoni, C.; Brorsen, K. R.; Gordon, M. S. Acc. Chem. Res. **2014**, 47, 2786–2794.

[255] Xie, W.; Gao, J. J. Chem. Theory Comput. **2007**, 3, 1890–1900.

[256] Jeziorski, B.; Moszynski, R.; Szalewicz, K. Chem. Rev. **1994**, 94, 1887–1930.

[257] Bogumil, J.; Szalewicz, K.; Chalasinski, G. Int. J. Quantum Chem. **1978**, 14, 271–287.

[258] Jansen, G. WIREs Comput Mol Sci **2014**, 4, 127–144.

[259] Williams, H. L.; Chabalowski, C. F. J. Phys. Chem. A **2001**, 105, 646–659.

[260] Werner, H.-J.; Knowles, P. J.; Knizia, G.; Manby, F.; Schütz, M. MOLPRO, version 2012.1, a package of ab initio programs. 2012; see http://www.molpro.net.

[261] Ansorg, K.; Tafipolsky, M.; Engels, B. J. Phys. Chem. B **2013**, 117, 10093–10102.

[262] Wheeler, S. E.; Bloom, J. W. G. J. Phys. Chem. A **2014**, 118, 6133–6147.

[263] Grimme, S. Angew. Chem. Int. Ed. **2008**, 47, 3430–3434.

[264] Martinez, C. R.; Iverson, B. L. Chem. Sci. **2012**, 3, 2191–2201.

[265] Hunter, C. A.; Sanders, J. K. M. J. Am. Chem. Soc. **1990**, 112, 5525–5534.

[266] Cozzi, F.; Cinquini, M.; Annunziata, R.; Dwyer, T.; Siegel, J. S. J. Am. Chem. Soc. **1992**, 114, 5729–5733.

[267] Sinnokrot, M. O.; Sherrill, C. D. J. Phys. Chem. A **2006**, 110, 10656–10668.

[268] Wheeler, S. E. J. Am. Chem. Soc. **2011**, 133, 10262–10274.

[269] Wheeler, S. E.; Houk, K. N. J. Am. Chem. Soc. **2008**, 130, 10854–10855.

[270] Walter, C.; Ruetzel, S.; Diekmann, M.; Nuernberger, P.; Brixner, T.; Engels, B. J. Chem. Phys. **2014**, 140, 224311.

[271] Ruetzel, S.; Diekmann, M.; Nuernberger, P.; Walter, C.; Engels, B.; Brixner, T. Proc. Natl. Acad. Sci. USA **2014**, 111, 4764–4769.

[272] Brückner, C.; Walter, C.; Stolte, M.; Braida, B.; Meerholz, K.; Würthner, F.; Engels, B. J. Phys. Chem. C **2015**, 119, 17602–17611.

[273] Wüthner, F.; Meerholz, K. Chem. Eur. J. **2010**, 16, 9366–9373.

[274] Kronenberg, N. M.; Deppisch, M.; Wurthner, F.; Lademann, H. W. A.; Deing, K.; Meerholz, K. Chem. Commun. **2008**, 6489–6491.

[275] Bürckstümmer, H.; Tulyakova, E. V.; Deppisch, M.; Lenze, M. R.; Kronenberg, N. M.; Gsänger, M.; Stolte, M.; Meerholz, K.; Würthner, F. Angew. Chem. Int. Ed. **2011**, 50, 11628–11632.

[276] Dieckmann, A.; Bässler, H.; Borsenberger, P. M. J. Chem. Phys. **1993**, 99, 8136–8141.

[277] Steinmann, V.; Kronenberg, N. M.; Lenze, M. R.; Graf, S. M.; Hertel, D.; Meerholz, K.; Bürckstümmer, H.; Tulyakova, E. V.; Würthner, F. Adv. Energy Mater. **2011**, 1, 888–893.

[278] Beverina, L.; Pagani, G. A. Acc. Chem. Res. **2014**, 47, 319–329.

[279] Huang, L.; Stolte, M.; Bürckstümmer, H.; Würthner, F. Adv. Mater. **2012**, 24, 5750–5754.

[280] Liess, A.; Huang, L.; Arjona-Esteban, A.; Lv, A.; Gsänger, M.; Stepanenko, V.; Stolte, M.; Würthner, F. Adv. Funct. Mater. **2015**, 25, 44–57.

[281] Würthner, F.; Wortmann, R.; Meerholz, K. ChemPhysChem **2002**, 3, 17–31.

[282] Mulliken, R. S.; Person, W. Molecular Complexes - A Lecture and Reprint Volume; Jon Wiley and Sons, 1969.

[283] Wolff, J. J.; Wortmann, R. Adv. Phys. Org. Chem. **1999**, 32, 123.

[284] Marder, S. R.; Cheng, L.-T.; Tiemann, B. G.; Friedli, A. C.; Blanchard-Desce, M.; Perry, J. W.; Skindhøj, J. Science **1994**, 263, 511–514.

[285] Würthner, F.; Archetti, G.; Schmidt, R.; Kuball, H.-G. Angew. Chem. Int. Ed. **2008**, 47, 4529–4532.

[286] Gieseking, R. L.; Risko, C.; Brédas, J.-L. J. Phys. Chem. Lett. **0**, 0, 2158–2162.

[287] Mo, Y.; Peyerimhoff, S. D. J. Chem. Phys. **1998**, 109, 1687–1697.

[288] Mo, Y.; Gao, J.; Peyerimhoff, S. D. J. Chem. Phys. **2000**, 112, 5530–5538.

[289] Heimbeck, A. Umgebungseinflüsse auf die Geometrie und elektronischen Eigenschaften von Merocyaninen. Bachelor thesis, Julius-Maximilians Universität Würzburg, 2012.

[290] Boariu, A.-D. Quantum Mechanical Description of Merocyanine Dyes and Analysis of the Electronic Structure as a Function of Environment Polarity. Diploma thesis, Julius-Maximilians Universität Würzburg, 2012.

[291] Liu, F.; Morokuma, K. J. Am. Chem. Soc. **2013**, 135, 10693–10702.

[292] Bletz, M.; Pfeifer-Fukumura, U.; Kolb, U.; Baumann, W. J. Phys. Chem. A **2002**, 106, 2232–2236.

[293] Buback, J.; Kullmann, M.; Langhojer, F.; Nuernberger, P.; Schmidt, R.; Würthner, F.; Brixner, T. J. Am. Chem. Soc. **2010**, 132, 16510–16519.

[294] Buback, J.; Nuernberger, P.; Kullmann, M.; Langhojer, F.; Schmidt, R.; Würthner, F.; Brixner, T. J. Phys. Chem. A **2011**, 115, 3924–3935.

[295] Ruetzel, S.; Diekmann, M.; Nuernberger, P.; Walter, C.; Engels, B.; Brixner, T. J. Chem. Phys. **2014**, 140, 224310.

[296] Cottone, G.; Noto, R.; Manna, G. L. Chem. Phys. Lett. **2004**, 388, 218–222.

[297] Futami, Y.; Chin, M. L. S.; Kudoh, S.; Takayanagi, M.; Nakata, M. Chem. Phys. Lett. **2003**, 370, 460–468.

[298] Baraldi, I.; Momicchioli, F.; Ponterini, G.; Tatikolov, A. S.; Vanossi, D. Phys. Chem. Chem. Phys. **2003**, 5, 979–987.

[299] Vahtras, O.; Almlöf, J.; Feyereisen, M. Chem. Phys. Lett. **1993**, 213, 514–518.

[300] Eichkorn, K.; Treutler, O.; Öhm, H.; Häser, M.; Ahlrichs, R. Chem. Phys. Lett. **1995**, 242, 652–660.

[301] Weigend, F.; Haser, M. Theor. Chem. Acc. **1997**, 97, 331–340.

[302] Dunning, T. H. J. Chem. Phys. **1989**, 90, 1007–23.

[303] Zhao, Y.; Truhlar, D. G. J. Phys. Chem. A **2006**, 110, 10478–10486.

[304] Weigel, A.; Pfaffe, M.; Sajadi, M.; Mahrwald, R.; Improta, R.; Barone, V.; Polli, D.; Cerullo, G.; Ernsting, N. P.; Santoro, F. Phys. Chem. Chem. Phys. **2012**, 14, 13350–13364.

[305] Pedone, A. J. Chem. Theory Comput. **2013**, 9, 4087–4096.

[306] Jacquemin, D.; Zhao, Y.; Valero, R.; Adamo, C.; Ciofini, I.; Truhlar, D. G. J. Chem. Theory Comput. **2012**, 8, 1255–1259.

[307] Becke, A. D. Phys. Rev. A **1988**, 38, 3098–3100.

[308] Renz, M.; Kess, M.; Diedenhofen, M.; Klamt, A.; Kaupp, M. J. Chem. Theory Comput. **2012**, 8, 4189–4203.

[309] Cao, J.; Wu, T.; Hu, C.; Liu, T.; Sun, W.; Fan, J.; Peng, X. Phys. Chem. Chem. Phys. **2012**, 14, 13702–13708.

[310] Mennucci, B. private communication.

[311] Jacquemin, D.; Chibani, S.; Le Guennic, B.; Mennucci, B. J. Phys. Chem. A **2014**, 118, 5343–5348.

[312] González-Luque, R.; Garavelli, M.; Bernardi, F.; Merchán, M.; Robb, M. A.; Olivucci, M. Proc. Natl. Acad. Sci. USA **2000**, 97, 9379–9384.

[313] Kobayashi, R.; Amos, R. D. Mol. Phys. **2013**, 111, 1574–1579.

[314] Scuseria, G. E.; Janssen, C. L.; Schaefer, H. F. J. Chem. Phys. **1988**, 89, 7382–7387.

[315] Pople, J. A.; Head-Gordon, M.; Raghavachari, K. J. Chem. Phys. **1987**, 87, 5968–5975.

[316] Heyd, J.; Scuseria, G. E. J. Chem. Phys. **2004**, 121, 1187–1192.

[317] Poelking, C.; Tietze, M.; Elschner, C.; Olthof, S.; Hertel, D.; Baumeier, B.; Würthner, F.; Meerholz, F.; Leo, K.; Andrienko, D. Nat. Mater. **2015**, 14, 434–439.

[318] Chen, Z.; Ying, F.; Chen, X.; Song, J.; Su, P.; Song, L.; Mo, Y.; Zhang, Q.; Wu, W. Int. J. Quantum Chem. **2015**, 115, 731–737.

[319] Castet, F.; D'Avino, G.; Muccioli, L.; Cornil, J.; Beljonne, D. Phys. Chem. Chem. Phys. **2014**, 16, 20279–20290.

[320] Wurthner, F. Chem. Commun. **2004**, 1564–1579.

[321] Li, C.; Wonneberger, H. Adv. Mater. **2012**, 24, 613–636.

[322] Zang, L.; Liu, R.; Holman, M. W.; Nguyen, K. T.; Adams, D. M. J. Am. Chem. Soc. **2002**, 124, 10640–10641.

[323] Wurthner, F.; Stolte, M. Chem. Commun. **2011**, 47, 5109–5115.

[324] Schmidt-Mende, L.; Fechtenkötter, A.; Müllen, K.; Moons, E.; Friend, R. H.; MacKenzie, J. D. Science **2001**, 293, 1119–1122.

[325] Howard, I. A.; Laquai, F.; Keivanidis, P. E.; Friend, R. H.; Greenham, N. C. J. Phys. Chem. C **2009**, 113, 21225–21232.

[326] Settels, V.; Liu, W.; Pflaum, J.; Fink, R. F.; Engels, B. J. Comput. Chem. **2012**, 33, 1544–1553.

[327] Seibt, J.; Marquetand, P.; Engel, V.; Chen, Z.; Dehm, V.; Würthner, F. Chem. Phys. **2006**, 328, 354–362.

[328] Bulovic, V.; Burrows, P.; Forrest, S.; Cronin, J.; Thompson, M. Chem. Phys. **1996**, 210, 1–12.

[329] Liu, W.; Settels, V.; Harbach, P. H. P.; Dreuw, A.; Fink, R. F.; Engels, B. J. Comput. Chem. **2011**, 32, 1971–1981.

[330] Klebe, G.; Graser, F.; Hädicke, E.; Berndt, J. Acta Crystallogr. Sect. B-Struct. Sci. **1989**, 45, 69–77.

[331] Zhao, H.-M.; Pfister, J.; Settels, V.; Renz, M.; Kaupp, M.; Dehm, V. C.; Würthner, F.; Fink, R. F.; Engels, B. J. Am. Chem. Soc. **2009**, 131, 15660–15668.

[332] Settels, V.; Schubert, A.; Tafipolski, M.; Liu, W.; Stehr, V.; Topczak, A. K.; Pflaum, J.; Deibel, C.; Fink, R. F.; Engel, V.; Engels, B. J. Am. Chem. Soc. **2014**, 136, 9327–9337.

[333] Shirai, S.; Iwata, S.; Tani, T.; Inagaki, S. J. Phys. Chem. A **2011**, 115, 7687–7699.

[334] Van Voorhis, T.; Kowalczyk, T.; Kaduk, B.; Wang, L.-P.; Cheng, C.-L.; Wu, Q. Annu. Rev. Phys. Chem. **2010**, 61, 149–170.

[335] Mead, C. A.; Truhlar, D. G. J. Chem. Phys. **1982**, 77, 6090–6098.

[336] Casanova, D. Int. J. Quantum Chem. **2015**, 115, 442–452.

[337] Hariharan, P.; Pople, J. Theor. Chim. Acta **1973**, 28, 213–222.

[338] Liu, W. Exciton Coupling in Valence and Core Excited Aggregates of π-Conjugated Molecules. Ph.D. thesis, Julius-Maximilians-Universität Würzburg, 2011.

[339] Schäfer, A.; Horn, H.; Ahlrichs, R. J. Chem. Phys. **1992**, 97, 2571–2577.

[340] Schäfer, A.; Huber, C.; Ahlrichs, R. J. Chem. Phys. **1994**, 100, 5829–5835.

[341] Chai, J.-D.; Head-Gordon, M. J. Chem. Phys. **2008**, 128, 084106.

[342] Nenon, S.; Champagne, B.; Spassova, M. I. Phys. Chem. Chem. Phys. **2014**, 16, 7083–7088.

[343] Mikoajczyk, M. M.; Zalesny, R.; Czyznikowska, Z.; Toman, P.; Leszczynski, J.; Bartkowiak, W. J. Mol. Model **2011**, 17, 2143–2149.

[344] Civalleri, B.; Presti, D.; Dovesi, R.; Savin, A. Chemical Modelling: Applications and Theory Volume 9; The Royal Society of Chemistry, 2012; Vol. 9; pp 168–185.

[345] Förster, T. Ann. Phys. **1948**, 437, 55–75.

[346] Walter, C.; Krämer, V.; Settels, V.; Engels, B. Chem. Unserer Zeit **2013**, 47, 142–142.

[347] Krämer, V. Validation of Semiempiric Methods fir the Description of Excited States of Aggregates of Perylene Bisimides. Bachelor thesis, Julius-Maximilians Universität Würzburg, 2012.

[348] Schatz, G. C.; Ratner, M. A. Quantum Mechanics in Chemistry; Dover Publications, Inc., 20082.

[349] Dirac, P. A. M. Proc. R. Soc. A **1927**, 114, 243–265.

[350] Fink, R.; Pfister, J.; Schneider, A.; Zhao, H.; Engels, B. Chem. Phys. **2008**, 343, 353–361.

[351] Hehre, W. J.; Stewart, R. F.; Pople, J. A. J. Chem. Phys. **1969**, 51, 2657–2664.

[352] Scholes, G. D.; Ghiggino, K. P. J. Chem. Phys. **1994**, 101, 1251–1261.

[353] Harcourt, R. D.; Scholes, G. D.; Ghiggino, K. P. J. Chem. Phys. **1994**, 101, 10521–10525.

[354] Scholes, G. D.; Harcourt, R. D.; Ghiggino, K. P. J. Chem. Phys. **1995**, 102, 9574–9581.

[355] Eaton, J. W.; Bateman, D.; Hauberg, S.; Wehbring, R. GNU Octave version 3.6.3 manual: a high-level interactive language for numerical computations; 2015.

[356] Kaminski, G.; Jorgensen, W. L. J. Phys. Chem. **1996**, 100, 18010–18013.

[357] Jorgensen, W. L.; Laird, E. R.; Nguyen, T. B.; Tirado-Rives, J. J. Comput. Chem. **1993**, 14, 206–215.

[358] Ponder, J. W.; Richards, F. M. J. Compu. Chem. **1987**, 8, 1016–1024.

[359] Hu, H.; Lu, Z.; Yang, W. J. Chem. Theory Comput. **2007**, 3, 1004–1013.

[360] Ferman, T., Justin; Valeev, E. F. Fundamentals of Molecular Integrals Evaluation.

[361] Valeev, E. F. The Root of All Good: Molecular Inetgrals. 2007.

[362] Smith, C.; Hall, G. Theor. Chem. Acc. **1986**, 69, 63–69.

[363] Braunschweig, H.; Dyakonov, V.; Engels, B.; Falk, Z.; Hörl, C.; Klein, J. H.; Kramer, T.; Kraus, H.; Krummenacher, I.; Lambert, C.; Walter, C. Angew. Chem. Int. Ed. **2013**, 52, 12852–12855.

[364] Tol, A. Synt. Met. **1995**, 74, 95–98.

[365] van Haare, J. A. E. H.; Havinga, E. E.; van Dongen, J. L. J.; Janssen, R. A. J.; Cornil, J.; Brédas, J.-L. Chem. Eur. J. **1998**, 4, 1509–1522.

[366] Zheng, S.; Barlow, S.; Risko, C.; Kinnibrugh, T. L.; Khrustalev, V. N.; Jones, S. C.; Antipin, M. Y.; Tucker, N. M.; Timofeeva, T. V.; Coropceanu, V.; Brédas, J.-L.; Marder, S. R. J. Am. Chem. Soc. **2006**, 128, 1812–1817.

[367] Aquilante, F.; Boman, L.; Boström, J.; Koch, H.; Lindh, R.; de Merás, A. S.; Pedersen, T. In Linear-Scaling Techniques in Computational Chemistry and Physics; Zalesny, R., Papadopoulos, M. G., Mezey, P. G., Leszczynski, J., Eds.; Challenges and Advances in Computational Chemistry and Physics; Springer Netherlands, 2011; Vol. 13; pp 301–343.

[368] Aquilante, F.; De Vico, L.; Ferré, N.; Ghigo, G.; Malmqvist, P.; Neogrády, P.; Pedersen, T. B.; Pitonák, M.; Reiher, M.; Roos, B. r. O.; Serrano-Andrés, L.; Urban, M.; Veryazov, V.; Lindh, R. J. Comput. Chem. **2010**, 31, 224–247.

[369] Veryazov, V.; Widmark, P.-O.; Serrano-Andrés, L.; Lindh, R.; Roos, B. r. O. Int. J. Quantum Chem. **2004**, 100, 626–635.

[370] Karlström, G.; Lindh, R.; Malmqvist, P.; rn O Roos, B.; Ryde, U.; Veryazov, V.; Widmark, P.-O.; Cossi, M.; Schimmelpfennig, B.; Neogrady, P.; Seijo, L. Comput. Mater. Sci. **2003**, 28, 222–239.

[371] Atkins, P. W.; Friedman, R. S. Molecular Quantum Mechanics; Oxford University Press, 1983.

[372] Kleinschmidt, M.; Tatchen, J.; Marian, C. M. J. Comput. Chem. **2002**, 23, 824–833.

[373] of Ockham, W. Quaestiones et decisiones in quattuor libros Sententiarum Petri Lombardi. 1495.

[374] Schaftenaar, G.; Noordik, J. J. Comput. Aid. Mol. Des. **2000**, 14, 123–134.

[375] Auerswald, J.; Engels, B.; Fischer, I.; Gerbich, T.; Herterich, J.; Krueger, A.; Lang, M.; Schmitt, H.-C.; Schon, C.; Walter, C. Phys. Chem. Chem. Phys. **2013**, 15, 8151–8161.

[376] Witte, G.; Wöll, C. Phys. Status Solidi A **2008**, 205, 497–510.

[377] Plasser, F.; Pasalic, H.; Gerzabek, M. H.; Libisch, F.; Reiter, R.; Burgdörfer, J.; Müller, T.; Shepard, R.; Lischka, H. Angew. Chem. Int. Ed. **2013**, 52, 2581–2584.

[378] Bonaccorso, F.; Sun, Z.; Hasan, T.; Ferrari, A. C. Nature Photon. **2010**, 4, 497–510.

[379] Shaik, S.; Shurki, A.; Danovich, D.; Hiberty, P. C. Chem. Rev. **2001**, 101, 1501–1540.

[380] Rubio, M.; Merchán, M.; Ortí, E.; Roos, B. Chem. Phys. **1994**, 179, 395–409.

[381] Send, R.; Kühn, M.; Furche, F. J. Chem. Theory and Comput. **2011**, 7, 2376–2386.